UNIVERSIDAD POLITÉCNICA DE MADRID

ESCUELA TÉCNICA SUPERIOR DE INGENIEROS INDUSTRIALES

PROPRIOCEPTIVE FORCE ESTIMATION AND CONTROL FOR TELEOPERATION IN RADIOACTIVE ENVIRONMENTS

DOCTOR OF PHILOSOPHY

AUTOMATION AND ROBOTICS

ENRIQUE CONSTANTINO DEL SOL ACERO

Ingeniero Industrial

2015

DEPARTAMENTO DE AUTOMÁTICA, INGENIERÍA ELECTRÓNICA E INFORMATICA INDUSTRIAL

ESCUELA TÉCNICA SUPERIOR DE INGENIEROS INDUSTRIALES

PROPRIOCEPTIVE FORCE ESTIMATION AND CONTROL FOR TELEOPERATION IN RADIOACTIVE ENVIRONMENTS

DOCTOR OF PHILOSOPHY

Author: Enrique Constantino del Sol Acero
Ingeniero Industrial

Advisors: Mr. Manuel Ferre Pérez
Dr. Ingeniero Industrial

Mr. Robin George Scott
PhD Mechanical Engineer

PROPRIOCEPTIVE FORCE ESTIMATION AND CONTROL FOR TELEOPERATION IN RADIOACTIVE ENVIRONMENTS

Autor: Enrique Constantino del Sol Acero

Tribunal

Presidente: D. Manuel Ángel Armada Rodríguez

Secretario: D. Miguel Hernando Gutiérrez

Vocal A: D. Jouni Mattila

Vocal B: D. Michael William Hardt González

Vocal C: D. Juan Antonio Escalera Piña

Suplente A: D. José María Azorín Poveda

Suplente B: D. Antonio Giménez Fernández

Acuerdan otorgar la calificación de:

Madrid, de de 2015

To my family: Mom, Dad and Julián and
to Maria

Agradecimientos

Durante los años en los que he realizado mi investigación y la escritura de esta tesis, he vivido experiencias inolvidables y he conocido personas que han marcado el desarrollo de mi trabajo.

No es fácil abandonar tu lugar de origen para empezar una nueva etapa en un país diferente, pero es una experiencia muy recomendable que gracias a la Comisión Europea y al gran programa Marie Curie he podido disfrutar.

Aún recuerdo la primera charla que tuve con Manuel Ferre acerca del que acabaría siendo mi futuro destino, Oxford Technologies. Debo dar las gracias a él y a sus consejos, con los que he aprendido todo lo que necesitaba saber para comenzar mi investigación. Sus enseñanzas y las discusiones que tuve con él siempre me motivaron y aportaron nuevos caminos por donde seguir mejorando. Una lástima que no hayamos podido pasar más tiempo juntos.

Por supuesto, no podía faltar mi agradecimiento a todo Oxford Technologies Ltd., en especial a Alan Rolfe que siempre me mostro su apoyo y confianza. Estoy seguro que jamás tendré un jefe al que admire tanto. Muchas gracias a mis supervisores durante los años de investigación, Robin Scott y Ryan King. Sus comentarios y ayuda fueron muy valiosos. Muchas gracias también a todos mis compañeros, en especial a Chris y Zino con quienes compartí más horas durante mi trabajo y con quienes pase muy buenos momentos. Gracias también a Richard, por compartir su experiencia en electrónica y radiación. Tampoco puedo olvidarme de Nelo y Simon que me ayudaron durante la revisión de esta tesis. Gracias otra vez al excelente equipo de OTL que tan bien dirigido está. Durante mi trabajo en las oficinas de Abingdon conocí lo que es de

verdad la manipulación remota y su importancia para la energía de fusión y el desmantelamiento nuclear. La creatividad de sus ingenieros y la forma de abordar los problemas de la industria me han aportado una experiencia de un valor incalculable.

Durante mi investigación he tenido el placer de conocer y colaborar con profesionales de diferentes instituciones dentro del programa PURESAFE, ejemplo de ello son Prithvi Pagala, Ramviyas Parasuraman, Héctor Martínez que se han acabado convirtiendo en amigos. También durante mis estancias en la UPM he tenido oportunidad de conocer a investigadores como José Breñosa que me facilitó la ya de por sí difícil tarea de toma de datos y Manuel Armada, director del Centro de Automática y Robótica UPM-CSIC. Gracias también a Rafael Aracil, cuyos consejos fueron claves para el desarrollo de la parte final de mi investigación.

Me gustaría resaltar también la inestimable ayuda que recibí durante mi estancia en el CERN de Pierre Bonnal y Keith Kershaw. Gracias Keith por tus siempre interesantes comentarios y recomendaciones.

Gracias también a Alex por sus comentarios sobre esta tesis y a aquellas tardes de fines de semana.

No me puedo olvidar de mis visitas a Tampere University of Technology y al GSI Helmholtz Centre for Heavy Ion Research donde recibí formación muy interesante y pude conocer de primera mano instituciones de investigación tan prestigiosas gracias a la excelente organización de Jouni Mattila, coordinador del programa PURSAFE.

Durante la última etapa de mi tesis tuve ocasión de colaborar con Fusion for Energy donde compartí muy interesantes reuniones con Emilio Ruiz Morales acerca de las implicaciones de cables muy largos en el control de motores. Aprendí mucho de sus ideas y espíritu crítico.

Por último, quisiera concluir recordando a las personas más importantes en mi vida, mis padres, mi hermano y mi pareja. Mi agradecimiento más sincero a María Carmen, sin ella nada de esto hubiera sido posible. Juntos nos embarcamos en esta aventura que es ir a vivir a oro lugar, tan diferente. Gracias por tu ayuda y paciencia. También muchas gracias a mi padre, del quien recibí la primera información sobre el programa de becas. Y como no, a mi madre, por echarme de menos y esperarme siempre con tanta ilusión. Gracias a Julián, por venir a verme y hacerme reír.

Enrique del Sol

Acknowledgements

During the years I have been performing my research and writing this thesis, I have lived unforgettable experiences and I have met people who have influenced the development of my work.

It is not easy to abandon your country of origin to start a new period in a different country, however it is quite advisable experience that thanks to the European Commission and the Marie Curie grants programme I have managed to enjoy it.

I still remember my first meeting with Manuel Ferre to discuss about what it would end up being my destiny, Oxford Technologies. Thanks to him and his advice with which I have learnt all I needed to start my research. His teachings and the discussions we maintained always motivated me and gave me new paths to follow and ways to improve. It is a shame we could not invest more time together.

Of course, it could not be missed in my acknowledgments, the reference to Oxford Technologies, especially to Alan Rolfe who always showed me his support and confidence. I am completely sure that I will never have a boss who I admire that much. Thank you very much to my supervisors during these years of research, Robin Scott and Ryan King. Their comments and help were greatly valuable. Thank you very much to my colleagues as well, especially to Chris and Zino with whom I shared most of the time during my work and spent so many good moments. Thanks as well to Richard, to share his expertise in electronics and radiation. I cannot forget Nelo and Simon who helped me during the review of this thesis. Thanks again to the excellent team of OTL which is managed that well. During my work in Abingdon's offices, I truly met what the remote handling is and its importance for the fusion energy and nuclear decommissioning. The creativity of his engineers and their way to solve industry problems have given me an invaluable experience.

During my research I have had the opportunity to meet and collaborate with professionals from different institutions within the PURESAFE program. Example of that are, Prithvi Pagala, Ramviyas Parasuraman, Héctor Martínez, who have ended up becoming friends. Also, during my secondments at UPM I had the opportunity of meet researchers such as: José Breñosa, who ease the difficult task of data acquisition and

Manuel Armada, director of Centre for Automation and Robotics UPM-CSIC. Thanks as well to Rafael Aracil, whose advises were key points for the development of the last part of this research.

I would like to emphasise as well the help I received during my secondments at CERN from Pierre Bonnal and Keith Kershaw. Thank you Keith for your always interesting comments and advices.

Thanks you Alex for his comments about this Thesis and the good moments that we had during the weekends.

I cannot forget my trips to Tampere University of Technology and GSI Helmholtz Centre for Heavy Ion Research where I received very interesting training and I could know in person important and prestigious research institutions thanks to the excellent organisation of Jouni Matila, coordinator of PURESAFE program.

During the last stage of my thesis I had the chance to collaborate with Fusion for Energy when I shared very interesting meetings with Emilio Ruiz Morales about the implications of very long cables in motor control. I learnt a lot from his ideas and curiosity.

And last but not least, I would like to conclude remembering the most important people in my life, my parents, my brother and my partner. My most sincere acknowledgement to María Carmen, without her, none of this would have been possible. Together we embarked on this adventure that is living in a different place, so different. Thanks for your support and patience. Also, thanks to my father from whom I received the first information about the grants program. And also to my mother, for missing me and always waiting for me with such illusion. Thank you Julián, for coming to see me and make me laugh.

Enrique del Sol

Resumen

A medida que se incrementa la energía de los aceleradores de partículas o iones pesados como el CERN o GSI, de los reactores de fusión como JET o ITER, u otros experimentos científicos, se va haciendo cada vez más imprescindible el uso de técnicas de manipulación remota para la interacción con el entorno sujeto a la radiación. Hasta ahora la tasa de dosis radioactiva en el CERN podía tomar valores cercanos a algunos mSv para tiempos de enfriamiento de horas, que permitían la intervención humana para tareas de mantenimiento. Durante los primeros ensayos con plasma en JET, se alcanzaban valores cercanos a los 200 µSv después de un tiempo de enfriamiento de 4 meses y ya se hacía extensivo el uso de técnicas de manipulación remota. Hay una clara tendencia al incremento de los niveles de radioactividad en el futuro en este tipo de instalaciones. Un claro ejemplo es ITER, donde se esperan valores de 450 Sv/h en el centro del toroide a los 11 días de enfriamiento o los nuevos niveles energéticos del CERN que harán necesario una apuesta por niveles de mantenimiento remotos.

En estas circunstancias se enmarca esta tesis, que estudia un sistema de control bilateral basado en fuerza-posición, tratando de evitar el uso de sensores de fuerza/par, cuyo contenido electrónico los hace especialmente sensibles en estos ambientes. El contenido de este trabajo se centra en la teleoperación de robots industriales, que debido a su reconocida solvencia y facilidad para ser adaptados a estos entornos, unido al bajo coste y alta disponibilidad, les convierte en una alternativa interesante para tareas de manipulación remota frente a costosas soluciones a medida.

En primer lugar se considera el problema cinemático de teleoperación maestro-esclavo de cinemática disimilar y se desarrolla un método general para la solución del problema en el que se incluye el uso de fuerzas asistivas para guiar al operador. A continuación se explican con detalle los experimentos realizados con un robot ABB y que muestran las dificultades encontradas y recomendaciones para solventarlas. Se concluye el estudio cinemático con un método para el encaje de espacios de trabajo entre maestro y esclavo disimilares. Posteriormente se mira hacia la dinámica, estudiándose el modelado de robots con vistas a obtener un método que permita estimar las fuerzas externas que actúan sobre los mismos. Durante la caracterización del modelo dinámico, se realizan varios ensayos para tratar de encontrar un compromiso entre complejidad de

cálculo y error de estimación. También se dan las claves para modelar y caracterizar robots con estructura en forma de paralelogramo y se presenta la arquitectura de control deseada. Una vez obtenido el modelo completo del esclavo, se investigan diferentes alternativas que permitan una estimación de fuerzas externas en tiempo real, minimizando las derivadas de la posición para minimizar el ruido. Se comienza utilizando observadores clásicos del estado para ir evolucionando hasta llegar al desarrollo de un observador de tipo Luenberger-Sliding cuya implementación es relativamente sencilla y sus resultados contundentes.

También se analiza el uso del observador propuesto durante un control bilateral simulado en el que se compara la realimentación de fuerzas obtenida con las técnicas clásicas basadas en error de posición frente a un control basado en fuerza-posición donde la fuerza es estimada y no medida. Se comprueba como la solución propuesta da resultados comparables con las arquitecturas clásicas y sin embargo introduce una alternativa para la teleoperación de robots industriales cuya teleoperación en entornos radioactivos sería imposible de otra manera.

Finalmente se analizan los problemas derivados de la aplicación práctica de la teleoperación en los escenarios mencionados anteriormente. Debido a las condiciones prohibitivas para todo equipo electrónico, los sistemas de control se deben colocar a gran distancia de los manipuladores, dando lugar a longitudes de cable de centenares de metros. En estas condiciones se crean sobretensiones en controladores basados en PWM que pueden ser destructivas para el sistema formado por control, cableado y actuador, y por tanto, han de ser eliminadas. En este trabajo se propone una solución basada en un filtro LC comercial y se prueba de forma extensiva que su inclusión no produce efectos negativos sobre el control del actuador.

Abstract

As the energy on the particle accelerators or heavy ion accelerators such as CERN or GSI, fusion reactors such as JET or ITER, or other scientific experiments is increased, it is becoming increasingly necessary to use remote handling techniques in order to interact with the remote and radioactive environment. So far, the dose rate at CERN could present values near several mSv for cooling times in the range of hours, which allowed human intervention for maintenance tasks. At JET, values close to 200 µSv have been measured after a cooling time of 4 months. Since then, the use of remote handling techniques became usual. There is a clear tendency to increase the radiation levels in the future. A good example is ITER, where values of 450 Sv/h are expected in the centre of the torus after 11 days of cooling. Also, the new energetic levels of CERN are expected to lead towards a more advanced remote handling means in this facility.

The framework of this thesis is based on these environments. It develops a bilateral control system based on force-position, trying to avoid the use of force/torque sensors, whose electronic content makes them very sensitive under radiation. Thus, the research it is focused on teleoperating industrial robots, which due to its well-known reliability, easiness to be adapted to harsh environments, cost-effectiveness and high availability, are considered as an interesting alternative to expensive custom-made solutions for remote handling tasks.

Firstly, the kinematic problem of teloperating master and slave with dissimilar kinematics is analysed and a new general approach for solving this issue is presented. The solution includes the use of assistive forces in order to guide the human operator. Coming up next, I explain with detail the experiments accomplished with an ABB robot, showing the difficulties encountered and the proposed solutions. This section is concluded with a method to match the master's and slave's workspaces when they present dissimilar kinematics. Afterwards, the research enters into the robot dynamics, with special focus on robot modelling. This has the purpose of obtaining a method that allows to estimate external forces acting on these devices. During the characterisation of the robot's parameters, a set of tests are performed in order to get to a compromise between computational complexity and estimation error. Key points for modelling and

characterising robots with a parallelogram structure are also given, and the desired control architecture is introduced. Once a complete model of the slave is obtained, different alternatives for external force estimation are reviewed. They allow to predict forces in real time, minimizing the position differentiation to reduce the noise of the estimation. The research starts by implementing classic state observers and then it evolves towards the use of Luenberger-Sliding observers whose implementation is relatively easy and the results are convincing.

I also analyse the use of proposed observer during a simulated bilateral control. During this experiment, the force feedback obtained with the classic techniques based on the position error is compared with a control architecture based on force-position, where the force is estimated instead of measured. It is proved how the proposed solution gives results comparable with the classical techniques, however, it introduces an alternative method for teleoperating industrial robots whose teleoperation in radioactive environments would have been impossible in a different way.

Finally, the problems originated by the practical application of teleoperation in the before mentioned scenarios are analysed. Due to the prohibitive conditions for every electronic equipment, the control systems should be placed far from the manipulators. This provokes that the power cables that fed the slaves devices can present lengths of hundreds of meters. In these circumstances, reflections are developed when implementing drives based on PWM technique. The occurrence of overvoltage is very dangerous for the system composed by drive, wiring and actuator, and has to be eliminated. During this work, a solution based on commercial LC filters is proposed and it is extensively proved that its use does not introduce adverse effects into the actuator's control.

Contents

List of Figures

List of Tables

Chapter 1 Introduction

This chapter introduces the work developed during this thesis. It explains the main areas of research in order to perform bilateral teleoperation in facilities with ionizing radiation. The requirements of such environments are also highlighted. Different methods and technologies are reviewed. The motivations behind the development of a new set of algorithms and methods, the main goals and the outline of this thesis are also introduced.

1.1 Overview

External force estimation methods provide means of quantification of the forces and torques exerted into a system without employing a direct measurement via force/torque sensor. Nowadays, most advanced force/torque sensors can provide a very reliable 6 degrees of freedom force measurement by attaching them on a robot end-effector or by means of using a torque meter in each robotic joint. These solutions although considered very reliable, are not always feasible or preferred, and other methods have to be explored. These methods are typically based on force observers and involve a complicated process of robotic modelling, parameter´s identification, design and final implementation. The final goal of this process is to obtain a reliable model which allows the prediction of the external forces applied into the robot by knowing the robot current state and the commanded input. The estimated external forces and torques can be used for different purposes such as condition monitoring, impact detection or force feedback.

The teleoperation of slave manipulators has been developed since mid-20^{th} century to carry out remote handling operations in certain environments where the human access is not possible or prohibitive. These environments are typically characterized by three different issues, which are: dangerous conditions, scale problems and productivity issues. Examples of dangerous conditions are the telerobotics operations deployed for bomb disposal robots, nuclear research, fission maintenance or fusion maintenance, fire-fighting robots, etc. When the environmental conditions are characterized by inaccessible environments, the areas to study are: duct cleaning robots, mega-assembly robotics or nano-assembly. In several circumstances, it can be more productive to design and build a robot to be teleoperated in a remote environment than carry out the same operation by means of human intervention. Some examples of this are: offshore wind farm, oilrig rescue, subsea operations, etc. There are also circumstances where the former issues are combined leading to a major problem, as for example, difficult scale conditions with productivity issues, as the surgical robotics.

Historically, the most dexterous remote handling operations have been developed for the nuclear industry to avoid the human exposure to radiation. They have employed articulated arms to reproduce the human movements into the remote environment. These are commanded by a master device controlled by an operator situated in a safe environment. The force feedback presented to the operator has been typically created by means of the positional error between master and slave, taking advantage of the backdrivable mechanical design of these haptic systems. Other solutions mount a 6 dof

force/torque sensor to measure directly the external forces applied on the manipulator´s end-effector. In this thesis, an alternative method is proposed, which makes use of the estimated joint torque to present the master device controlled by the operator with a scaled version of the predicted torque. This solution opens new paradigms to the nuclear research with the use of more cost-effective industrial robots without back-drivable design avoiding the use of electronic equipment on the end-effector. In order to provide a realistic force feedback to the human operator, advances in the following areas are required: i) dissimilar master-slave teleoperation algorithms which are able to optimise the use of the workspace, ii) robot modelling and parameters identification, iii.) force estimation algorithms with proper implementation and iv.) motor control by means of long cables.

In this thesis, an overview of the currently available technologies for robot model characterization, force estimation and its application for teleoperation are considered with special focus to radioactive environments. These sorts of environments introduce tough constraints that need to be overcome. Applications of this technology are described.

This work has been funded by a 3-year "Marie Curie Early Stage Initial Training Network" fellowship, under the European Community's Seventh Framework Programme, contract number PITN-GA-2010-264336-PURESAFE. During the development of this thesis I have investigated the above mentioned topics, I have participated in numerous project meetings, conferences, joint-events and attended courses related to my research interest with the objective of reducing the human intervention for increased safety in ionizing environments. Most of the research have been carried out in the Research Department at Oxford Technologies Ltd. in Abingdon, United Kingdom. Also, in collaboration with the CERN (acronym for Conseil Européen pour la Recherche Nucleaire) I performed studies for the use of a teleoperated Schunk ® modules based robotic arm with the purpose of performing metrology experiments and alignment of the LHC (Large Hadron Collider). I have also collaborated with Fusion for Energy, the European Union's Joint Undertaking for ITER and the development of fusion energy, during my study on the control performance of electric motors driven by long cables for remote handling applications. This work was carried out inside of the Task Order 16 between Fusion for Energy and Oxford Technologies Ltd. for the ITER project.

1.2 Radiation tolerance of telerobotics systems

In this section, a review of the main effects due to the radiation on telerobotics systems is performed in order to justify the selected approach and clarify the issues found during this research.

Due to the radiation levels in most modern nuclear facilities or nuclear experiments are increasing, new protection measures are needed and the use of remote handling techniques becomes crucial. Different scientific facilities are mentioned here as examples, where the techniques developed in this research could be applied. These are also facilities which have been related somehow with this research. These are: CERN (Organisation Européenne pour la Recherche Nucléaire / European Organisation for Nuclear Research), ITER (International Thermonuclear Experimental Reactor) and JET (Joint European Torus).

CERN is a European organization whose purpose is to operate the world's largest particle physics laboratory. At CERN, physicists and engineers are probing the fundamental structure of the universe by means of accelerating particles and making them to collide together at close to the speed of light [1]. The collision of high energy particles produces the liberation of γ-rays, neutrons, muons, etc. While at CERN the main purpose is to study the basics forms of matter, ITER and JET are fusion experiments whose aim is to prove the production of energy via atomic fusion. Both use the tokamak concept where a plasma volume made with hydrogen isotopes is confined with extremely powerful magnetic fields around the torus. JET's primary task has been to prepare the scientific community for the construction and operation of ITER, acting as a test bed for ITER technologies and plasma operating scenarios [2]. The JET experiment is situated in Culham (UK) and ITER is being constructed in Cadarache, south France. During the fusion experiments, deuterium and tritium are forced to interact with each other, releasing helium, neutrons and energy. The fusion neutrons interact atomically with the elements of the vessel wall causing prompt and residual radiation as beta particles and gamma.

There are four main types of radiation relevant to fusion and fission represented in Figure 1-1 together with their penetration power [3]:

- **Gamma radiation:** denoted as γ, is electromagnetic radiation of high frequency and therefore high energy. Gamma rays are ionizing radiation and thus, biologically hazardous. They are classically produced by the decay from high energy states of atomic nuclei (gamma decay).

- **Beta radiation:** Beta particles are high-energy, high-speed electrons or positrons emitted by certain types of radioactive nuclei such as potassium-40. The beta particles emitted are a form of ionizing radiation also known as beta rays.
- **Alpha radiation:** Alpha particles consist of two protons and two neutrons bound together into a particle identical to a helium nucleus, which is generally produced in the process of alpha decay, but may be produced also in other ways and given the same name. They are a highly ionizing form of particle radiation, and have low penetration depth. They are able to be stopped by a few centimetres of air, or by the skin.
- **Neutron radiation** is a kind of ionizing radiation which consists of free neutrons. A result of nuclear fission or nuclear fusion, it consists of the release of free neutrons from atoms, and these free neutrons react with nuclei of other atoms to form new isotopes, which, in turn, may produce radiation. Neutrons have a 12 minute half-life so do not exist for long outside the nucleus. They are produced in abundance in Tokomaks.

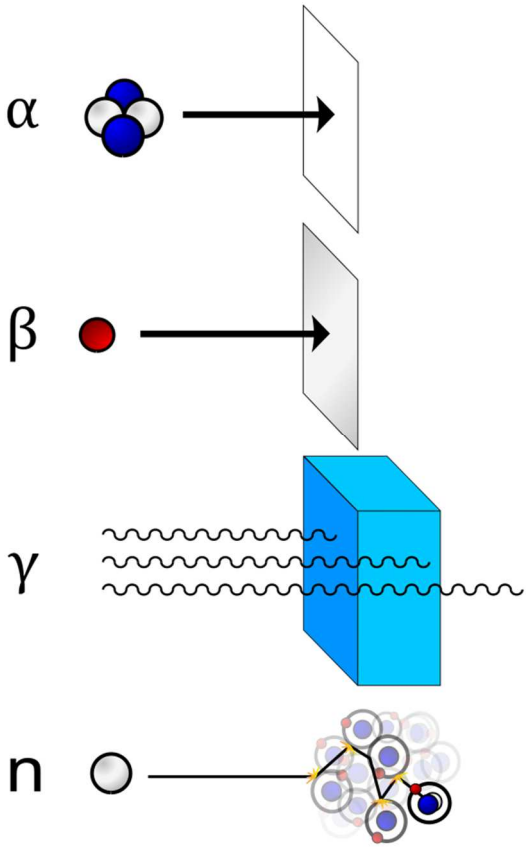

Figure 1-1. Penetration capabilities of the main radioactive particles (Retrieved from http://www.hardhack.org.au/book/export/html/37 on 26/07/2014)

1.2.1 Need for remote handling

There are two main effects due to the radiation impact into the human being, deterministic and stochastic effects. While the deterministic effect is characterized by the destruction of a huge number of cells and an easily quantifiable effect into the organs, the stochastic effect is characterized by a modification at a cellular level which increases the probability of several illnesses [4]. In order to describe the radiation into biological level, the equivalent dose is expressed in Sievert (Sv) and it is the product of the absorbed dose expressed in Gray (Gy) times the radiation weighting factor (See equation 1.1). That factor takes values ranging from 1 for X-rays and γ-rays to 20 for alpha particles. The protons have a weighting factor of 2 and the neutron radiation presents a weighting factor dependent on the energy level.

$$\mathrm{E_{dose}} = \mathrm{W_r} \cdot \mathrm{A_{dose}} \tag{1.1}$$

The radiation threshold model followed by the CERN radiological protection group assumes that under certain level of radiation, called threshold level, the radiation is armless. The threshold dose of the deterministic effects is higher than 0.5 Gy for an acute irradiation and higher than 0.5 Gy per year for a prolonged irradiation for all tissues except the eyes. The semi-lethal dose for an acute whole body irradiation is estimated in 5 Gy, while the CERN annual dose limits for workers is between 20 mSv/year and 6 mSv/year depending on the category [5]. A different source with similar limits is the UK Health and Safety Executive which establishes a total dose for employees of 20 mSv/year. For special employees, it establishes a limit of 100 mSv/year in 5 years with no more than 50 mSv in a single year [6].

CERN's accelerators in operation can produce an intense radiation fields inside the tunnels, mainly near the collimators areas. The ambient dose rates are in the order of 20 to 200 Sv/h [7] would lead to death in a few minutes for a person being exposed to an experiment inside the tunnels. For that reason, a cooling time is required before starting the manual maintenance of those areas. That cooling time should be in the order of 4 months for time-consuming interventions [8] in order to obtain a residual dose rate of several mSv/h which is significant but not prohibitive for maintenance works, when compared with the limits. Inside of the ITER torus and 11 days after shutdown the level of radiation will rise to 450 Sv/h in the middle of the torus, while it will reach 267 Sv/h above the cassette dome. If the time is increased up to 4 months after shutdown, those last values decrease very slowly some tens, but nevertheless these dose rates will be still much higher than at CERN facility [9]. In accordance with ITER design description document [10] and [11], the typical RH (Remote handling) operations such as the replacement of heavy in-vessel components will be carried out in a

radioactive environment of 10 kGy/h gamma dose rate, high temperatures ranging from 50 to 200°C, and total gamma dose going from 1 to 100 MGy [12]. Other example of facility emitting ionizing radiation is the JET experimental reactor which was the first operational fusion experiment capable of producing energy. The dose rate level at JET facility 137 days after shutdown is 209 µS/h into the port plasma centre which is several orders of magnitude lower that ITER [13].

Figure 1-2. MANTIS (MANipulator Transport and Inspection System), June 1978, Retrieved 23 August 2014, from CERN. http://cds.cern.ch/record/969176

Due to the discrete radiation levels observed at CERN and the rigorous spatial constraints found inside the tunnels, the remote handling activities in this facility have been limited to force feedback operations using Mantis in the 70s and 80s (Figure 1-2), radiations surveys, preprogramed routines carried out with the ISOLDE robots (Figure 1-3) and remote operated cranes [14]. However, as the experiments require more and more energy, the need of accomplish with the ALARA principles sets the objectives of increasing the remote handling activities. At JET, remote handling operations have been carried out since the late-1990s by using a Mascot servo-manipulator transported by the JET articulated boom (Figure 1-4) [15]. This manipulator provides force feedback to a kinematically identical master by means of applying a force proportional to the positional error. While at CERN and JET complete remote handling solutions for all the tasks were not considered during the design phase, at ITER it will be crucial to have complete remote handling solutions due to the hazardous environment [8], [16].

For this next generation of ITER-like fusion reactors, more demanding radiation conditions are expected and new hydraulic manipulators are being developed (e.g., [17], [18], [19] together with rad-hard modifications of COTS manipulators [20]).

Figure 1-3. ISOLDE facility at CERN. Retrieved 23 August 2014, from CERN http://cds.cern.ch/record/42934

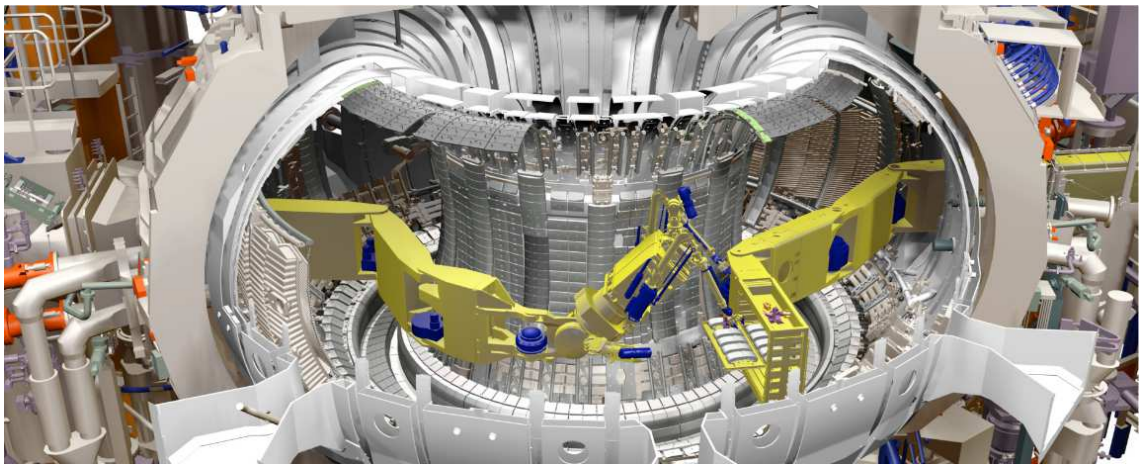

Figure 1-4. JET boom transporter carrying a Mascot manipulator inside the torus. Retrieved 23 August 2014, from http://www.ccfe.ac.uk/rh.aspx

1.2.2 Radiation tolerance of telerobotics systems

The first master-slave manipulators were intrinsically tolerant to the radiation due to its mechanical nature. Nowadays, the increasing amount of electronics included in the modern robots and manipulators make them weaker under radiation conditions, and components like sensors, drives and electronic circuits have increased the sensitivity to radiation of these robots. The radiation susceptible elements of the modern manipulators are usually divided in 3 categories [21]: 1.) the actuators, including the gears and positional feedback devices (encoders, resolvers, etc.), 2.) sensors and 3) the wiring and other communication devices as additional electronic circuits, analogue to digital converters, radio links and sensors' circuitry.

1.2.2.1 Motors

The radiation on the electric motors can produce a decrease in performance or a total failure in the system affecting mainly to the winding insulator, bearings lubricant, wiring for power and sensors, connectors and commutation electronics. The degradation can also be produced as an indirect effect of the radiation due to, e.g. the gamma heating causing too high internal temperature [21]. A radiation hardening version of a motor can be obtained by radiation hardened cables, radiation hardened grease or grease free bearings and total absence of electronics. Typically a radiation resistant of several MGy can be achieved by this method.

A study of the ITER project Japan Domestic Agency [22] has tested 6 commercially AC servo motors under gamma radiation, resulting in one failure after 3.47 MGy due to the radiation damage of electric insulator (Polyester) of the windings and the rest resisting more than 10 MGy. These motors were equipped with hard rad grease (GK-1) which is able to resist up to 25 MGy. For even further radiation resistance, solid lubricant called diamond like carbon can be used, this material is theoretically not affected by gamma rays.

In [23] different results on radiation over motors are presented under a study for ITER, resulting on a radiation resistance depending strongly on the lubricant used. If the wiring insulator is chosen properly between some commons insulators for cables such as Polyimide, Polyamide or PEEK, the motor can withstand several MGy with even using standard commercial lubricants. For even more radiation resistance special grease or solid lubricants are recommended.

1.2.2.2 Force sensor for robots and radiation performance

With the increasing performance in manipulator robots and even in humanoid robots playing a fundamental role in the industry as well as in scientific areas, the use of force sensors, fundamentally in the gripper, has become necessary [24]. These sensors are used to feel the applied force upon the objects where its load will be measured. The most used force and torque sensors for robots are strain gauges based in piezoelectric effects where a Wheatstone bridge circuit is used to measure the resistance variation with the strain which is then exploited to obtain a signal proportional to the input force. But not every type of sensor is able to be used in a robotic application. Even the most sophisticated sensors which are able to measure forces and torques with 6 dof with a very small noise in the measures have to fulfil the requirements of robotic applications in terms of size, cost and the special issues of each application.

Figure 1-5. ATI Gamma 6-axis force torque transducer.

Figure 1-6. Honeywell FSS1500NSB force sensor.

There are mainly three types of force sensors available in the market [25]. These are the so called load cells (see Figure 1-5. ATI Gamma 6-axis force torque transducer.), able to measure forces and torques in several dof and the small sensing elements based on piezoresistive transduction. This last type can be split up in two categories: sensors

which use some sort of steel ball to concentrate the force to a silicon sensing element (Figure 1-6) and sensors that consist of piezoresistive foil layers (Figure 1-7).

The so called silicon-sensing elements do not present a good sensitive range for remote handling applications, going up to 15 N [25], which is not enough for most of manipulation tasks. The silicone is also sensitive to radiation, not being able to cope with more than 10 kGy [26], which indicates that this type of sensing equipment should be avoided for telerobotics operations under radiation.

Simple load cells provided by Sensy and based on strain gauges have been evaluated under radiation conditions for ITER [27]. They do not present any signs of failure for radiation above 18 MGy, whereas than a JR3 6 axis Force/Torque sensor has been irradiated with 9 MGy finding that is not working anymore.

Figure 1-7. FlexiForce foil sensor.

Several strain gauges have also been tested under radiation in [27]. These have been encapsulated in specific polymers resistant to radiation and present very good behaviour under radiation. A different source [21] explains a set of tests performed on strain gauges, load cells and 6 axis force/torque sensors, having shown that hardened versions can withstand more than 1 MGy without significant decalibration effects In [23] it can be found that simple force sensors using basic strain gauge technology are considered useable under radiation for ITER since strain gauges withstand up to 100 MGy. The Japan agency for ITER evaluated both foil and capsule type strain gauges under radiation, with success up to at least 20 MGy.

In the AREVA recycling plant described in [28], a Staubli RX robot was used equipped with a hard-rad ATI force sensor. These new sensors called DeltaRad and ThetaRad Sensors manufactured by the well-known ATI Company are prepared to support more than 10 kGy [29]. This meets the requirements of the AREVA facility in terms of radiation tolerance but would not meet the 1 MGy of ITER necessities. These sophisticated multi-axis force-moment sensors have yet to be found in a rad-hard form. Usually these involve on-board electronics, which should be avoided or replaced with a custom made rad-hard version.

Other completely different type of force sensing is illustrated in [30] where a hydraulic manipulator prepared for ITER uses the difference of pressure between each hydraulic chamber in order to calculate the torque exerted in each joint. This hydraulic manipulator is prepared to support the ITER requirements for its operational area of an estimated dose rate of 300 Gy/h and the accumulated dose of 1 MGy.

In [22], an irradiation tests have been performed on amplifier for strain gauge in order to find which amplifier on the market could be used from the point of view of radiation-hardness and a rad-hard operational amplifier HS1-5104ARH-Q provided by Interstil has been found to operate until the guaranteed value of 1 kGy without deviation and from 2 kGy up to 471 kGy with some characteristics deviating from specification.

To summarize, both traditional technology based on strain gauges and the new Flexi Force sensors present a good behaviour under radiation. The problem associated to the use of sensor technology is the amplification techniques used to convey the sensors' output signal in a usable way and the combination of measuring elements to create a 6 dof sensor. Because it is important to place the amplification close the sensors in order to avoid noise, new approaches based on encapsulating the amplification phase in a rad-hard polymer are being tested [31]. The electronics used in these experiments are based on a rad-hard FPGA which is much more radiation resistance than conventional electronics. The shielding options becomes practical for radiation levels up to kGy, but for even more radiation resistance, the shielding becomes impractical due to its enormous dimensions. Obviously this solution requires additional research and development which increases the cost of the final solution, thus, avoiding the use of external sensing equipment in a remote handling application would be convenient.

1.2.2.3 Electrical cables and connectors

Most cables are based on polymeric insulation which can be used in areas with low background radiation level. In critical areas where the dose levels become high mineral insulation or more modern materials have to be used. Robotics sensors and actuators

can be placed on the manipulator arm and on the end effector itself where higher doses are presented. The cabling connections around the manipulator have to present high level of flexibility that can be compromised due to the radiation effects in the insulation. A minimum requirement of 1 MGy resistance is set in [21], level where the cables should keep their electrical and mechanical characteristics. At those levels, flexible polymeric insulation, such as PVC (polyvinyl chloride) and PE (polyethylene) are not resistant to radiation and lose their properties at even lower values. For better behaviour under radiation, Radox (polyolefin), PEEK (polyetheretherketone) or Kapton (polymide) materials are preferred. These cables are usually more rigid and that causes greater stress at connectors. Remotely operated connectors with PEEK insulation have been shown very resistant, up to high total doses of 10 MGy [21].

1.2.2.4 Lubricants

- **Grease lubricant for motors:** grease lubricants are typically inexpensive in comparison with solid lubricants although major concerns of the grease lubricants are hardening due to radiation and wearing under high temperature operation [32]. The GK-1 grease lubricant develop by the Japan Agency for ITER has been found to resist up to a limit of 10 MGy. This is not a standard lubricant since it has been modified to increase its radiation hardening properties. Other four types of grease lubricants were developed GS-1, GS-4, GS-7 and GS-13-2.
- **Ball bearings:** the life of the bearing strongly depends on lubrication of the retainer. Some macromolecule materials and self-lubricant alloys are promising materials as the retainer for radiation use. For this, three kind of macromolecule materials (A, B and C types) have been developed, two kinds of self-lubricant alloys (D, and E types) have been applied to the retainer and one ceramics ball bearing without retainer has also been tested (F type).
- **Reduction gearbox:** a reduction gearbox is combined to be used with a motor. The Harmonic Drive type reduction gear box is simple in structure and is low in amount of grease for lubrication compared with other types. Two types of Harmonic Drives which were lubricated with two different greases were tested (SK-2, standard type grease and GK-1 rad-hard grease). They were found to withstand between 20 and 30 MGy. [32]

1.3 Motivation: sensorless teleoperation of industrial robots under radioactive conditions

The radioactive environments can be significantly different from each other depending on the dose rate emitted and with them the requirements of the manipulators or robots used within them. As discussed previously, in order to cope with the less demanding doses, it is likely enough to mount a hard-rad force/torque sensor in the robotic gripper, increasing with this the total cost of the robot or developing a customized shielding for a conventional sensor equipped with amplifier. When the radiation dose rate becomes very high, a hydraulic solution can be implemented with the consequent leaking risk. If that risk is wanted to be totally discarded as well as to maintain a solution with components off-the-shelf, when the dose rate increases such as in ITER-like projects, a sensorless approach can be used. This term indicates the indirect end-effector's force and actuator's torques estimation without using force and torque sensors. This research proposes a sensorless force estimation of industrial robots applied to teleoperation in radioactive environments.

Conventional master-slave devices have exploited one of the main requirements for bilateral teleoperation which is the backdrivable design of the manipulators [33] [34]. This characteristic facilitated the use of the positional error between master and slave to estimate the external forces on the slave side. Nevertheless, the conventional industrial robots are non-backdrivable due to its mechanical properties such us, high reduction gears, high friction or non-backdrivable gear design, i.e. worm gears.

Figure 1-8. Worm gears. Retrieved on 25/08/2014 from http://www.societyofrobots.com

Specific solutions of rad-hard dexterous and backdrivable manipulators are more costly than standard industrial solutions, thus, the approach presented in this thesis looks

into the possibility of adapting conventional robots to be used in those facilities. It would be very useful to take advantage of the big stock of industrial manipulators on the market and, through basic modifications to ensure radiation resistance, achieve a sensorless remote handling solution at a competitive price. This research will also help robot manufacturers to develop new designs where the teleoperation in such environments is considered as a possibility. This will ensure the correct selection of mechanical components so the radiation hardness is guaranteed.

This approach would enhance the cost-effectiveness of the remote handling solution by avoiding using expensive sensors, or specific manipulator design. This would also avoid the installation of new sensor´s wiring, developing new technology to shield the sensor's amplifier by limiting the use of electronic equipment.

The sensorless approach would avoid replacing every industrial robot based on electrical actuators for a new and relatively high cost hydraulic solution with the disruptions that this change would cause. This method is also applicable when a redundant system is required. If a traditional electrical slave equipped with force sensor is used, it would be convenient to provide the system with a redundant force estimation that allows the manipulator to continue its tasks in case of failure of any sensor when the device cannot be easily removed from inside of the facility.

With a relatively low computational effort, this thesis proves that it is possible to estimate external forces acting on a manipulator on real time. This method will use no more hardware than the robot controllers. In the worst case, when measurement of proprioceptive variables such as, motor current when using electric actuators or differential pressure when using hydraulic robots are not provided, off-the-shelf, additional and inexpensive hardware might be necessary.

Due to radiation conditions, the slaves devices are typically placed at long distances from their control cubicles. When operating with electrical motors controlled by Pulse Width Modulation (PWM), an overvoltage tends to be developed on both motor and drive's end. The need of finding and testing convenient solutions to this issue motivates the last chapter of this thesis. An extensive set of experiments is designed to prove that the solution found is acceptable within the requirements of teleoperation. This study fills the gap of this research that takes into account not only theoretical problems but also issues derived from the real implementation.

1.4 Objectives and Scope

The goal of this thesis is to gain more understanding in the sensorless force estimation and control of industrial robots. This will allow a more flexible approach to perform remote handling in radioactive environments. This work starts by studying mechanisms to teleoperate bilateral systems with dissimilar master-slaves devices and continues researching into the dynamic problem. Afterwards, the bilateral control is analysed and finally the issues derived with the practical implementation due to the long distances between slave device and control cubicle. Requirements for a teleoperation based force estimation will be presented for both hardware and software. Different observer based techniques are compared into simulation and real experiments in order to obtain a preferred solution. The goals of this thesis can be summarized as follows:

- Define a kinematic approach to convey force feedback teleoperation with dissimilar master and slave devices that is suitable to teleoperate an industrial robot with a general purpose master device. This approach should cope with workspaces differences.
- Establish a general mechanism to model the dynamics of an industrial manipulator in order to be used for force estimation in teleoperation.
- To develop and compare different approaches for external force estimation for teleoperation based on an implementation of the slave's dynamic model.
- Evaluate the different approaches used to estimate forces on a bilateral control.
- Handle the issues derived with the practical implementation of the algorithms and in particularly, the control of electric motors for dexterous manipulators over very long cables. Propose technical solutions to these issues and evaluate the performance of the proposed solutions.

1.5 Outline

This thesis presents an analysis of the remote handling issue in facilities emitting ionizing radiation and the related requirements that make this problem highly demanding in comparison with other environments. The state of the art of the force feedback teleoperation in these scenarios is presented and the problem of using industrial robots for force feedback teleoperation. A recommended approach to solve this problem is given, firstly studying the different kinematic issue and afterwards, focusing on the dynamics. Different methods for force estimation are presented with special interest in

the observer techniques. Finally, an evaluation of several methods is shown and analysed on a bilateral teleoperation. Solutions to the practical implementation of the algorithms and control systems are given in order to cope with the very long cables required. The outline of this thesis is as follows:

- **Chapter 2** introduces the state of the art on force feedback teleoperation under radiation and it continues studying the force estimation issue for robots.
- **Chapter 3** describes the kinematic problem during a dissimilar master slave teleoperation and evaluates methods to cope with this issue.
- **Chapter 4** establishes a general method of modelling and identifying robots model to be used for force estimation in force feedback teleoperation.
- **Chapter 5** presents the estimation of external forces for robots based on different methods. From the evaluation of the forward dynamics equation to the use of Luenberger-Sliding observers. In this chapter results during a simulated bilateral teleoperation are given and a comparison of the main two teleoperation architectures is analysed.
- **Chapter 6** deals with the practical implementation of robot control during teleoperation in radioactive environments.
- **Chapter 7** summarizes the conclusions and the main contributions of this work.

Chapter 2 State of the art

Remote handling is introduced in this chapter with special focus in radioactive facilities, which establish a more demanding set of requirements. A review of the current techniques to handle these issues is presented here, together with a summary of the control methods employed. The current state on teleoperating industrial robots is shown, highlighting the main issues related to this activity. To conclude, a review of the main algorithms to estimate external forces for robots is exposed for those circumstances where the use of other feedback methods is not appropriate.

2.1 Teleoperation in scientific facilities under radiation

Teleoperation is an area that maintains a significant interest into the research community. There are considerable benefits of teleoperating remote devices when the conditions in the remote environment are not suitable for human intervention, mainly due to dangerous conditions, scale or productivity issues. The science field which originated teleoperation was the nuclear industry with the first developments carried out by Raymond C. Goertz for the US Atomic Energy Commission [35] with the aim of avoiding human intervention (See Figure 2-1).

Figure 2-1. Ray Goertz experimenting with mechanically linked manipulators. Retrieved from http://mabe.utk.edu on 28/08/14

Afterwards, other industries, as the space exploration, were involved in this research [36], leading to diverse manipulation systems. Some examples of this are the dual-arm force reflecting system developed by Bejczy et al. at the Jet Propulsion Laboratory (JPL) [37] (See Figure 2-2), the manipulator included in the Japanese Experimental Module (JEM) or the remote manipulator system developed by Canada for the NASA Space Shuttle back in 1989 [38]. Nowadays more applications are using telerobotics approaches to cope with those environments where the human presence is not suitable, e.g. minimally invasive surgery [39], explosive disarming [40], [41], sub-sea applications [42] or power line maintenance [43].

In these kind of operations, providing the operator with information about the remote environment, such as position, orientation, forces etc., improves the operator's understanding of the remote environment and, therefore, the task performance. For that reason, when designing such teleoperation systems, one must consider which signals to pass between the master manipulator and the slave manipulator.

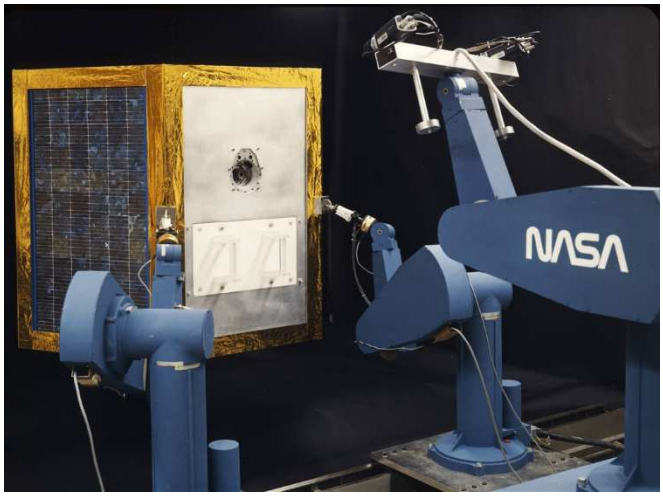

Figure 2-2. Dual-arm force reflecting system developed by Bejczy for the JPL. Retrieved from http://www.jpl.nasa.gov/ on 30/08/14

With this in mind, in 2011 Oxford Technologies Ltd. (UK) developed a state of the art standard work cell to be used on the ITER remote handling control room (See Figure 2-3). This work cell was equipped with all the hardware and software components required to create a functional work cell, which is able to simulate any ITER RH task. Two main criteria have been determinant in the final design of the standard work cell, the RH capabilities required by the project and the human factors. Due to the enormous dimension and variety of remote operated components inside the ITER project, it is expected that several modes of operation will be presented and not only one standard work cell is envisaged to control each RH activity but also other modes are expected including parallel mode and co-operative operation.

With the variety of RH activities that can be carried out at ITER, many different slaves are expected to be operated. In order to cope with this diversity and to avoid the creation of dedicated work cells for each RH task to be undertaken, several general master manipulators able to control each different slave were selected during a study carried out for ITER [44] and two possibilities were finally approved: Dexter manipulator manufactured by Oxford Technologies Ltd and Virtuose 6D40-40 supplied by Haption. Additional master devices can be found in Table 2-1 to Table 2-5. Both haptic devices are tendons-based transmission allowing to place the actuators far from the

joints reducing the reflected mass and inertia [45]. There are two possibilities of operation envisaged for manipulation tasks at ITER which are divided in one arm manipulation and two arms manipulation [44].

Figure 2-3. Standard work cell developed for ITER by Oxford Technologies Ltd.

For the first type of operation both masters can be used whereas for the more complex operations only Dexter will be used [46]. These standard arms are able to control different slaves that will be in general kinematically dissimilar, creating therefore the necessity of having a dissimilar master-slave algorithm to cope with that variety.

Figure 2-4. Work envelope of Dexter 20, developed by Oxford Technologies Ltd.

Figure 2-5. Virtuose 6D40-40 master arm designed for manipulation in hostile environments. Retrieved from http://www.est-kl.com on 30/08/14.

Reference	Company	Product/Solution
1	Telerob	EMSM-2B Master Arm
2	CARRS (Wälischmiller)	TELBOT Master Arm
3	Haption	Virtuose 6D40-40
4	Cybernétix	MAESTRO
5	Cybernétix	MA23M master (discontinued)
6	Oxford Technologies	Dexter

Table 2-1. Remote handling master arms.

Reference	Company	Product/Solution
7	Haption	Virtuose 6D35-45
8	FCS Moog	HapticMaster
9	Sensable	PHANTOM Premium 3.0/6DoF
10	Force Dimension	sigma.7
11	Force Dimension	delta.6
12	Novint	Falcon
13	MPB Technologies	Freedom 7S
14	Quanser	5 DoF Haptic Wand
15	Mimic Technologies	Mantris
16	Butterfly Haptics	Maglev 200

Table 2-2. Haptic interfaces

Reference	Company	Product/Solution
17	Barrett	WAM 7DoF
18	KUKA	Lightweight robot 4+
19	Haption	Inca6D

Table 2-3. Research devices.

Reference	Company	Product/Solution
20	Schilling	Master Controller
21	Perry Slingsby Systems	Master Controller
22	International Submarine Engineering	Master Controller
23	Kraft	Master Controller

Table 2-4. Subsea manipulator controllers.

Reference	Company	Product/Solution
24	Spaceapplications	SAM: Sensoric Arm Master Exoskeleton
25	Haption	Able

Table 2-5. Exoskeletons.

Bilateral teleoperation typically involves some force feedback from the slave's environment to the master's side. The two most common teleoperation architectures are position-position and force-position [47]. The former approach is based on producing in the master's side a force feedback proportional to the positional error between master and slave. This exploites the backdrivability properties of the slave manipulator [33]. Position controllers in both master and slave's sides ensure that the two devices are tracking each other. This approach has been extensively used in the nuclear industry, e.g. at JET in UK (Joint European Torus) [49], [50], CEA (Commission de Energie Atomique) in France [35], CERN (European Organization for Nuclear Research) [50], [51].

At JET, a master-slave system based on a Mascot servo-manipulator (See Figure 2-6) has been used from the first remote handling interventions carried out in 1998 to replace the divertor modules [49] to nowadays. This backdrivable manipulator based on tendons to transmit the torques to each joint from the motors placed on the shoulder has been transported around the torus with the help of an articulated boom (See Figure 1-4 in 1.2). All other equipment required inside the torus was transferred through a second port using a special end-effector mounted on a short articulated boom (See Figure 2-7).

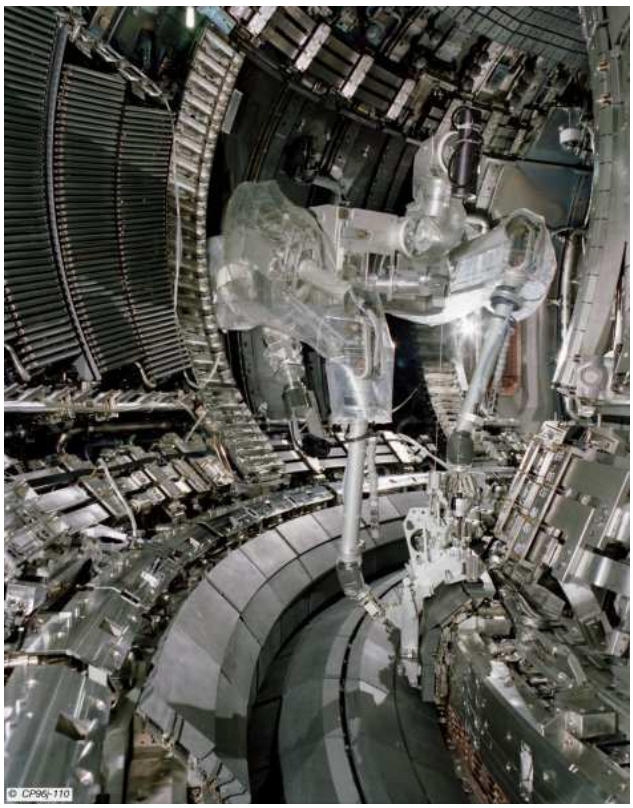

Figure 2-6. Mascot manipulator inside the JET torus. Retrieved on 28/08/14 from http://www.efda.org/2011/09/internal-view-of-the-jet-vacuum-vessel-10/

At CERN, a MANTIS manipulator was extensively used from the 70s to facilitate remote maintenance in areas where although the personal access was not forbidden, it had to be minimized. MANTIS was composed by a 4 wheel drive vehicle and a force-reflecting hydraulic servo manipulator inspired on the MASCOT. That remote handling system also provided force feedback based on positional error [102].

Although the increase of the energy in the experiments carried out at CERN is involving a further investment in remote handling, nowadays less dexterous manipulation tasks are carried out. Some examples are the KUKA robots employed at the ISOLDE facility (Figure 2-8), the LHC remote inspection measurement train called TIM, TAN mini remote crane, TCC2 inspection platform, WANF dismantling and the LHC collimator handling [14].

While the ISOLDE experiment remote handling strategy is based on an industrial robots with pre-programmed routines, at CERN most of the remote handling devices tested at the moment are based on cranes (TAN mini remote crane, LHC collimator handling), fork lift equipment (WANF dismantling device) or simple handling devices with no force feedback capabilities. Other devices are being used for remote inspections as the TIM mono rail train for visual inspections and radiation surveys inside the LHC tunnel (see Figure 2-9) and TCC2 inspection platform [14].

Figure 2-7. Multi drawer task module to be transported by the short articulated boom. Retrieved 23 August 2014, from http://www.ccfe.ac.uk/rh.aspx

Figure 2-8. KUKA robot transporting an activated target mock-up at ISOLDE facility at CERN. Retrieved from http://home.web.cern.ch/about/updates/2014/08/isolde-back-target-after-shutdown on 30-8-2014.

The developments presented previously are focused on solving a particular remote handling issue for a specific facility. In addition, CERN has identified a need for a general purpose manipulator mounted in a remote operated vehicle (ROV) to carry out several manipulation tasks in the radioactive areas of the accelerator. The identified off-the-shelf solution has been a Telemax ROV from Telerob (Germany) (See Figure 2-10). This vehicle is equipped with tracks capable of climbing stairs and it is fitted with a 6 dof manipulator arm.

Figure 2-9. TIM monorail inspection train for surveys at LHC.

The ITER remote handling system presents the major challenge for telerobotics up to date. Although most of remote operations do not consider time delays issues because all manipulators and controllers will be nearby, different major challenges are

expected such us demanding dose rates, very heavy payloads, the necessity of considering recovery scenarios due to the impossibility of human access, etc.

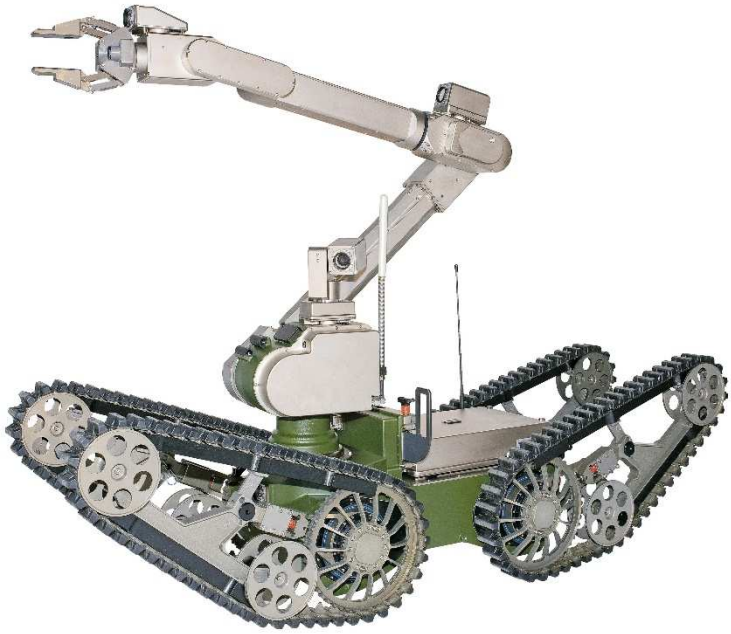

Figure 2-10. Telemax ROV from Telerob GmbH - Cobham plc. Retrieved from http://www.tez.com.tr on 30/08/2014

Most of remote handling operations at ITER will be performed using applications-based manipulators, specially designed and tested to fulfil the requirements of a particular operation [10], [11], [8], [16], [53]. An example of this operation is the ITER blanket remote handling system, being developed by the Japan Atomic Energy Agency (JAEA) [10]. The ITER Vessel wall is composed by a number of very heavy tiles, called blankets. For regular maintenance of these 4 tonnes tiles, it is necessary to remotely exchange this modules due to the high levels of gamma radiation. The remote manipulation of these modules comprises a big manipulator called the In-Vessel Transporter (IVT) which is moved on a rail and a vision system using hard-rad cameras for installing and grasping while avoiding the contact [53].

In the ITER remote handling system it can be found several types of hydraulic solutions, naturally resistant to the radiation and using water instead of oil, as hydraulic fluid. This is important to avoid leaks inside the ITER vessel, which in case of being oil, could produce dramatic effects during the plasma operations. Crucial research in this aspect is being carried out in the Technical University of Tampere (TUT, Finland) for the ITER Divertor Remote Handling module developing the WHMAN manipulator (See Figure 2-11). WHMAN is a teleoperated water hydraulic manipulator arm with force feedback equipped with seven direct driven joints, which provide six degrees of

freedom [30], [54]. The WHMAN is able to transport up to 100 kg payload when fully extended, and because the guidelines for the design come from the ITER project constraints, the manipulator is designed to be radiation tolerant against a dose rate of 300 Gy/h and a total dose of 1 MGy. All transducers are based on analogue technology without integrated electronics using a dual-speed resolver for the rotational joints and a LVDT-type for the prismatic. The force feedback is created via the differential pressure from each hydraulic chamber and from a six-axis force-torque sensor (JR3), allowing an accurate force feedback control in various remote handling scenarios [30], [54]. The use of a sensor with internal electronics in a radiation hardened robot should be carried out only for validation purposes, otherwise the performance of the whole system can be seriously affected.

In the ITER Neutral Beam Cell (NB), a complete remote handling solution has been planned, involving a monorail crane, the Beam Source Remote Handling Equipment (BS-RHE), Beam Line Transporter (BLT) (See Figure 2-12), Upper Port Remote Handling Equipment (UP-RHE) and Tools [55]. The conceptual design of the BLT involves an articulated boom porting a dexterous manipulator. The whole set, boom and manipulator is able to slide on a rail system. The articulated boom comprises of three link sections with actuated joints. The far end of the boom contains a pitch and roll joint where a mast hinge is attached and a rack and pinion within it is used to drive an outer telescopic joint [55]. The manipulator model ported in this remote handling solution will be a dexterous servo-mechanism, part of a master-slave, man in the loop system. The same concept will be employed on the BS-RHE to enable the extraction and installation of a radioactive source.

In the nuclear fission industry an important aspect is the robotic inspection of old nuclear power plants. The Swedish power plant Ringhals 1 is an 830 MW BWR reactor which used a couple of OC Robotics´ snake-arm robots to inspect a leaking area and carry out components manipulation in extremely inaccessible locations. This robotic snake has ten segments and a total of 23 degrees of freedom including a two-axis wrist [56]. Although having a complete set of end-effectors, the OC Robotics' snake-arms (Figure 2-13) do not provide force feedback to the operator, therefore the feeling of presence in the remote environment is dismissed and the operations can be more prolonged.

The German nuclear engineering specialist Nukem has produced a number of robotic products aimed specifically at decommissioning tasks. For example, the Artisan 100 is a high-power hydraulic manipulator which is designed for handling and size reduction operations in highly radioactive environments [56]. It presents up to 1 MGy of radioactive tolerance and it is even suitable for explosive environments.

Figure 2-11. WHMAN water based hydraulic manipulator. Retrieved on 7/09/2014 from http://sine.ni.com/cs/app/doc/p/id/cs-14767

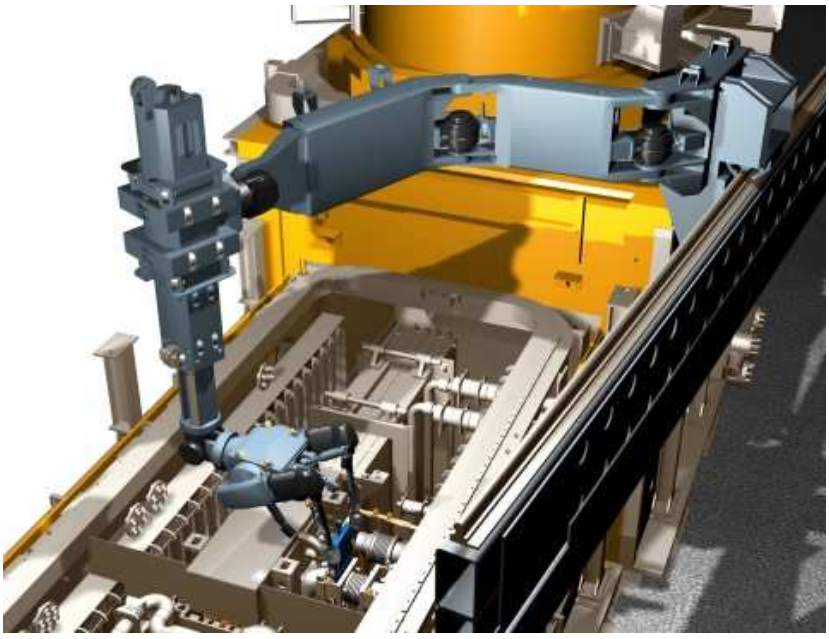

Figure 2-12. Beam Line Transporter, Remote Handling System of the Neutral Beam. Retrieved on 7/9/2014 from http://www.ccfe.ac.uk/news_detail.aspx?id=174

The Titan 3 and Titan 4 (Figure 2-14) are hydraulic manipulators manufactured by FMC Technologies. They have been used in the nuclear industry but they are much

more frequent in subsea operations employed in large ROV´s working in the offshore industry. This arm is made primarily in titanium and is powered by hydraulics [57].

There is a considerable number of hydraulic manipulators which have been used in the nuclear industry or at subsea operations such as RT 7 Compact, Commander Manipulator developed by INBIS working in a partnership with BNFL Engineering Limited, TA 30 Storm Manipulator which was used in 2 nuclear facilities and 30 offshore and uses a feedback approach called hybrid feedback control system [58], Kraft Predator used in nuclear facilities at USA, Kraft GRIPS, Raptor Manipulator, Magnum Manipulator, Maestro and Kodiak. Their electric counterparts are also widely used in the nuclear industry as A1000 manipulator and Telbot from Wälischmiller Engineering, Telbot, EMSM 2C and EMSM 3 Manipulator used at Karlsruhe nuclear facility and in the Spallation Neutron Source Target System at the Oak Ridge National Laboratory (USA) [59], TR 4350 Manipulator, deployed in 2 nuclear facilities in the US, TR 6350 and Helios initially manufactured by GEC Alstrom Schilling.

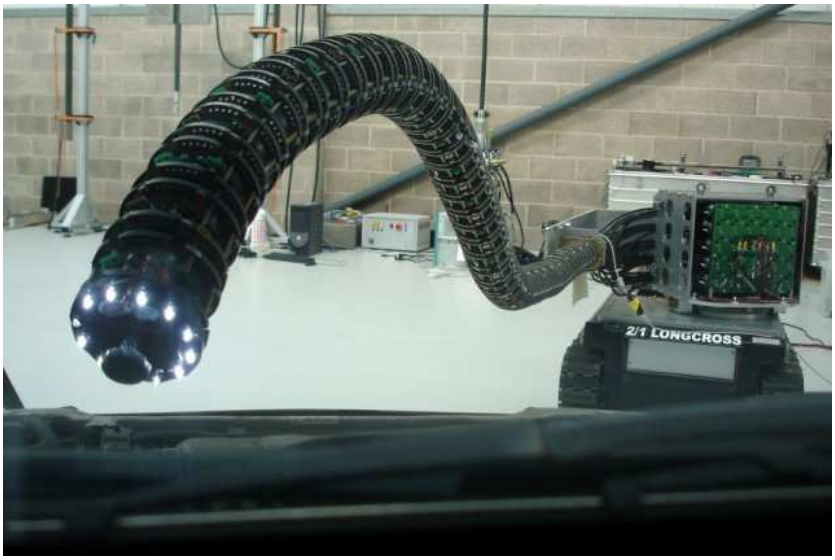

Figure 2-13. OZ robotics snake-arm for survey operations. Retrieved on 10/09/2014 from http://www.ocrobotics.com/products--services/

A totally different approach are the widely used master-slave manipulators with through-wall mounting for nuclear environments. In these devices, master and slave are typically mechanically linked and divided in three parts, the cold arm or master, through wall tube and the hot arm (slave). The obvious drawback of these devices are the access limitations since they are fixed to a wall and no additional displacement can be performed with them to overcome unexpected situations. Also, the operator is performing the manipulation task from the other side of the wall with all the risk related to this proximity. Such slaves are used commonly inside of Hot Cells (See Figure 2-15),

used in the nuclear-energy and nuclear-medicines industry when there is a need of handling radioactive sources. Some examples of master-slave manipulator mechanically linked are: A100 (Figure 2-16) and A202 from Hans Wälischmiller, E-HD and Type 7 manufactured by RTS Innovation, MA 11.80 and MT 200 both distributed by La Calhene presenting a force feedback of 1:1 and VNE 80 a manual operation manipulator with motor driven telescopic motion.

Figure 2-14. Titan 4 hydraulic manipulator. Retrieved on 14/09/2014 from http://www.fmctechnologies.com

Figure 2-15. Hot Cells at the Argonne National Laboratory. Retrieved on 14/09/2014 from http://en.wikipedia.org/wiki/Hot_cell.

Figure 2-16. Master-Slave HWM A-100. Retrieved on 14/09/2014 from www.hwm.com

2.2 Teleoperation of industrial robots

Remote handling interventions in hazardous facilities involving high dexterity have been typically carried out with low reduction gears and a low weight-to-payload ratio slave manipulators. This has been done to achieve force reflection capability by using the positional error as a measure of the environmental force. The positional feedback and the backdrivable design of the manipulator [33] made it possible for the first bilateral control architectures. The robot reflected the position of the operator in the remote environment making it more secure system for a robot sharing the environment with humans or interact with remote objects. Newer control techniques as force-position control schemes transmit the environmental forces to the operator along with position and other parameters. The force is acquired by specially designed force and torque sensors [28], [60] or sensorless force feedback approach. This is the case of the Atomic Energy Commission in France (CEA), which has been developing advanced technological solutions in the fields of teleoperation, remote handling and robotics, in collaboration with industrial partners (COGEMA, EDF, FRAMATOME) and for its own needs. Their research has tried to solve current problems and develop new technologies for on-going and future remote handling applications. An example of this is the dexterous arm for teleoperation called BD250 developed by CEA and COGEMA. It is a 7 axis redundant manipulator with 25 kg of payload and radiation tolerant up to 10 kGy. It provides force feedback control [61]. Most of the slaves developed by the French Commission are teleoperated by using the Virtuose haptic master mentioned before. They also have extensive experience on teleoperating industrial robots with force feedback by mounting a 6 axis torque-force sensor on the robot end-effector. In [61] and [62] it is shown how the use of and STAÜBLI robot with force-feedback teleoperation provides a dramatic cost reduction and higher performance (See Figure 2-17). They claim that the performance achieved during teleoperation of industrial robots is good enough to carry out high precision tasks in a remote way and to handle heavier loads than those encountered in manufacturing robotics applications. Loads up to 100 daN are transported with these robots in certain conditions [61]. They use a proprietary master-slave controller termed MT200-TAO which seems to fit their applications perfectly. Nevertheless, it has not been found as a commercial solution. In Figure 2-18, a RX90 robot fitted with an ATI Delta Rad F/T sensor which is able to withstand up to 10 kGy of accumulated dose is shown. With this hard-rad sensor and a specific design of new electronics components which are able to cope with the required dose a complete set of hard-rad teleoperation system has been developed. It is composed by a digital transmission network called NEUROBOT, a high signal multiplexor,

the master and slave devices and the force sensor. There are several examples of industrial robots teleoperation in the nuclear industry, but the majority of them implement solutions based on force/torque sensors. Sung Ho Ahn et al. explain the implementation of a high gear ratio manipulator for the remote handling of spent fuel bundles in [63]. They ensure that most of force reflecting manipulators present low weight-to-payload ratio, which make them unsuitable for many potential application areas even when implementing force reflecting capability. The need of handling heavy weights drive the solution through the use of powerful industrial slaves.

In [64] a Staübli RX170 was also used in the French Nuclear Industry to carry out remote manipulation tasks using a backdrivable master arm MA23 and a six axis force/torque sensor manufactured by ATI. The main advantages of using such system compared with solutions based on specific nuclear manipulators are reliability; flexibility; quicker and safer; reduced risks for projects and lower costs. The MA23 was firstly introduced by the CEA in the eighties as a master-slave servo controlled arms but was replaced later by the newer Virtuose [65].

2.3 Bilateral control algorithms

The variety of bilateral control systems in the literature addresses the transparency and stability issues arising from the dynamics of the devices and communication effects [60]. In the telerobotics community, transparency is understood as a property of the bilateral system when the remote environment is exactly reproduced at the master side. This is, the operator feels as if he was directly interacting the remote environment. Stability is a basic requirement of every control system [66].

The classification of bilateral control algorithms generally attend to the type of signals exchanged between master and slave. Examples of this are: Position-Position, Force-Position or Force-Velocity. Another classification consider the number of magnitudes communicated, i.e. the number of virtual channels used for the interconnection of master and slave. In the literature, two-, three- and four-channel architectures have been considered so far.

Position-Position Control Scheme

The simplest bilateral control scheme to be implemented is Position-Position architecture (Figure 2-19). This is due to the lack of force measurement or position differentiation. Only the master and slave joints' position are needed. This scheme has been applied widely since the development of the first nuclear industry [67], [68]. In the

diagram of Figure 2-19 the master and slave devices are represented by the blocks M(s) and S(s) respectively. Their controllers are represented by the gains k_{pm} and k_{ps} and the effect of the environment is represented by the gain k_e. This simplification represents the environment as a spring with an elastic constant equal to the environment constant. In such system, the interaction forces between master, slave and environment are proportional to the slave´s position variation.

Figure 2-17. Manipulation with a RX130 robot. Retrieved on 11/09/2014 from [62].

In Figure 2-19 the f_h variable is the force exerted by the human operator to the master. If that force is not compensated by the force reflected by the master, f_m, the master device will move to a new position which will match with the operator position ($X_m = X_h$). As a consequence of that movement, new position references will be sent to the slave´s control loop. With this mechanism, the master guides the slave at the same time it is aware of the exerted forces. The position of each device will be used as a reference for the other device. Therefore, the position error e_p is calculated as a difference between master and slave´s position. The force reflected to the operator (f_m) is proportional to the positional error according to the master controller gain (k_{pm}) and the force applied to the slave´s actuators is also dependent on the positional error between master and slave thorough the slave´s gain (k_{ps}). In this control scheme, the positional difference between both devices is represented on the master as a resistant force against its movements, this effect is termed drag effect and it can be considered

as one of the drawbacks of the position-position architecture. In [60] it is also mentioned how this approach it is very stable in comparison with different control schemes and it has been widely tested.

Figure 2-18. RX90 robot fitted with DELTA RAD F/T sensor. Retrieved on 11/09/2014 from [63].

In is important to mention that position-position will not work with non-backdrivable slaves since great gear ratios will produce a scaling of the environmental forces by reducing the slave´s positional error to a minimum. With such small or zero positional error, the estimated environmental forces would be negligible [69] although the forces being exerted by the real slave could be enormous. Also, only the resistant forces to the slave's movement could be detected when the slave is in movement. If any external force is applied when the slave is stopped they would not be transmitted into positional error due to the non-backdrivability of the mechanism.

Force-position Control Scheme

The force-position control scheme is presented in [60] as an improved version of position-position, although that is not totally clear since in a considerable number of dexterous operations around the world position-position is still used. They claim that the improvement is obtained due to the lack of drag effect since the force feedback presented to the operator (f_m) now comes from measurements of the exerted force. This

kind of control has been implemented in many bilateral systems as those described in [70], [60], [61], [62].

In [60] a comparison between position-position and force-position is presented using a test bench with a Kraft hydraulic manipulator. Although no forces due to drag effect are observed, gravity and inertia seem to play a role when using sensor and a small force is reflected to the operator in this case. Contact forces are felt correctly and a better performance than with position-position is achieved.

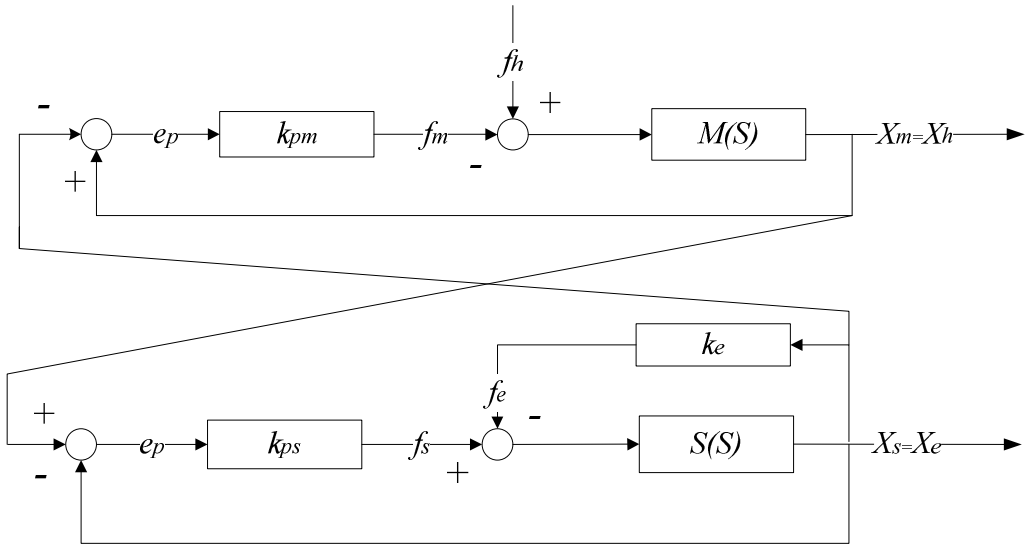

Figure 2-19. Basic Position-Position bilateral control.

Different approaches

For teleoperation in large workspaces there is some interest in the so called "rate-position" control which implements a position control inside a dexterous sphere and it is able to switch to rate control when the user goes beyond a certain region. This has been inspired in the rate control of cranes by means of a joystick (usually with one degree of freedom). Their results in terms of accuracy and time employed to complete a task prove it as an interesting option for implementation in real environments [71].

In Dexter 20 and in the Mascot manipulator used at JET, a four-channel control algorithm with force feedback based on position and velocity error is being employed for high dexterity remote handling operations. This scheme is represented in Figure 2-22

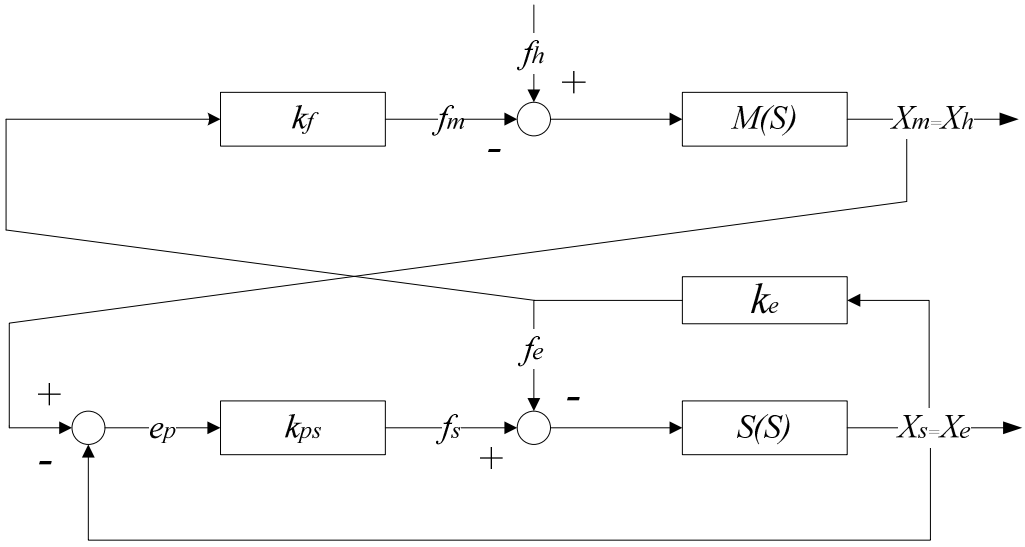

Figure 2-20. Force-Position bilateral control.

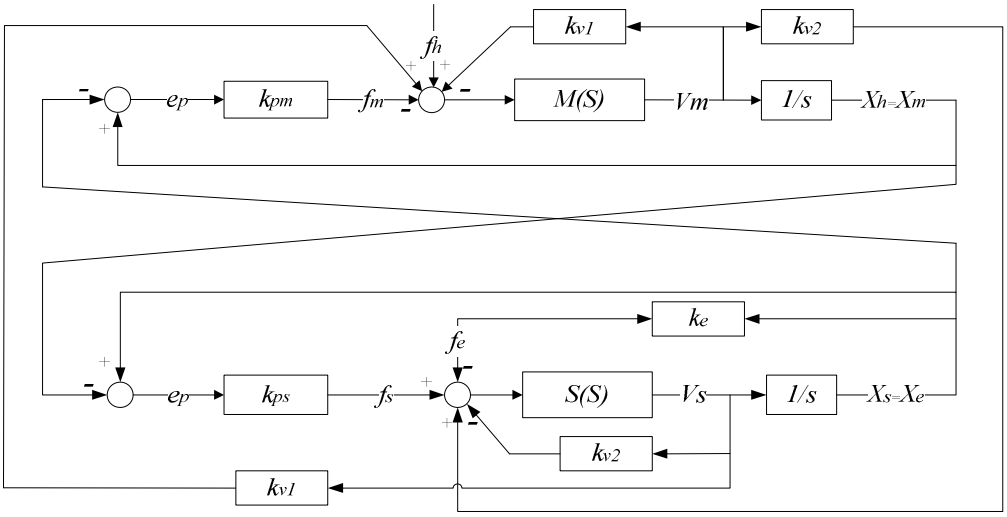

Figure 2-21. For sake of clarity the velocity error is represented with two gain blocks instead of one gain block used for the positional error. The concept is similar than PP control although a damping term for the velocity is included here.

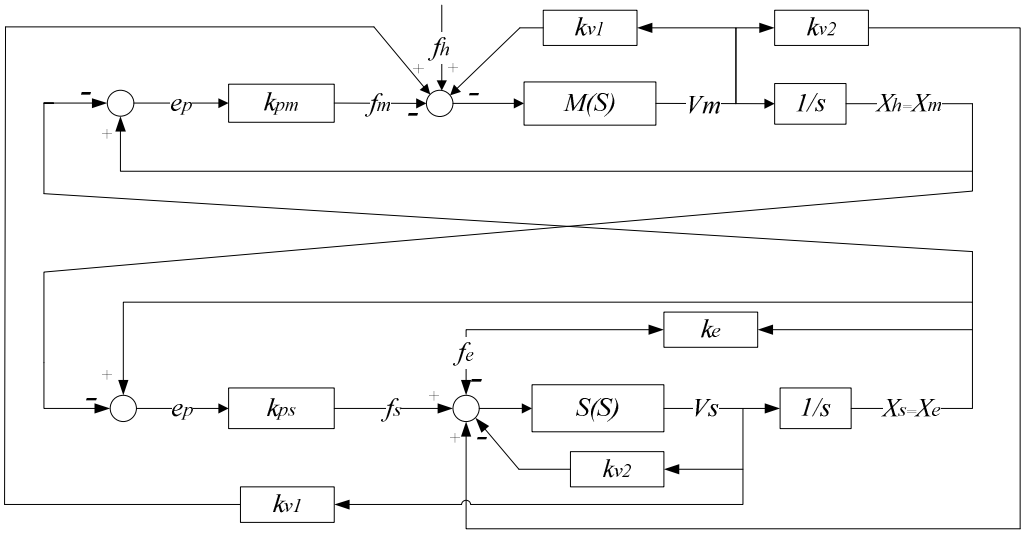

Figure 2-22. Four channel Position and Velocity bilateral algorithm used by Dexter manipulator.

2.4 Force estimation for industrial robots

Most of bilateral control architectures developed to employ industrial robots for remote handling operations use force/torque sensors due to the need of applying any force-position bilateral control. These kind of sensors are typically placed on the robot's end-effector which implies that only external forces on that end can be measured. These devices also require additional wiring in the robot and cannot withstand the high dose rates of the high energy scientific facilities due to the utilization of electronics [72]. Moreover, force sensors can be expensive and can increase the production cost of the robot. Therefore, a different research line seeks to develop an approach where the benefits of a force sensing equipment are obtained without the need of using such devices. This research area looks in force estimation methods and it is mainly focused on disturbance observers.

The area of research involving disturbance observers provides a useful framework for the problem of estimating external forces acting on a manipulator. Disturbance observers have been widely proposed for motion control and collision control applications [73], [74], [75], for determining disturbance forces such as friction. Estimation techniques based on observers for robot motion control were carried out by Ohishi et al. [76], [77], [78] using a nominal model of the robot. In this work a disturbance torque is calculated by subtracting the nominal torque to the motor torque provided by the

actuators while performing position control. The value of the nominal torque is calculated with a nominal inertia for every link. This method seeks to decouple the joint control by treating the effect of coupled inertia, Coriolis torque, friction and external effects as a disturbance torque. This basically consists on a feed-forward torque control with the nominal values of inertia. No distinction between the effect of external forces and the coupled inertia, Coriolis and friction is done. The method was tested with a 3-DOF robot.

The first observers for robots which use the complete manipulator model were implemented by S. Nicosia and P. Tomei and a large amount of research has been derived from their findings. Their aim was to design observers to perform robotic control without using velocity measurements which tend to introduce a big amount of noise [79]. The dynamic model of a manipulator can be written in the following way:

$$u = H(q)\ddot{q} + C(q,\dot{q}) + \tau_g(q) + \tau_f(\dot{q}) \tag{2.1}$$

Where,

u: denotes the vector of motor input torques exerted in each joint.

$H(q)$: is the symmetric positive definite robot inertia matrix which is bounded for any q.

$C(q,\dot{q})$: is the the centrifugal and Coriolis forces matrix in the Cristoffel form.

$\tau_g(q)$: is the gravity forces vector.

$\tau_f(\dot{q})$: is the friction torques vector, $\tau_f(\dot{q}) = F \cdot \dot{q}$

Assuming the joint displacements as the output variables of the robot system, the observer output would be the following:

$$y = q \tag{2.2}$$

And defining the observed state as $\hat{y}$ and the observation error as $\tilde{y} = y - \hat{y}$, the proposed observer is described by:

$$\begin{cases} \dot{\hat{x}}_1 = \hat{x}_2 + \ k_D\tilde{y} \\ \dot{\hat{x}}_2 = H^{-1}(y)\big[-C\big(y,\dot{\hat{x}}_1\big)\dot{\hat{x}}_1 + u + k_P\tilde{y} - \tau_g(q) - F\dot{\hat{x}}_1\big] \\ \hat{y} = \hat{x}_1 \end{cases} \tag{2.3}$$

Where k_D is a positive scalar constant and k_P is a symmetric positive definite matrix. They prove the convergence of this observer by using Lyapunov if the joint velocities

are assumed to be bounded and the initial observation error belongs to a suitable region of attraction.

Afterwards, P.J. Hacksel and S.E. Salcudean [80] employed the mentioned observer to estimate external forces on robots by splitting the total force in two terms, the control force and the environmental force: $f = f_{con} + f_{env}$ .On the robot state, the term f is applied while in the observer, only the known control force f_{con} is taken into account. By calculating the observed estimation error they yield to:

$$\mathrm{H(q)\ddot{\tilde{x}}_1 + C(q,\dot{q})\dot{\tilde{x}}_1 + C\big(q,\dot{\hat{x}}_1\big)\dot{\tilde{x}}_1 = -K_p\tilde{x}_1 - K_v\ H(q)\dot{\tilde{x}}_1 + u_{env}} \tag{2.4}$$

Which has an equilibrium point that acts as a stretched spring:

$$\mathrm{\tilde{x}_1 = K_p^{-1} u_{env}} \tag{2.5}$$

They found that in equilibrium, the external force can be assumed to be proportional to the observation error and establish the conditions for that to happen. From [79] they get the condition of bounded joint velocities. Also, if $k_c > 0$ is such that $\|C(q,\dot{q})\| \leq k_c\|\dot{q}\|$ and $k_v > k_c M/\ \lambda\_min\ (H)$, then the equilibrium point, $\big[\tilde{x}_1, \dot{\tilde{x}}_1\ \big] = [0,0]$, is asymptotically stable, and a region of attraction is given by (2.6).

$$\mathrm{S = \{\ \ x\epsilon\mathbb{R}^{2N}\text{: } \|x\| < \sqrt{\sigma_{min}(Hd)\ /\sigma_{max}\ (Hd\ ))}\ \ \Big(\frac{\lambda_{min}(H)k_v}{k_c} - M\Big)\}} \tag{2.6}$$

Where $Hd = diag[K_p, H(q)]$, and σ_{min} and σ_{max} denote the minimum and maximum singular value, respectively. A constant environmental force can shift the equilibrium from $\big[\tilde{x}_1, \dot{\tilde{x}}_1\ \big] = [0,0]$ to $\big[\tilde{x}_1, \dot{\tilde{x}}_1\ \big] = [K_p^{-1}u_{env}, 0]$ and has a shifted region of attraction as in (2.6), [80].

The same approach is employed again in [81] to predict the external forces acting in an ABB IRB2000 robot at the Robotics Lab, in Lund. The ABB control hardware has been replaced by an external VME-based control computer. They establish that external forces at robot end-effector can be estimated with the following expression:

$$\phi_2\ddot{\tilde{x}}_1 + \phi_1\dot{\tilde{x}}_1 + \phi_0\tilde{x}_1 = J^T F \tag{2.7}$$

With

$\phi_2 = H(x_1)$

$\phi_1 = C(x_1, \dot{x}_1) + C\big(x_1, \dot{\hat{x}}_1\big) + \tau_f + H(x_1)K_1$

$\phi_0 = K_2$

The environmental force is estimated by:

$$\hat{F} = J^{T\dagger}(x_1)\phi_0\tilde{x}_1 \tag{2.8}$$

With † denoting the matrix pseudo-inverse.

This observer has the advantage of no assuming a measurement of the joint velocities. However, it has the following drawbacks [82]:

- It needs to compute the Coriolis matrix for different input values, and also the friction effects separately.
- It assumes a perfect model of the manipulator, because otherwise, the observation errors will be manifested has an external force offset.
- Means of calculating the observer gains K_i are not provided.
- A good value of the external force is only guaranteed at steady state, this is when $\dot{\tilde{x}}_1 \simeq 0$, and $\ddot{\tilde{x}}_1 \simeq 0$. The Coriolis term is very hard to compute or measure and the force estimation may have large error and slow response to external force steps.

Different approaches based on robust observers [82], [83], [84], [85], [86] were also focused on avoiding the smaller stability margins of the disturbance observers during motion control [87]. Particularly interesting is the work of Adrià Colomé et al. in [82] during their experiments with a cable driven robot called WAM. They use an observer based again in [79], where only the inertial term is calculated with an a-priori knowledge of the robot and the rest is learnt by using methods like Locally Weighted Projection Regression (LWPR) and Local Gaussian Process (LGP). These approaches allow to improve the model even when the system is in operation. The observer makes use of the position and velocity errors with the related differentiation errors due to the numerical differentiation. They also find high complexity driving the robot with low control gains due to the static friction and cogging effects which are impossible to learn by the algorithm.

The proposed observer in [82] it is based in [88] and it estimates the state and the disturbance at the same time. The robot state space is represented in (2.9) while the observer state space equations are in (2.10).

$$\dot{x} = Ax + B(x)d + \Gamma^*(u, x) \tag{2.9}$$

Where d is the disturbance external torque with the sign changed, and $A = \begin{bmatrix} 0 & I \\ 0 & 0 \end{bmatrix}$, $B = \begin{bmatrix} 0 \\ H^{-1}(x_1) \end{bmatrix}$ and

$\Gamma^*(u_c, x) = \begin{bmatrix} 0 \\ \Gamma\ (u, x) \end{bmatrix}$

Where, $\Gamma\ (u_c, x) = M^{-1}(x_1)[u_c - C(x_1, x_2)x_2 - \tau_f - \tau_g]$. While the state observer is defined in the following way:

$$\dot{\hat{x}} = A\hat{x} + B\hat{d} + K(x - \hat{x}) + \Gamma^*(u, \hat{x}) \tag{2.10}$$

With this, the external force estimation is derived and it yields:

$$\hat{d} = M(\hat{x}_1)\left(\dot{\hat{x}}_2 + \Sigma(x_2 - \hat{x}_2)\right) + \hat{n}(\hat{x}_1, \hat{x}_2) - u_c \tag{2.11}$$

Where $\hat{n}(\hat{x}_1, \hat{x}_2)$ is the learned function which comprises the Coriolis Effect, friction torque and gravity torque and Σ is a set of gains. With this approach, the measurement of the joint velocity is necessary, but at the same time, no requirements for the system to be in equilibrium is given. The approximate value of the learned function will appear as an error in the contact force estimation, although this may happen in most of model based observers.

Different techniques are based in Ohishi's previous work and have employed the adaptive disturbance observer scheme [89] testing the proposed method for a 2-DOF planar robot. This research presents a novel approach in which a simple disturbance observer is developed with the nominal model of a robot. This model matches with the Ohishi's work in the sense that the nominal inertia of each axis is used as a constant inertia matrix with only diagonal terms. Additional torque due to the coupled inertia, Coriolis, friction, etc. is considered torque disturbance together with the external torque. In absence of external forces the disturbance observer is used to calibrate a complete model of the robot by adjusting it using the gradient method. Once the model is calibrated, it is used to compute in real time the external force by subtracting the model output to the observer output (See Figure 2-23). The main drawback of this algorithm is the necessity of using the velocity and acceleration values in real time in order to estimate the external forces and the errors in the dynamic model which will produce noise in the force estimation. Nevertheless this method involves an improvement with respect Ohishi previous work solving the lack of estimation of some torque components, which is accomplished with the use of the model.

In [90] a H^∞ robust force observer (See Figure 2-24) is designed with the objective of controlling a robot joint by joint and considering all the force effects, except the nominal inertia, as a disturbance. This research completes the Ohishi work in robot control with robust observers. Again, the external force is estimated inside the entire disturbance, being impossible its independent determination. In Figure 2-24 $Pm(s)$ represents the nominal model of the plant. In the lower part the real plant is represented with the real inertia and viscous damping. $H(s)$ of the force observer is designed by the mixed sensitivity method.

Kalman filter has also been used to estimate external disturbances. In [91] the Adaptive Kalman Filter (AKF) is employed to estimate the disturbances of a 2 DOF robot. The particular advantage of using this method is the continuous updating of the noise covariance during the disturbance estimation process. Unfortunately this research does not details the effect of considering a 6 DOF robot without having the complete model. The theoretical solution works well with 1 DOF DC motor and all the disturbance is due to external torque effects, but when considering a 6 DOF robot, if the complete model is not considered, it would be difficult to distinguish the external torque from the internal torques caused by un-modelled effects.

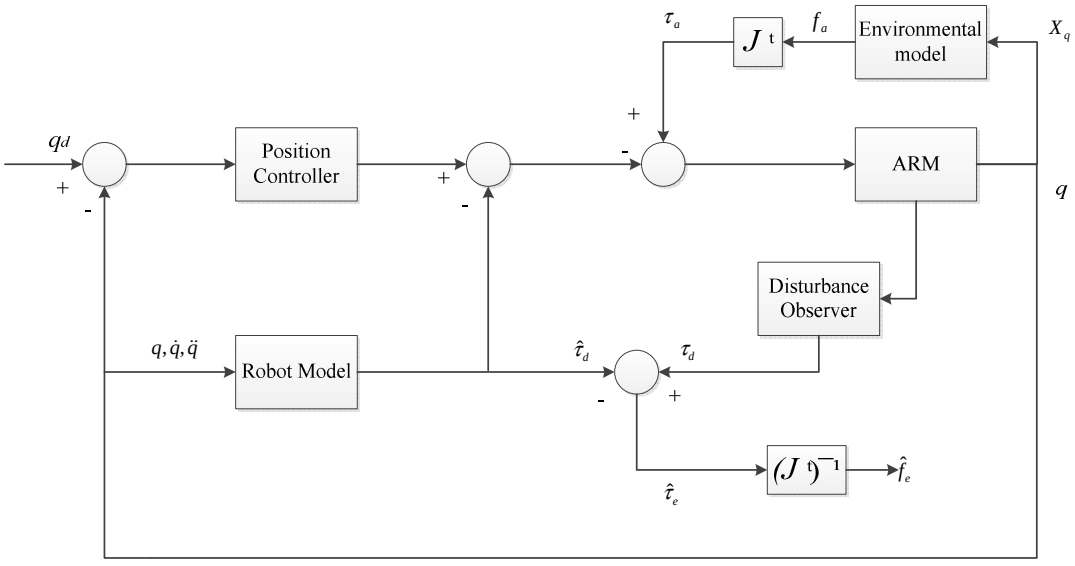

Figure 2-23. Block diagram of the force estimator.

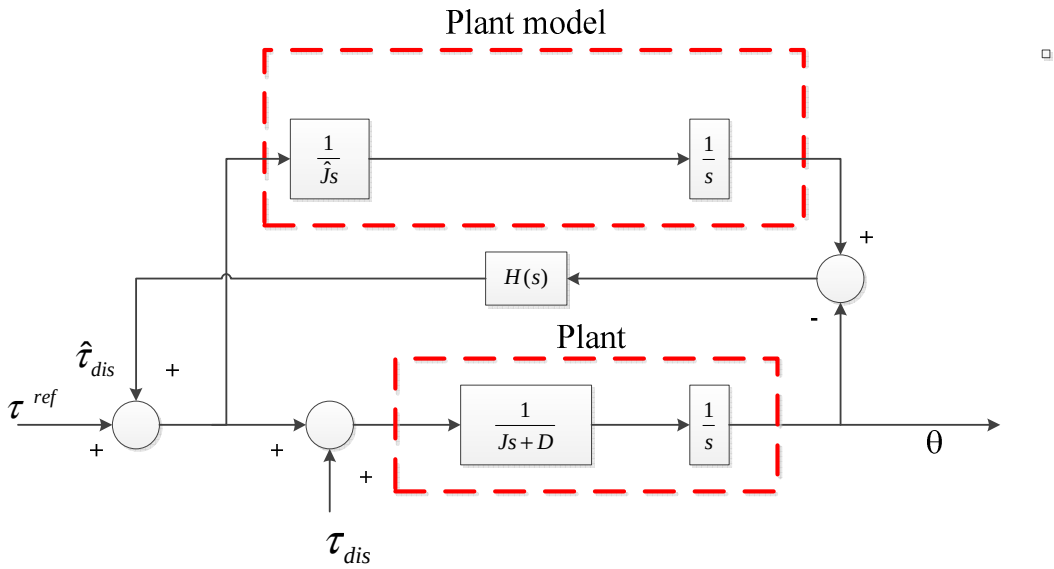

Figure 2-24. Block diagram of robust force observer.

Additionally in [91], an alternative approach based on disturbance observers is used where a PID-like observer gain is employed to guide the observer convergence. The drawbacks of this method are similar than in the AKF implementation due to the lack of complete model for a 6 DOF robot.

Canudas de Wit and Slotine introduced the concept of sliding observers for robot manipulators [92]. The sliding observers had been used before to control highly nonlinear processes through using a nonlinear control action. This technique has been good for controlling certain systems where the control chattering is not important, as in motor control, but cannot be used when no chattering is allowed. In state observers is clear that discontinuities in control action are not important since it is not a real system and the chattering problem is not considered. They prove the exponential convergence of sliding state observers under some circumstances and show the results when applying a time-varying gain observer. This technique is excellent when the exact model of the system is not known since observation errors tend to zero asymptotically.

Sliding observers have also been use in teleoperation to estimate velocities and forces in presence of delays in [93] by using only position measurements. Although this had been tested only in simulation. This observer will be discussed later since it constitutes a key point in this thesis.

In [94] three non-conventional state observers are compared, these are: high-gain observers, sliding mode and nonlinear extended state observers. The high-gain observer [95] of a plant described by (2.12) is indicated by (2.13).

$$\ddot{y} = f(y, \dot{y}, w) + k \cdot u \tag{2.12}$$

$$\begin{cases} \dot{\hat{x}}_1 = \hat{x}_2 + \ h_1(y - \hat{x}_1) \\ \dot{\hat{x}}_2 = f_0 + b_0 u + \ h_2(y - \hat{x}_1) \end{cases} \tag{2.13}$$

Where f represents the dynamics of the plant and disturbance, w is the unknown input disturbance, u is the control action and y is the output that can be measured. f_0 is a nominal model of the function f. With this, the estimation error equations are described by (2.14).

$$\begin{cases} \dot{\tilde{x}}_1 = - \ h_1 \tilde{x}_1 + \tilde{x}_2 \\ \dot{\tilde{x}}_2 = - \ h_2 \tilde{x}_1 + \delta(x, \tilde{x}) \ \tilde{x} = \begin{bmatrix} x_1 - \hat{x}_1 \\ x_2 - \hat{x}_2 \end{bmatrix} \end{cases} \tag{2.14}$$

Where $\delta(\cdot) = f(\cdot) - f_o(\cdot)$. The convergence of the error is achieved in absence of disturbance if the observer gain matrix is designed such that the matrix A_0 is Hurwitz. That is, for every positive constants h_1 and h_2. In the presence of δ, the observer gains are adjusted as (2.16).

$$A_0 = \begin{bmatrix} -h_1 & 1 \\ -h_2 & 0 \end{bmatrix} \tag{2.15}$$

$$h_1 = \frac{\gamma_1}{\varepsilon}, \;\; h_2 = \frac{\gamma_2}{\varepsilon} \tag{2.16}$$

Where $0 < \varepsilon \ll 1$, and the gains γ_1 and γ_2 can be determined via pole placement.

The sliding observer is explained extensively in chapter 5 and Annex III and no more detail will be given here. Both high-gain observer and sliding require some knowledge of the plant dynamics. An alternative method termed Nonlinear Extended State Observer has been created by Han [96] as follows. The plant in (2.12) is firstly augmented as:

$$\begin{cases} \dot{x}_1 = x_2 \\ \dot{x}_2 = x_3 + b_0 u \\ \dot{x}_3 = f(y, \dot{y}, w) \\ y = x_1 \end{cases} \tag{2.17}$$

Where f is an extended state, x_3. Here both f and its derivative are assumed unknown. By making f a state it is now possible to estimate it by using a state estimator. Han proposed and nonlinear observer for (2.17) as follows:

$$\begin{cases} \dot{z}_1 = z_2 + \beta_1 g_1(e) \\ \dot{z}_2 = z_3 + \beta_2 g_2(e) + \;\; b_0 u \\ \dot{z}_3 = \beta_3 g_3(e) \end{cases} \tag{2.18}$$

Where $e = y - z_1$ and z_1 is the estimation of the function f. Then, $g(\cdot)$ is defined has a modified exponential gain function:

$$g_i(e, \alpha_i, \delta) = \begin{cases} |e|^{\alpha_i} sign(e), |e| > \delta \\ \frac{e}{\delta^{1-\alpha_i}}, |e| \leq \delta \end{cases} \quad \delta > 0 \tag{2.19}$$

As α_i is chosen between 0 and 1, g_i yields high gain when error is small. δ is a small number to limit the gain in the neighbourhood of the origin. Starting with linear gain $g_i(e, \alpha_i, \delta) = e$, the pole placement method can be used for the initial design of the observer, before the nonlinearities are added to improve the performance.

The comparison of these three types of observers is accomplished in [94], proving best performance for the Nonlinear Extended Observer and followed closely by the Sliding Gain Observer.

In parallel with the force estimation techniques, based on disturbance observers, another research approach has been using sensor fusion has been developed to reduce the noise levels of the force sensors. In [97], [101] the information from a force sensor is fused with an accelerometer measurement in order to eliminate the effect of the tool inertia in the force sensor measurements. This sensor fusion is performed with the

Kalman filter In [98], data from force sensors and position encoders are fused. In [99] and [100] data gathered by means of a force sensor is combined with visual information to estimate position measurements between a grasped object and other objects in the environment

Chapter 3 New approach for dissimilar master-slave teleoperation

A general bilateral framework to cope with the dissimilarities of master and slave is presented in this chapter. Two new functional blocks are added to the conventional bilateral control scheme in order to cope with the differences in kinematics and dynamics when teleoperating a slave with a dissimilar master. A set of requirements for teleoperating an industrial robot is introduced, where some variables as the bilateral loop frequency or the command execution time are introduced. A detailed explanation of the use of assistive forces in order to guide the operator when performing a task is also given in this chapter. To conclude, the real issues encountered when teleoperating an ABB IRB 2400-16 with a Phantom OMNI are explained in detail, especially the optimisation technique used for the scaling of the workspace.

3.1 Dissimilar master-slave teleoperation requirements

In this section, the requirements for a dissimilar master slave teleoperation are presented. The developed method should cope with the kinematic and dynamic differences between master and slave and it is specially focused to teleoperate an industrial robot by means of a desktop haptic master.

In the industry is very common the need of teleoperating a slave with a kinematically dissimilar master due to the fact that in most cases the slave device is optimised for the task and the master device is optimised to be used by the operator.

A general approach shall be introduced in this chapter to manage all the events occurring during a teleoperation task, e.g. the managing of kinematic differences, creation of assistive forces to assist the operator, a method for scaling in position, and force feedback when non-backdrivable slaves and no sensors are employed.

An improved version of the axis-crossing method presented in [48] is suggested here in order to check when the position pointed by the haptic device belongs to the slave's workspace. When this condition is not verified, this method also helps to calculate the assistive forces which have to be applied on the haptic device to guide the operator through the correct path.

In order to obtain a smooth and stable bilateral control, it is well-know from the literature that at least 1 KHz real-time update rate is advised in order to achieve the required haptic fidelity [106]. The ability to reach the required frequencies is studied in detail in the particular case of an ABB robot with an SC4+ controller. Also, a discussion about different robot manufacturers is proposed at the end

Different methods have been developed in the past to cope with the workspace scaling issues. Having kinematically different devices with different workspace sizes leads to scaling problems. The human operator uses a haptic device to steer e.g. an industrial robot during a handling process. These haptic devices are usually designed for the convenience of the human operator and not prepared for the huge size of industrial robots which are prepared for handling heavy loads. Therefore, the physical workspace of a desktop haptic device is significantly smaller than the target workspace of the slave. In these circumstances, the human operator will not be able to reach and interact with objects located outside this limited workspace. To overcome this problem, several scaling techniques have already been reported in the literature [103], [104] (See overview in Table 3-1). The most common technique is position control, by which the displacements of the haptic device are scaled, translated and mapped to the motions of the slave. Position control with indexing is used to solve when the operator reaches

the limit of the workspace of the haptic device during position control. This is achieved by disconnecting the communication channel between haptic device and manipulator, typically by pressing a button, then moving the handle of the haptic device back to its origin. Afterwards the communication is resumed. Ballistic control is another method of copping with the workspace limits of the haptic device which adjusts the scale dynamically depending on the velocity at which the device is travelling within its workspace. Rate control is also used to manage the scaling problem. The displacements of the haptic device are interpreted as a velocity commands in the slave robot. Some hybrids controllers make use of a division of the master workspace in two regions, in the inner region, position control will be used whereas in the outer region, rate control is used to be able to reach big workspaces. Another technique called workspace drift control was introduced for manipulation in virtual environments.

Method	**Pros**	**Cons**
Position control	Simple Understandable Direct kinematic correspondence	Poor spatial resolution in case of large scaling
Ballistic control	Adaptive scaling factor Linear and nonlinear scaling factors	Complex implementation
Rate control	Simple Understandable Infinite workspace	No direct kinematic correspondence
Workspace drift control	Manipulating large objects Using small haptic device	Only virtual environments Conservative method
Hybrid position / rate control	Position and rate control at once No manual switching	Complex implementation

Table 3-1. Overview of scaling techniques.

3.2 Proposed general approach for bilateral teleoperation

Figure 3-1 represents an approach of a bilateral teleoperation where only conventional positional and force feedback are considered. Also, no delay in transmission of the

information is taken into account. The operator (human) exchanges forces and torques with the master device, in such a way that they both share their position, $x_h = x_m$, at all time. While the operator applies position commands and reaction forces, the haptic master conveys the external forces, measured or estimated from the environment, assistive and dragging forces, to the operator. The measured or estimated forces, which are transmitted to the human, have been previously processed in the dissimilar dynamics block and sent to the master controller as reference torques for the master joints. The assistive forces are those ones artificially created and conveyed to the operator in order to ease the teleoperation tasks. These can be vibratory, kinaesthetic or from different type and their objective is to guide the operator in his movement along the master´s workspace. On the other hand, the dragging forces are unintentional forces created in some control architectures where the force feedback depends on the positional and velocity errors. Due to the fact that, in some control schemes such as position-position a positional error is required in order to produce a set of torques that will move the slave manipulator towards the master´s pose and vice versa. In these cases, the operator would feel a resistive force like if he was continuously pulling from the haptic device. Finally, the inertial forces arise by the fact that the master device is not ideal, and it presents mass and inertia which will induce a reaction force to the movement.

In the most common scenario, the master control system would receive the positional feedback from the master device and send the appropriate joint torque to the haptic master, i.e. current to the actuators if an electrical manipulator or voltage to the valves if a hydraulic device. The master control is in charge of interfacing with the dissimilar kinematics algorithm by sending the master´s position and receiving the forces to be applied. The assistive forces are calculated in the dissimilar kinematics block in order to correct the trajectory of the human operator in a way such the movement is always performed inside the slave's workspace. Afterwards, these are processed in the dissimilar dynamics block to be transformed into the joint space. The remaining forces are calculated by the dissimilar dynamics block depending on the external forces or control scheme utilised. This block typically employs the master's jacobian to transform the external forces and torques from cartesian space to the master's joints space.

The dissimilar kinematic block interfaces the master´s control with the slave´s control in a way such the master´s end-effector pose and position is mimicked by the slave's end-effector as much as possible. The slave´s control will close the loop with the slave device by controlling its position by means of torque commands applied on its actuators.

A state observer of the slave is introduced here as a general scenario for those control schemes where a force has to be estimated without using force sensors, central topic of

this research. In a common scenario, this observer would receive the torque command issued to the slave device, and all the available feedback from it, such as position, velocity or acceleration. With this information, it will estimate the value of the external forces and torques applied on the slave, if any. Afterwards, the dissimilar dynamic block will transform all these forces from the slave´s reference to the master´s reference.

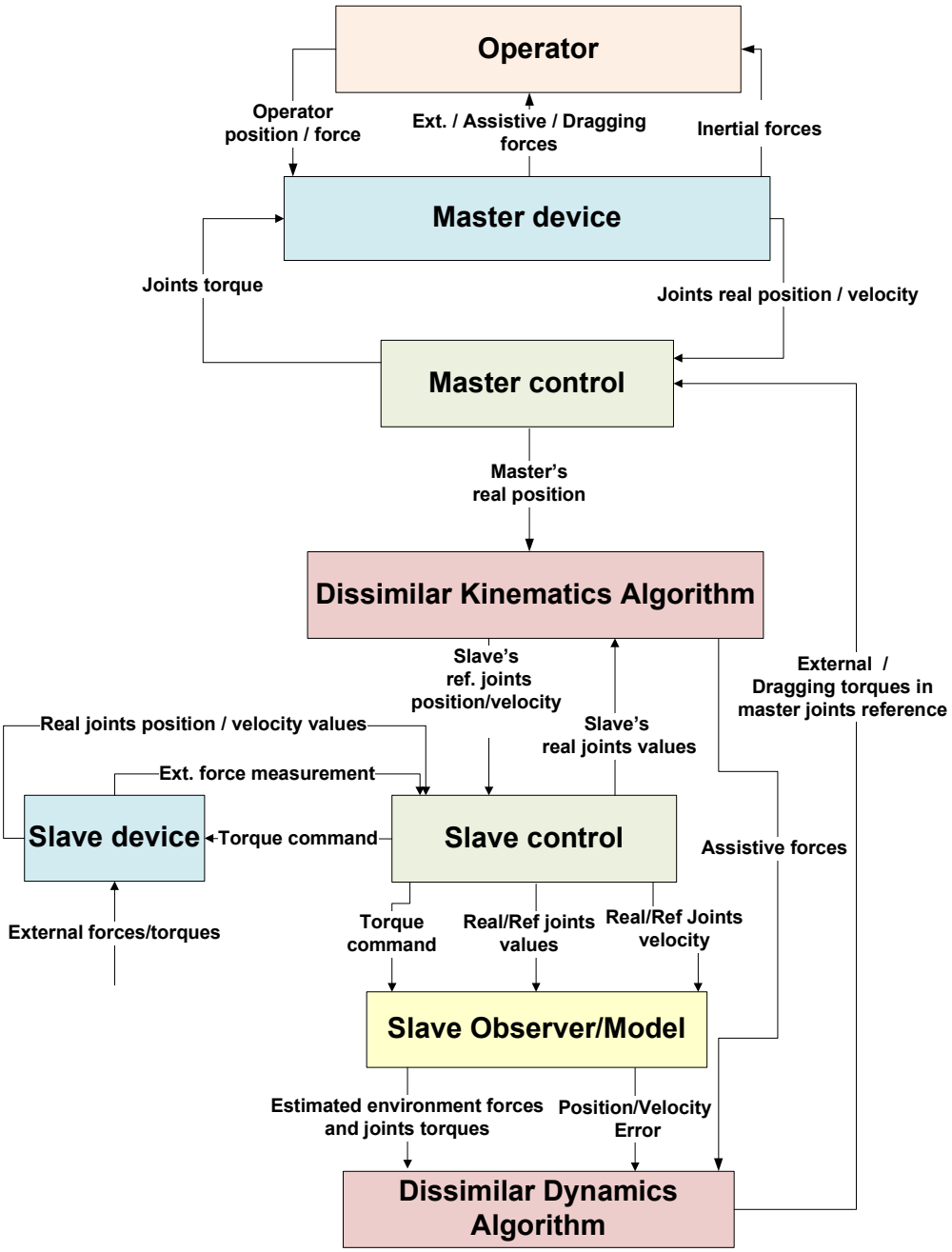

Figure 3-1. General control scheme for a bilateral system for dissimilar master-slave.

3.3 Kinematics considerations

The block diagram represented in Figure 3-3 describes, in pseudo-code, the before mentioned, dissimilar kinematics algorithm, that is executed in each cycle of the bilateral control. This algorithm receives the input position from the master´s control and a flag indicating whether the bilateral control has already started or not. Afterwards, a set of parameters which define the kinematic structure of both master and slave, the starting transformation matrix and joint limits are loaded in memory. During the first execution, independently whether the master is at home position or not, it will lead to the calculation of the master´s direct kinematics in order to find the transformation matrix. This is indicated by (3.1) and particularized for a 6 dof robot which relates the base system (0) with the end-effector system (6).

$$T = {}^{0}A_1 \cdot {}^{1}A_2 \cdot {}^{2}A_3 \cdot {}^{3}A_4 \cdot {}^{4}A_5 \cdot {}^{5}A_6 \tag{3.1}$$

Where, the ${}^{i-1}A_i$ matrices are the Denavit-Hartemberg homogeneous matrices for transforming a vector expressed in system $i-1$ to a vector expressed in system i. These set of matrices can be calculated with a well-known expression once the Denavit-Hartemberg parameters of a manipulator have been established (θ_i, d_i, a_i, α_i).

Once the Denavit-Hartemberg rules have been followed to number and choose the reference system, the mentioned expression is applied to obtain each transformation matrix. The parameter θ_i, is the angle that has to be turned around z_{i-1} such as x_{i-1} and x_i become parallel. In a similar manner, the parameter d_i is the distance measured along z_{i-1} that would have to displace $\{S_{i-1}\}$ such as x_{i-1} and x_i become aligned. Also, the parameter a_i is the distance measured along x_i (which now agrees with x_{i-1}) so its origin matches completely with $\{S_i\}$. Finally, the angle α_i is the angle to be turned around x_i, such as the new system $\{S_{i-1}\}$ matches with $\{S_i\}$.

After obtaining the transformation matrix, the position of the haptic master is compared with a standard initial position fixed a priori. In order to avoid an abrupt tracking of the master, the initial position and pose of the slave should be made similar to the master at the starting point. A methodology for performing the initial coordination will be explained below.

If the fixed starting point is given by (3.2), the vectors n, o, a are referred to the orientation of the end-effector with respect the base system and the vector p expresses the position of the end-effector with respect the base.

$$T_{start} = \begin{pmatrix} n_{xo} & o_{xo} & a_{xo} & p_{xo} \\ n_{yo} & o_{yo} & a_{yo} & p_{yo} \\ n_{zo} & o_{zo} & a_{zo} & p_{zo} \\ 0 & 0 & 0 & 1 \end{pmatrix} = [\bar{n}_o, \bar{o}_o, a_o, p_o] \tag{3.2}$$

$$T\,{}_i^m = \begin{pmatrix} n_{x_i} & o_{x_i} & a_{x_i} & p_{x_i} \\ n_{y_i} & o_{y_i} & a_{y_i} & p_{y_i} \\ n_{z_i} & o_{z_i} & a_{z_i} & p_{z_i} \\ 0 & 0 & 0 & 1 \end{pmatrix} = [\bar{n}_i, \bar{o}_i, a_i, p_i]^m \tag{3.3}$$

In order to compare each homogeneous matrix of the master ($T\,{}_i^m$) with T_{start}, orientation and position are compared separately. The orientation is compared by calculating the angle between both reference systems by means of the three direction cosines and the position difference is easily calculated by the absolute value of the error for each coordinate.

$$\bar{\varepsilon} = \begin{pmatrix} \text{acos}(\bar{n}_o \cdot \bar{n}_i) \\ \text{acos}(\bar{o}_o \cdot \bar{o}_i) \\ \text{acos}(\bar{a}_o \cdot \bar{a}_i) \end{pmatrix} \tag{3.4}$$

$$\bar{\rho} = \begin{pmatrix} |p_{xo} - p_{x_i}| \\ |p_{yo} - p_{y_i}| \\ |p_{zo} - p_{z_i}| \end{pmatrix} \tag{3.5}$$

Where p_{xo}, p_{yo} and p_{zo} are the components of the $\bar{p}_{start}$ vector which defines the starting point with respect the base origin.

Only when the angular distance falls inside the allowed tolerance for the angular error, and the Cartesian distance is inside the tolerance for the positional error, is when both transformation matrices are considered similar. This is given by (3.6) and (3.7):

$$if\ (\varepsilon_1 < \varepsilon_{1_{MAX}})\ AND\ (\varepsilon_2 < \varepsilon_{2_{MAX}})\ AND\ (\varepsilon_3 < \varepsilon_{3_{MAX}}) \tag{3.6}$$

$$if\ (\rho_1 < \rho_{1_{MAX}})\ AND\ (\rho_2 < \rho_{2_{MAX}})\ AND\ (\rho_3 < \rho_{3_{MAX}}) \tag{3.7}$$

The fulfilment of conditions (3.6) and (3.7) will trigger a conditional flag which enables the bilateral tracking.

That process will allow the master and slave to converge before the beginning of the bilateral loop. Until the haptic-master does not acquire the wanted position and orientation, the slave will not perform any movement and the forces exerted by the master will be zero.

Once the operator reaches the desired starting point with the appropriate orientation, the algorithm will start to calculate continuously the inverse kinematics of the slave,

in order to check if the commanded point is inside of the slave's workspace. The equation (3.8) shows how the slave´s inverse kinematics is applied receiving the transformation matrix of the master as an input.

$$\left[Q\ {}^{m}_{i}\right] = Slave\_IK(T\ {}^{m}_{i}) \tag{3.8}$$

The inverse kinematics will provide with the necessary joint values that the slave should have to allow the manipulator's end-effector to reach the position commanded by the master's end-effector. In that case, the slave's control will receive those joints values as a reference.

$$\begin{cases} if\ \forall\ Q_i \in [q^s_{i,MIN}, q^s_{i,MAX}] \rightarrow T\ {}^{m}_{i}\ belongs\ to\ Slave's\ workspace \\ if\ \forall\ Q_i \notin [q^s_{i,MIN}, q^s_{i,MAX}] \rightarrow T\ {}^{m}_{i}\ does\ not\ belong\ to\ Slave's\ workspace \end{cases} \tag{3.9}$$

When the result of the inverse kinematics checking indicates that the haptic master is pointing to a position or presenting a pose which is not reachable by the slave, a force proportional to the distance between the current point and the workspace border will be conveyed to the master in order to force the operator returning inside the allowed workspace. The position of the slave will not be modified. In some cases it might be convenient to correct the master´s pose as well, so it will belong to the dexterous pose of the slave in the Cartesian point where the master is pointing inside the slave´s workspace. This can be done by finding the closest angular position to which the haptic master has to be rotated so it enters into the dexterous workspace of the slave.

For the simplest scenario where only reachable workspace is considered, the slave forward kinematics is calculated with the angular joints values which will be typically slightly out of range, but which still will generate valid Cartesian coordinates. This assumes that the bilateral loop has already started and the master has entered in a non-reachable position by the slave. The transition between the inner and outer part of the slave workspace will happen in two consecutive time instants spaced by the sample time T_S, normally on the order of 1 ms. Let us consider these two transformation matrices T_p and T_{out} as the previous point which still belonged to the slave workspace and the first point which does not belong, respectively. The distance between these two points in Cartesian space can be calculated with the position vector of both matrices.

$$T\ {}^{s}_{p} = [\bar{n}_p, \bar{o}_p, \bar{a}_p, \bar{p}_p]^s \ \text{ and } \ T\ {}^{s}_{out} = [\bar{n}_{out}, \bar{o}_{out}, \bar{a}_{out}, \bar{p}_{out}]^s$$

$$distance = \left\| \bar{p}_p - \ \bar{p}_{out} \right\| \tag{3.10}$$

The direction of the force, in this case, is calculated relatively to the starting point although a different convention could be chosen.

$$\bar{v}_{force} = \bar{p}_{out}\text{-}\bar{p}_{start} \tag{3.11}$$

And the force value would be proportional to the calculated distance and with the direction pointing to $\bar{p}_{start}$.

$$\bar{F}_{Assistive} = K_{assistive} \cdot distance \cdot \ \bar{v}_{force}/\|\bar{v}_{force}\| \tag{3.12}$$

A different scenario arises when the master is out of the slave workspace before the bilateral loop starts. This situation can occur while the operator is manoeuvring during his search for the starting point. In this circumstance, no $\bar{p}_p$ exists and the assistive force has to be calculated in a different way.

The framework shown in Figure 3-3 implements the calculation of the assistive force that guides the operator to return to the slave's workspace if the bilateral loop has not started yet. If that situation arises, the slave will have not executed any movement and it will be on hold, waiting for the master to reach the starting point. In order to obtain the assistive forces, an extended version of the Axis-Crossing Method Winding Number Algorithm, developed by Alciatore and Miranda in 1995, has been implemented. In addition, it also provides the distance of the master's Cartesian position to the slave's workspace border. This can also be used when a numerically more efficient method is desired to determine if a point belongs to a workspace without needing the calculation of the inverse kinematics.

3.3.1 Improved axis-crossing method

The axis-crossing method presented in [48] determines very efficiently if a point is within a polygon independently of the shape of this. It also generates the winding number, which measures not only whether the polygon $\boldsymbol{C}$ encloses the point $\boldsymbol{X}$, but also how many times and in which direction, $\boldsymbol{C}$ winds around $\boldsymbol{X}$. This last property is not of special interest in robotics because of the nature of the workspaces, however the primary function of this algorithm presents some interest. By transforming the robot workspace in a polygon with the number of segments depending on the desired accuracy it is possible to employ this method.

The winding number (w) can present these different values:

$$\begin{cases} 0 \quad ix\ X\ is\ not\ inside\ C \\ n > 0 \quad if\ C\ winds\ around\ x\ n\ times\ conterclockwise \\ n < 0 \quad if\ C\ winds\ around\ x\ (-n) times\ clockwise \end{cases} \tag{3.13}$$

Where $X = (x_0, y_0) \in \mathbb{R}^2$ is the point to test, $C = \bigcup_1^n \overline{v_i v_{i+1}}$ is the closed polygon to be tested, and $\bar{v}_1$,..., $\bar{v}_n$ are the ordered vertices of C, where $\bar{v}_i = (x_i, y_i)$.

Without loss of generality, it is assumed that X is the origin, which can be obtained by translating all the vertices of the polygon so in the end, X occupies the origin's position. Since the point-in-polygon test is invariant under horizontal and vertical translations, this operation simplifies the algorithm. The pseudo-code which implements the conventional axis-crossing method [48] is shown in Figure 3-4. The evaluation of w determines if the point X is inside the workspace.

Once w is present, the algorithm extension shown in Figure 3-5 allows the identification of the nearest polygon edge to X and the calculation of the force vector which will be supplied to the master in order to guide the operator so this can return into the workspace. In the axis-crossing method extension, the Euclidean distance from X to the middle point of each polygon edge is calculated and the nearest edge is selected. Secondly, a perpendicular force to that edge and passing through X is created to be conveyed to the haptic master.

With this method, it is possible to control a manipulator with a kinematically different master having a standard initial pose and position which will ensure a safe system. Nevertheless, in order to implement this algorithm, it is necessary to solve the inverse kinematics of the slave by either numerical or analytical methods.

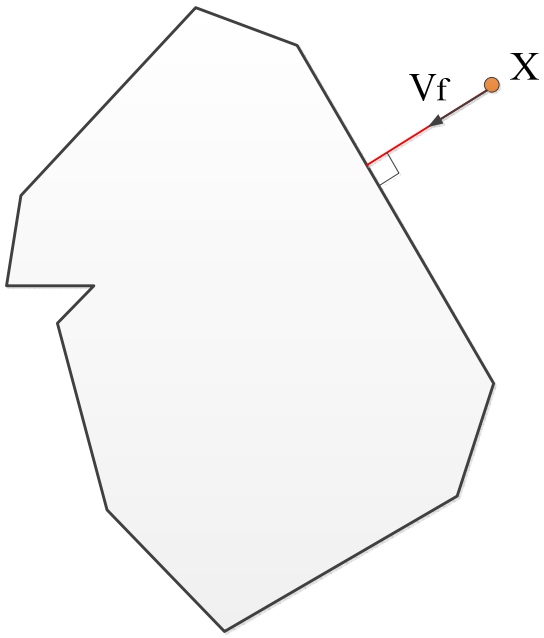

Figure 3-2. Example of calculation of the assistive force when a commanded point is out of slave´s workspace.

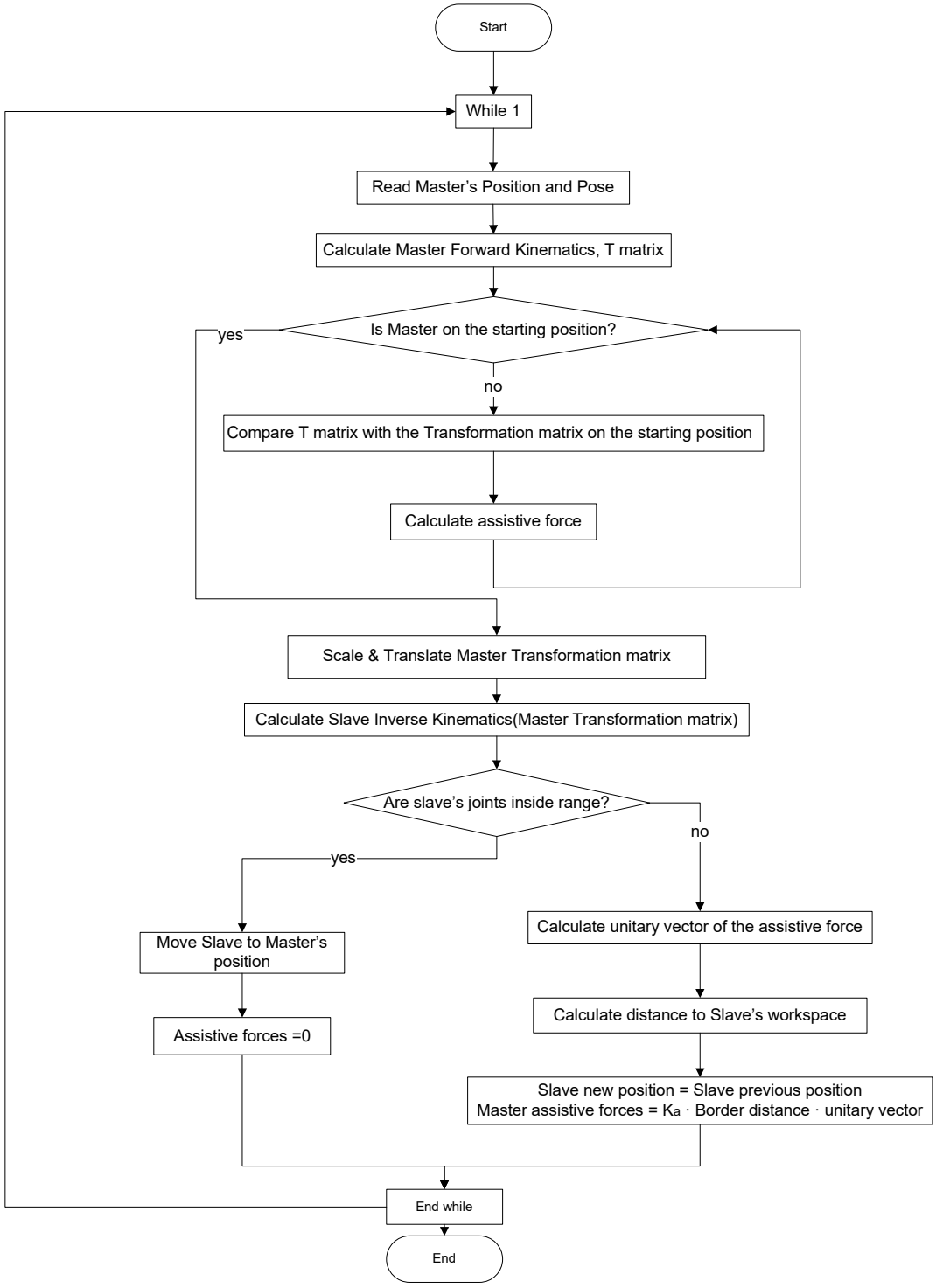

Figure 3-3. Dissimilar kinematics algorithm.

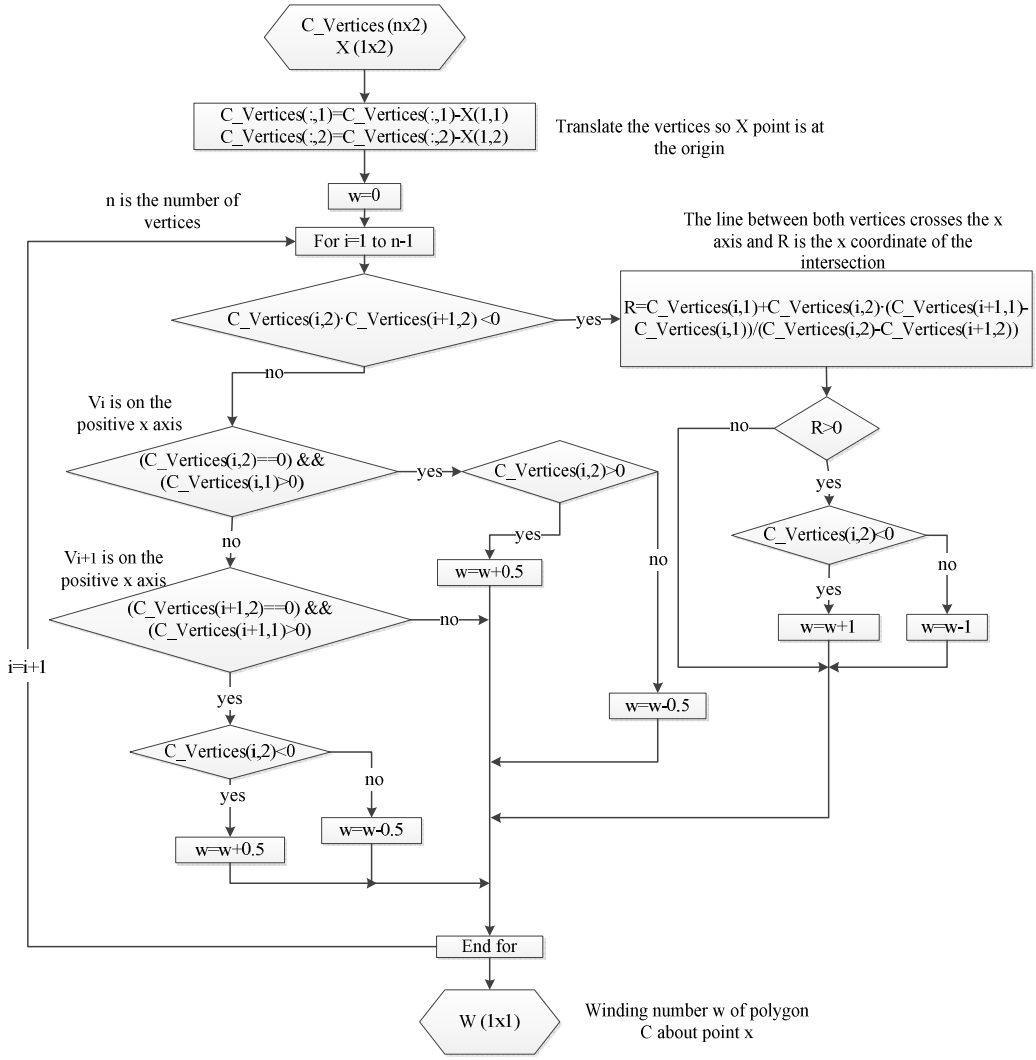

Figure 3-4. Pseudo-code of the axis-crossing method for determining if a point is inside a polygon.

3.4 Dynamics considerations

This section continues with the flowchart of Figure which describes the general framework of teleoperation for dissimilar master and slave. In addition to the assistive forces, created to help the operator, and processed in the dissimilar kinematics block, the major part of the dynamic content is based on the external forces sensed or estimated and the dragging forces provoked depending on the chosen control algorithm. The output of the force estimation process, carried out in the slave observer block, are the estimated forces and torques in Cartesian space referred to the slave´s system and the errors in position and velocity, of the real slave, with respect the master.

The dissimilar dynamics algorithm is in charge of transforming these forces from the slave´s reference to joint torques applied on the haptic master.

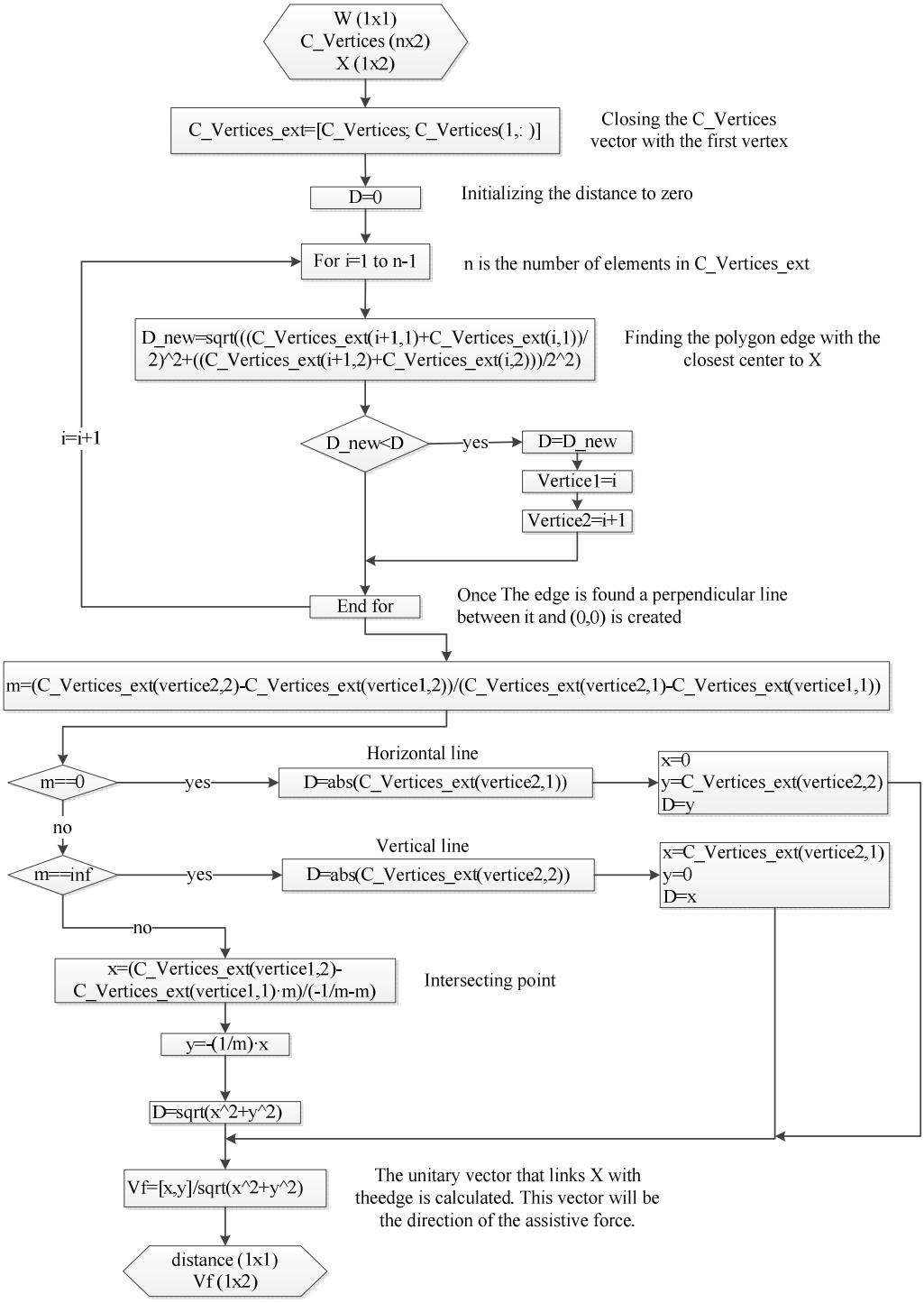

Figure 3-5. Extension of the axis-crossing method to calculate the direction of the assistive force.

It applies the equation (3.14) and scales the forces conveniently.

$$\tau = J^T F \tag{3.14}$$

Where τ is the joints' torques that have to be applied on the master's joints in order to replicate the forces and torques given by F on the master's Cartesian space. The J^T denotes the master´s jacobian transpose which depends only on the joints values.

In Figure 3-6 a case example of the bilateral control based on two channels, position and velocity used in Dexter 20 is shown. It is worth noting that the forces $k_{v1} \cdot V_m$ and $e_p \cdot k_{pm}$ would be also calculated inside the dissimilar dynamic block. By doing this, every force and torque that is going to be conveyed to the operator is firstly processed in this functional block.

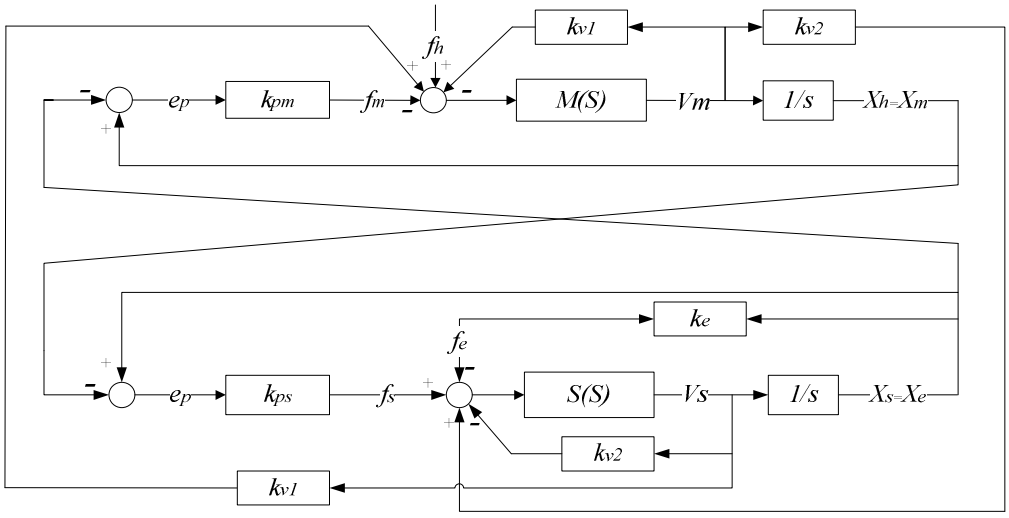

Figure 3-6. General bilateral control used in Dexter 20.

3.5 Case example: Teleoperating an ABB IRB 2400-16

With the objective of testing the algorithms explained in this chapter, an experimental setup was planned and commissioned. This setup was based on a bilateral control with dissimilar master and slave. The master used was the Phantom OMNI, manufactured by Sensable (Figure 3-7) whose characteristics are detailed in Annex I. It is worth noting that this haptic master presents 6 dof of positional feedback although only 3 dof of force feedback. The first three joints are the only ones creating torque which is able to render a force in (x, y, z) in the master tip. The slave device used for his experiment was the industrial robot ABB IRB 2400-16, controlled using an SC4+ controller shown in Figure 3-8 and with its main characteristics described in the Annex

I. The robot controller is equipped with the operating system BaseWare OS. This system controls every aspect of the robot, like motion control, development and execution of application programs communication etc. For additional functionality, the robot can be equipped with optional software for application support - for example gluing and arc welding, communication features - network communication - and advanced functions such as multitasking, sensor control etc, although that was not the case of this experiment.

In Figure 3-9 the interface between the different elements of the experiment is shown. A PC running LabView 2011 was dedicated to interface the different components and provide the human interface. The master control was written in C code and called from the LabView interface. Both pieces of software were communicating with each other by means of TCP sockets. The master control was running at 1 KHz.

Figure 3-7. Phantom OMNI haptic master from Sensable.

In order to interface with the slave, only a serial port RS 422 was available in the SC4+ controller but no Ethernet was included in it. Also, there were no real time communication utilities or multi-tasking options like those ones used for correcting the trajectory while welding or painting in the manufacturing industry.

The lack of communication utilities was the main drawback when teleoperating this robot and it was the cause of the very low loop frequency obtained. In [52], the research of a Swedish university, proposed to use additional hardware parts such as a PowerPC board, a PMC-PCI interface and a flash disk which are added to the original SC4+ controller to be able to run software in a fastest way and improve the communication

capabilities. Nevertheless, this system is still under development, and it is of extremely difficult implementation and there is not enough information for its development, so it could not be implemented. The specifications of this industrial robot can be seen in the Annex I.

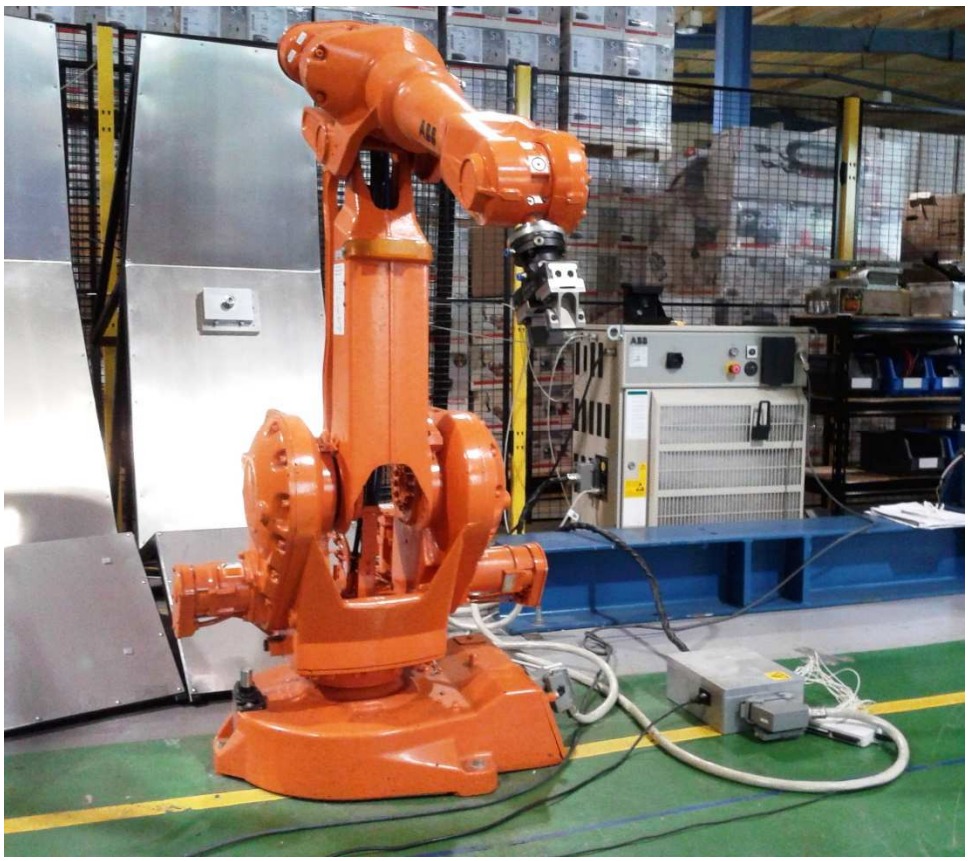

Figure 3-8. ABB IRB 2400-16 with SC4+ controller.

In Figure 3-9, it is shown how, the human machine interface (HMI) running in the PC with LabView, is connected to the robot controller via serial channel. Independently of the communication channel used, the information transmitted between the LabView controller and the robot controller corresponds to the diagram of Figure 3-3. This means that only the reference value of the 6 joints is commanded to the robot controller, liberating the SC4+ of accomplishing the laborious inverse kinematics. Thereby, the robot controller function was just executing a continuous loop that reads joints reference value coming from the dissimilar kinematics algorithm and writing real joints' value. The pseudo-code of the ABB language (RAPID) used for teleoperating is represented in Figure 3-10. A loop is executed continuously to read the new target joints' values, execute the movement and send the real joints' values back to the PC controller.

Different approaches can be used in order to read and send information back to the robot controller depending on the instructions used to read and write data on the serial channel. For the RAPID language used on the ABB robots and basic serial communication, the following variants for reading and writing are available: reading instructions and writing instructions (See Table 3-2 and Table 3-3) [105].

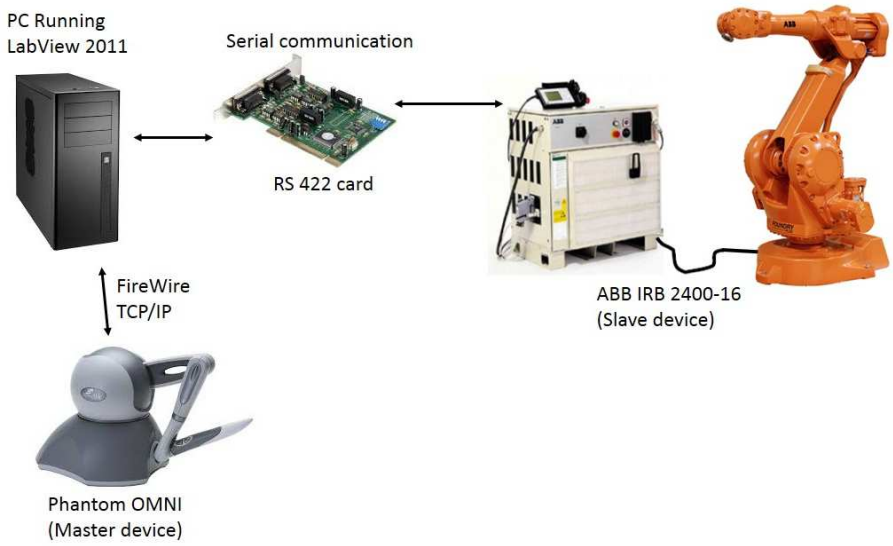

Figure 3-9. Experimental setup for teleoperating the ABB IRB 2400-16.

Reading instructions in RAPID code	
ReadBin	(Read Binary) is used to read a byte (8 bits) from a file or serial channel. This function works on both binary and character-based files or serial channels.
ReadNum	ReadNum (Read Numeric) is used to read a number from a character-based file or serial channel.
ReadStr	ReadStr (Read String) is used to read a string from a character-based file or serial channel.
ReadStrBin	ReadStrBin (Read String Binary) is used to read a string from a binary serial channel or file.

Table 3-2. Reading instructions available in RAPID code.

A string based communication was implemented due to the relative easiness of use in comparison with binary based instructions, with `ReadNum` and `Write` instructions. The complete source code is completely shown in Annex I.

Writing instructions in RAPID code	
Write	Write is used to write to a character-based file or serial channel. The value of certain data can be written as well as text.
WriteAny Bin	WriteAnyBin (Write Any Binary) is used to write any type of data to a binary serial channel or file.
Writ- eStrBin	WriteStrBin (Write String Binary) is used to write a string to a binary serial channel or binary file.
WriteBin	WriteBin is used to write a number of bytes to a binary serial channel

Table 3-3. Writing instructions available in RAPID code.

The additional StopMove and ClearPath instructions play a crucial role in a teleoperation software. Ideally the slave robot should follow perfectly the master's command with minimum error. However during practical implementation it might be a common situation when the slave manipulator cannot replicate the master's movements as fast as it should due to mechanical limitations or due to a slow loop frequency. If this is the case, it is important to be able to correct the trajectory on real time. When the slave is moving and before it reaches the target joint value there might be a new available joint target from the master.

The only way of issuing a new command for the slave is interrupting the current command and executing a new one. To interrupt the current path these two instructions have to be executed in RAPID, StopMove to stop the current planned path and ClearPath to clear the planned movement. This strategy produced a discontinuous robot movement because move and stop commands were continuously issued. Ideally, if a robot with an open control architecture is used, torque commands could be issued instead of position commands, improving the control efficiency and speed. But unfortunately, in a closed system as the one present in ABB, this option could not be used and only position commands can be issued. Other alternative to improve the control smoothness could be to perform velocity control in a way such that the robot does not have to stop its movement in each iteration. Unfortunately this option was not available either.

3.5.1 Delay issues found during the RS422 serial communication and RAPID program execution

Different programming and communication techniques were tested under the development of the optimum teleoperation control. Some of them have already been explained before, and some others related with the loop delay will be commented here.

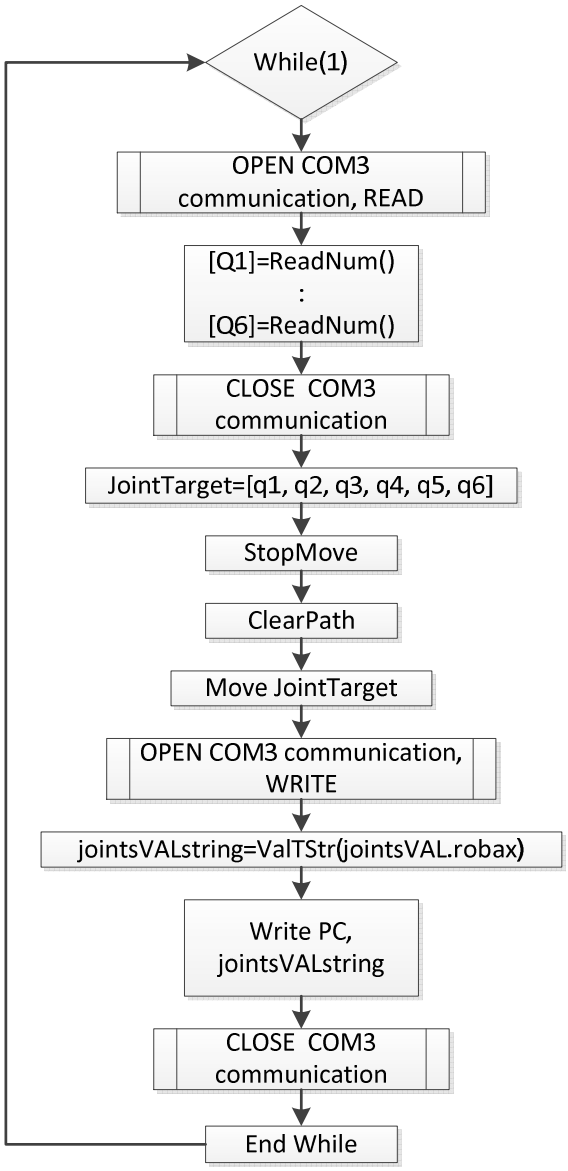

Figure 3-10. Pseudo-code of RAPID program running on the SC4+ controller.

In a serial communication channel, a common baud rate between sender and receiver has to be established. Different baud rates were tested with the objective of increasing as much as possible the loop frequency of the bilateral control. The measured bilateral loop frequency with each baud rate was the indicated by Table 3-4. It can be seen how the obtained frequency is slow and it is not able to overcome the 13 Hz barrier. In order to study the origins of this unacceptable delay, experiments were performed to measure the execution time of simple instructions written on RAPID code. The methodology used to measure the execution time was the following: certain digital outputs of the SC4+ controller were turn high and low before and after a command execution.

They were read with an oscilloscope in order to estimate the elapsed time during the execution of basic instructions.

Baud rate	**Max loop frequency [Hz]**
600	0.5
1200	1.08
2400	2
4800	3.7
9600	13
19200	13
38400	13

Table 3-4. Bilateral loop frequency reached at different baud rates.

The IO unit used for measuring the time lapses was the DSQ328, consisting in 16 digital inputs and 16 digital outputs. The results obtained, which are summarized in Table 3-5, are the following:

A. Changing the state of a digital output.

The time elapsed on changing the state of a digital output was characterized to take into account the minimum amount of time required for measuring the rest of instructions. These set of commands shown in Table 3-5 (Test 1) turn the first digital output on, then off and finally on again. With this methodology it is possible to characterize the time invested in changing the value of a digital output. This set of instructions produce a voltage profile as shown in Figure 3-11. This result means that the first two instructions that turn on and off the digital output 1 have a time lapse of 5 ms, or approximately 2.5 ms in executing each instruction.

B. Write a binary data on the serial channel

The same procedure was applied for the set of commands shown in Table 3-5, test 2. They took a total time of 6.5 ms. This result helps to infer the time needed to write a binary number, which is around 1.5 ms.

C. String conversion and writing on the serial channel

In Table 3-5, test 3 it can be seen that the total time expend on this operation is 6.5 ms, which gives a total time for the string conversion and sending of 1.5 ms.

D. Time invested in reading 6 joints' values

It is important to estimate the required time taken by the robot controller in reading the 6 joint values because these set of instructions are going to be repeated in each

cycle and the total time should be minimized. In Table 3-5 test 4, the total time taken by this set of instructions is 35 ms. Due to the basic set of on and off instructions takes 5 ms, it is possible to infer that the reading of 6 joints values takes 30 ms.

E. Time invested on reading 6 joints values with channel opening and closure.

It is shown in Table 3-5, and test number 5, than the total time for this set of instruction was 40 ms. This establishes the time required for opening and closing the communication channel in approximately 10 ms.

F. String operations.

Some string manipulations were also quantified to check if the predicted longer operation times were finally measured. The time on reading a string with the values of 6 joints turned out to be 25 ms, and this proved that string operations were not particularly slower.

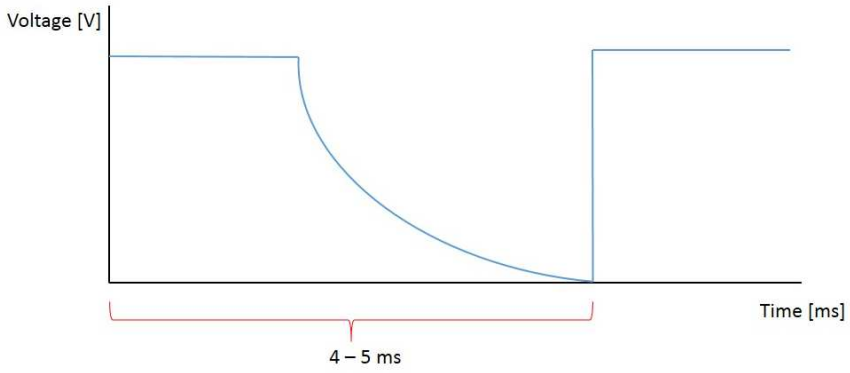

Figure 3-11. Oscilloscope waveform recreation of test A.

G. Stop the movement and clear the path

Finally the set of instructions for stopping a movement and clearing the buffer of stored movements were analysed and the results clearly indicated the origin of the big delay measured during the teleoperation loop.

The movement stopping command turned out to be just 1 ms operation, while clearing the buffer took up to 300 ms.

H. Moving operations

The execution of a moving operations was also analysed. It was found that, as expected, that the time invested for the robot to move was obviously dependent on the target

point to be reached. Nevertheless, for a static target position, this is, executing a target position that is the same than the current one, the amount of time required for executing the move operation without the concurrent movement was approximately of 100 ms. The concurrent movement allows the execution of the following operations at the same time than the movement is being accomplished. Unfortunately there is a limitation of 5 instructions in succession, so this strategy could not be employed in an infinite loop.

3.5.2 Discussion about timing analysis

The methodology employed for measuring the instruction time using an oscilloscope to register the signal coming from the digital outputs of the controller board, proved to be successful. The large amount of time employed by the robot controller (SC4+) in executing simple set of instructions together with the slowness of the communication channel resulted in a very slow loop frequency of around 13 Hz. This low frequency created a very jittery movement and an erroneous reference tracking since the slave was not able to follow the master properly. With the default loop configuration, every time a movement instruction is executed, the controller waits until it is finished before a new movement command is executed. The slow loop frequency and this characteristic provoked a big error when tracking the master. The operator moved the master much faster than the slave was able to update its position. This operating condition was the cause of instabilities and poor performance on the bilateral control. With the objective of increasing the performance, the ability of interrupting the robot movement to update the robot target position on real time was investigated. The only option available without having additional and expensive software extensions was to use the couple of instructions before mentioned of stopping the movement and clearing the buffer. This set of commands allows to stop the current joint target value and prepare the controller for the new one by clearing the planned path. It has been shown the large amount of time required for clearing the buffer which decreased the loop time to around 4.5 Hz. These values are significantly smaller than those ones recommended in the literature as in [33], [60], [106] where values ranging from 100 Hz to 1000 Hz are recommended for positional bandwidth. Even faster frequencies are recommended in order to obtain a good force response [60].

Test Nº	**Description**	**RAPID code**	**Time [ms]**
1		`SetDO, do1, 1`	7.5

	Changing the value of a digital output.	`SetDO, do1, 0` `SetDo, do1, 1`	

2	Write a binary q on the serial channel	`SetDO, do1, 1`
		`WriteAnyBin, q1`
		`SetDO, do1, 0`
			6.5

3	String conversion and write to the serial channel	`SetDO, do1, 1`
		`String=ValToString(ValueJoint1)`
		`Write PC, String`
		`SetDO, do1, 0`
			6.5

4	Reading 6 joints values	`SetDO, do1, 1`
		`Read q1`
		`….`
		`Read q6`
		`SetDO, do1, 0`
			35

5	Time invested on reading 6 joints values with channel opening and closure	`SetDO, do1, 1`
		`Open PC`
		`Read q1`
		`….`
		`Read q6`
		`Close PC`
		`SetDO, do1, 0`
			40

6	Stop a movement	`StopMove`	1
7	Clear the buffer	`ClearPath`	300

Table 3-5. Timming analysis for SC4+ controller instructions.

The loop frequency obtained during the practical implementation on the ABB IRB 2400-16 with the SC4+ controller, would make a bilateral teleoperation unpractical. Typical values obtained when the slave is in movement are in the order of 4 Hz due to strong hardware limitations. Given the time required by the controller to execute some basic functions, even updating the communication channel and installing Ethernet would not guarantee much better performance. During conversations with ABB representatives from United Kingdom, the best time response they had achieved was a position update frequency range of 100 ms to 200 ms, meaning that the maximum achieved loop frequency was 10 Hz. This is not much faster than the frequency achieved in this experiment. However, it is expected that in newer controller versions, i.e., IRC5 the controller speed would be faster, allowing a better performance of the teleoperation tasks when force feedback is needed. It seems that ABB does not facilitate the rapid interfacing with the low level control system on its robots, giving the research community difficult alternatives such as the mentioned in [52]. It was possible to find out that the team of Lund University have manage to run the teleoperation loop at 250 Hz using the IRC5 controller after an intense research carried out during years. However,

for force-controlled manipulation and teleoperation applications, especially in stiff environments, there is a unanimity of the literature, that control rates of more than 1 KH are essential to avoid damaging the robot and its environment [106]. In this sense it has been an effort of the research community to overcome the limitations of the commercially available control systems for the industrial robots manipulators [108]. Also, although ABB seems reluctant to allow a quick access to its controller, several industrial robots suppliers including Mitsubishi [109], COMAU Robotics [110], KUKA Roboter GmbH [111], and Staubli [112] have introduced a possibility of interoperability of their robot controllers with control algorithms executing on external computers and developed new control interfaces enabling open communication channels with rates higher than 1 kHz in some cases.

3.5.3 Dissimilar kinematic solution based on optimum manipulability. Application of sequential quadratic programming (SQP) for obtaining an optimal workspaces overlap.

When teleoperating a slave with a dissimilar master one must pay attention on how the master's movements are tracked by the slave. In positional terms, the tracking conditions can be classified in two different modes, relative and absolute. A teleoperation algorithm is carried out in relative mode when the master´s movements are imitated by the slave by doing only relative movements. This is, starting from different initial positions, an increment of Δx of the master will be followed by an increment of $s \cdot \Delta x$ on the slave, where s is the scale. An absolute tracking mode is when not only the increment in the coordinates are tracked, but also, the absolute positions. The last method presents the advantage of having the master and slave with the same position and orientation at all times, facilitating the understanding of the situation by the master's operators and the intuitiveness of the whole system. Also, with this technique the workspaces can be better exploited. This technique has been employed during the teleoperation of the ABB robot with the Phantom master.

Although both systems present joints similarities, as it is described in Annex I, the joints' range differs. The links' length also differs considerably, provoking a situation where the workspaces are greatly different. The similar configuration of joint 1, allows to reduce 1 order the 6 dof problem by symmetry criteria. In this scenario, with the problem reduced to a 5 dof, one must fix a geometrical transformations which allow to map both Cartesian spaces. Different criteria could be used for solving this issue, i.e. maximizing the workspace overlap by scaling and translating the master´s workspace, reducing the slave's task space to a preferred manipulability area, etc. Independently

of the selected criteria it is important to highlight that for every reachable Cartesian point in the three-dimensional space there might be an infinite number of different orientations the manipulator can present. For this reason, it would be impractical to carry out the workspaces mapping based on an exhaustive study of every possible pose that both master and slave could have in each Cartesian point. A common criteria is to analyse the reachable workspaces by accounting only joint movements which produce a displacement of the end-effector in a plane. In practical terms, this means taking into account only joints 2 and 3 and 5 of master and slave. By doing this, the end-effector coordinates in Cartesian space are projected over a radial plane defined by two perpendicular axis, the first rotational axis (vertical) and a radial axis which rotates with joint 1.

In order to transform the Cartesian coordinates from the master space to the radial plane, the transformation indicated by (3.15) is used.

$$\begin{cases} \rho^r_{m=\sqrt{(x_m \cdot s)^2+(y_m \cdot s)^2}} \\ z^r_m = z_m \end{cases} \tag{3.15}$$

Where the duple $(\rho^r_m\ , z^r_m)$ define the new master's coordinates in a radial plane and (x_m, y_m, z_m) are the Cartesian coordinates of the master. This duple resultant from the forward kinematics of the haptic device has to be properly scaled and translated with appropriate values in order to achieve the selected overlapping criteria. Let us call $\bar{p}\,^r_m$, the end-effector's position vector, projected on a radial plane, output value from the forward kinematics transformation of a vector of joint values $\bar{q}$. Applying (3.17) will lead us to define the new master´s position $\bar{p}\,'_m$ resulting from the scaling and transformation of the original projected value.

$$\bar{p}\,^r_m = FK(\bar{q})|_{q_1=cte} \tag{3.16}$$

$$\bar{p}\,'_m = s \cdot \bar{p}\,^r_m - \bar{t} \tag{3.17}$$

By doing this, it is possible to reduce the search of an optimum overlap between master and slave's workspaces to the search of the appropriate translation vector on the plane, $\bar{t}$ and the scale factor (s) to be applied on the master's coordinates.

The problem of finding appropriate values for $\bar{t}$ and s in a way that the overlapping is maximized and the desired manipulability criteria are fulfilled is an optimisation problem which can be established as follows:

$$\begin{pmatrix} \bar{t}_{opt} \\ s_{opt} \end{pmatrix} = \min f\begin{pmatrix} \bar{t} \\ s \end{pmatrix}, \tag{3.18}$$

$$\begin{cases} \bar{t}_{min} < \bar{t} < \bar{t}_{max} \\ s_{min} < s < s_{max} \end{cases}$$

Where f is the cost function and $\bar{t}_{\,min}$, $\bar{t}_{\,max}$, s_{min} and s_{max} the extreme values of the variables, constituting a set of 6 inequality constraints. The selection of the cost function represents the key point during the optimisation process and its final result is highly dependent on the right selection of this function. In this research, it has been found important to optimize the transformation vector and scale based on the manipulability of both master and slave. A robot manipulability is a scalar value w defined by (3.18) [115]. Where $J(\bar{q})$ is the jacobian matrix depending on the joint vector $\bar{q}$. The manipulability index measures the easiness of changing arbitrarily the position and orientation of the end-effector at the tip of the manipulator, which is also related with the distance to the singular points.

$$w = \sqrt{\det J(\bar{q})\, J(\bar{q})^T} \tag{3.19}$$

If for some $\bar{q}$ vectors, it is found that $rank\big(J(\bar{q}\,)\big) < m$, where m is the dof number of the robot, then we say that the manipulator is in singular state [115]. The value of the manipulability index in a certain point of the manipulator's workspace increases with the distance to a singular point. For this reason it would be convenient on the point of view of the manipulation dexterity, to place the master's workspace wherever the manipulability of the slave is greater. Also, a good criteria to reject points in both workspaces, is to choose those ones with less manipulability.

Being $\mathcal{M}$ and $\mathcal{S}$ the workspaces of master and slave respectively, the common area is denoted by $\mathcal{M}\bigcap\mathcal{S}$. We say that the manipulability is lost in those areas which do not intersect. Let us define the two different zones where the manipulability is lost in both spaces as $\mathcal{M}_{loss}$ and $\mathcal{S}_{loss}$., being $\mathcal{M}_{loss} = \{\forall\ x,\ (x\ \in \mathcal{M}) \wedge\ (x\ \notin \mathcal{M}\bigcap\mathcal{S})\}$ and $\mathcal{S}_{loss} = \{\forall\ x,\ (x\ \in \mathcal{S}) \wedge\ (x\ \notin \mathcal{M}\bigcap\mathcal{S})\}$. It is thus possible to define a new index which measures the loss of manipulability of both devices as: $W_{\mathcal{M}_{loss}}$ and $W_{\mathcal{S}_{loss}}$ as in (3.20) and (3.21).

$$W_{\mathcal{M}_{loss}} = \frac{1}{\mathrm{Max}(\det J_M(\bar{q}_M) J_M(\bar{q}_M)^T} \iint_{\mathcal{M}_{loss}} \sqrt{\det J_M(\bar{q}_M)\, J_M(\bar{q}_M)^T}\ ds \tag{3.20}$$

$$W_{\mathcal{S}_{loss}} = \frac{1}{\mathrm{Max}(\det J_S(\bar{q}_S) J_S(\bar{q}_S)^T} \iint_{\mathcal{S}_{loss}} \sqrt{\det J_S(\bar{q}_S)\, J_S(\bar{q}_S)^T}\ ds \tag{3.21}$$

Where $J_M(\bar{q}_M)$ and $J_S(\bar{q}_S)$ are the jacobians of master and slave respectively. It is important to note that both indexes are normalized to avoid numerical inconsistencies since the jacobian is influenced by the links' length. Also the achieved manipulability in the common area could be defined accordingly. For sake of simplicity let us define first the normalization values as:

$$N_m = \frac{1}{\mathrm{Max}(\det J_M(\bar{q}_M) J_M(\bar{q}_M)^T} \tag{3.22}$$

$$N_s = \frac{1}{\mathrm{Max}(\det J_S(\bar{q}_S) J_S(\bar{q}_S)^T} \tag{3.23}$$

And then, the manipulability achieved on the common area will be:

$$W_{\mathcal{M}\cap\mathcal{S}} = N_m \cdot N_s \iint_{\mathcal{M}\cap\mathcal{S}} \sqrt{\det J_S(\bar{q}_S)\, J_S(\bar{q}_S)^T}\, \sqrt{\det J_M(\bar{q}_M)\, J_M(\bar{q}_M)^T}\; ds \quad (3.24)$$

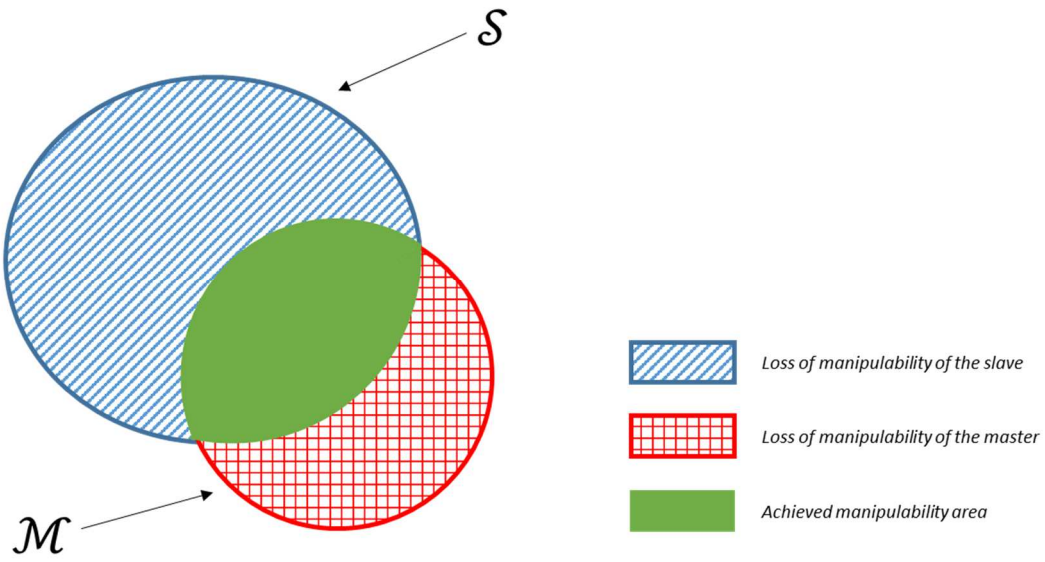

Figure 3-12. Schematic workspaces representation and manipulability zones.

This is a pure kinematic criteria that allows to define the cost function f that minimizes the loss of manipulability and maximizes the achieved manipulability.

$$f = \frac{W_{\mathcal{M}_{loss}} + W_{\mathcal{S}_{loss}}}{W_{\mathcal{M}\cap\mathcal{S}}} \quad (3.25)$$

In order to evaluate the f function, both workspaces were discretized up to the centimetre level and represented in two matrices of (500 x 500) where each element corresponds to 1 cm^2. The forward kinematics of each device was used to fill in those workspaces matrices when going through all the joints whose variation keeps the manipulators in a plane. This is, joints 2, 3 and 5 where covered for the master and slave in small intervals. The indexes of the matrices were given by the coordinates (ρ_m^r, z_m^r) of the end-effector projected on a radial plane, which are output of the forward kinematics. The value given to the element indicated by this duple is the normalized manipulability. With these operations, two workspaces were obtained composed by a cloud of sparse points (See Figure 3-13 and Figure 3-14).

To facilitate the optimisation process, both workspaces composed by sparse points were extended so the final workspaces do not present any point with no manipulability value. This action of eliminating the alternating zeros was performed to ease the later algorithm. Once this has been carried out, the Matlab® Optimisation Toolbox was

used to find the optimum values for the scale s and the transformation vector $\bar{t}$ which minimize the cost function f.

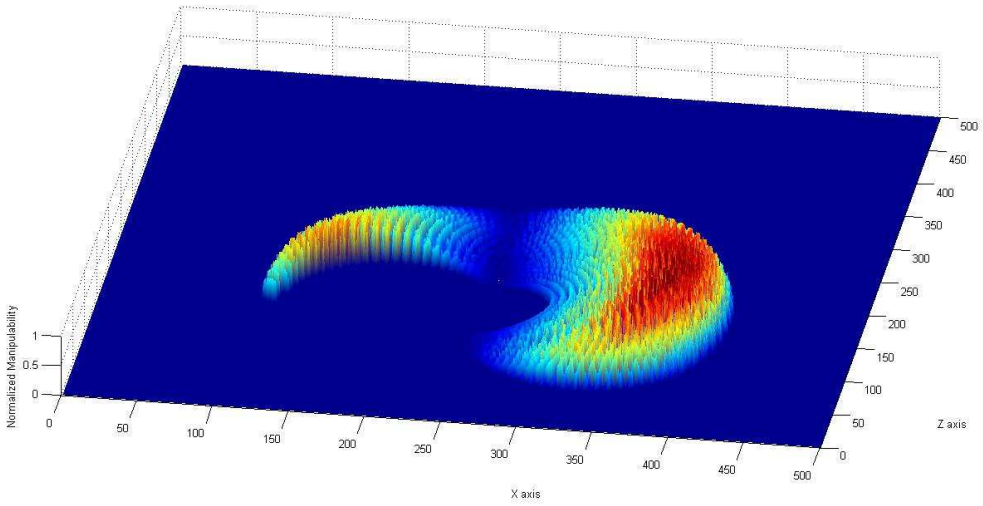

Figure 3-13. Normalized manipulability of the ABB IRB 2400-16.

The Sequential Quadratic Programming algorithm was used due to its power for resolving constrained nonlinear optimisation processes. The constraints were fixed to limit the variation of the variables so they belong to a sensible range, as given by (3.26).

The starting point for the algorithm was estimated manually with a scale of 8 and a translation vector of $(\rho_m^r, z_m^r) = (1.014, 0.769)$ [8] (See Figure 3-16). After 10 iterations and 131 function evaluations, the optimum point was reached for: $= 7.57$, $\rho_m^r = 0.657\ m$ and $z_m^r = 0.537\ m$. Figure 3-15 shows the final intersection of the two workspaces with the optimum parameters for the scale and transformation vector. In this figure, two different workspaces are displayed. The green line corresponds to the ABB IRB 2400-16 industrial robot and the blue line corresponds to the Phantom OMNI workspace, scaled and moved to a the starting point of the optimisation process. The original master's workspace is denoted by the orange line, and the result of scaling the master´s workspace by a factor of 8 is shown by the red continuous line. The purple diamond indicates the starting point of the bilateral control.

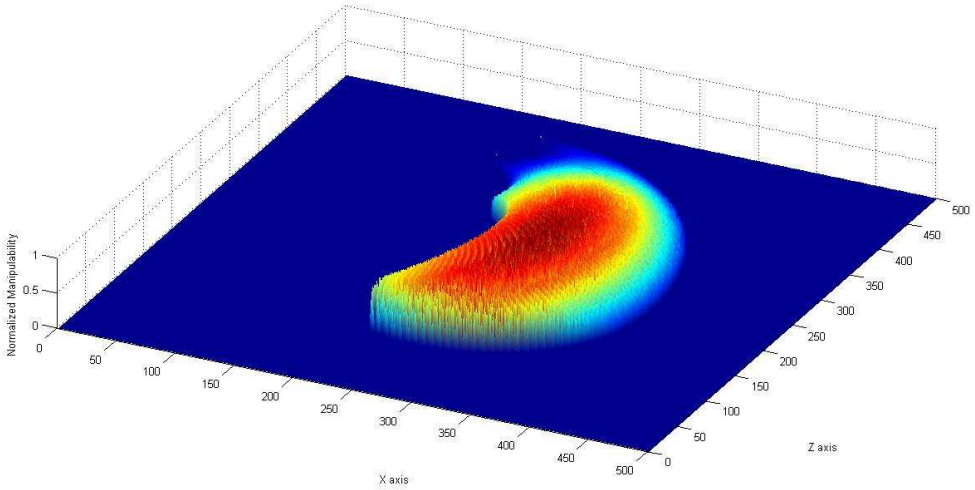

Figure 3-14. Normalized manipulability of the Phantom OMNI with a scale factor of x8.

$$\begin{cases} 1 < s < 12 \\ -3 < \rho_m^r, z_m^r < 3 \end{cases} \tag{3.26}$$

3.5.4 Starting the bilateral loop and assistive forces

This section describes the steps carried out for initiating the bilateral loop and the creation of assistive forces in the haptic master in order to guide the operator to return to the correct path once he has abandoned the slave's workspace.

In Figure 3-16 four workspaces are shown. These are: slave's workspace in green, the master workspace in orange and additional modifications to this in order to optimize the overlapping. These were detailed before. The starting point for the optimisation algorithm carried out in previous section is indicated by the blue workspace of Figure 3-16, which means a scale factor of x8 and a translation vector of (-1.014, -0.769). The starting position of the bilateral teleoperation has been established on the purple point of Figure 3-16, which corresponds to a high manipulability area of both slave robot and haptic master. Also, it has been considered as a comfortable position for the operator to reach, even when reducing the allowed positional and pose errors.

When the bilateral loop is initiated, the haptic master occupies its hold position which corresponds with the tip inserted into master's base, as shown in Figure 3-7. This position, indicated by the yellow point in Figure 3-16, does not belong to the slave's workspace. During the initial period, the operator should manoeuvre the master up to the slave's starting position in order for the bilateral control to start. During this

coordination trajectory, no assistive forces are exerted and the operator is able to move the master freely until the tracking mode is activated.

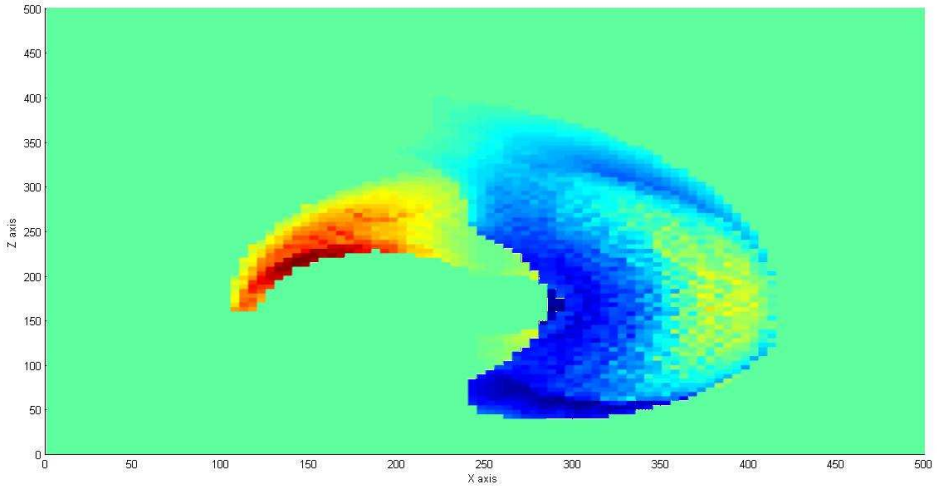

Figure 3-15. Intersection of master and slave workspaces corresponding to the optimum found by SQP algorithm.

When the bilateral control is started and before the operator reaches tracking position, the slave is programmed to go to the starting position and hold until the tracking is activated. Once the master has reached this point, the tracking starts and master and slave are linked. In the specific case of this bilateral control, the selected starting position for the slave was determined by (3.15).

$$T_{Start} = \begin{pmatrix} 0.9995 & 0 & 0.0292 & 0.2431 \\ 0 & -1 & 0 & 0 \\ 0.0292 & 0 & -0.9995 & 0.1841 \\ 0 & 0 & 0 & 1 \end{pmatrix} \tag{3.27}$$

The maximum angular error allowed to the haptic master in order to start the tracking phase corresponds with the expression (3.7) and the selected value was: $\varepsilon_i = 0.2\ rad$. However, the maximum error in Cartesian position, was fixed dependant on the scale, following the formula in (3.28).

$$\bar{\rho} = \frac{0.2}{Scale}(\bar{i}, \bar{j}, \bar{k})\ [m] \tag{3.28}$$

These manually tuned values gave a compromise between positioning accuracy and speed of positioning for the human operator. A test case designed to evaluate the effects of the assistive forces algorithm is shown in Figure 3-17 to Figure 3-20. In them, the bilateral control is initiated with the master device on its parking position as mentioned before. The operator guides the master through a trajectory indicated by the

dashed line until it reaches the starting position indicated by a red cross in Figure 3-17.

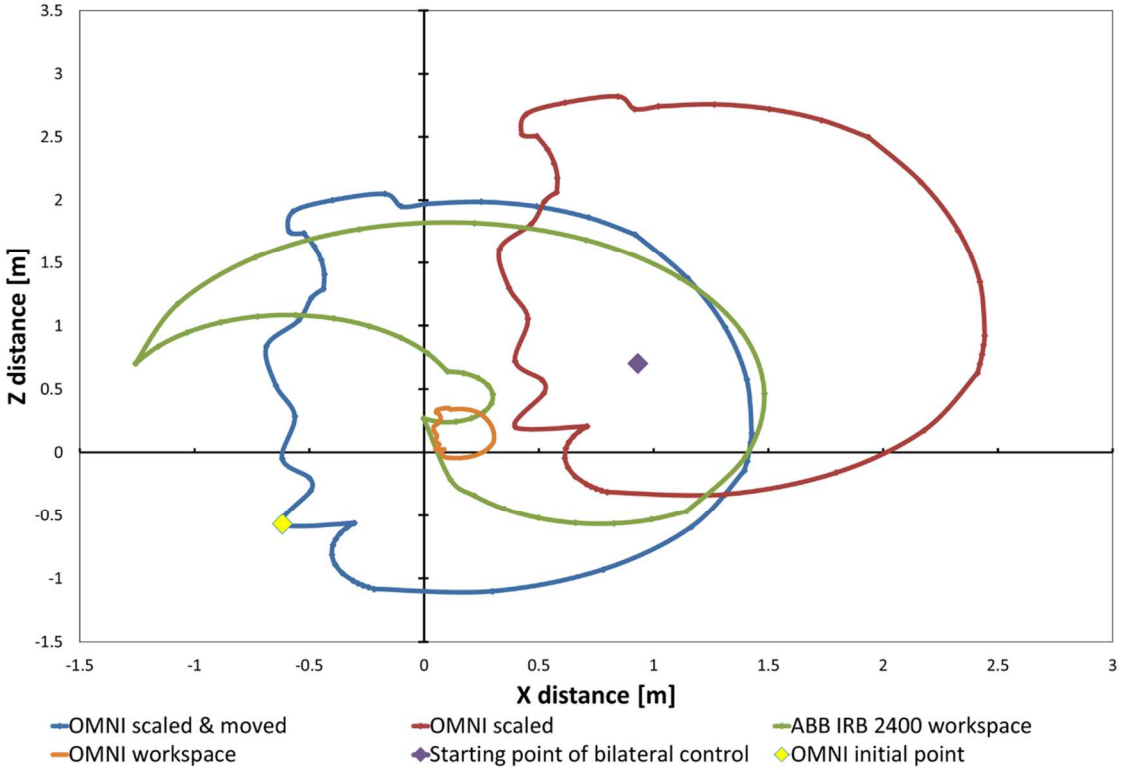

Figure 3-16. Projected workspaces of ABB IRB 2400-16 and Phantom OMNI. Slave workspace generated by the first two dof, while master workspace generated by the last 5 dof. The final master's position corresponds to a scale of x8 and translation in coordinates of -1.014 m on the radial coordinate and -0.769 m on the vertical coordinate.

This process might require some time depending on the calibration of the positional and angular thresholds. Also, during this period and until master and slave are not linked, no assistive forces are exerted. This is shown in Figure 3-19 and Figure 3-20. After initiating the tracking, the slave device follows master's movements until its workspace limits. When the master reaches a non-possible position for the slave, this stops and waits for the master to return. The operator can actually go beyond slave's limits but the assistive forces and torques shown in these figures force him to return. The effectiveness of the assistive force will depend on the calibration of the elastic constant.

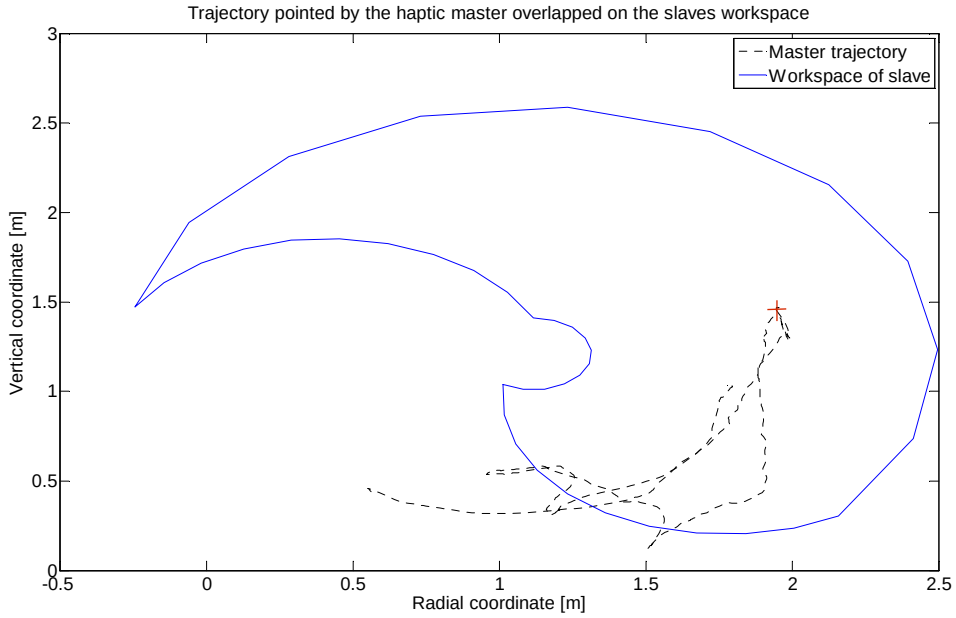

Figure 3-17. Trajectory of the haptic master tip during a movement. The first part of the trajectory starts outside the slave's workspace. The bilateral teleoperation starts when the master reaches the starting point indicated with a red cross. During the execution of the trajectory, the master leaves the slave's workspace and assistive forces are created conveniently.

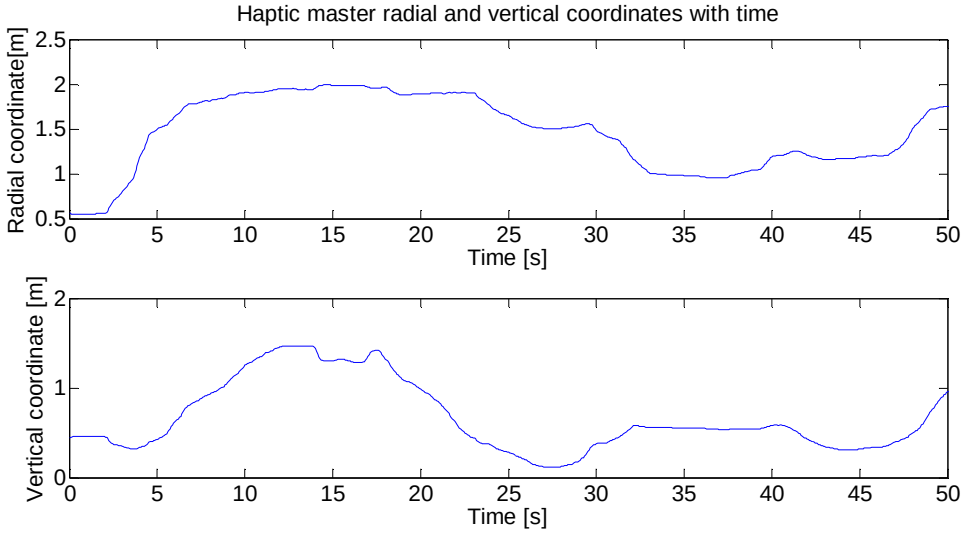

Figure 3-18. Radial and vertical coordinates during the execution of the trajectory.

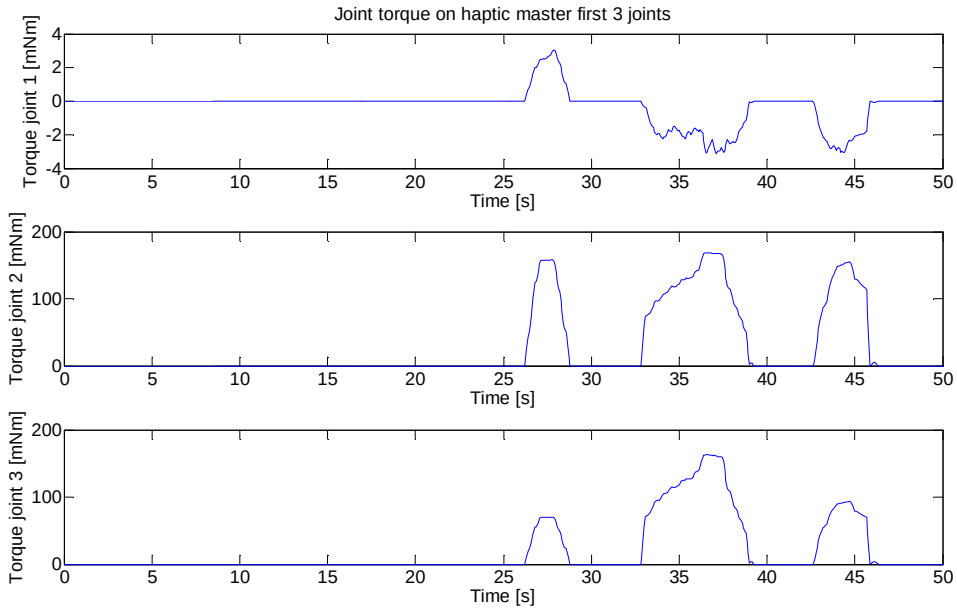

Figure 3-19. Assistive torques on the first three degrees of freedom. These efforts are created to guide the operator to return to the slave´s workspace.

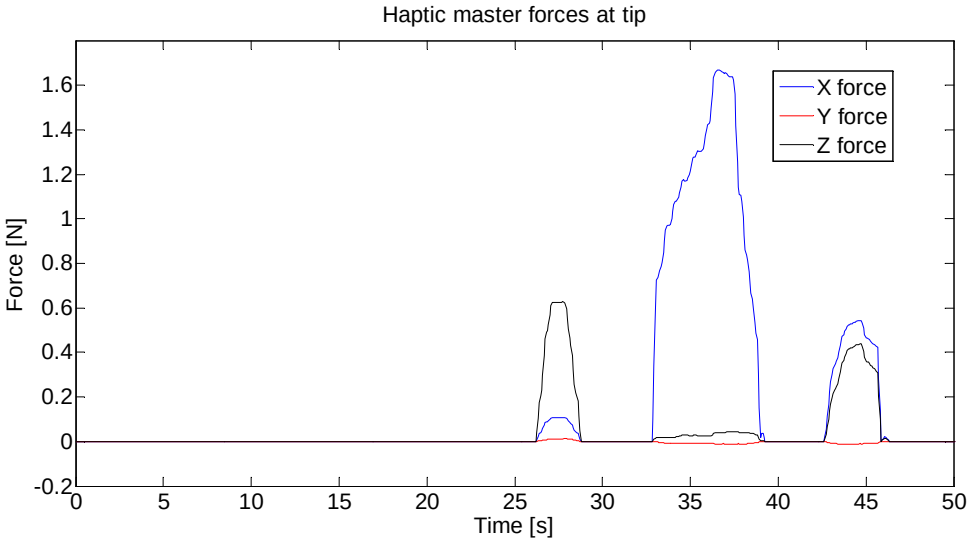

Figure 3-20. Cartesian forces on the master tip during trajectory of Figure 3-17.

3.6 Conclusions and discussion

In this chapter, the bilateral control with a kinematically dissimilar master and slave has been presented. Most of the issues arisen during teleoperation of devices with different kinematics have been reviewed here. It has been highlighted the advantages and

disadvantages of employing the explained methodology. The teleoperation algorithms have been proved to be successful to teleoperate and industrial robot with a haptic master under the point of view of the kinematics. Nothing has been detailed here in relation to the always necessary force feedback, this will be deeply developed in the following chapters.

This chapter was started by proposing a framework to develop a general master-slave teleoperation where the most important interactions between elements in the system such as slave, haptic master and environment have been highlighted. This new approach includes the concept of force estimation in addition of force measurement.

A method for determining if a point is inside a polygon called axis-crossing method have been adapted for the calculation of assistive forces in the first stages of bilateral control. During this period of time, the coordination between master and slaves has not been established yet and this new approach is helpful in determining the distance between the point referred by the master and slave's workspace with minimum computational effort.

It has been shown a methodology for solving the kinematic disparities between master and slave in order to perform teleoperation when the workspaces are different. Also, an optimised implementation of guiding and assistive forces has been demonstrated to help the operator during the teleoperation task.

These techniques have been successfully applied on teleoperating an ABB industrial robot where the pros and cons have been widely explained with special emphasis on the timing analysis. Although a control system such the one used has been enough for a kinematic study and an open loop teleoperation, more open control architectures should be used when using industrial robots for bilateral teleoperation with force feedback.

An innovative metric and technique based on optimum manipulability has been developed during this chapter, in order to establish optimised values for the scaling and translation between different workspaces. The manipulability of both devices is originally combined with the workspace to find a good value for the kinematic transformation where the manipulability is optimised. This is always needed when teleoperating master and slave with dissimilar kinematics.

Experiments proving the good performance of the assistive forces in guiding the operator to the correct area inside manipulator's workspace have been also presented at the end of the chapter filling the gap on the kinematic study related to dissimilar teleoperation.

Chapter 4 Robot modelling and identification for teleoperation on radioactive environments

This chapter introduces the need of employing a dynamic model of the slave in order to estimate the environmental forces and torques applied on it. These will be fedback to the operator during the teleoperation process. Traditionally this task would have been done by force/torque sensors attached on the tip of the end-effector, but given the high radiation requirements of the environment, a new approach has to be developed. This brings additional difficulties such as robot modelling and parameter identification which have to be performed accordingly to the teleoperation requirements.

Experiments have been designed for a hydraulic manipulator presenting a closed loop structure which was included in the model. New ways for identifying these robotics structures are given. Different techniques for parameter identification are evaluated and new design criteria is proposed that proves to increase the model performance.

4.1 Introduction

It has been explained in chapter 2 that when performing a teleoperated control of industrial robots, a force-position control scheme is typically employed due to the non-backdrivability of these manipulators [28], [60], [61], [62]. Due to the mechanical design of these devices, it is not possible to use the positional error as a force estimator. If teleoperating these devices using conventional position-position control, excessive forces could be applied corresponding to a small or null positional errors. But not only a force-position control scheme would be used when the slave is not backdrivable, also when the undesirable effects of position-position, such as drag effect, should be avoided.

In Figure 4-1 the schematic of force-position algorithm is shown, pointing out the position that a force/torque sensor would occupy on this algorithm to measure the external forces and conveying them to the operator.

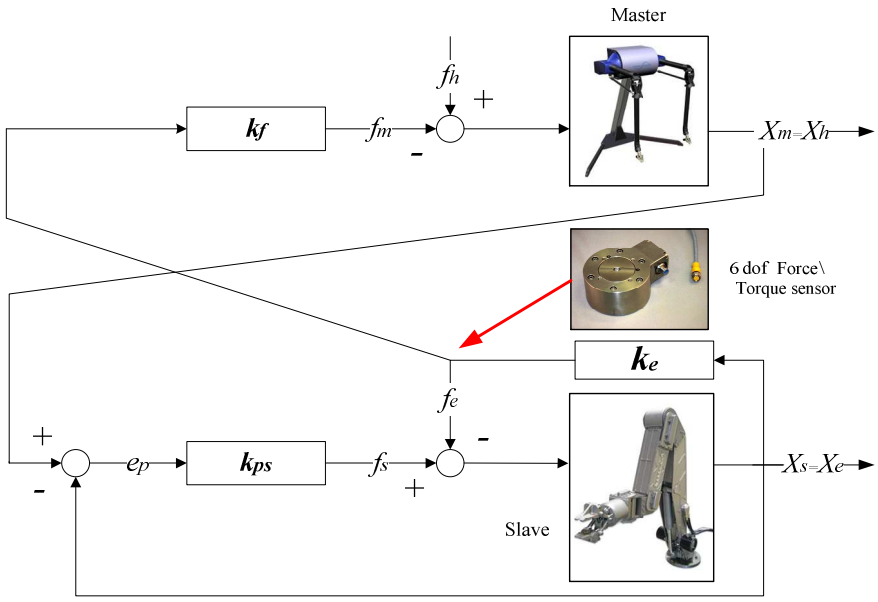

Figure 4-1. Force-Position bilateral control with force measurements performed with a 6 dof force/torque sensor.

There are some situations in which the force/torque sensor cannot be used or it is unpractical, such as when performing remote handling tasks in highly radioactive environments or when the hardware cost has to be minimized. Especially in facilities where the dose rate can overcome the tenth of kGy [26], no commercial electronic-based solutions to measure forces have been found so far. The approach presented in this research is displayed in Figure 4-2 where the force/torque sensor is substituted by a dynamic model of the robot or a force observer. The central idea is to convey to the

operator the estimation of environmental forces as if they were measured by the sensor. Several approaches can be used to perform this estimation, but most of them make use of the knowledge of the slave's dynamic model, the commanded torque and the state space variables of the manipulator. As described in chapter 2, some approaches try to reduce the complexity of the model and implement a learning algorithm to avoid the analytic calculation [82], some others are based on Kalman [93], [101], [98], [94], [95] or Luenberguer [80], [81], observers, but almost all of them need at least a basic model of the slave manipulator.

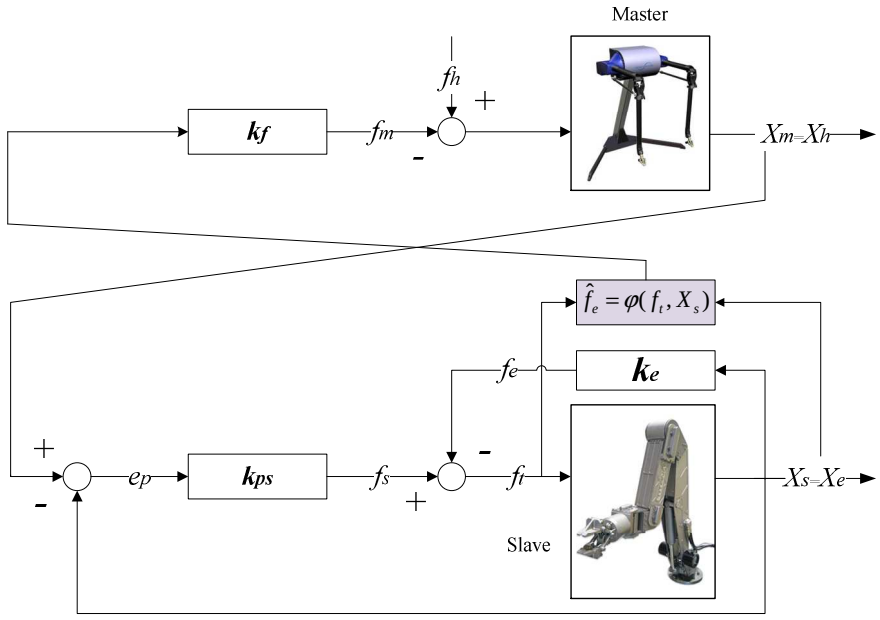

Figure 4-2. Force-Position with force estimations performed with a dynamic model.

In this chapter, the methodology used for modelling a robot for teleoperation is extensively analysed and applied on the dynamic model identification of a hydraulic manipulator Kraft GRIPS. Different techniques for parameter identification are evaluated and the best one is selected.

4.2 Defining the dynamic model

The conventional robotics equation describing the inner forces (4.1) of a kinematic chain of rigid forces in the absence of external forces can be obtained by employing any established algorithm, e.g. Newton-Euler iterative method or the Lagrangian method.

$$\tau_m = H(q) \cdot \ddot{q} + C(q, \dot{q})\dot{q} + \tau_g(q) + \tau_f(\dot{q}) \tag{4.1}$$

where,

τ_m: vector of motor torques exerted in each joint.

$H(q)$ is the robot inertia matrix, which is a function of the joints' values.

$C(q, \dot{q})$: is the Coriolis and centripetal forces vector, which also depends on the joints' values and velocities.

τ_g: is the gravity forces vector depending on the robot position.

τ_f: is the friction torques vector. In general terms, it also dependent on the joints velocities.

Although the friction is a complex nonlinear phenomenon, in many robotics applications it is modelled by considering only the Coulomb term and viscous friction yielding to (4.2).

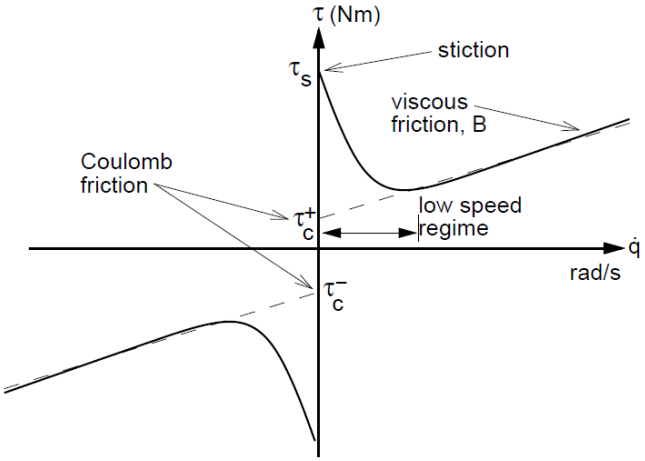

Figure 4-3. Typical shape of friction torque versus joint speed.

$$\tau_f = f_c sign(\dot{q}) + f_v \dot{q} \tag{4.2}$$

This expression of the friction maintains the linear model and ensures the possibility of applying linear estimators for the model identification. In (4.1), the motor torque is also linear with the inertial parameters. On a hydraulic actuator based on servo-valves the motor torque τ_m can be estimated by using the expression in (4.3) [66], where K_p is a constant and ΔP is the differential pressure between the two chambers of the hydraulic actuator.

$$\tau_m = K_p \cdot \Delta P \tag{4.3}$$

Similar expression is often employed to estimate the motor torque in an electrical actuator, such as the three-phase brushless motors, typically mounted in robotics. Instead of using the differential pressure, the measured quadrature current is employed to estimate the feedback torque by using the motor torque constant in $[Nm/A]$. The quadrature current is proportional to the amplitude of the three-phase current, thus either the amplitude or the RMS value can be easily obtained from it.

$$\tau_m = K_e \cdot I_q \tag{4.4}$$

When no access to the quadrature current is possible, the Park transformation [113] can be used to transform a three-phase system (i_a, i_b, i_c) into a direct and quadrature system (i_d, i_q, i_o) (4.5).

$$i_{dqo} = K \cdot i_{abc} = \sqrt{\frac{2}{3}} \begin{pmatrix} cos(\theta) & cos(\theta - 2\pi/3) & cos(\theta + 2\pi/3) \\ -sin(\theta) & -sin(\theta - 2\pi/3) & -sin(\theta + 2\pi/3) \\ \frac{\sqrt{2}}{2} & \frac{\sqrt{2}}{2} & \frac{\sqrt{2}}{2} \end{pmatrix} \cdot \begin{pmatrix} i_a \\ i_b \\ i_c \end{pmatrix} \tag{4.5}$$

4.2.1 Modelling a robot with closed loops

It is common of several manipulators, especially those ones with bigger payloads, to include a closed loop in the serial chain to allow the placement of one actuator closer to the base and making possible to distribute the mass symmetrically. Therefore, the problem of yielding to a model described by (4.1) needs to take into account the closed loop and apply a loop closure function to the tree dynamics obtained by e.g. the Newton-Euler algorithm. This procedure is generously described in [114] by Roy Featherstone by creating a connectivity graph for a rigid body system. A robot described as a connectivity graph is simplified by representing the bodies and joints as a nodes and arcs respectively. A graph is a topological tree if there exists exactly one path between any two loops in the graph. If the connectivity graph of a rigid body system is a topological tree, then we call the system itself a kinematic tree [114].

Whether G is any connectivity graph, a spanning tree of G, denoted G_t, is a subgraph of G, containing all of the nodes in G, toghether with any subset of the arcs in G such as G_t is a topological tree.

If q is the vector of joint values for the spanning tree for a given closed loop system, and let y be a vector of independent joint variables for the same system. It is possible to define the relationship (4.6).

$$q = \gamma(y) \tag{4.6}$$

Differentiating this equation as in [114] yields to (4.7):

$$\dot{q} = G\dot{y} \tag{4.7}$$

Where,

$$G = \frac{\partial \gamma}{\partial y} \tag{4.8}$$

G is the loop closure function. Defining G_u and G_0 as containing the rows of the actuated and the unactuated degrees of freedom, respectively. These matrices are related to G by an $n\ x\ n$ permutation matrix designed by Q in the equation (11).

$$G = Q \begin{bmatrix} G_u \\ G_0 \end{bmatrix} \tag{4.9}$$

It is shown in [114] than the torque of the y joints can be calculated by having the tree torques, τ_{ID} , and applying (4.10) if the system is properly actuated. This is, if G_u is invertible, and therefore, there is a unique solution.

$$\tau = {G_u}^{-T} G^T \ \tau_{ID} \tag{4.10}$$

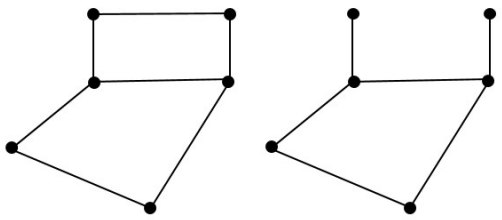

Figure 4-4. Original graph of a closed loop system and a possible spanning tree.

4.3 Parameter identification

When modelling a real robot one must consider the kinematics and dynamics of it. While the kinematic model only requires knowledge of the relative movement of each link and the links dimensions, a dynamic model needs more advance knowledge of the robot parameters. This model relates robot motion to joint torques, and describes the rigid-body dynamics of the robot including Coulomb and viscous friction in the joints. The additional parameters required for the proper construction of this model apart from the friction are: links' masses, first mass moments, moments of inertia, position of the centre of gravity, and other considered nonlinear effects.

Although inertia estimations can be derived from CAD drawings, robot manufactures do not provide these drawings for all parts of the robot, for example, parts manufactured by external suppliers. Also, it is common to find inaccurate models that for

example do not include the void in hollow links, leading to incorrect density calculations and thus incorrect inertias and centres of gravity. Dismantling the robot and carrying out links measurement is not always the most convenient option. Moreover, estimates of friction components are not provided by the manufacturer and they cannot be foreseen from the first principles.

Experimental identification of the robot parameters using motor torques and motion data is thus needed to cope with the lack of knowledge of some of the robot variables and the drifting of some of them during the time.

Traditionally this problem has been solved [115], [116], [117], [118] following the approach presented in Figure 4-5. The model equations are created based on the Newton-Euler algorithm, revealing a linear dependence on the inertial parameters. With this model, appropriate conditions are created for applying least mean squares for parameters estimation.

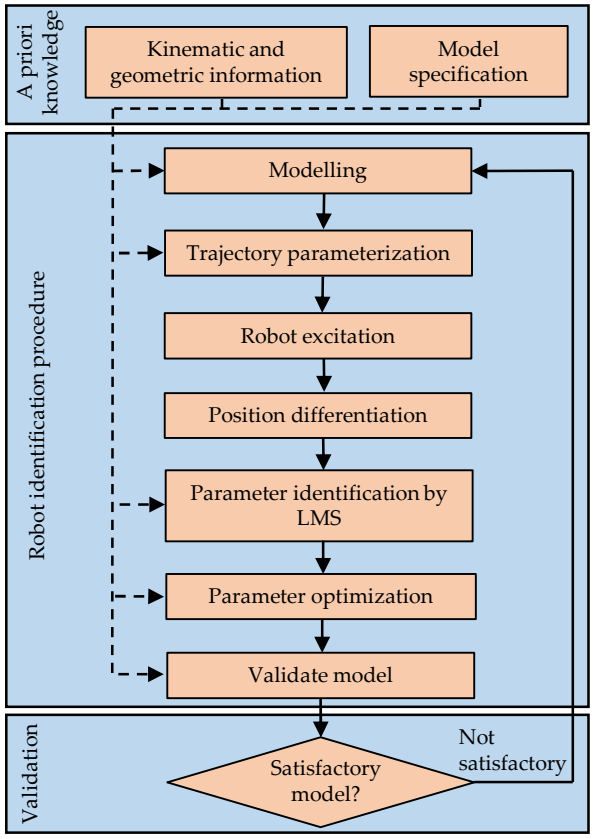

Figure 4-5. Robot identification and validation flowchart.

This procedure begins from an a priori knowledge of the robot in form of the kinematic configuration, links' dimensions, specification and minimum requirements for the dynamic model. Although there are also techniques to calibrate the robot's kinematic

parameters [119], this is not considered as critical as identifying the dynamic condition since the kinematic configuration can be extracted easier from CAD models.

During the modelling stage, the key point is to transform the equation (4.1) into a linear expression with the robot parameters. This is obtained applying the so called Modified Newton-Euler algorithm.

From the classical Newton-Euler equations in spatial vectors given by (4.11) [119], it can be expressed the spatial force acting on the last link n of a robot and referred to its origin as:

$$f_n = I_n \cdot a_n + v_n \times I_n \cdot v_n \tag{4.11}$$

Substituting for the spatial inertia I_n, the spatial acceleration a_n, and the spatial velocity v_n, of a link n operating and simplifying, yields to the matrices product expression (4.12) for the spatial force.

$$f_n = \begin{pmatrix} 0 & -S(\ddot{d}_{on}) & L(\ddot{\omega}_n) + S(\omega_n)L(\omega_n) \\ \ddot{d}_{on} & S(\dot{\omega}_n) + S(\omega_n)S(\omega_n) & 0 \end{pmatrix} \times \begin{pmatrix} m_n \\ m_n c_n \\ l(\bar{I}_n) \end{pmatrix} \tag{4.12}$$

Where S indicates the skew-symmetric operator, L is an operator which transforms a vector in a 3×6 matrix as in (4.13) and l is and operator which transforms a matrix in a vector with its elements following an increasing order.

$$L(a) = \begin{pmatrix} a_1 & a_2 & a_3 & 0 & 0 & 0 \\ 0 & a_1 & 0 & a_2 & a_3 & 0 \\ 0 & 0 & a_1 & 0 & a_2 & a_3 \end{pmatrix} \tag{4.13}$$

$$l(\bar{I}_n) = \begin{pmatrix} I_{11} \\ I_{12} \\ I_{13} \\ I_{22} \\ I_{23} \\ I_{33} \end{pmatrix} \tag{4.14}$$

Or, in a more compact form, the spatial force acting on that robotic link:

$$f_n = A_n \cdot \phi_n \tag{4.11}$$

And with this expression it would be possible to estimate the inertial parameters of the last link and the load attached to the end –effector. However here the interest lays on identifying the inertial and mass parameters of the whole robotic structure and the effect of all links should be taken into account. Defining f_{ij} as the spatial force at joint i due to movement of j alone. Then f_{ii} is the spatial force at i due to its own movement. The equivalent expression for the (4.11) would thus be (4.12) where n it

has been substituted by i. And the superscript i has been added to indicate that the vectors are expressed in terms of joint i.

$$ {}^{i}f_{ii} \;\; = {}^{i}A_{i} \;\cdot \phi_{\;i} \tag{4.12} $$

In this way, the total spatial force at joint, ${}^{i}f_{i}$, it is the sum of the spatial forces ${}^{i}f_{ij}$ for all links j distal to i, following the results of [119].

$$ {}^{i}f_{i} \;\; = \sum_{j=1}^{n} {}^{i}f_{ij} \tag{4.13} $$

The spatial force ${}^{i}f_{ij}$ at joint i its determined by the spatial force transformation matrix ${}^{i}X_{j}^{F}$,

$$ {}^{i}f_{i,i+1} = \;\; {}^{i}X_{i+1}^{F} \;\; {}^{i+1}f_{i+1,i+1} \tag{4.14} $$

So the forces and torque on link i due to the movements of the link j can be obtained by cascading a series of transformation matrices:

$$ {}^{i}f_{i,j} = \;\; {}^{i}X_{i+1}^{F} \;\; {}^{i+1}X_{i+2}^{F} \ldots {}^{j-1}X_{j}^{F} \;\; {}^{i}f_{j,j} = {}^{i}X_{j}^{Fj} \;\; A_{j} \cdot \phi_{\;j} \tag{4.15} $$

With this approach, the spatial forces of a serial chain robot can be easily expressed in a matrix:

$$ \begin{pmatrix} {}^{1}f_{1} \\ {}^{2}f_{2} \\ \vdots \\ {}^{n}f_{n} \end{pmatrix} = \begin{pmatrix} {}^{1}X_{1}^{F1}A_{1} & {}^{1}X_{2}^{F2}A_{2} & \ldots & {}^{1}X_{n}^{Fn}A_{n} \\ 0 & {}^{2}X_{2}^{F2}A_{2} & \ldots & {}^{2}X_{n}^{Fn}A_{n} \\ \vdots & \vdots & \ddots & \vdots \\ 0 & 0 & \ldots & {}^{n}X_{n}^{Fn}A_{n} \end{pmatrix} \begin{pmatrix} \phi_{1} \\ \phi_{2} \\ \vdots \\ \phi_{n} \end{pmatrix} \tag{4.16} $$

Or in compact form: $f \;\; = A \;\; \cdot \phi \;\;$. Since only the torque τ_i can be usually measured around the axis z_i, the spatial force can be projected around that rotation axis and simplifying (4.16) to:

$$ \tau = K\phi \tag{4.17} $$

Where, $\tau_i = \begin{pmatrix} z_i \\ 0 \end{pmatrix} \cdot f_i$, $K_{ij} = \begin{pmatrix} z_i \\ 0 \end{pmatrix} {}^{i}X_{j}^{Fj} \;\; A_j$, $\phi = \begin{pmatrix} \phi_{\;1} \\ \cdot \\ \cdot \\ \phi_{\;n} \end{pmatrix}$

However, for the very common manipulator with a closed loop such the one presented in Figure 4-6, equation (4.16) has to be adapted with the inclusion of the closed loop. In order to perform this adaptation, firstly (4.16) is modified so to include the spanning tree joints as the graph of Figure 4-7. That leads to an expression similar to (4.18) for the matrix A when a non-serial manipulator is modelled.

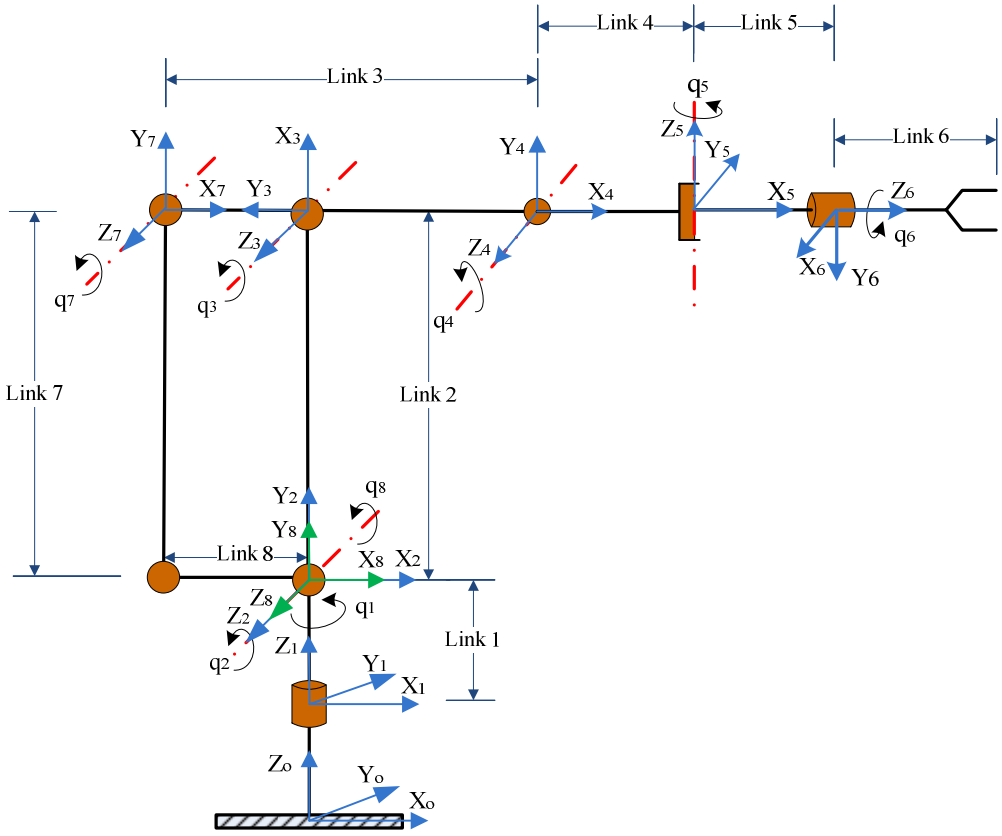

Figure 4-6. Schematic of a manipulator with a closed loop.

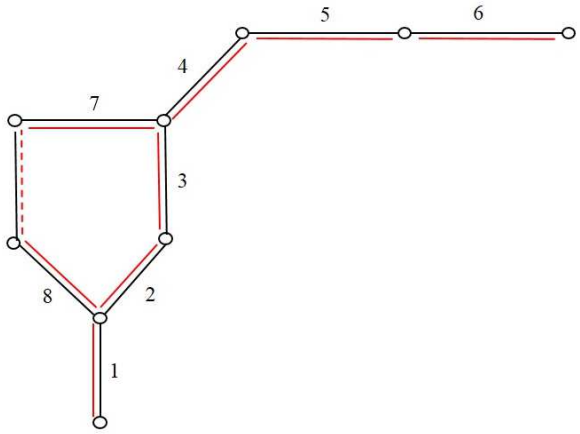

Figure 4-7. Graph of a manipulator with closed loop. Dashed line indicates the chord or extra joint no included in the spanning tree represented with red continuous line.

$$A = \begin{pmatrix} {}^{1}X_{1}^{F1}A_{1} & {}^{1}X_{2}^{F2}A_{2} & {}^{1}X_{3}^{F3}A_{3} & {}^{1}X_{2}^{F4}A_{4} & {}^{1}X_{2}^{F5}A_{5} & {}^{1}X_{2}^{F6}A_{6} & {}^{1}X_{7}^{7}A_{7} & {}^{1}X_{8}^{8}A_{8} \\ 0 & {}^{2}X_{2}^{F2}A_{2} & ... & ... & ... & ... & {}^{2}X_{7}^{7}A_{7} & 0 \\ 0 & 0 & {}^{3}X_{3}^{F3}A_{3} & ... & ... & ... & {}^{3}X_{7}^{7}A_{7} & 0 \\ 0 & 0 & 0 & {}^{4}X_{4}^{F4}A_{4} & ... & ... & 0 & 0 \\ 0 & 0 & 0 & 0 & {}^{5}X_{5}^{F5}A_{5} & ... & 0 & 0 \\ 0 & 0 & 0 & 0 & 0 & {}^{6}X_{6}^{F6}A_{6} & 0 & 0 \\ 0 & 0 & 0 & 0 & 0 & {}^{7}X_{6}^{F6}A_{6} & {}^{7}X_{7}^{7}A_{7} & 0 \\ 0 & 0 & 0 & 0 & 0 & 0 & 0 & {}^{8}X_{8}^{8}A_{8} \end{pmatrix} \quad (4.18)$$

In order to take the closed loop into account, for a given spanning tree of the robot with an observation matrix A , it is straight forward to apply (4.19) to obtain the closed loop observation matrix A_{CL} of (4.20).

$$\tau = {G_u}^{-T} \cdot G^T \cdot A \cdot \emptyset \quad (4.19)$$

$$\tau = A_{CL} \cdot \emptyset \quad (4.20)$$

By projecting the spatial forces as in (4.17) and expressing the matrix in a more compact way it is yielded to:

$$\tau = K_{CL}\, \emptyset \quad (4.20)$$

Where τ is the vector of measured input torque for a given point with particular conditions of pose, velocity and acceleration, K_{CL} is the regressor matrix, - also called observation matrix-, with any closed loop of the robot taken into account and ϕ is the vector of dynamic parameters. The inertial parameters are the link mass, centre of mass moment, and inertias with respect to each link i frame: $m_i, cx_i, cy_i, cz_i,\ Ixx_i, Iyy_i, Izz_i,\ Ixy_i,\ Ixz_i, Iyz_i$. These can also be augmented with frictional parameters such as f_{ci} and f_{vi} following the friction model given in (4.2).

The regressor matrix of (4.20) includes the data gathered for only one sample point in certain kinematic conditions. The matrix K_{CL} and vector τ are augmented with P data points of a programmed trajectory to achieve a complete excitation of the robot. From now on, in this chapter τ and K will indicate the augmented vector and matrix of a complete trajectory.

$$\tau = \begin{pmatrix} \tau_1 \\ \vdots \\ \tau_P \end{pmatrix}, \quad K_{CL} = \begin{pmatrix} K_{CL_1} \\ \vdots \\ K_{CL_P} \end{pmatrix},$$

where now, τ is a vector of $n \cdot P \times 1$, with n the degrees of freedom of the robot and K_{CL} is a $n \cdot P \times a \cdot n$, with a the number of parameters being identified, commonly 10 or 12.

Once a convenient set of data points have been sampled, one could employ the least mean squares solution to get the parameters which best approximate the collected data.

$$\phi = ({K_{CL}}^T K_{CL})^{-1} {K_{CL}}^T \tau \tag{4.21}$$

However, the matrix ${K_{CL}}^T K_{CL}$ is typically non-invertible due to the loss of rank derived from the fact that not a complete force and torque sensing is presented on the 6 degrees of freedom of each joint and just a torque estimation can be done in each joint's axis. In order to cope with that issue, an a-priori parameter estimation ϕ_0 can be introduced here to build the damping least squares solution.

$$\phi = ({K_{CL}}^T K_{CL} + \lambda^2 I)^{-1} {K_{CL}}^T \tilde{\tau} \tag{4.22}$$

Where λ is the damping factor and $\tilde{\tau} = \tau - K_{CL}\phi_0$. The damping factor modifies the singular value decomposition of the least mean squares solution and then balances the final adjustment between a well fitted least mean squares solution and the a-priori knowledge. Depending on the reliability of the a-priori information, λ can be increased accordingly avoiding the loss of rank of the regressor matrix.

Figure 4-8. Solution variability with damped least mean squares.

This a-priori information can be obtained from the CAD model of the robot, a previously fitted model or an initial guess.

4.3.1 Obtaining the excitation trajectories, data processing and position differentiation.

In order to solve the least mean squares problem, a set of sample points must be collected in an appropriate way. The performance of the estimation will be seriously affected by the way these points are calculated. The process of working out the most convenient trajectories for robot's parameters identification is called trajectory parameterisation.

Several techniques have been applied to trajectory parameterization for robot dynamic model identification, e.g. finite sequences of joints accelerations [120], fifth order polynomials and periodic trajectory [116]. The polynomial technique is adequate for industrial manipulators which only accept velocity commands while periodic trajectory is more adequate for open control systems.

In this research a trajectory that can be parameterised by finite Fourier series is employed since processing a periodic and band-limited measure is more accurate and has more advantages in terms of signal processing [116]. Thus, each robotic joint is parameterised as follows in (4.23):

$$q_i(t) = q_{i0} + \sum_{k=1}^{N}(a_{i,k}\sin(k\omega_f t) + b_{i,k}\cos(kw_f t) \tag{4.23}$$

Where t is the time and ω_f is the fundamental frequency of the excitation trajectories and should be chosen carefully not to excite the un-modelled dynamics of the manipulator. The coefficients $a_{i,k}$ and $b_{i,k}$ are the amplitudes of the sine and cosine functions, and q_{i0} the joint offset. By selecting appropriate values of the amplitudes and fundamental frequency, the joint workspace varies together with the joint speed. In the next section different frequencies are utilized covering the maximum joint positional and acceleration range without compromising the robot structural flexibilities.

The problem of finding the coefficients $a_{i,k}$, $b_{i,k}$ and q_{i0} is called trajectory optimisation and several approaches have been used in the literature. A popular optimisation criterion is known as a d-optimality and it is based on the logarithm of the determinant of the covariance matrix of the model parameter estimation [115]. Other methods are centred on minimizing cost functions dependent on the condition number and the singular values of the observation matrix.

Two different methods have been tested in this research for obtaining the coefficients $a_{i,k}$, $b_{i,k}$. Firstly, a method based on trial and error and secondly two different optimisation processes with very different number of parameters. The results of these methods are then compared and evaluated, analysing the main differences encountered.

During the trial and error approach, trajectories based in equation (4.23) have been designed with $N = 1$ and the robotic joints have been moved independently. After data acquisition process and signal conditioning, this has been followed by an elimination process of those points which fulfil that the condition number of the observation matrix is above a certain threshold, established on 100 from experience of the statistical community [119]:

$$cond(A_i) > 100 \tag{4.24}$$

The second method implies designing trajectories based again in (4.23) although the coefficients have been obtained through an optimisation process based on sequential quadratic programming. $N = 1$ has also been used to be able to compare the results with the first method. Finally, the last method uses $N = 5$ where more complex trajectories excite the robot dynamics.

The calculated trajectories are then programmed in the robot controller. The robot repeats the trajectory during a certain number of periods while the measured joints values are acquired by the DAQ system.

Calculation of the observation matrix requires estimation of joints velocities and accelerations. Since most manipulators do not have accelerometers, a numerical differentiation must be carried out. The approach employed here is based on a well-established procedure for offline signal processing where the exact differentiation is done by transforming the position signal to the frequency domain using the discrete Fourier transform (DFT). Thereafter, the spectrum is multiplied by a rectangular window which selects the appropriate frequencies and sets to zero all other frequencies. Then the derivate in the frequency domain is realized multiplying the spectrum by $2\pi k f_s/P$, where P is the number of time domain samples, f_s is the sampling frequency and k the index of the selected frequencies in the discrete spectrum. The result is then transformed back to the time domain using the inverse Fourier transform. The results after applying this method eliminate all the noise but that contained in the selected frequencies.

The actuator torque data are obtained applying either equation (4.3) or (4.4) with data from the robot manufacturer or a previous torque constant identification phase.

4.4 Optimisation of identified parameters

The fact that the solution of the identified inertial parameters provided by the LMS does not necessarily present physical sense makes their use with certain control schemes very difficult. Also, this issue makes their application for integrating the robot equations of motion, impossible. This prevents its use for dynamic simulation, which invalidates a powerful tool in robotic system design [117], [116]. This issue suggested to include additional requirements on the model which are transformed into an optimisation stage after the parameter identification. This promising approach makes use of constrained optimisation tools to adjust the LMS result up to get a set of parameters with physical sense. The physical meaning of the identified parameters can be guaranteed imposing appropriate constraints during the estimation.

During this research, it has been found that the nonlinear optimisation problem of finding the optimum set of parameters gives a solution influenced by the initial condition and typically presenting larger RMS error than the output obtained with the LMS method if the initial condition is not very accurate. However, the large improvement achieved on their physical feasibility overcomes the drawbacks of obtaining an estimator with increased error. Thus, one must try to find a compromise between large prediction error and physical sense.

When identifying inertial parameters, they can be divided in three groups depending on the robot structure: fully identifiable, completely unidentifiable and identifiable in linear combinations [118]. Some parameters cannot be identifiable due to the restricted motion near the base and the lack of full force sensing in every joint. By using numerical analysis of the regressor matrix it is possible to identify a base set of parameters which represents the whole ϕ vector via a linear combination matrix L.

$$\phi_B = L \cdot \phi \tag{4.25}$$

The base set of parameters will produce the same torque than the extended set of parameters for a given observation matrix. Considering the best solution of the equation (4.20) the one provided by LMS method (ϕ_{LMS}), the optimisation problem tries to find a compromise between the solution provided by LMS and a solution which accomplishes with the physical feasibility aforementioned. Ideally the new set of optimised parameters will have similar base than the LMS solution and it will be physically feasible. The method used for determining the linear combination matrix L is thus useful to compare the base parameters of two different sets.

The approach presented here improves the guidelines given in [117] by creating two different metrics to quantify the magnitude to minimize, these are the torque error e_τ which takes into account the divergence between the measured torque and the torque produced by the identified parameters and the base error $e_\phi$which counts for the deviation with respect the base parameters. The main improvement presented here with respect the classical approach given by (4.26) consists in introducing a weighting vector w_j in order to normalise the effect of the different torque amplitude depending on the joint. The final expression is shown in (4.27) where * represents element-wise multiplication of vectors.

$$e_\tau = (\tau - A_{CL}\phi_B)^T(\tau - A_{CL}\phi_B) \tag{4.26}$$

$$e_\tau = w_j * (\tau - A_{CL}\phi_B)^T w_j * (\tau - A_{CL}\phi_B) \tag{4.27}$$

Where ϕ_B is given by (25) and represents the current base parameter solution and ϕ' the current vector of dynamic parameters. This is, the solution corresponding to the current iteration. The error with respect the base parameters is the following:

$$e_\phi = (\phi_B - L\phi'_{LMS})^T(\phi_B - L\phi'_{LMS}) \tag{4.28}$$

Where ϕ'_{LMS} is the parameters solution given by the LMS method. With the errors already defined, it is straight forward to infer the cost function of the optimisation problem which will be:

$$f = w_\tau e_\tau + w_\phi e_\phi \tag{4.29}$$

Where w_τ and w_ϕ are the weighting factors used to vary the influence of both metrics.

Different types of constraint equations should be defined here. In the literature, conditions are usually given for the links' masses and inertias. However, in this research it has been proved that the introduction of an additional type of constraints is necessary to ensure the feasibility of the model. These will be called here, "link coherence constraints". The usual constraints presented in the literature are: the positive mass value of every link and the definite positiveness of each link's inertia matrix (${}^iI_{cog}$). The link coherence constraints are related with the location of the link's centre of gravity. Although it is intuitive that each link's centroid has to be content inside the cuboid of minimum volume where the link can be inscribed, this condition is not implicit in the previous conditions and has to be added independently. Otherwise the obtained parameters might not produce a definite positive manipulator's inertia matrix. When having certain a priori information of the robotic system, e.g. in case of having a CAD model from the manufacturer, as occurs in this research, it is sensible to assume that the centres of gravity of each link should not differ much from those calculated from the model. Thus, the optimisation problem can be established as follows:

$$\phi_{opt} = \min f(\phi') \tag{4.30}$$

$$\begin{cases} m_i > 0 \\ eig({}^iI_{cog}) > 0 \end{cases} \tag{4.31}$$

$$\begin{cases} cx_i \in [cx_{i\ Min}, cx_{i\ Max}] \\ cy_i \in [cy_{i\ Min}, cy_{i\ Max}] \\ cz_i \in [cz_{i\ Min}, cz_{i\ Max}] \end{cases} \tag{4.32}$$

Where (4.30) states the objective of minimizing the cost function f while the constraints dictated by (4.31) and the centre of gravity constraints (4.32) are accomplished. The problem presented above constitutes a constrained nonlinear optimisation

problem. Algorithms like the Sequential Quadratic Programing have been proved efficient to solve this kind of problem [117], [121].

4.4.1 Numerical calculation of the base parameters, L matrix.

The calculation of the matrix L it is crucial to apply the optimisation technique mentioned before which looks for a parameters solution whose base is similar than the base given by least mean squares. The technique employed in this research is based in [122] where the QR decomposition of the regressor matrix is used to find the minimum number of parameters. This method can be summarized on the following steps:

1.) Find the orthogonal-triangular (QR) decomposition of the regressor matrix K_{CL}. This produces unitary Q, upper triangular R and a permutation matrix E so that $K_{CL} \cdot E = Q \cdot R$. The column permutation E is chosen so the absolute value of the main diagonal of R is decreasing.

2.) Defining the numerical tolerance (ε_n) to obtain the rank of the observation matrix. Due to round off errors the tolerance its defined in [122] as:

$$\varepsilon_n = abs(eps \cdot R_{11}) \tag{4.33}$$

Where *eps* is the precision of the machine which is being used for computation and R_{11} the first element of the R matrix.

3.) Determining again the QR decomposition of the observation matrix without any pivoting E. This will be valuable to find the rank of the observation matrix. This will allow to obtain the matrices Q' and R' so $K_{CL} = Q' \cdot R'$. The rank (b) is determined by the number of elements of the main diagonal of R' which are greater than ε_n.

4.) Decomposition of R in $R_1(b\ x\ b)$ and R_2 $(b\ x\ c-b)$ so that $R = [R_1\ , R_2]$ and c is the number of parameters used.

5.) Choosing the columns to be deleted. The $c-b$ diagonal elements R_{ii} which are smaller than the tolerance indicate the subscripts i of the columns of K_{CL} to be deleted. With this, a permutation matrix P is obtained such that: $P \cdot \phi$ gives an sorted set of parameters whose first elements are the parameters which can be identified independently and the second set are the parameters which cannot. Also the matrix K_{CL}, can be sorted in the same way: $K_{CL} \cdot P$.

6.) Performing a QR decomposition of the sorted matrix $K_{CL} \cdot P$ gives: $[K_{CL1}, K_{CL2}] = [Q_1 \cdot R_1 \; Q_1 R_2]$, where R_1 is a regular $b \; x \; b$ matrix. Then it is possible to deduce $K_{CL2} = K_{CL1} \cdot R_1^{-1} R_2$, which expresses the c-b columns of K_{CL2} as linear combinations of K_{CL1}.

7.) In order to get finally explicit relationship for the parameters P is divided in two elements as follows: P_1 includes the first b rows and c columns of P. P_2 has the rest of rows of P. The matrix which expressed the linear dependencies can be obtained as: $L = (P_1 + R_1^{-1} \cdot R_2 \cdot P_2)$

4.5 Experiments using a hydraulic manipulator, KRAFT GRIPS

The experimental setup is composed by the following elements:

- 1 x KRAFT GRIPS hydraulic telemanipulator.
- 1 x NI-PXIe-8108 Real Time controller.
- 1 x PC running Labview 2011 interfacing with the PXI.
- 1 x Force/Torque sensor, ATI, Gamma SI-130-10.
- 1 x Resilient interface with an elastic constant of 5000[N/m].

The Kraft GRIPS (Figure 4-9) manipulator from Kraft Telerobotics has been used in a number of teleoperation applications such as underwater and maintenance of electrical lines [43]. One of the main advantages of this manipulator is the possibility of evaluating experimental control algorithms in a commercial platform. GRIPS is a 7 dof hydraulic manipulator with a maximum payload of 45 kg at full extension and a horizontal reach of 1.289 m. It is equipped with 6 force controlled servo-valves controlling the first 5 axis and the gripper. The 6^{th} axis is controlled in position with a fixed torque of 20 Nm. A potentiometer for measuring the angular position of each joint is used in the six dof within a range of ± 10 V. The servo-valves signals are proportional to the difference of pressure between the two chambers of each hydraulic actuator. This signal ranging ± 6 V is proportional to the applied torque. The output signal of each servo-valve together with the potentiometers signals were sampled at 1 KHz by means of the PXI. In every test included in this paper the gripper was not mounted and the force/torque sensor along with the spring were mounted on the end-effector provided by the last link.

The robot model for the first 5 dof contains 10 barycentric parameters and 2 friction parameters per link. The tie bar parallel to the second link between the shoulder and the elbow creates a closed loop structure included in the model. Three different approaches have been tested and evaluated for identification the robot's dynamics parameters. The first method involves independent joint excitation. This is, the different robotic joints are excited sequentially and the excitation trajectory is calculated by trial and error with a reduced number of parameters. Later, two different methods are also evaluated where all the joints are excited simultaneously with different optimised trajectories.

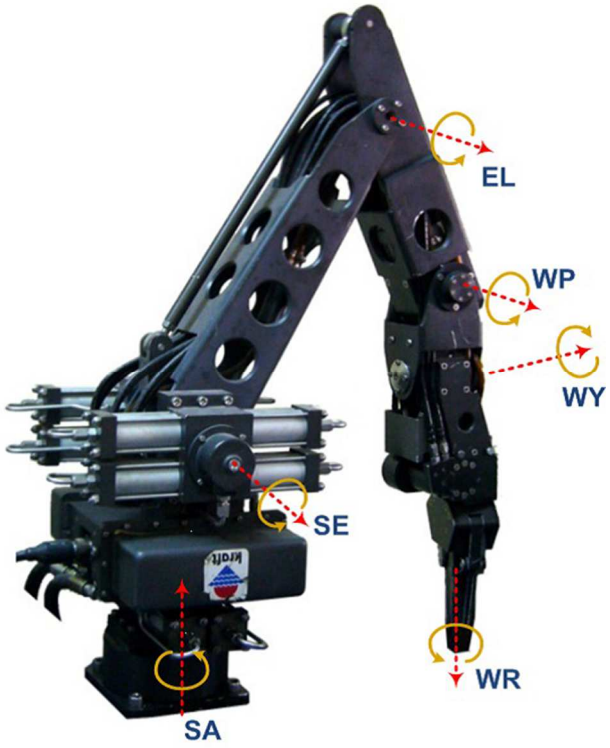

Figure 4-9. Kraft GRIPS hydraulic telemanipulator.

Very different number of parameters are tested and compared. The three methods are evaluated in this chapter by comparing the root mean square of the error between predicted torque and motor torque in each joint and conclusions are obtained.

4.5.1 Calculation of identification trajectories

4.5.1.1 Independent excitation

A set of trajectories corresponding to equation (4.34), which is (4.23) particularised for $N = 1$ was programmed in order to perform independent joint movements at different excitation frequencies. The complete range of frequencies is shown in Table 4-1. The amplitudes $a_{i,k}$ and $b_{i,k}$ are equal and corresponding with the amplitude column of the table. These were chosen in a way that maximizes the angle covered by each joint. Afterwards, as it will be explained in the next sections, a discard process was carried out with all the gathered sample points based on applying equation (4.24) to the observation matrix. This guarantees a minimum quality of each selected sample point.

$$q_i(t) = a_i \sin(k\omega_f t) + b_i \cos(k w_f t) \tag{4.33}$$

Joint No	**Min. ω_f [rad/s]**	**Max. ω_f. [rad/s]**	**Amplitude**
1	0.1916	2.4903	0.8200
2	0.6283	5.0265	0.2500
3	0.4054	3.8406	0.7750
4	0.6386	5.7114	0.4950
5	0.6414	8.2498	0.5000

Table 4-1. Maximum and minimum excitation frequencies during the identification.

4.5.1.2 Simultaneous excitation with N=1

During this set of tests, the parametric trajectories correspond to the equation (4.35), where each joint trajectory is defined by three parameters.

$$q_i(t) = q_{i_0} + a_i \sin(k\omega_f t) + b_i \cos(k w_f t) \tag{4.35}$$

However in choosing the excitation frequency one must reach a compromise between covered space and enough excitation of the dynamic properties of the robot. If selecting low fundamental frequencies w_f, the excitation period increases and a larger part of the robot workspace can be covered at the cost of longer measurement time. However, if using higher fundamental frequencies, which implies higher velocities and accelerations, the inertias are excited accordingly [115]. For this test, a constant $k = 1$ and fundamental frequency $\omega_f = 0.2\pi$ were selected in order to obtain a period of approximately 10 seconds for each trajectory. A sampling frequency of 1 kHz was used during the experiment which results in 10,000 sample points.

The obtaining of the trajectories' parameters has been carried out in several ways in the literature. In some works, sometimes intuitively designed special motions of one or several joints are employed [123], [124], [125], [126], [127]. Other researches have made use of any optimality criteria during an optimisation process [128], [129], [130], [131]. In this research, an optimisation process based on Sequential Quadratic Programming has been employed to select adequate parameters minimizing a cost function that takes into account the condition number of the observation matrix and a factor of workspace coverage. The cost function $f(q_{i_0}, a_{i,k}, b_{i,k})$ is described by (4.36).

$$\begin{cases} f\big(q_{i_0}, a_{i,k}, b_{i,k}\big) = w_1 f_1 + w_2 f_2 + w_3 f_3 \\ f_1 = cond(A_i) \\ f_2 = \frac{1}{\min(\sigma_i)} \\ f_3 = \frac{1}{\sum_{i=1}^{N}(max(q_i) - \min(q_i))} \end{cases} \tag{4.36}$$

Where w_i are conveniently selected weights, σ_i are the singular values of the regressor matrix A_i and q_i are the joints values. With this strategy we ensure that joint space is covered and the regressor matrix presents good properties.

The optimisation based on SQP admits a set of linear and nonlinear constraints to be applied on the solution. The only set of constraints used during the optimisation trajectories has been the condition that each joint trajectory needs to be inside the joint's range. The optimisation problem is then completed with the inequality constraint expressed in (4.36).

$$\forall\ q_{i_0}, a_{i,k}, b_{i,k}, /\ q_i(t)\ \in [q_i \inf limit, q_i \sup limit] \tag{4.37}$$

Where $t \in [0, T]$, and $, T = 2\pi/\omega$

The algorithm requires the establishment of an initial condition, which was taken as the unitary vector for q_0, and zeros for a_0 and b_0. After running the optimisation process, the resulting parameters are given by Table 4-2.

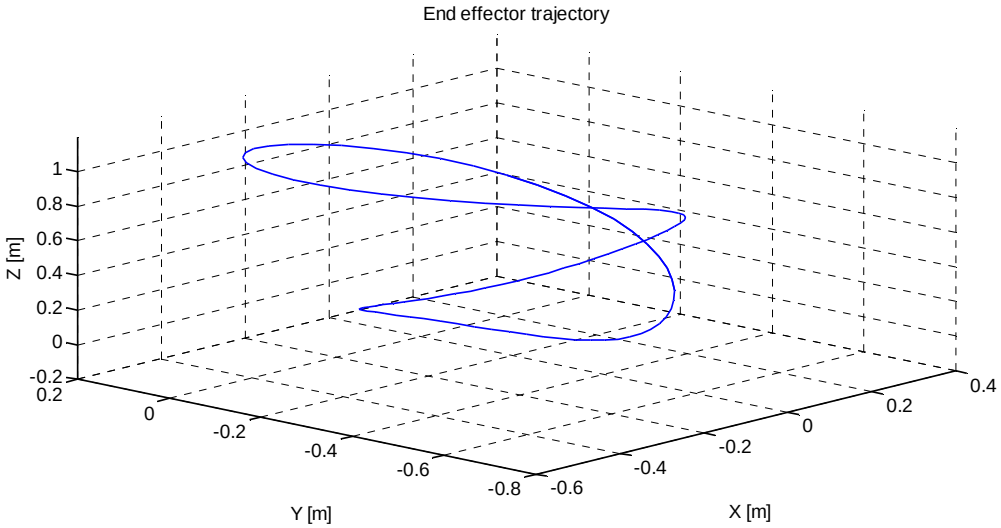

Figure 4-10. Resulting end-effector trajectory when using 2 parameters per joint.

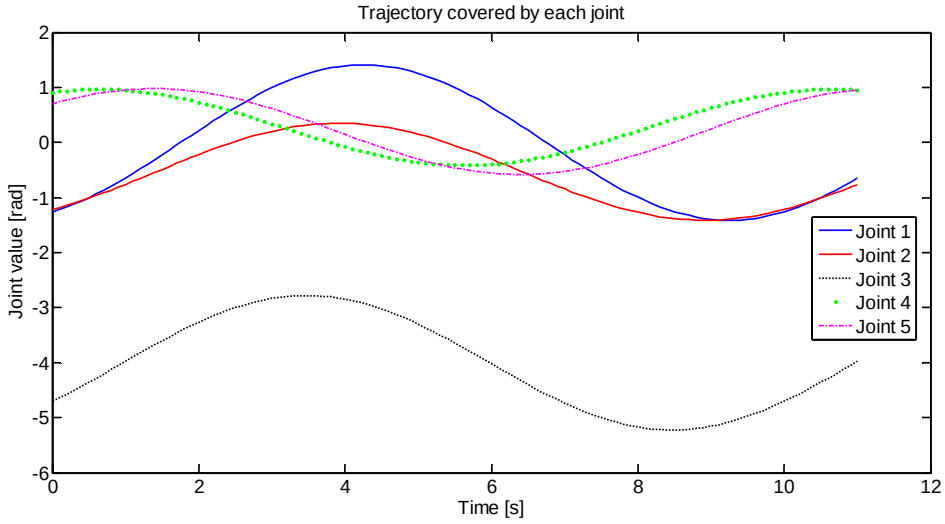

Figure 4-11. Trajectory covered by the first 5 dof. Resulting from an optimisation process.

w	$0.2 \cdot \pi$
k	1.0000
a_1	0.6390
a_2	0.5525
a_3	1
a_4	0.2715
a_5	0.6
a_6	1.3731

b_1	-1.2590
b_2	-0.6855
b_3	-0.7
b_4	0.6347
b_5	0.5
b_6	-0.3256
q_{01}	0
q_{02}	-0.5303
q_{03}	-4
q_{04}	0.28
q_{05}	0.2
q_{06}	0

Table 4-2. Parameters found after SQP optimisation.

4.5.1.3 Simultaneous excitation with N=5

A similar procedure than in previous section was implemented, although this time the number of harmonics was increased to 5. It was expected that major excitation of the inertias was carried out and better results achieved. The followed trajectories were identical to equation (4.23) particularised for $N = 5$. The set of obtained coefficients are shown in Table 4-3. As before, the angular frequency was 0.6283 rad/s.

$\boldsymbol{q_{01}}$	0.0000
$\boldsymbol{q_{02}}$	-0.9384
$\boldsymbol{q_{03}}$	-4.6800
$\boldsymbol{q_{04}}$	0.3978
$\boldsymbol{q_{05}}$	0.5421
$\boldsymbol{q_{06}}$	-0.0795

Table 4-3. Values of the joint offset for each joint after an optimisation based on SQP for N=5.

	$\boldsymbol{a_1}$	$\boldsymbol{a_2}$	$\boldsymbol{a_3}$	$\boldsymbol{a_4}$	$\boldsymbol{a_5}$
$\boldsymbol{q_1}$	-0.0004	0.0004	0.0001	0.0001	1.4106
$\boldsymbol{q_2}$	0.1876	-0.2768	0.3163	-0.3168	-0.0989
$\boldsymbol{q_3}$	0.1526	-0.2531	0.3014	-0.2588	-0.0288
$\boldsymbol{q_4}$	-0.0293	-0.0892	0.2021	-0.3180	-0.2407
$\boldsymbol{q_5}$	-0.2029	0.2134	-0.1387	0.0669	-0.2102

q_6	0.1752	0.0879	-0.2041	0.5955	0.9028

Table 4.4. Values for the parameter a for each joint after an optimisation based on SQP for N=5.

	b_1	b_2	b_3	b_4	b_5
q_1	0.0005	-0.0001	-0.0002	-0.0002	-0.2222
q_2	-0.2998	0.1318	-0.0277	-0.0746	0.0596
q_3	-0.2621	0.1600	-0.0166	-0.0863	0.1457
q_4	0.0768	0.1532	-0.2813	0.2294	0.1072
q_5	0.2912	-0.1590	0.0889	-0.0549	0.1176
q_6	0.1132	-0.2730	0.4866	-0.3009	0.0738

Table 4-5. Values for the parameter b for each joint after an optimisation based on SQP for N=5.

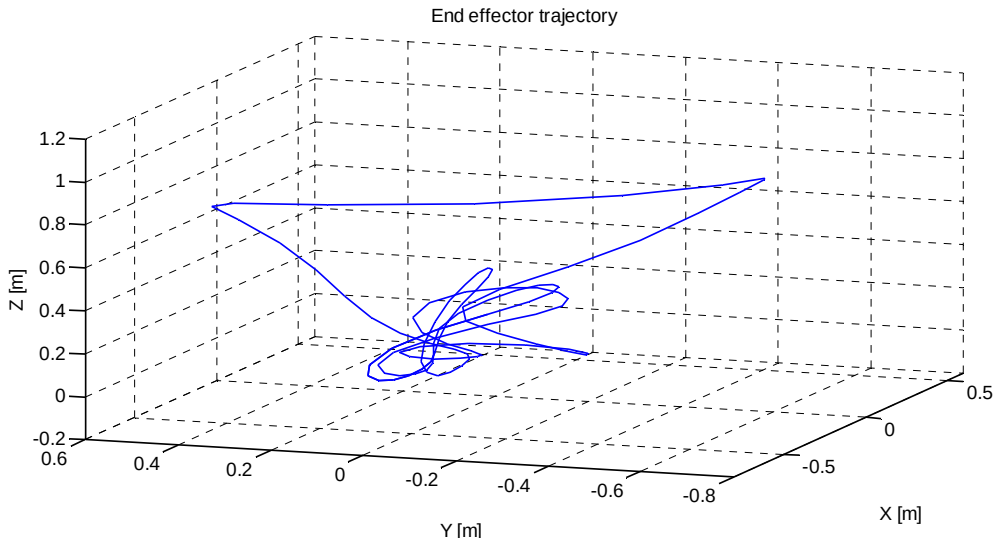

Figure 4-12. End-effector trajectory when implementing joint's trajectories with N=5.

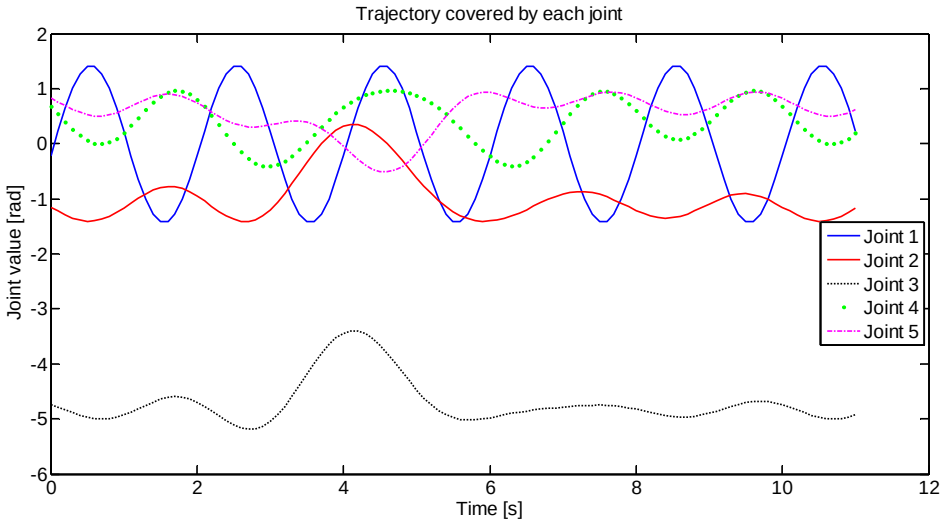

Figure 4-13. Trajectory covered by the first 5 dof. Resulting from an optimisation process.

4.5.2 Parameter identification

The procedure explained exhaustively in 4.2 was implemented during these experiments. For a parameter identification based on damped least mean squares, an a-priori knowledge of the system is necessary. As it has been explained before on this thesis, the CAD model of the robot can be used for this purpose. Later, the equation (4.21) can be applied to obtain the desired vector of parameters.

4.5.2.1 A priori knowledge

A CATIA V5© model of the KRAFT GRIPS manipulator was available from the manufacturer. Unfortunately this model did not represent the robot accurately in terms of masses and inertias. For example, the internal characteristics of each link or actuator were not represented, being only representative the external shape. With this representation style, the actuator cylinders were rendered as solid bodies instead of being hollow cylinders. The hoses were also omitted in this model.

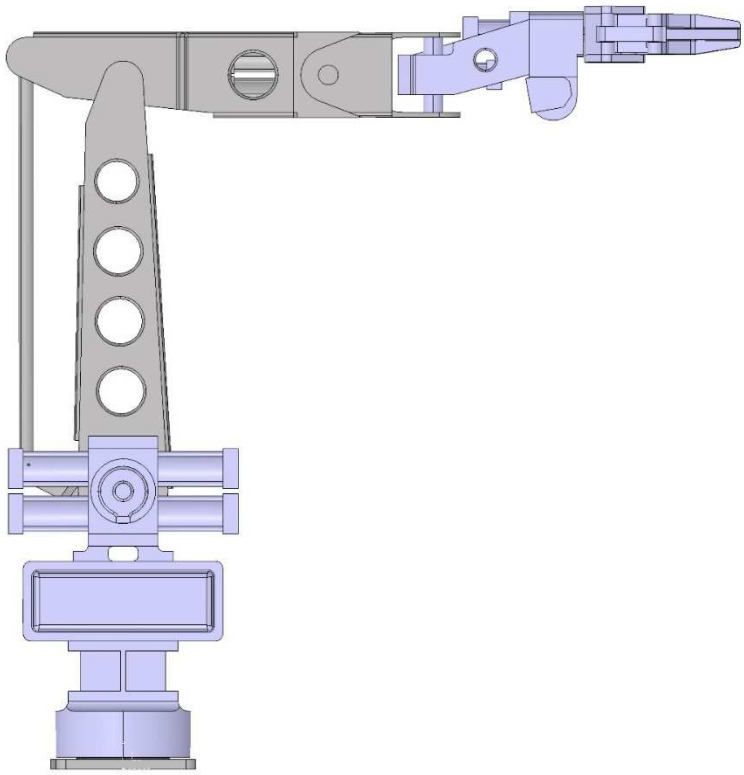

Figure 4-14. CATIA model of the KRAFT GRIPS manipulator.

Once having an approximate model of the manipulator, the first possible option is to assume that the mass is evenly distributed throughout its volume. This option was possible after obtaining the total mass from the manufacturer. Once all these data was gathered, the CATIA software was utilised to calculate the masses of each link, first mass moment with respect the centre of mass and moments of inertia of each link with respect the reference system displayed in Figure 4-6. The resultant parameters are shown in Table 4-6. One can easily realise that most of mass is concentrated on the first links, leaving very little for the last two links. This is due to the non-realistic effect produced by using a non-hollow model. It is worth highlighting that with this approach one ensures that every a-priori parameters present physical sense.

In addition to the inertial parameters, in order to complete the manipulator model, it is crucial to model the actuators' torque properly. For that reason, the torque constant of each actuator and the links' friction has to be estimated as well. This will allow to complete all the necessary data to apply equations (4.2) and (4.3). In this research, no additional information from the manufacturer could be gathered and appropriate tests had to be designed to calculate those values.

Parameters	**Link 1**	**Link 2**	**Link 3**	**Link 4**
$m\ [Kg]$	41.614	3.645	5.007	0.689
$m \cdot c_x\ [Kg \cdot m]$	-0.109	-0.003	0.038	0.044
$m \cdot c_y\ [Kg \cdot m]$	0.002	0.828	-0.779	0.000
$m \cdot c_z\ [Kg \cdot m]$	7.532	0.000	0.000	0.000
$I_{xx}\ [Kg \cdot m^2]$	1.442	0.296	0.195	0.002
$I_{xy}[Kg \cdot m^2]$	0.002	-0.003	0.000	0.000
$I_{xz}[Kg \cdot m^2]$	-0.020	0.000	0.000	0.000
$I_{yy}[Kg \cdot m^2]$	1.392	0.013	0.010	0.005
$I_{yz}[Kg \cdot m^2]$	0.000	0.000	0.000	0.000
$I_{zz}[Kg \cdot m^2]$	0.095	0.293	0.4261	0.004

Table 4-6. Inertial parameters measured in the CAD model, links 1 to 4.

Parameters	**Link 5**	**Link 6**	**Link 7**	**Link 8**
$m\ [Kg]$	4.758	1.500	0.731	0.453
$m \cdot c_x\ [Kg \cdot m]$	0.456	0.000	0.000	-0.021
$m \cdot c_y\ [Kg \cdot m]$	0.003	0.000	-0.190	0.000
$m \cdot c_z\ [Kg \cdot m]$	0.087	0.045	0.000	0.000
$I_{xx}\ [Kg \cdot m^2]$	0.011	0.003	0.042	0.000
$I_{xy}[Kg \cdot m^2]$	0.000	0.000	0.000	0.000
$I_{xz}[Kg \cdot m^2]$	0.011	0.000	0.000	0.000
$I_{yy}[Kg \cdot m^2]$	0.072	0.003	0.000	0.003
$I_{yz}[Kg \cdot m^2]$	0.000	0.000	0.000	0.000
$I_{zz}[Kg \cdot m^2]$	4.758	0.001	0.042	0.453

Table 4-7.Inertial parameters measured in the CAD model, links 5 to 8.

For estimating the torque constant of each joint, a set of tests were designed where the robot exerted a force approximately perpendicular to a plain surface with each joint. A 6-dof force/torque sensor placed on the robot tip was used to measure that force and the robot jacobian was employed to project the end-effector torques and forces into the joint to be analysed. In Figure 4-15 the joint differential pressure scaled by a factor of 10 is displayed in green and the forces and torques measured with the sensor and projected on axis 1 are represented in red. The relationship of the two graphs is represented as a cloud of points in Figure 4-16. By applying least squares it is possible to get a solution for the torque constant in equation (4.31).

$$\bar{\tau} = k_p \cdot \overline{\Delta P} \tag{4.38}$$

Where k_p is the torque constant based on the differential pressure of the hydraulic actuators in $[\frac{Nm}{V}]$ and , $\overline{\Delta P}$ is the vector of differential pressure in volts. The length of the vector is the number of sampling points used to calculate the torque constant. And $\bar{\tau}$ is the vector of measured and projected torque on each link, in $[Nm]$.

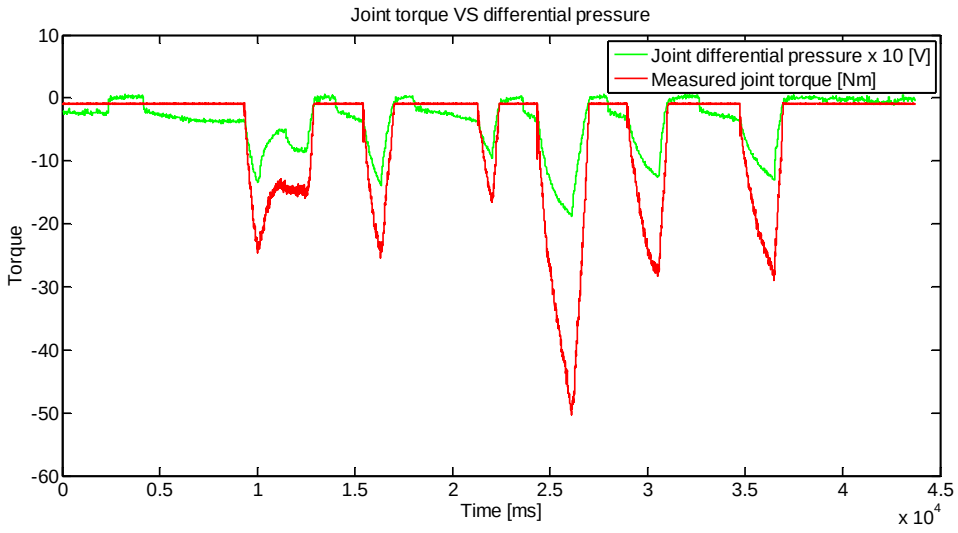

Figure 4-15. Projected torque and differential pressure for joint 1.

The small steps which appear in the differential pressure of Figure 4-15 are produced by the inertial effort the hydraulic actuator suffers when moving the manipulator. They are omitted during the calculations by setting up two thresholds in the collected data. Only the sampling points which produce a force between these thresholds are used. The results are summarized in Table 4-8 for the first 5 degrees of freedom which are those ones with pressure feedback. The last joint does not present a torque control. Only in the third joint a voltage offset was observed. In addition to the torque constant, a complete set of experiments were realised to characterise the friction behaviour of the hydraulic robot. Each joint was moved at a constant speed and a different speeds to neglect the inertial torque. The differential pressure in each actuator was sampled for each speed level. In Figure 4-17, joints' friction graphs are represented.

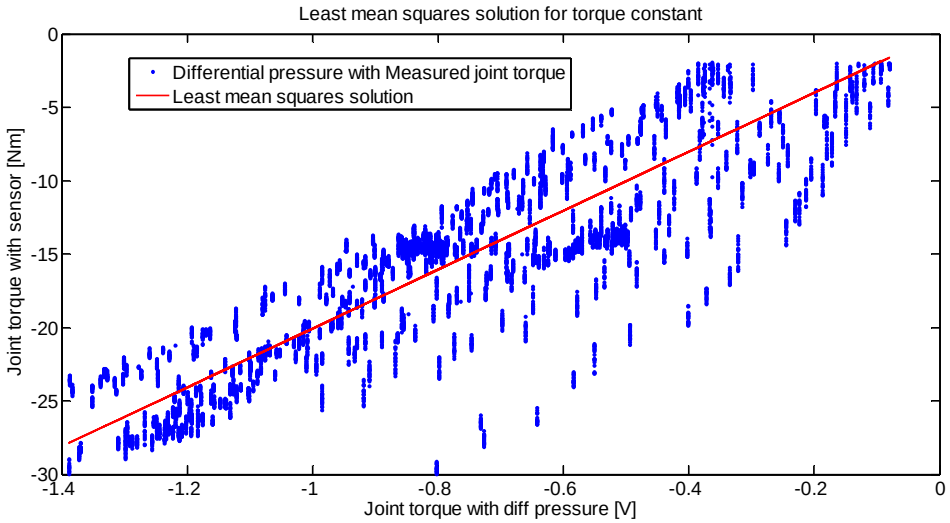

Figure 4-16. Least mean squares solution for the relationship differential pressure VS projected joint torque.

It is common from most robotic actuators to present different friction depending on the sense of rotation. This fact has been checked during the experiments and two different group of lines appear represented, one for each velocity direction. The linearization of the sampled data is shown in a form of equation in each graph. If no transformation was performed on the data, this would lead to an equation of the type:

$$\begin{cases} \tau_f = K_p(f_{c1} sign(\dot{q}) + f_{v1}\dot{q}\ ) & if\ \dot{q} > 0 \\ \tau_f = K_p(f_{c2} sign(\dot{q}) + f_{v2}\dot{q}) & if\ \dot{q} < 0 \\ \tau_f = 0 & if\ \dot{q} = 0 \end{cases} \tag{4.39}$$

However, in order to use the modified Newton-Euler method to identify the friction parameters, these have to be transformed into a more linearized expression similar to (4.40) which takes also into account the voltage offset in the joints. This is shown in the figure by the linearized lines.

$$\tau_f = K_p(f_c sign(\dot{q}) + f_v\dot{q} - V_{offset}) \tag{4.40}$$

With these considerations, the summary of the friction data from the robot is given in Table 4-9. These experiments complete a set of trials necessary to perform a minimum robot modelling. Once these parameters are obtained the a-priori knowledge of the robot is complete and next steps forward can be performed. It is worth summarising that the parameters obtained for an a-priori model are: the kinematic characteristics, dynamic parameters such as masses, mass moments, inertias, actuator torque constants and joints' friction.

Joint No.	Torque constant [Nm/V]	Offset [V]
1	23.769	-0.053
2	-85.617	0.044
3	-22.0233	-1.468
4	40.180	-0.060
5	-15.040	-0.060

Table 4-8. Torque constants value of KRAFT GRIPS for the joints with pressure feedback.

Joint No.	f_c [V]	f_v [V · s/rad]
1	-0.0716	-0.0314
2	-0.0680	-0.0614
3	-0.0936	-0.0417
4	-0.2928	-0.1669
5	-0.2789	-0.1100

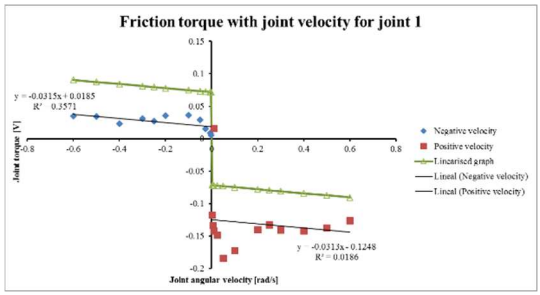

Fig. a.) Friction torque for joint 1.

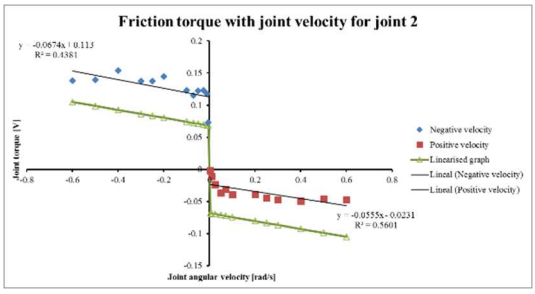

Fig. b.) Friction torque for joint 2.

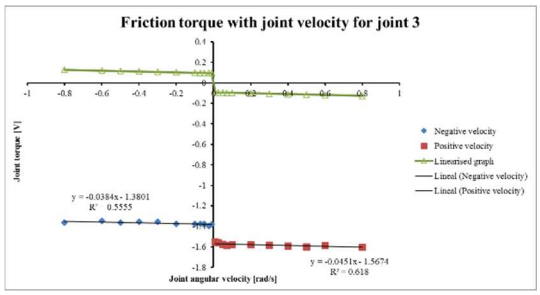

Fig. c.) Friction torque for joint 3.

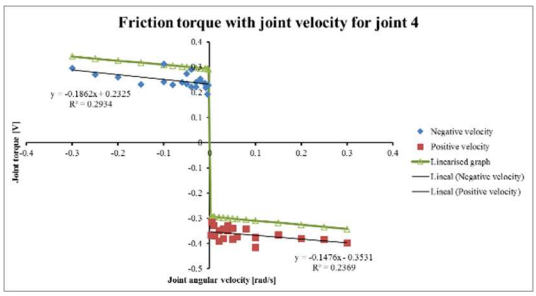

Fig. d.) Friction torque for joint 4.

Table 4-9. Linearized friction coefficients for KRAFT GRIPS joints.

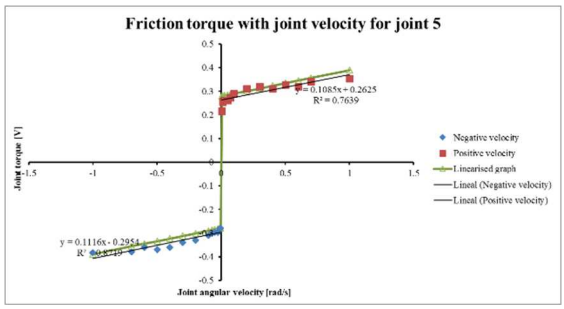

Fig. e.) Friction torque for joint 5.

Figure 4-17. Friction torque with joint velocity for KRAFT GRIPS' joints.

4.5.2.2 Damped least mean squares

With the a-priori information already gathered it is now possible to apply equation (4.22) with a determined λ which adjust the confidence in the a-priori parameters. Three different optimised trajectories were obtained in section 4.3 and thus, here three different set of damped least mean squares solutions will be achieved.

Independent excitation

For the first case scenario where the joints excitation was carried out independently, 2000 sampling points were selected for different frequencies, and a vector of parameters was calculated by damped least mean squares for different values of λ. Each resultant vector of parameters was used afterwards to replicate the torque with the given kinematics conditions. This is, for each sampling point, the necessary torque to excite the robot was calculated with the identified parameters. The set of parameters with least torque error with respect the real motor torque was selected. For each i sampling point, a regressor matrix A_i whose values depend not only in the position, but also in the joint speed and acceleration was computed. During the data acquisition, only joint positions and differential pressure were gathered and thus, joint velocity and acceleration were obtained during an off-line signal processing. One of the advantages of having induced a periodic movement in each joint is the easiness of applying signal processing methods for obtaining the velocity and acceleration. It has been seen how one of the best methods to perform this operation off-line [115] is accomplishing a filtering on the frequency domain by multiplying the Discrete Fourier Transform of the signal by a rectangular window. The window is made by filling with zeros where the non-desired frequencies and ones where the frequencies that should be maintained

are. Afterwards an Inverse Fourier transform can be accomplished and the resultant signal is almost noise-free. In order to perform a differentiation on the frequency domain, the resulting spectrum after performing the DFT is then multiplied by $j\omega$ in the frequency domain, which is equivalent to the differential operator. Afterwards, the time domain signal is restored by performing the Inverse Fourier Transform.

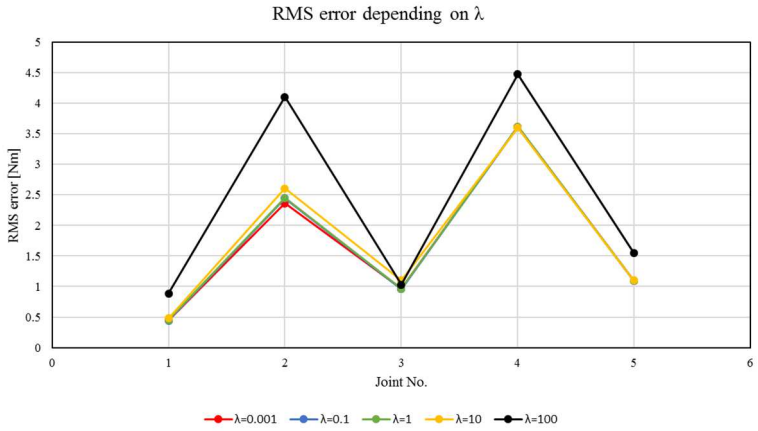

Figure 4-18. Root mean square error for of motor torque for identified parameters depending on lambda.

Parameters	**Link 1**	**Link 2**	**Link 3**	**Link 4**
$m\ [Kg]$	41.614	3.645	4.874	0.378
$m \cdot c_x\ [Kg \cdot m]$	-0.109	-0.078	-1.141	0.258
$m \cdot c_y\ [Kg \cdot m]$	0.002	-0.591	1.055	0.168
$m \cdot c_z\ [Kg \cdot m]$	7.532	0.000	-0.056	-0.052
$I_{xx}\ [Kg \cdot m^2]$	2.805	1.755	-0.451	-0.980
$I_{xy}[Kg \cdot m^2]$	0.002	0.912	-0.916	-0.669
$I_{xz}[Kg \cdot m^2]$	0.000	0.087	-0.266	-0.311
$I_{yy}[Kg \cdot m^2]$	2.755	-1.675	0.361	0.573
$I_{yz}[Kg \cdot m^2]$	0.000	0.107	0.015	-0.063
$I_{zz}[Kg \cdot m^2]$	-0.322	1.441	5.518	-1.633
$f_c[Nm]$	-0.179	-0.812	0.281	-1.847
$f_v[Nm \cdot s/m]$	-2.833	-18.846	2.375	-13.490

Table 4-10. Inertial parameters identified through LMS, links 1 to 4. Independent link excitation.

The root mean square error of the torque with the identified parameters for the identification trajectories is given in Figure 4-18 for several values of lambda parameter.

For a small value of lambda the least mean squares solution is more accurate, however its values diverge from the a-priori solution. It is not crucial to maintain the solution very close to the CAD values because it is known they are not completely true, but at least physical sense on the parameters is necessary. A compromise solution should be taken and then $\lambda = 10$ is selected to represent the best approximation of the robot parameters for the given trajectory. The resultant values for the chosen value of λ are collected in Table 4-10 and Table 4-11.

Parameters	**Link 5**	**Link 6**	**Link 7**	**Link 8**
$m\ [Kg]$	4.457	1.166	0.825	0.453
$m \cdot c_x\ [Kg \cdot m]$	0.240	0.028	-0.397	-0.905
$m \cdot c_y\ [Kg \cdot m]$	0.132	0.020	1.331	-0.046
$m \cdot c_z\ [Kg \cdot m]$	0.345	-0.046	-0.057	0.000
$I_{xx}\ [Kg \cdot m^2]$	-3.092	0.125	1.343	0.351
$I_{xy}[Kg \cdot m^2]$	-1.726	-0.071	0.914	0.922
$I_{xz}[Kg \cdot m^2]$	0.142	-0.003	0.144	0.082
$I_{yy}[Kg \cdot m^2]$	0.600	0.171	-1.688	-0.763
$I_{yz}[Kg \cdot m^2]$	0.062	0.011	-0.175	-0.281
$I_{zz}[Kg \cdot m^2]$	-0.078	0.027	-1.709	0.400
$f_c[Nm]$	-0.817	0.006	-2.232	1.203
$f_v[Nm \cdot s/m]$	-3.409	-0.248	-1.367	3.179

Table 4-11. Inertial parameters identified through LMS, links 5 to 8.

Eigenvalues	**Link 1**	**Link 2**	**Link 3**	**Link 4**
λ_1	2.804	2.003	5.530	-1.804
λ_2	2.755	-1.905	-1.054	-1.057
λ_3	-0.322	1.421	0.950	0.822

Table 4-12. Eigenvalues of the inertia matrices, links 1 to 4.

Eigenvalues	**Link 5**	**Link 6**	**Link 7**	**Link 8**
λ_1	-3.780	0.223	-2.063	-1.329
λ_2	1.281	0.074	1.599	0.880
λ_3	-0.072	0.026	-1.589	0.437

Table 4-13. Eigenvalues of the inertia matrices, links 1 to 4.

It is important to note that the least mean squares solution does not guarantee physical feasibility of the parameters, which is crucial for some tasks as robot control. In this

solution, all the link masses have been positive. To guarantee the physical feasibility of the inertia matrices, these have to be definite positive which is accomplished if their eigenvalues are positive and non-zero. For the eight inertia matrices shown before the eigenvalues are given in Figure 4-12 and Figure 4-13.

	Joint1	**Joint 2**	**Joint 3**	**Joint 4**	**Joint 5**
RMS [Nm]	0.7329	3.58	0.986	4.98	1.18

Table 4-14. RMS errors for the identification trajectories when using parameters calculated through damped least mean squares.

Simultaneous excitation with $N = 1$ and $N = 5$

The same technique for parameter identification was employed for the more advanced trajectories detailed in section 4.5.1. The resultant parameters are detailed in Table 4-15 to Table 4-18.

Parameters	**Link 1**	**Link 2**	**Link 3**	**Link 4**
$m\ [Kg]$	41.614	3.645	3.075	-2.676
$m \cdot c_x\ [Kg \cdot m]$	-0.109	-1.254	-4.539	0.018
$m \cdot c_y\ [Kg \cdot m]$	0.002	-3.109	3.948	0.601
$m \cdot c_z\ [Kg \cdot m]$	7.532	0.000	-0.582	-1.708
$I_{xx}\ [Kg \cdot m^2]$	2.805	1.520	-2.198	-1.437
$I_{xy}[Kg \cdot m^2]$	0.002	-1.337	0.632	-0.874
$I_{xz}[Kg \cdot m^2]$	0.000	-0.157	1.939	-1.027
$I_{yy}[Kg \cdot m^2]$	2.755	-2.786	0.762	-0.315
$I_{yz}[Kg \cdot m^2]$	0.000	1.120	-4.315	-1.595
$I_{zz}[Kg \cdot m^2]$	-1.668	-0.115	-0.099	5.276
$f_c[Nm]$	-2.594	6.441	-1.851	-4.914
$f_v[Nm \cdot s/m]$	-6.269	-5.794	-2.228	-10.685

Table 4-15. Inertial parameters identified through LMS, links 1 to 4. Excitation trajectory based on 2 parameters per joint.

Parameters	**Link 5**	**Link 6**	**Link 7**	**Link 8**
$m\ [Kg]$	1.477	-1.697	-0.758	0.453
$m \cdot c_x\ [Kg \cdot m]$	0.594	0.037	1.123	4.686
$m \cdot c_y\ [Kg \cdot m]$	-0.483	0.059	-3.405	3.305
$m \cdot c_z\ [Kg \cdot m]$	0.805	0.692	-0.150	0.000

I_{xx} $[Kg \cdot m^2]$	2.252	0.421	1.108	0.752
$I_{xy}[Kg \cdot m^2]$	-0.344	0.084	-1.335	-0.626
$I_{xz}[Kg \cdot m^2]$	-0.228	0.483	0.647	0.946
$I_{yy}[Kg \cdot m^2]$	1.707	0.769	-2.799	-2.510
$I_{yz}[Kg \cdot m^2]$	-0.375	-0.023	-2.562	4.256
$I_{zz}[Kg \cdot m^2]$	-0.291	0.175	-1.359	-1.200
$f_c[Nm]$	-2.735	-0.305	0.805	-0.606
$f_v[Nm \cdot s/m]$	-11.568	0.511	-0.889	0.825

Table 4-16. Inertial parameters identified through LMS, links 5 to 8. Excitation trajectory based on 2 parameters per joint.

Parameters	**Link 1**	**Link 2**	**Link 3**	**Link 4**
m $[Kg]$	41.614	3.645	2.637	-3.046
$m \cdot c_x$ $[Kg \cdot m]$	-0.109	-0.461	-0.992	1.043
$m \cdot c_y$ $[Kg \cdot m]$	0.002	-4.209	3.437	0.165
$m \cdot c_z$ $[Kg \cdot m]$	7.532	0.000	0.200	0.171
I_{xx} $[Kg \cdot m^2]$	2.805	2.416	0.557	0.051
$I_{xy}[Kg \cdot m^2]$	0.002	-0.396	1.048	0.257
$I_{xz}[Kg \cdot m^2]$	0.000	-0.664	-0.267	-0.006
$I_{yy}[Kg \cdot m^2]$	2.755	-1.584	0.104	0.294
$I_{yz}[Kg \cdot m^2]$	0.000	-0.385	-0.113	-0.098
$I_{zz}[Kg \cdot m^2]$	0.430	-0.517	-3.801	-0.456
$f_c[Nm]$	0.455	5.864	-0.518	-4.560
$f_v[Nm \cdot s/m]$	-3.114	3.069	-6.910	-22.291

Table 4-17. Inertial parameters identified through LMS, links 1 to 4. Excitation trajectory based on 5 parameters per joint.

Parameters	**Link 5**	**Link 6**	**Link 7**	**Link 8**
m $[Kg]$	1.153	-2.063	-1.257	0.453
$m \cdot c_x$ $[Kg \cdot m]$	0.702	-0.137	0.197	3.928
$m \cdot c_y$ $[Kg \cdot m]$	-0.163	-0.100	-2.185	0.175
$m \cdot c_z$ $[Kg \cdot m]$	0.218	0.198	0.212	0.000
I_{xx} $[Kg \cdot m^2]$	-0.261	-0.106	2.005	0.094
$I_{xy}[Kg \cdot m^2]$	0.198	-0.025	-0.394	-1.042
$I_{xz}[Kg \cdot m^2]$	-0.139	0.000	0.445	-0.111
$I_{yy}[Kg \cdot m^2]$	-0.023	-0.104	-1.597	0.246
$I_{yz}[Kg \cdot m^2]$	0.000	-0.023	1.161	0.402

$I_{zz}[Kg \cdot m^2]$	0.038	-0.005	0.327	0.198
$f_c[Nm]$	-1.898	1.098	2.024	-2.322
$f_v[Nm \cdot s/m]$	-6.894	-1.595	-0.629	0.605

Table 4-18. Inertial parameters identified through LMS, links 5 to 8. Excitation trajectory based on 5 parameters per joint.

	Joint1	**Joint 2**	**Joint 3**	**Joint 4**	**Joint 5**
2 parameters	1.193	1.600	1.043	1.631	0.775
5 parameters	1.040	3.058	1.703	2.098	1.452

Table 4-19. RMS errors [Nm] for the identification trajectories when using parameters calculated through damped least mean squares. Comparison between optimised trajectories with 2 and 5 parameters.

4.5.2.3 Parameters optimisation

The technique explained in 4.3 was used here to optimize the three set of parameters found with LMS for the three different trajectories. The initial condition for every case is the solution found with least mean squares. The optimisation algorithm selected was Sequential Quadratic Programming due to its flexibility with these type of constraints and its proven ability for this type of problems.

Independent excitation

For this set of data, the weight factors which appear in equation (4.29) where evenly selected as $w_\tau = 1$ and $w_\phi = 1$. For this reason, both error components presented the same influence on the optimisation process.

Parameters	**Link 1**	**Link 2**	**Link 3**	**Link 4**
$m\ [Kg]$	41.614	3.645	4.000	0.300
$m \cdot c_x\ [Kg \cdot m]$	-0.109	0.399	-1.738	0.682
$m \cdot c_y\ [Kg \cdot m]$	0.002	1.772	0.744	-0.141
$m \cdot c_z\ [Kg \cdot m]$	7.532	-30.000	30.000	-7.380
$I_{xx}\ [Kg \cdot m^2]$	12.664	7.044	0.103	0.099
$I_{xy}[Kg \cdot m^2]$	10.066	1.395	0.003	0.000
$I_{xz}[Kg \cdot m^2]$	-0.012	0.160	-0.190	0.000
$I_{yy}[Kg \cdot m^2]$	17.274	0.380	0.104	0.098

$I_{yz}[Kg \cdot m^2]$	-0.012	0.029	-0.220	0.000
$I_{zz}[Kg \cdot m^2]$	0.101	2.195	12.435	0.100
$f_c[Nm]$	-0.182	-0.970	0.239	-1.840
$f_v[Nm \cdot s/m]$	-2.830	-12.026	9.149	-13.490

Table 4-20. Inertial and friction parameters optimised through SQP from the initial solution based on LMS, links 1 to 4.

Parameters	**Link 5**	**Link 6**	**Link 7**	**Link 8**
$m\ [Kg]$	4.000	0.100	0.100	0.453
$m \cdot c_x\ [Kg \cdot m]$	0.572	0.092	-0.697	-0.786
$m \cdot c_y\ [Kg \cdot m]$	0.050	0.086	0.467	0.539
$m \cdot c_z\ [Kg \cdot m]$	0.680	-0.418	-22.789	-30.000
$I_{xx}\ [Kg \cdot m^2]$	0.099	0.124	0.099	0.100
$I_{xy}[Kg \cdot m^2]$	0.000	0.000	0.000	0.000
$I_{xz}[Kg \cdot m^2]$	0.000	-0.020	0.000	-0.005
$I_{yy}[Kg \cdot m^2]$	0.099	0.100	0.099	0.103
$I_{yz}[Kg \cdot m^2]$	0.000	0.000	0.000	-0.030
$I_{zz}[Kg \cdot m^2]$	0.099	0.116	0.099	0.461
$f_c[Nm]$	-0.808	-0.026	-2.258	1.244
$f_v[Nm \cdot s/m]$	-3.415	-0.244	-8.226	10.000

Table 4-21. Inertial and friction parameters optimised through SQP from the initial solution based on LMS, links 5 to 8.

Eigenvalues	**Link 1**	**Link 2**	**Link 3**	**Link 4**
λ_1	25.295	7.328	12.441	0.099
λ_2	4.641	2.189	0.099	0.098
λ_3	0.101	0.099	0.099	0.099

Table 4-22. Inertia matrices' eigenvalues of the optimised parameters, links 1 to 4.

Eigenvalues	**Link 5**	**Link 6**	**Link 7**	**Link 8**
λ_1	0.099	0.140	0.099	0.463
λ_2	0.099	0.099	0.099	0.099
λ_3	0.099	0.099	0.099	0.100

Table 4-23.Inertia matrices' eigenvalues of the optimised parameters, links 5 to 8.

The initial condition is given by the parameters of Table 4-10 and Table 4-11. An optimisation process using the MATLAB© R2014a Optimisation Toolbox was carried out using sequential quadratic programming as explained in 4.4. A sensible set of limit values was established for every parameter so the optimisation process did not output a value too far from the realistic solution. Nonlinear constraints to force definite positive eigenvalues and positive masses have been used. The starting point of the optimisation algorithm was chosen as the least mean squares solution. With this approach, the parameters are varied in a way that the output function takes into account the torque prediction error and the divergence of the new base of parameters with respect the base calculated via LMS.

	Joint1	**Joint 2**	**Joint 3**	**Joint 4**	**Joint 5**
RMS $[\boldsymbol{Nm}]$	1.81	4.14	1.24	5.05	0.43

Table 4-24. RMS errors for the identification trajectories with optimised parameters.

In Table 4-24 the RMS errors for the identified trajectories calculated with optimised parameters are shown. It is worth noting that the total RMS error is greater than the calculated via the LMS solution of Table 4-14. This effect is the usual because the optimisation algorithm tends to deteriorate the results obtained with least mean squares in exchange for a realistic physical sense towards the fulfilling of the constraints and bounds.

Simultaneous excitation with $N = 1$ and $N = 5$

The resulting optimised parameters for the Kraft manipulator are shown in Table 4-25 and Table 4-26 for the simultaneous excitation with $N = 1$ and in Table 4-27 and Table 4-28 for $N = 5$. In every solution presented here, the links' masses are positive and the inertia matrices are definite positive.

Parameters	**Link 1**	**Link 2**	**Link 3**	**Link 4**
$m\ [Kg]$	41.614	3.645	4.000	0.300
$m \cdot c_x\ [Kg \cdot m]$	-0.109	-1.233	-4.514	-0.575
$m \cdot c_y\ [Kg \cdot m]$	0.002	-7.769	5.802	-6.612
$m \cdot c_z\ [Kg \cdot m]$	7.532	26.200	-24.500	-9.689
$I_{xx}\ [Kg \cdot m^2]$	18.845	3.023	0.264	0.806
$I_{xy}[Kg \cdot m^2]$	-7.676	-0.347	0.082	0.073
$I_{xz}[Kg \cdot m^2]$	0.033	-0.038	0.588	-1.005
$I_{yy}[Kg \cdot m^2]$	9.868	0.238	0.296	0.235

$I_{yz}[Kg \cdot m^2]$	-0.023	0.005	0.713	-0.485
$I_{zz}[Kg \cdot m^2]$	0.193	0.196	5.278	6.893
$f_c[Nm]$	-2.558	-0.003	-5.197	-4.911
$f_v[Nm \cdot s/m]$	-6.240	-0.051	3.546	-10.682

Table 4-25. Inertial and friction parameters optimised through SQP from the initial solution based on LMS, links 1 to 4. Optimised trajectory with two parameters per joint.

Parameters	**Link 5**	**Link 6**	**Link 7**	**Link 8**
$m\ [Kg]$	4.000	0.100	0.100	0.453
$m \cdot c_x\ [Kg \cdot m]$	4.213	0.003	1.158	4.644
$m \cdot c_y\ [Kg \cdot m]$	-0.489	0.048	-3.381	3.355
$m \cdot c_z\ [Kg \cdot m]$	8.037	-3.354	29.691	0.000
$I_{xx}\ [Kg \cdot m^2]$	0.605	1.067	3.308	0.188
$I_{xy}[Kg \cdot m^2]$	-0.316	0.119	-0.482	-0.001
$I_{xz}[Kg \cdot m^2]$	-0.202	0.326	0.576	0.001
$I_{yy}[Kg \cdot m^2]$	1.047	1.422	0.271	0.192
$I_{yz}[Kg \cdot m^2]$	-0.340	-0.014	-0.090	0.001
$I_{zz}[Kg \cdot m^2]$	0.689	0.319	0.303	0.189
$f_c[Nm]$	-2.736	-0.279	-2.332	5.848
$f_v[Nm \cdot s/m]$	-11.570	0.543	-6.700	6.630

Table 4-26. Inertial and friction parameters optimised through SQP from the initial solution based on LMS, links 5 to 8. Optimised trajectory with two parameters per joint.

Parameters	**Link 1**	**Link 2**	**Link 3**	**Link 4**
$m\ [Kg]$	41.614	3.645	4.000	0.300
$m \cdot c_x\ [Kg \cdot m]$	-0.109	0.140	-2.132	0.547
$m \cdot c_y\ [Kg \cdot m]$	0.002	-8.305	4.938	-0.014
$m \cdot c_z\ [Kg \cdot m]$	7.532	0.000	30.000	-8.986
$I_{xx}\ [Kg \cdot m^2]$	29.917	3.203	0.100	0.129
$I_{xy}[Kg \cdot m^2]$	3.492	0.184	0.000	-0.012
$I_{xz}[Kg \cdot m^2]$	0.002	-0.497	0.000	0.025
$I_{yy}[Kg \cdot m^2]$	0.526	0.111	0.100	0.105
$I_{yz}[Kg \cdot m^2]$	0.000	-0.030	0.000	-0.011
$I_{zz}[Kg \cdot m^2]$	0.100	0.180	0.100	0.122
$f_c[Nm]$	0.000	0.000	-1.371	-5.615

$f_v[Nm \cdot s/m]$	-2.625	0.000	-6.640	-20.000

Table 4-27. Inertial and friction parameters optimised through SQP from the initial solution based on LMS, links 1 to 4. Optimised trajectory with five parameters per joint.

In Table 4.29 the RMS errors of each trajectory are presented with their respective set of parameters. Although one cannot exactly compare the two sets because their errors are evaluated against different trajectories, it is however possible to compare them against their non-optimised counterpart shown in Table 4-19. It seems clear that the optimisation process increases the RMS error when correcting the physical sense. A compromise must be achieved.

Parameters	**Link 5**	**Link 6**	**Link 7**	**Link 8**
$m\ [Kg]$	4.000	0.100	0.100	0.453
$m \cdot c_x\ [Kg \cdot m]$	30.000	-0.087	0.526	3.552
$m \cdot c_y\ [Kg \cdot m]$	-0.180	-0.045	-4.345	1.105
$m \cdot c_z\ [Kg \cdot m]$	0.333	-29.502	-21.125	0.000
$I_{xx}\ [Kg \cdot m^2]$	0.103	4.394	1.376	0.102
$I_{xy}[Kg \cdot m^2]$	0.114	-0.046	0.012	-0.008
$I_{xz}[Kg \cdot m^2]$	-0.117	0.029	-0.413	0.024
$I_{yy}[Kg \cdot m^2]$	8.202	4.393	0.100	0.135
$I_{yz}[Kg \cdot m^2]$	-0.022	0.024	-0.004	-0.108
$I_{zz}[Kg \cdot m^2]$	8.175	0.100	0.234	0.428
$f_c[Nm]$	-1.931	0.272	0.000	-1.603
$f_v[Nm \cdot s/m]$	-7.018	-2.428	0.000	0.916

Table 4-28. Inertial and friction parameters optimised through SQP from the initial solution based on LMS, links 5 to 8. Optimised trajectory with five parameters per joint.

	Joint1	**Joint 2**	**Joint 3**	**Joint 4**	**Joint 5**
2 *parameters*	3.990	3.496	2.542	1.705	0.789
5 *parameters*	1.535	5.912	3.271	2.709	1.582

Table 4.29. RMS errors [Nm] for the identification trajectories when using parameters calculated through damped least mean squares. Comparison between optimised trajectories with 2 and 5 parameters.

4.5.3 Validation experiment

To verify the proposed method, the three sets of optimised parameters were evaluated by predicting the motor torque for the identification trajectories. Afterwards, the three different methods, i.e. independent excitation, optimised trajectory with two parameters and optimised trajectory with 5 parameters are compared together on their three different trajectories in order to validate the proposed parameters. This allows the comparison of the three different identification trajectories directly and the effectiveness of their solution. The RMS errors of each experiments are provided for comparison.

4.5.3.1 Independent excitation

The estimated joint torques for joints 1 to 5 are shown in the figures below. Two different set of parameters have been used for comparison purposes, the LMS parameters without optimisation and the optimised parameters.

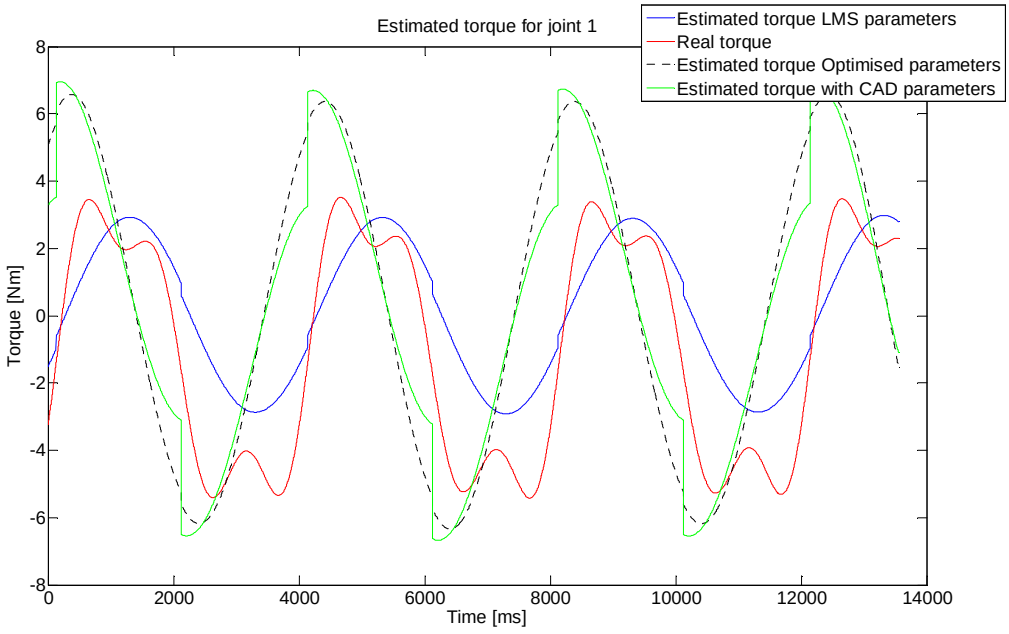

Figure 4-19. Estimated and measured torques for identification trajectories on joint 1.

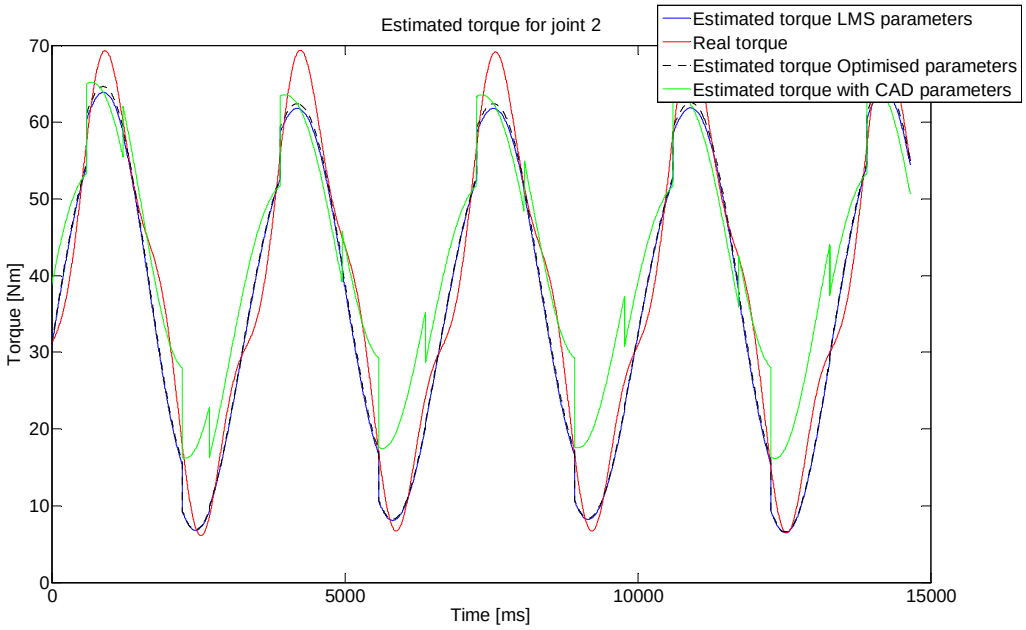

Figure 4-20. Estimated and measured torques for identification trajectories on joint 2.

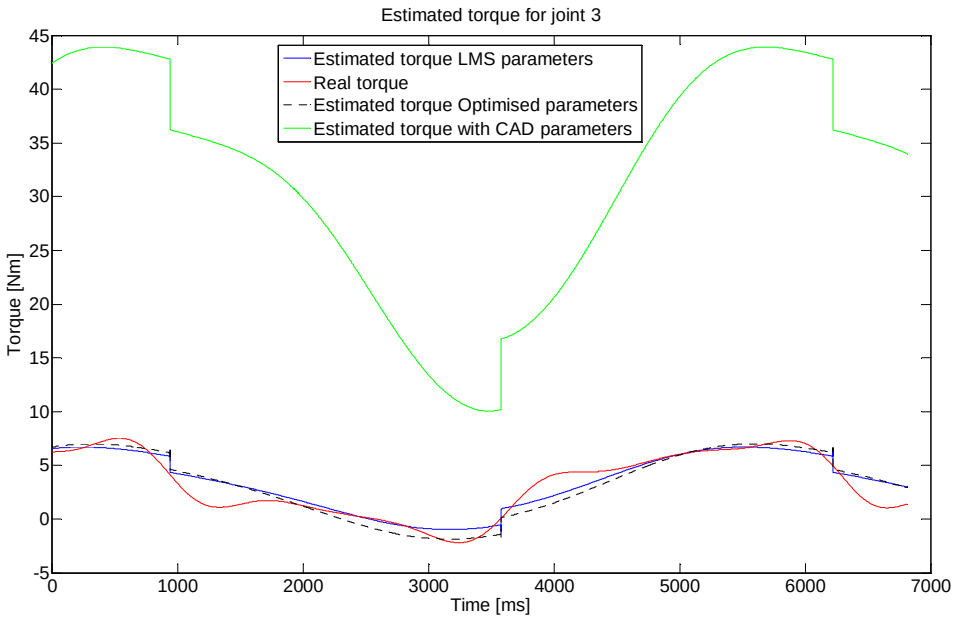

Figure 4-21. Estimated and measured torques for identification trajectories on joint 3.

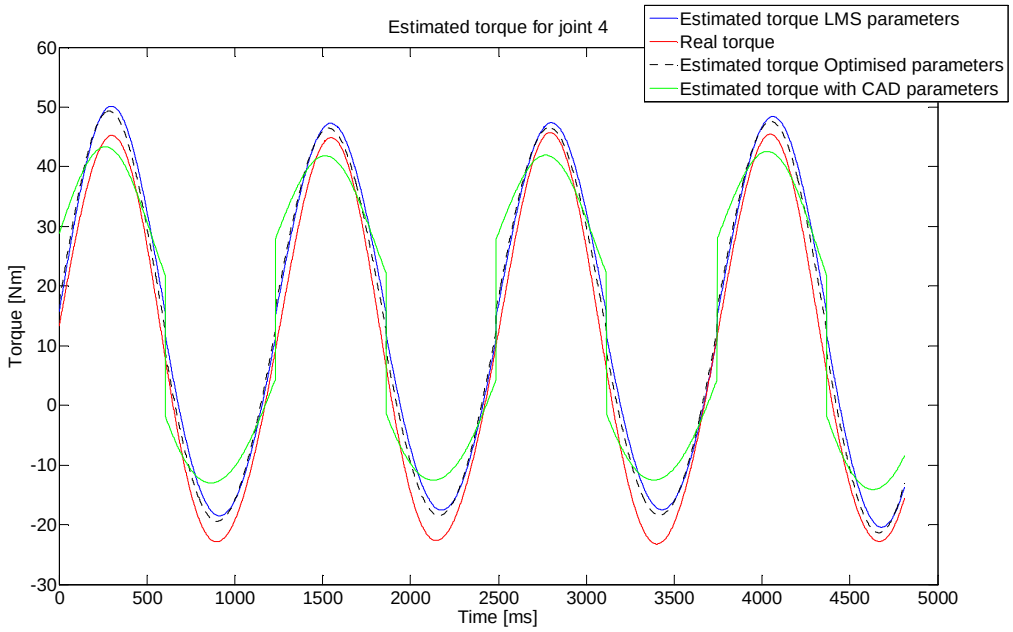

Figure 4-22.Estimated and measured torques for identification trajectories on joint 4.

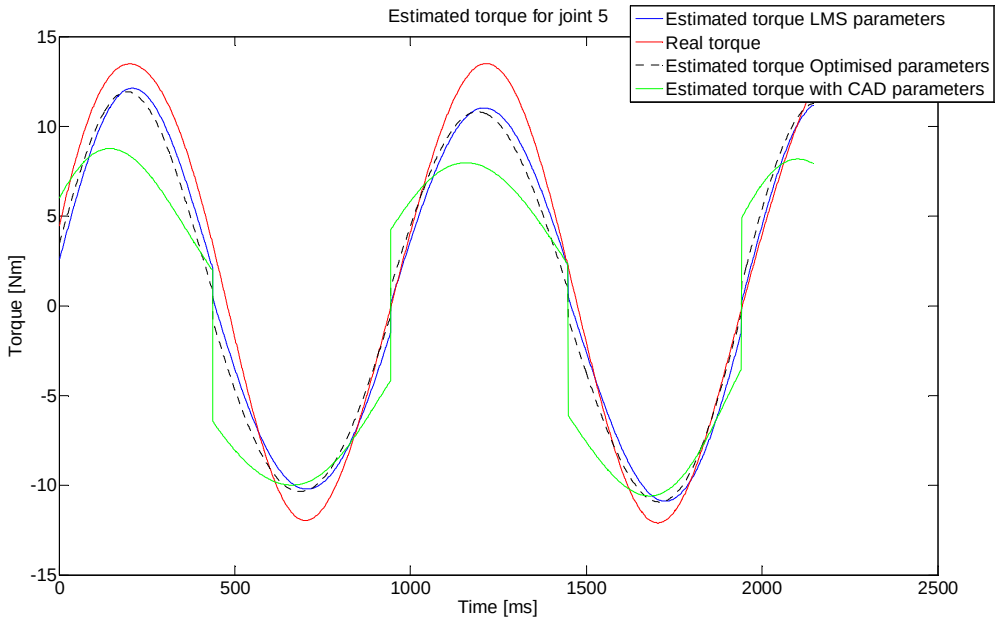

Figure 4-23. Estimated and measured torques for identification trajectories on joint 5.

In Figure 4-19 to Figure 4-23 the estimated torque for every set of parameters is presented. It is clear how the a priori parameters calculated with the CAD measurements and assuming uniform density are improved by the estimation done via least mean

squares for all joints. The optimised set also improves the a-priori knowledge although this is done in less amount due to the price paid by giving the parameters physical sense. The estimation carried out for joint 3 with the CAD parameters fails completely and is dramatically corrected by the other methods. In every joint apart from the first one, the optimisation does not deteriorate the predictor substantially. However in the first joint the error is greater due to the action of the hydraulic hoses in the table which creates a strong nonlinear and unpredictable effect on the torque.

4.5.3.2 Simultaneous excitation with N=1

In Figure 4-24 to Figure 4-28 the estimated torques are compared against the real torque measured in the Kraft manipulator for the optimised parameters based on $N = 1$. It is seen how the estimation based on pure LMS gives the best results in terms on error, however in order to get a realistic model one must choose between the parameters with physical sense, which are the a-priori knowledge and the optimised set. In every joint the optimisation set of parameters improves the predicted torque calculated with its CAD counterpart. Caution must be taken when comparing the first joint due to the harmful effect of the hydraulic hoses.

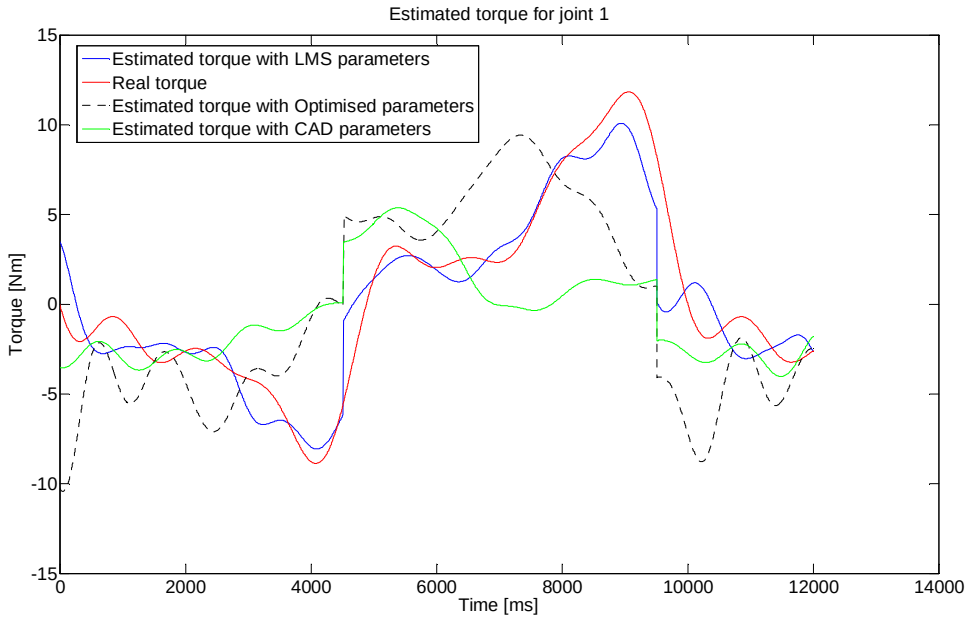

Figure 4-24. Estimated and measured torques for identification trajectories on joint 1. Simultaneous joint excitation with N=1.

The differences on joint 2 are small and the a-priori model matches well with the real observations. However this is not the case of the third joint where the least mean

squares solution and the optimised set improve the prediction dramatically. The step effect observed on the optimised parameters is due to the friction parameter which causes a torque step when changing the direction of the speed. The estimations obtained for joints 4 and 5 are also very good in comparison with the CAD model.

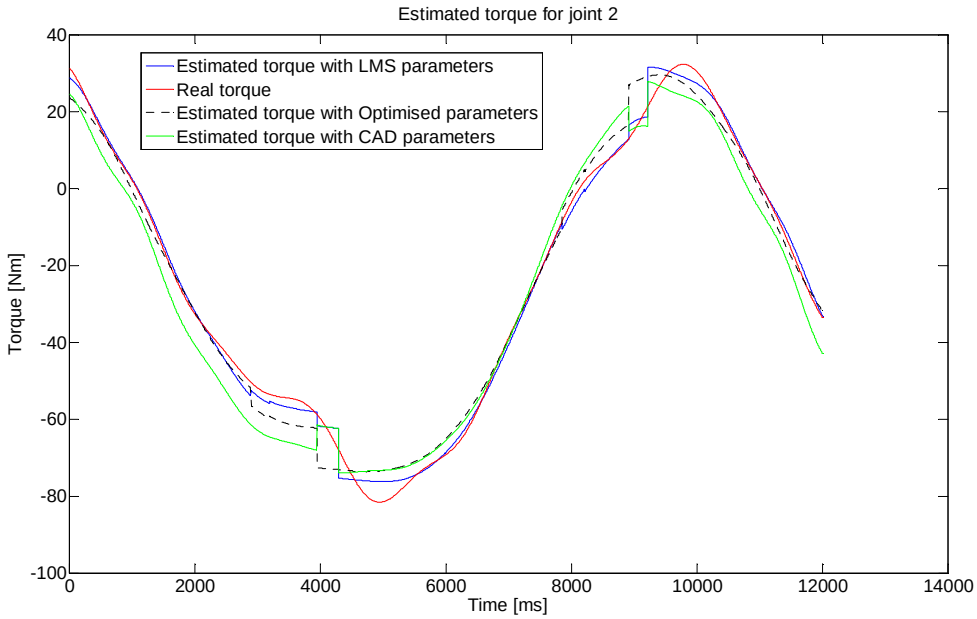

Figure 4-25. Estimated and measured torques for identification trajectories on joint 2. Simultaneous joint excitation with N=1.

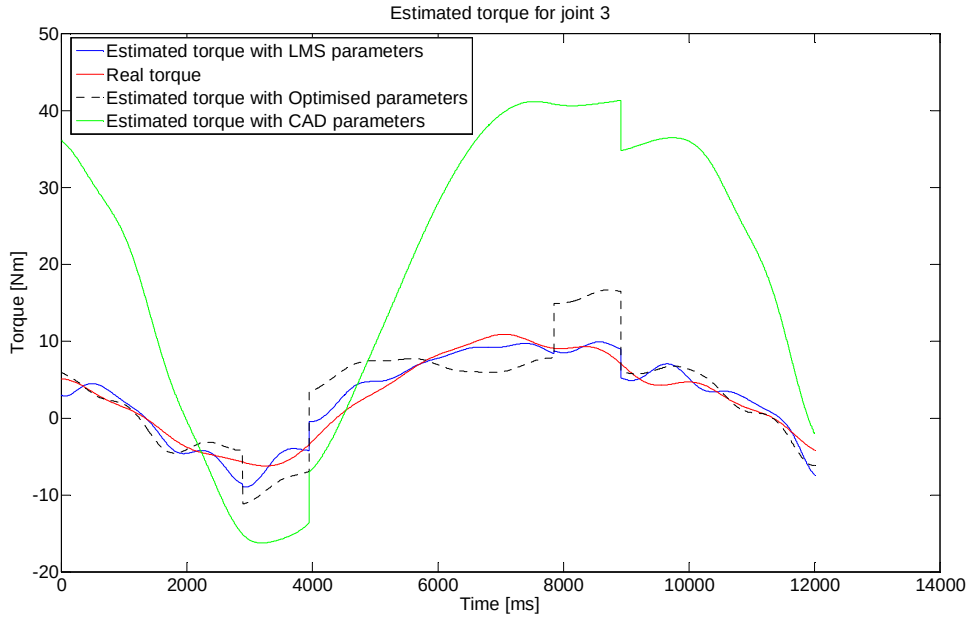

Figure 4-26. Estimated and measured torques for identification trajectories on joint 3. Simultaneous joint excitation with N=1.

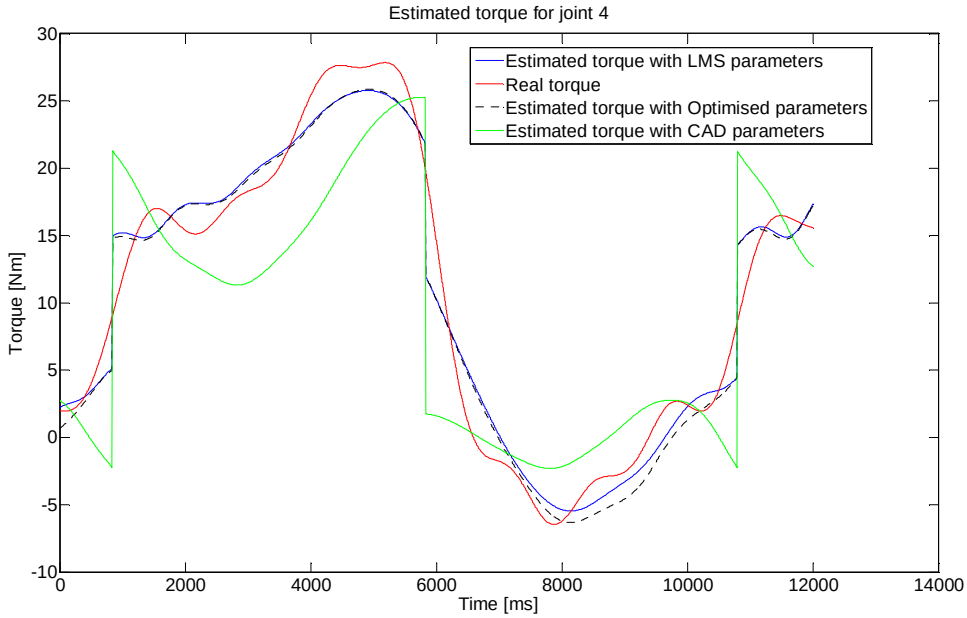

Figure 4-27. Estimated and measured torques for identification trajectories on joint 4. Simultaneous joint excitation with N=1.

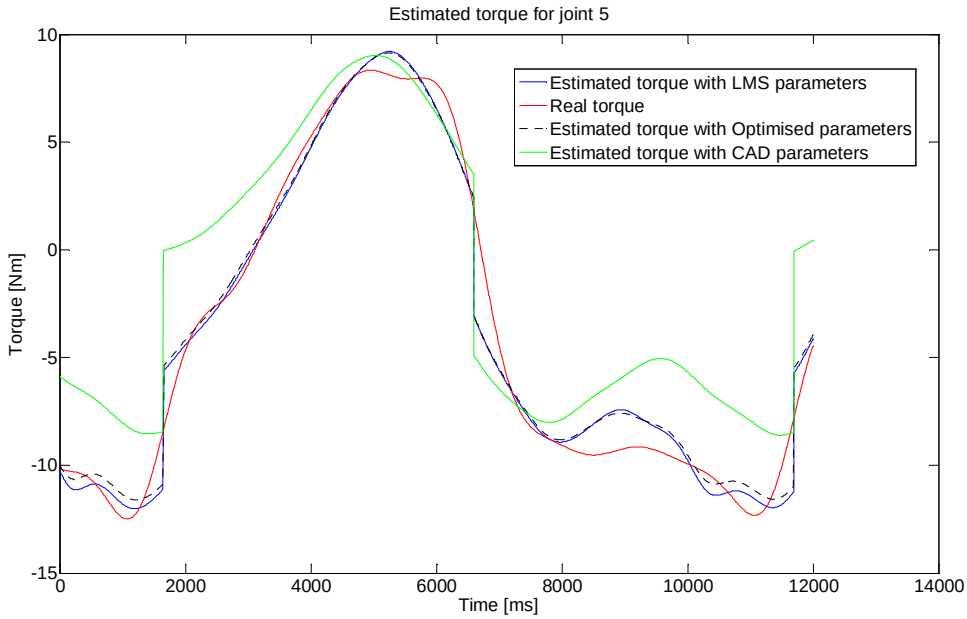

Figure 4-28. Estimated and measured torques for identification trajectories on joint 5. Simultaneous joint excitation with N=1.

4.5.3.3 Simultaneous excitation with N=5

The same approach is taken for the more elaborated trajectories obtained with a more complex excitation. On this case, more harmonics are involved on each joint's trajectory and it is expected that more speed and acceleration are required to fulfil them. A complete set of torque estimation is presented from Figure 4-29 to Figure 4-33 showing the improvements achieved with the proposed identification procedure.

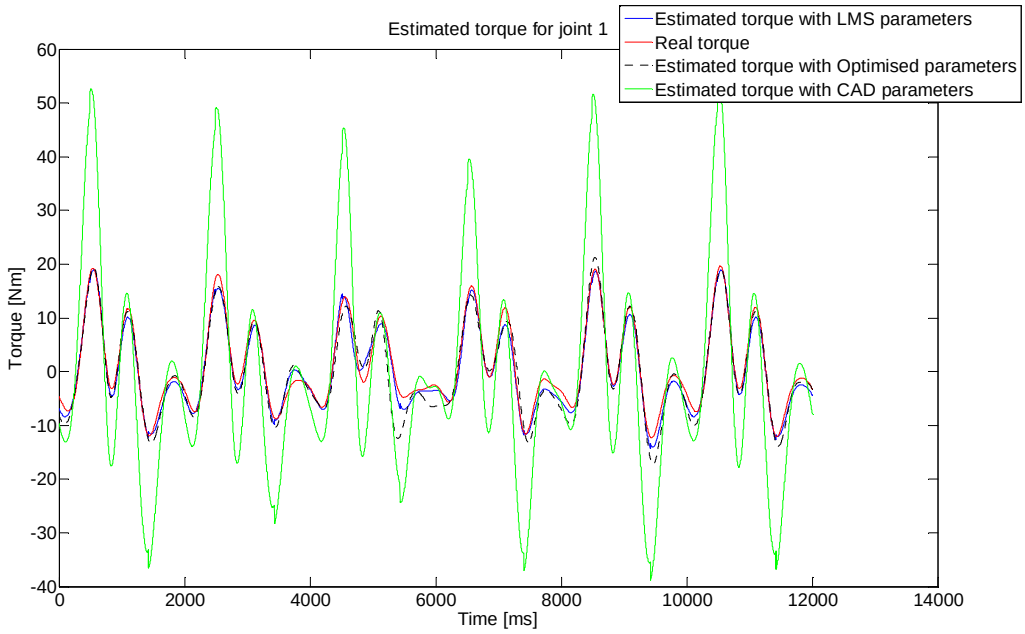

Figure 4-29. Estimated and measured torques for identification trajectories on joint 1. Simultaneous joint excitation with N=5.

The estimated torques of joint 1 shown in Figure 4-29 show a poor performance of the CAD parameters in comparison with the identified parameters. It also proves again how the estimation quality of the optimised parameters is worse than their LMS counterpart. The graphs of Figure 4-34 showing the acceleration of the joint 1 prove the great influence of the acceleration in the motor torque, mainly on the inertial torque. One can then guess that the inertial components calculated via the CAD model are not correct and lead to incorrect joint torques on the first joint when the accelerations are increased. This effect is not such in Figure 4-24 due to the more reduced accelerations. On joint 2, the results are impressive and it is possible to see a good torque estimation even for larger accelerations. The optimised parameters improve the performance of the CAD ones. The same situation arises on joint 3 although this time the effect is considerably more important. The performance of the optimised parameters overcomes the a-priori model and it is not far from the LMS solution. On the last two joints the estimation is also very good, leading to an improved model.

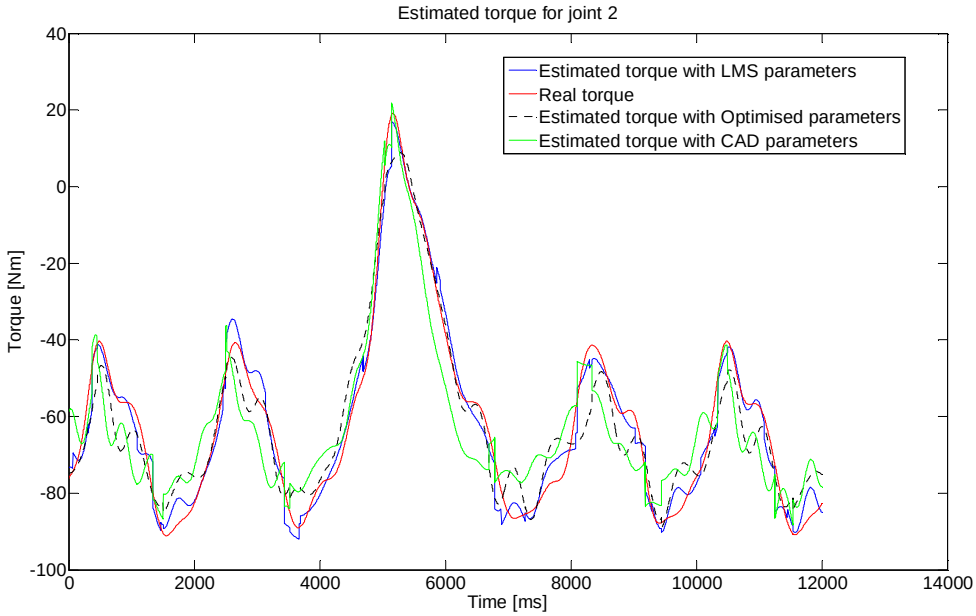

Figure 4-30. Estimated and measured torques for identification trajectories on joint 2. Simultaneous joint excitation with N=5.

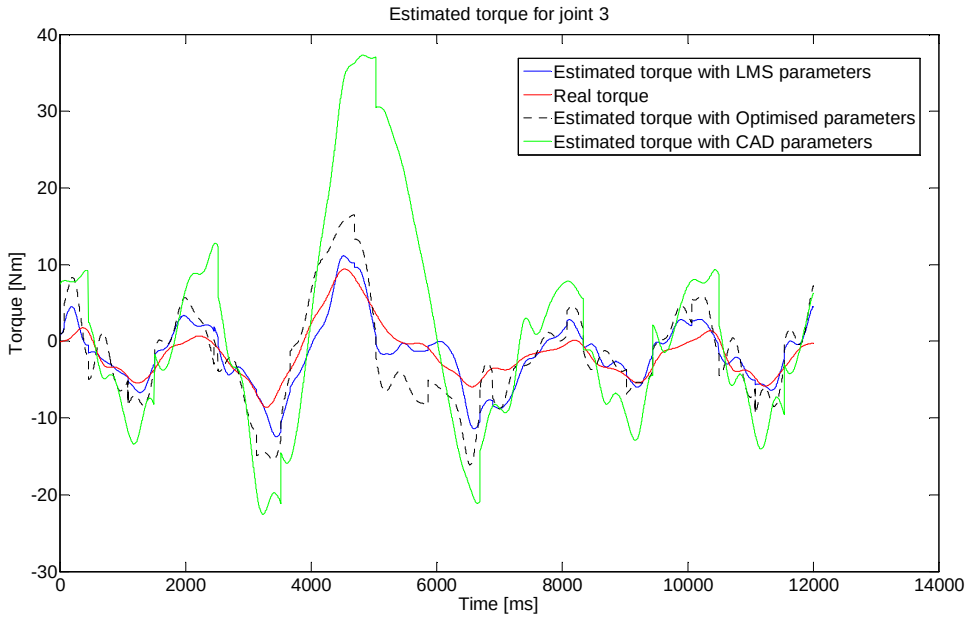

Figure 4-31. Estimated and measured torques for identification trajectories on joint 3. Simultaneous joint excitation with N=5.

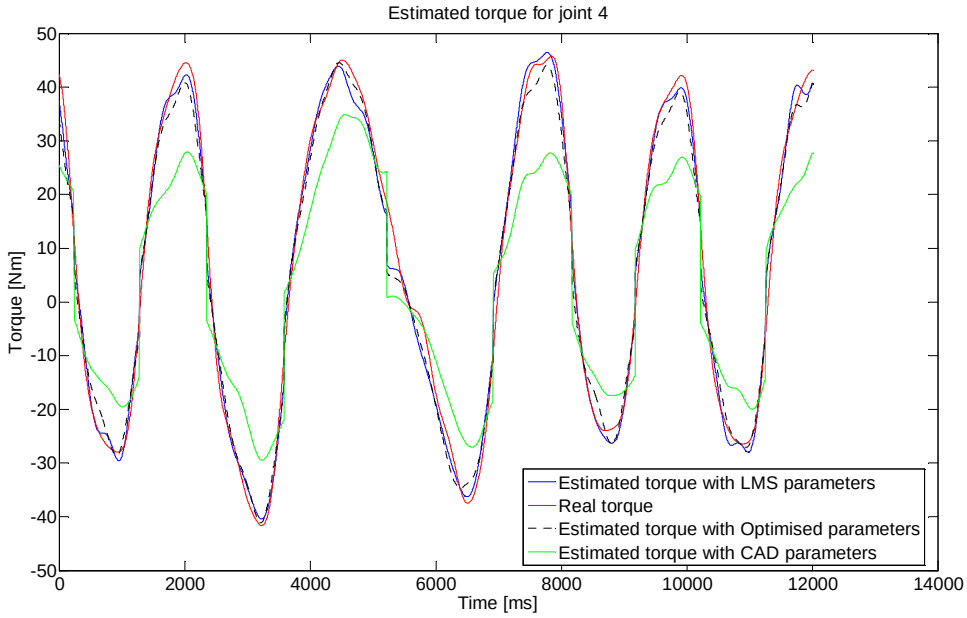

Figure 4-32. Estimated and measured torques for identification trajectories on joint 4. Simultaneous joint excitation with N=5.

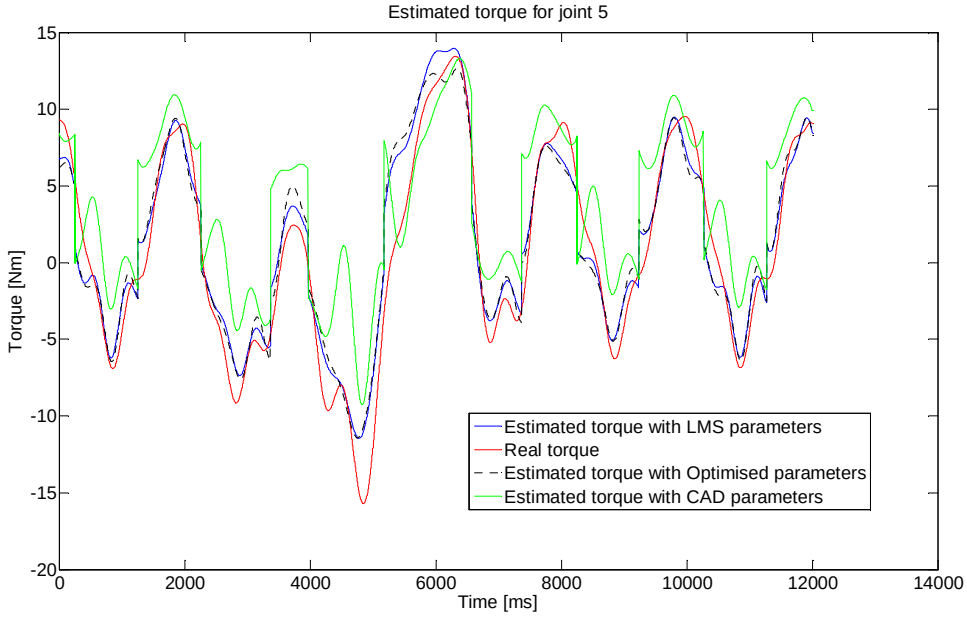

Figure 4-33. Estimated and measured torques for identification trajectories on joint 5. Simultaneous joint excitation with N=5.

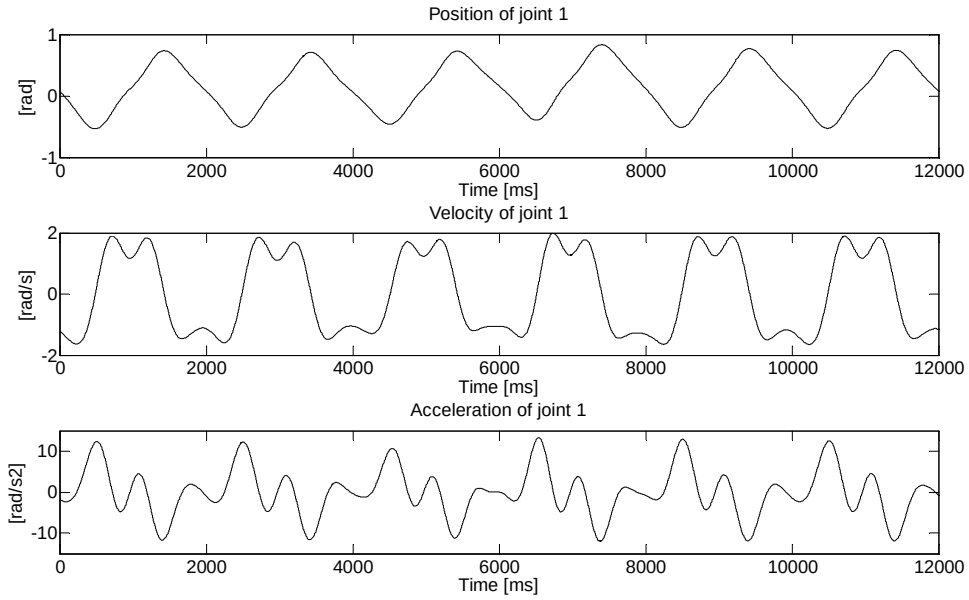

Figure 4-34. Kinematic conditions of joint 1 during the identification trajectory.

4.5.3.4 Comparison of the three optimised set of parameters

For validation purposes the torques involved on the two trajectories used for parameters identification are examined for the three set of optimised parameters that have been found. These are compared and validated against the real torque measured on the hydraulic manipulator.

Trajectory A: Simultaneous excitation with N=1

During this trajectory, displayed in Figure 4-10 the kinematic conditions are displayed below for each joint together with the torque estimation for each set. The RMS errors of each estimation are shown in Table 4-31.

Trajectory	**Sampled points**
Independent excitation	42000
Simultaneous N=1	12000
Simultaneous N=5	12000

Table 4-30. Number of sampled points utilised in each identification trajectory.

For sake of clarity let us denote the three different set of parameters as: N0, N1 and N5 for the independent excitation, simultaneous with N=1 and simultaneous excitation with N=5 respectively. The number of sampling points used during these three trajectories are shown in Table 4-30. The considerably big amount of sampling points of the independent trajectory is justified due to the variety of frequencies included.

During the torque estimation for joint 1, although the set N5 presents the smallest error, the friction effect of the hoses deteriorates the performance of the estimation and leads to unexpected torques.

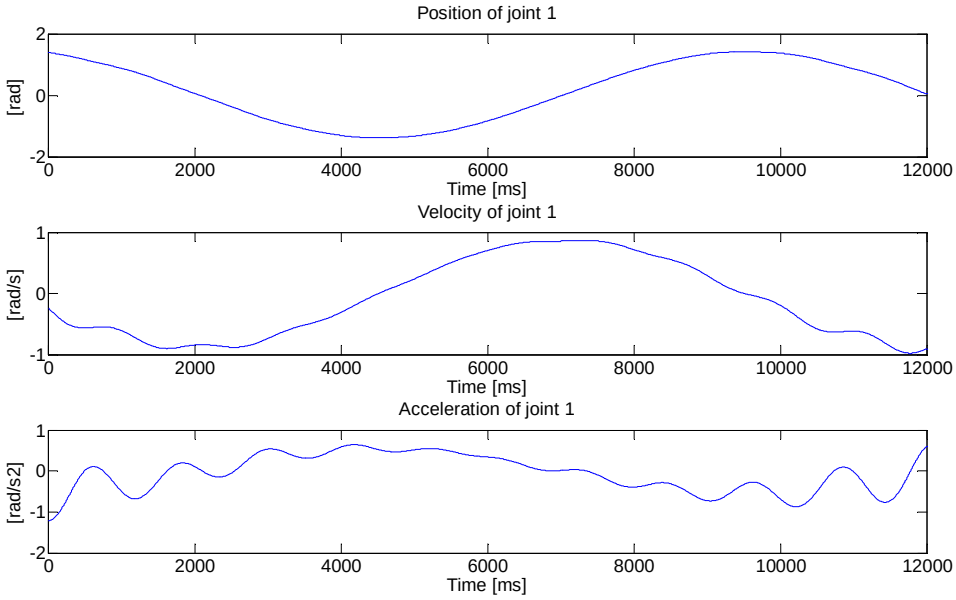

Figure 4-35. Kinematic conditions during trajectory A for joint 1.

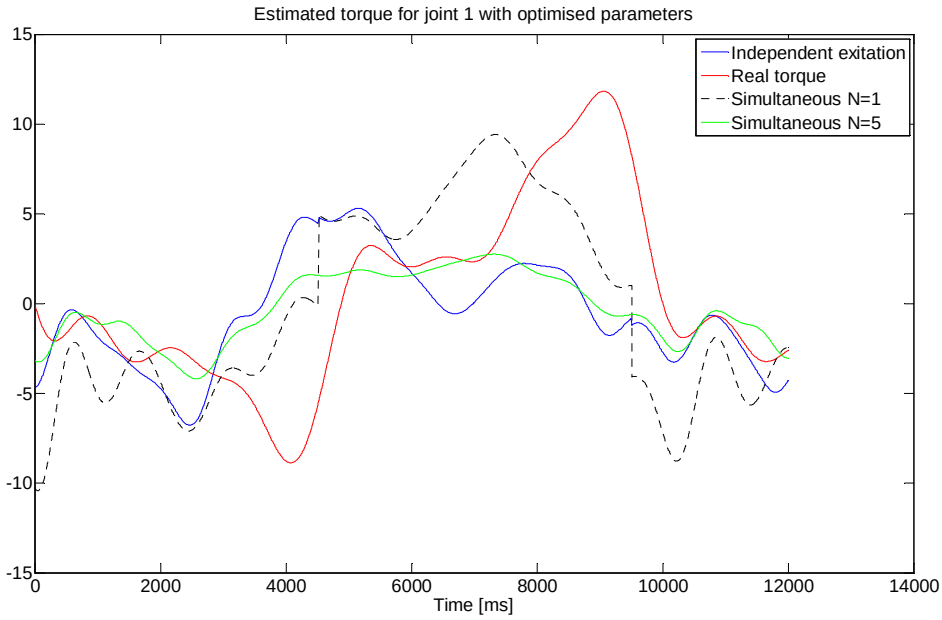

Figure 4-36. Torque estimation for joint 1 during trajectory A.

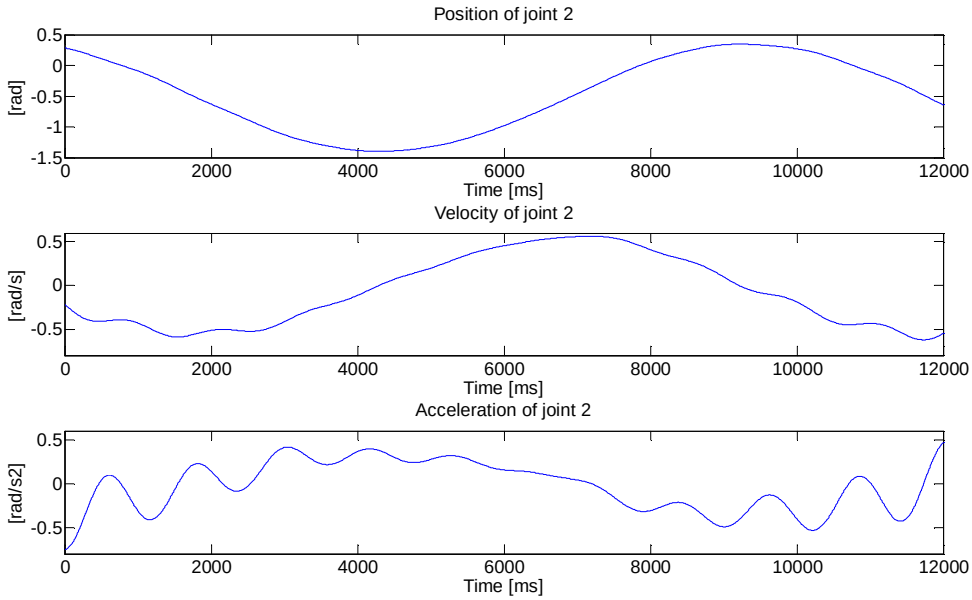

Figure 4-37. Kinematic conditions during trajectory A for joint 2.

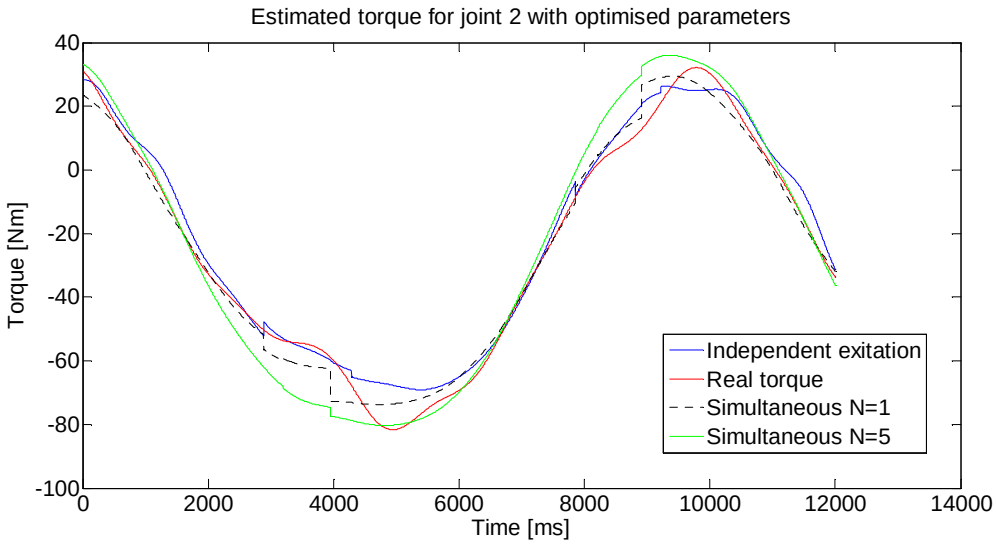

Figure 4-38. Torque estimation for joint 2 during trajectory A.

The predicted torques for joint 2 are displayed in Figure 4-38 showing a good performance for every set of parameters although this time N1 gives the best approximation. It is expected this to happen since N1 has been optimised for this trajectory. Surprisingly the independent excitation behaves better than N5 for this joint. The same effect is observed on joint 3.

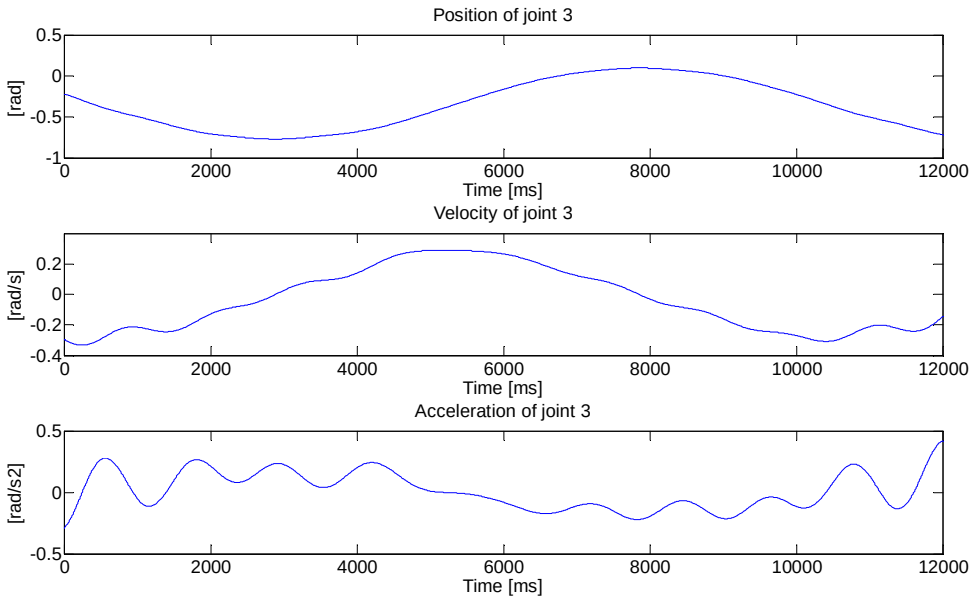

Figure 4-39. Kinematic conditions during trajectory A for joint 3.

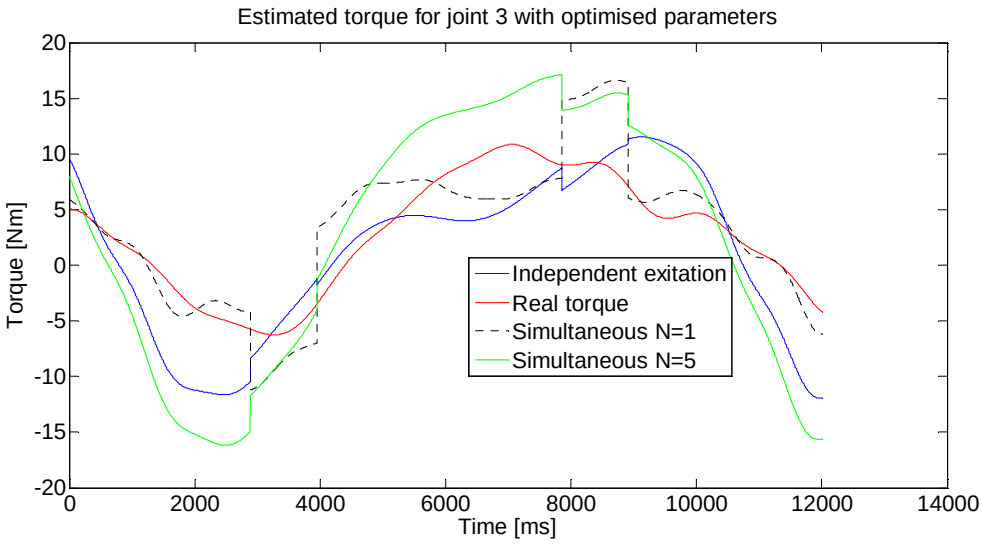

Figure 4-40. Torque estimation for joint 3 during trajectory A.

The estimated torques for joint 4 present a-priori more expected behaviour than in previous joints. The same situation arises for the last joint equipped with force feedback. Finally the average result for every joint given in Table 4-32 proves that the best approximation for trajectory A is the set N1 which was an expected result since this set of parameters was obtained from the same trajectory. One can also see how the parameterised trajectory with ten parameters per joint (N=5) is superior to the independent excitation even when having a big difference on sampling points number.

RMS values of the torque estimation error [Nm]						
	Joint1	**Joint 2**	**Joint 3**	**Joint 4**	**Joint 5**	**Average**
Independent exc.	5.68	4.03	3.67	6.63	5.71	5.14
Simultaneous N=1	3.98	3.49	2.54	1.70	0.78	2.50
Simultaneous N=5	3.02	6.03	5.89	3.88	3.39	4.44

Table 4-31. RMS error [Nm] for the three different set of parameters during trajectory A.

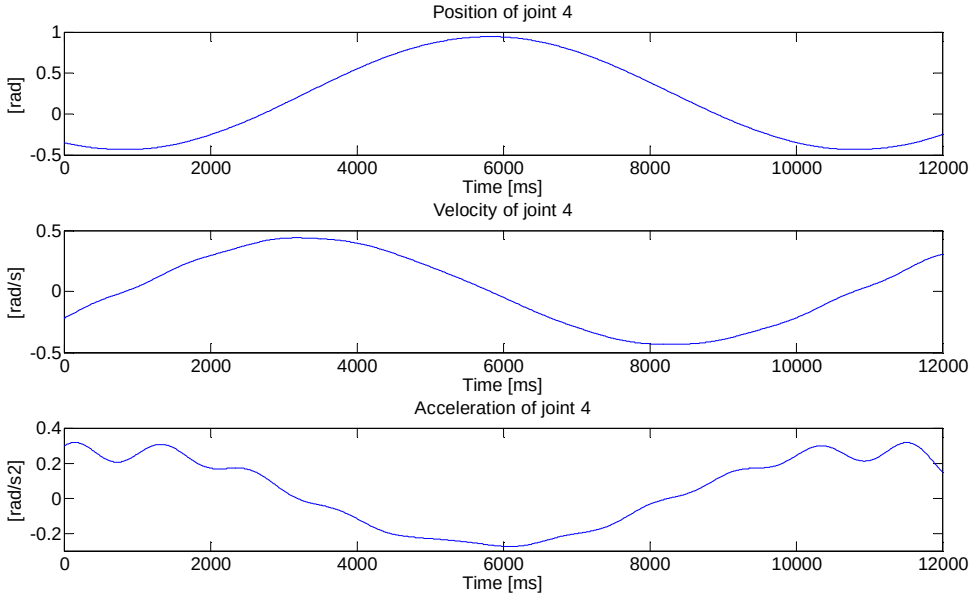

Figure 4-41. Kinematic conditions during trajectory A for joint 4.

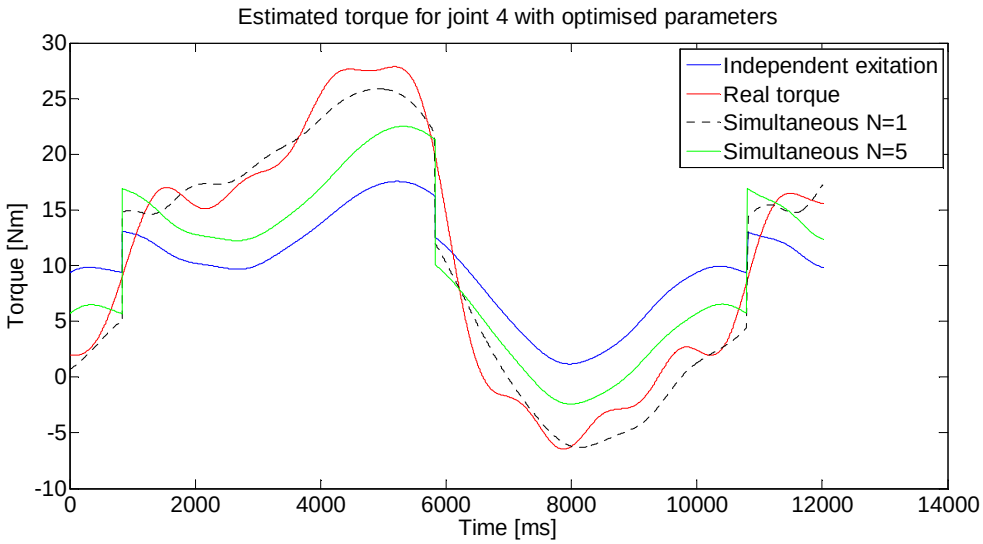

Figure 4-42. Torque estimation for joint 5 during trajectory A.

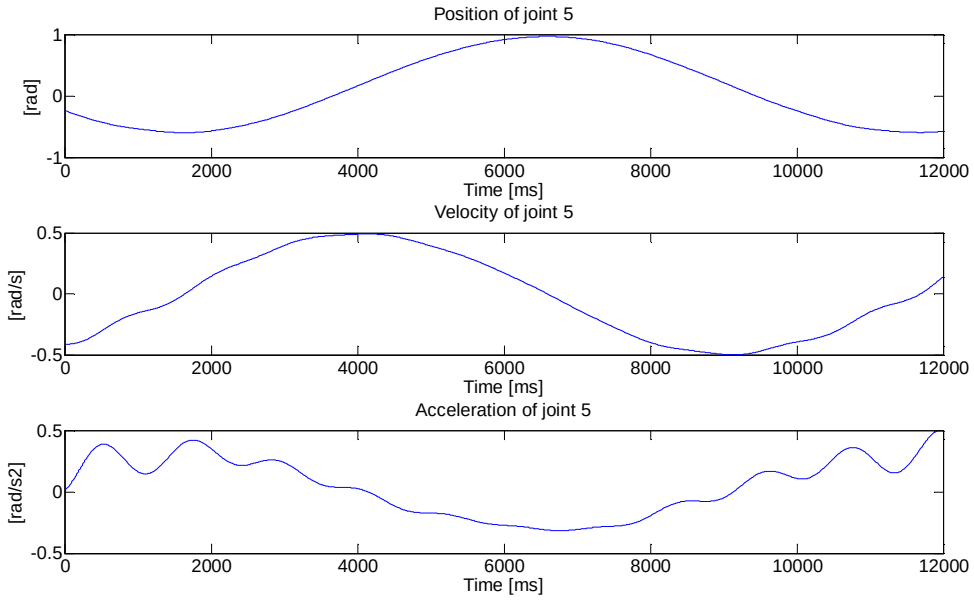

Figure 4-43. Kinematic conditions during trajectory A for joint 5.

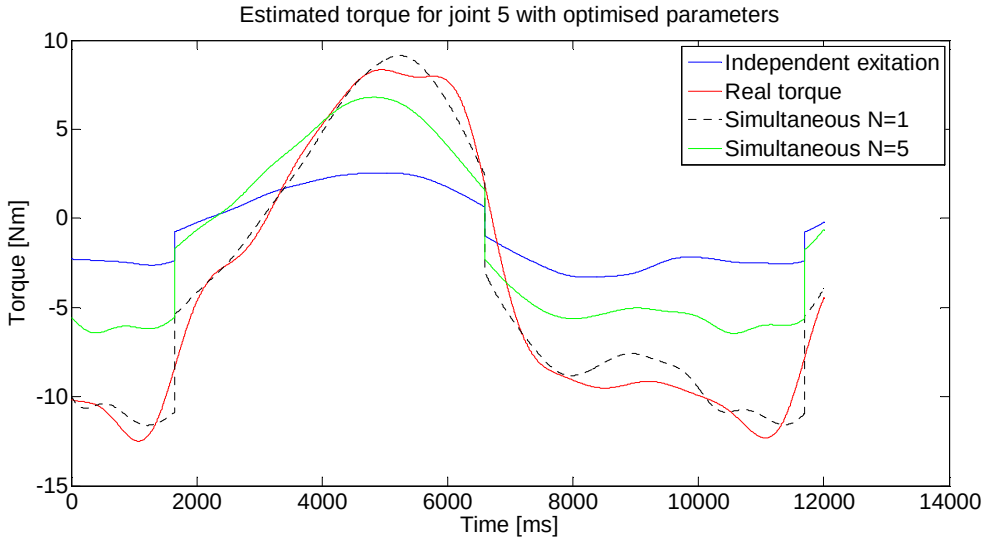

Figure 4-44. Torque estimation for joint 5 during trajectory A.

Trajectory B: Simultaneous excitation with N=5

The trajectory of the end effector in Cartesian space during this trajectory is given in Figure 4-12. It is clear how the speed and accelerations have been increased in this trajectory with respect trajectory A. This produces that the set of parameters estimated using lower frequencies tend to give poorer results. This effect is particularly

exaggerated on the first joint due to the great acceleration of its trajectory and the enormous inertia with respect the first axis.

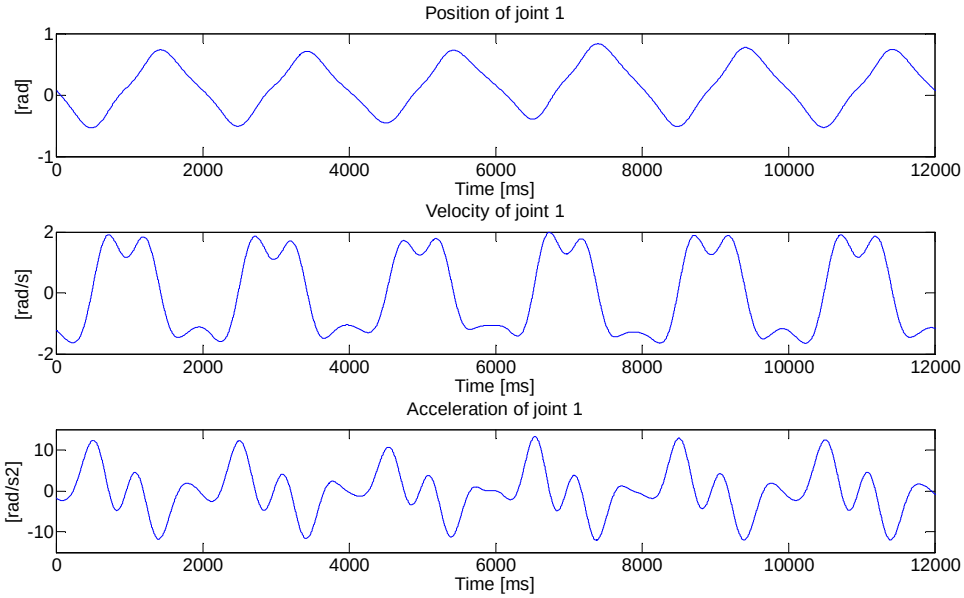

Figure 4-45. Kinematic conditions during trajectory B for joint 1.

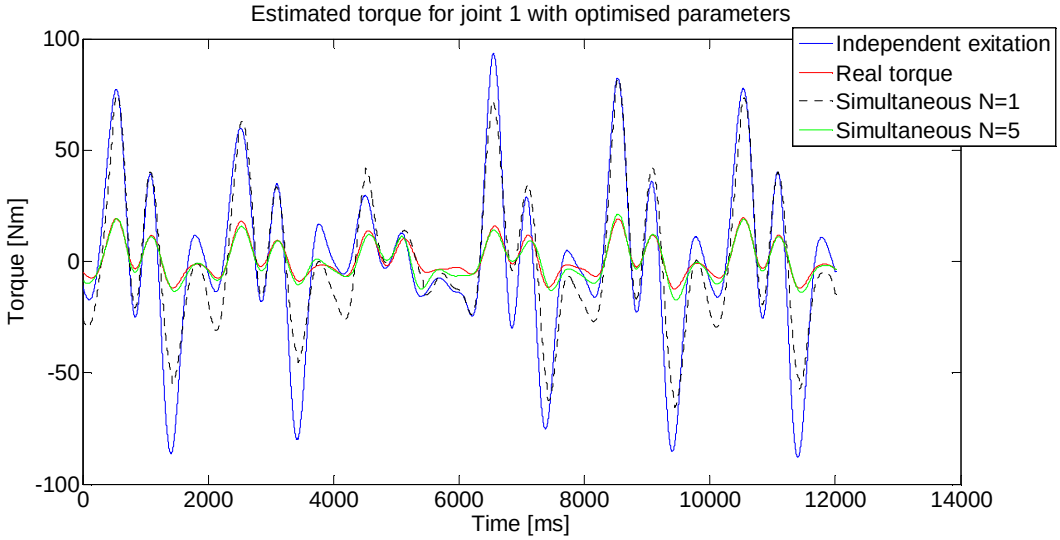

Figure 4-46. Torque estimation for joint 1 during trajectory B.

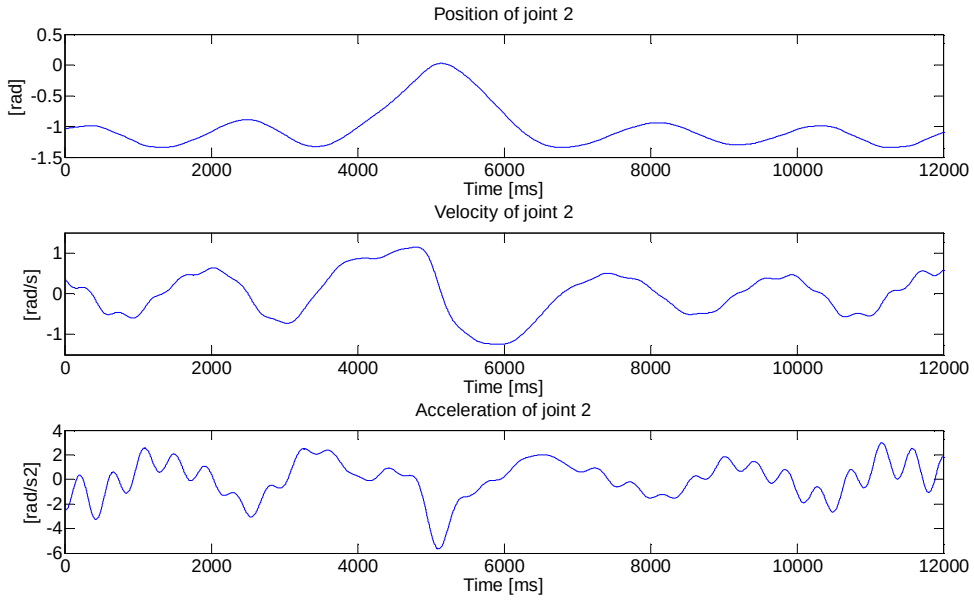

Figure 4-47. Kinematic conditions during trajectory B for joint 2.

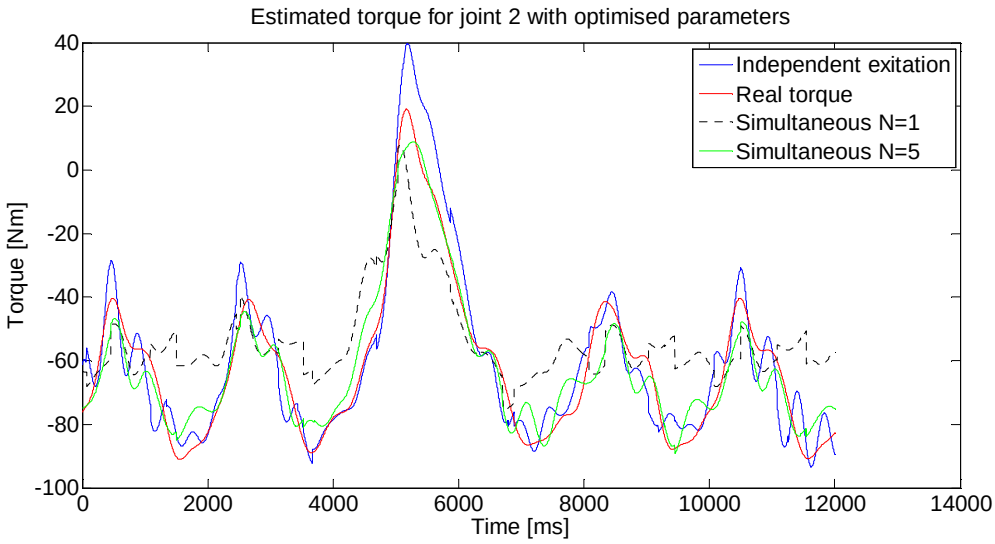

Figure 4-48. Torque estimation for joint 2 during trajectory B.

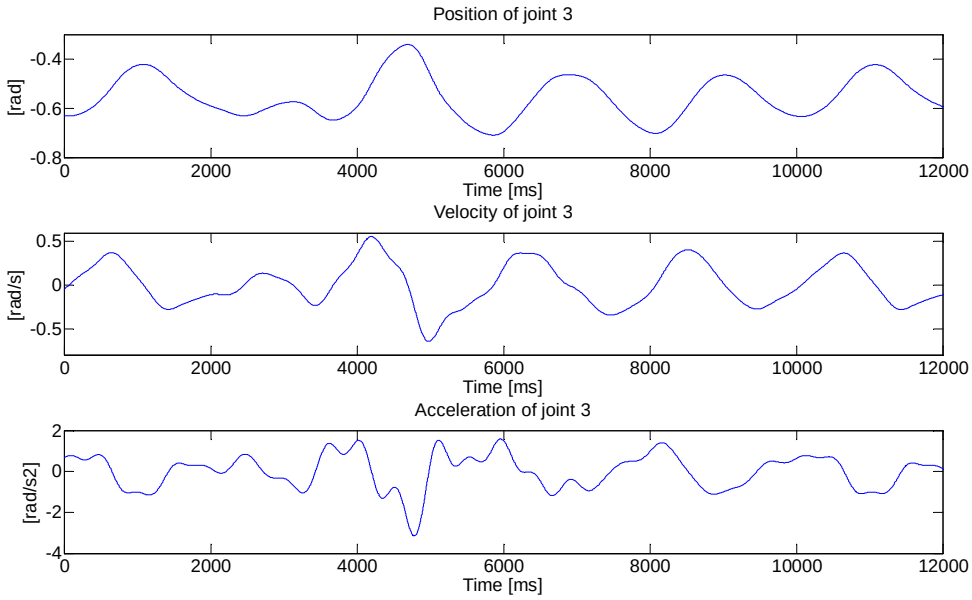

Figure 4-49. Kinematic conditions during trajectory B for joint 3.

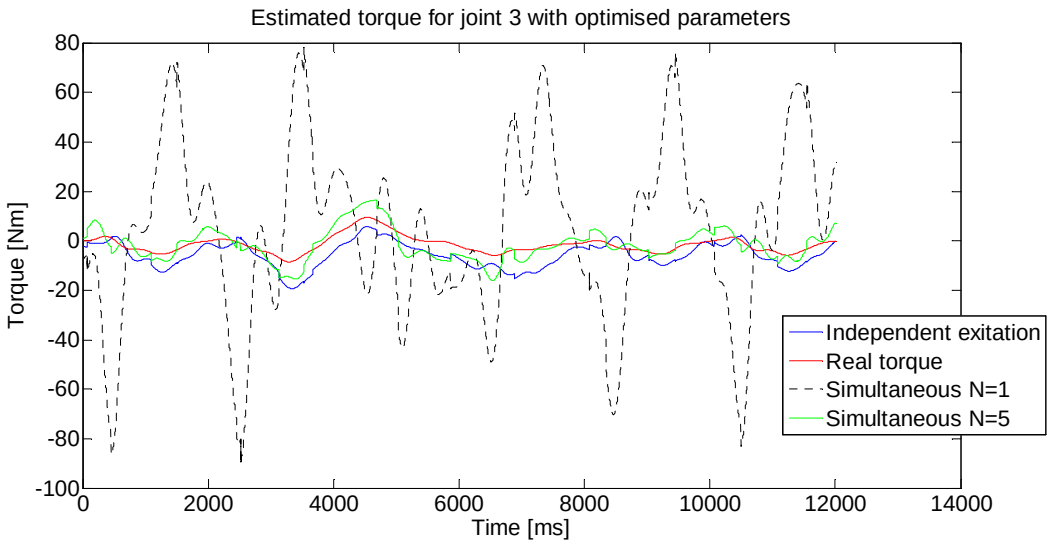

Figure 4-50. Torque estimation for joint 3 during trajectory B.

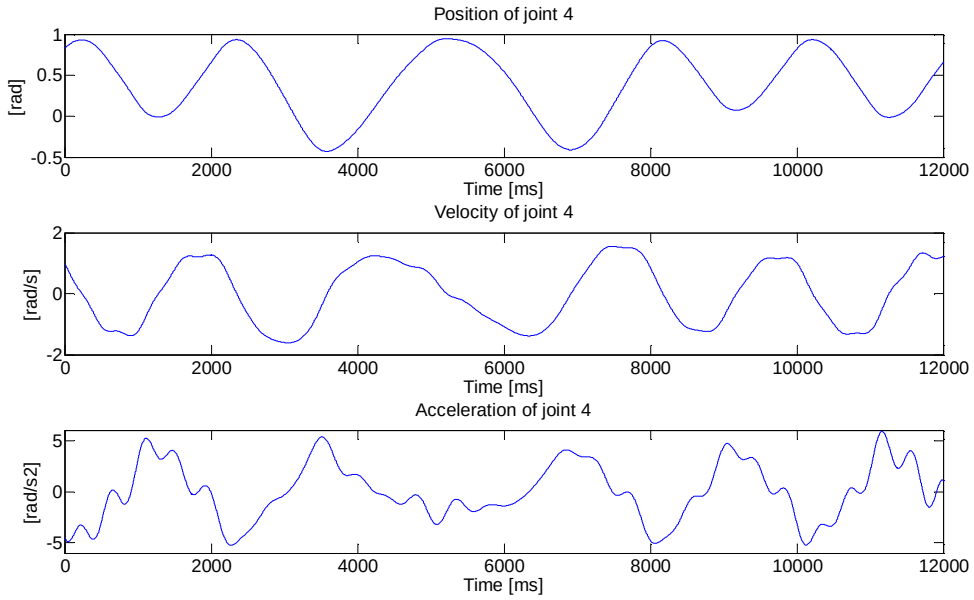

Figure 4-51. Kinematic conditions during trajectory B for joint 4.

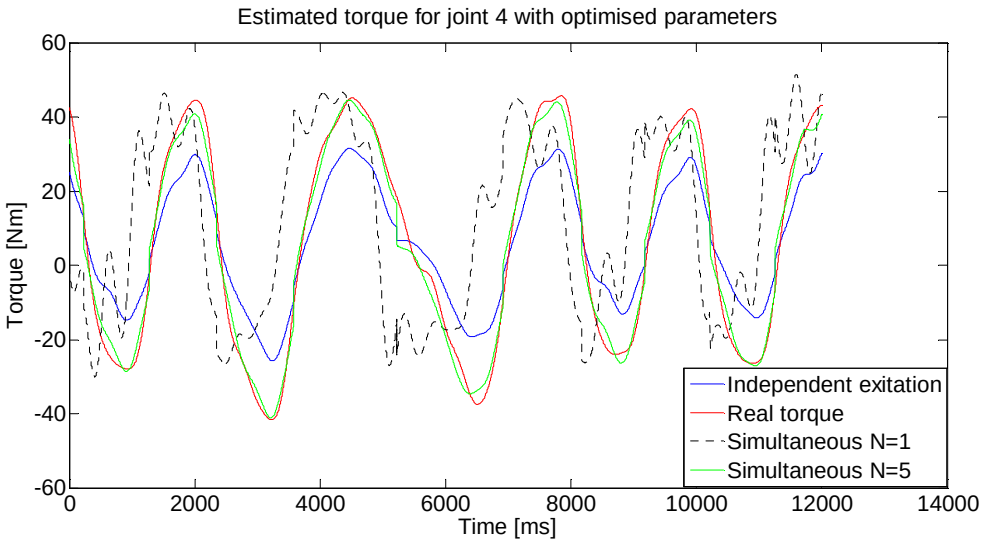

Figure 4-52. Torque estimation for joint 4 during trajectory B.

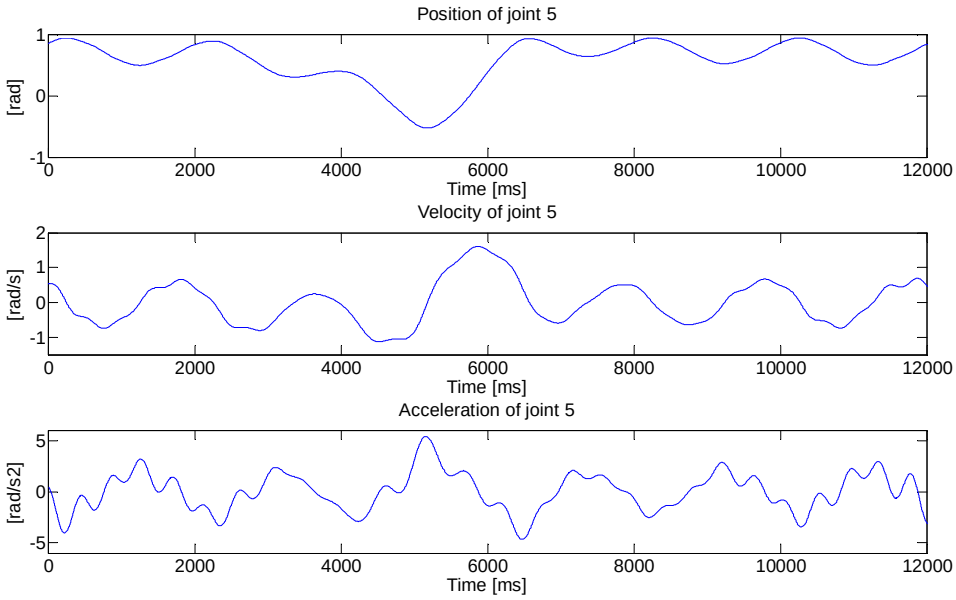

Figure 4-53. Kinematic conditions during trajectory B for joint 5.

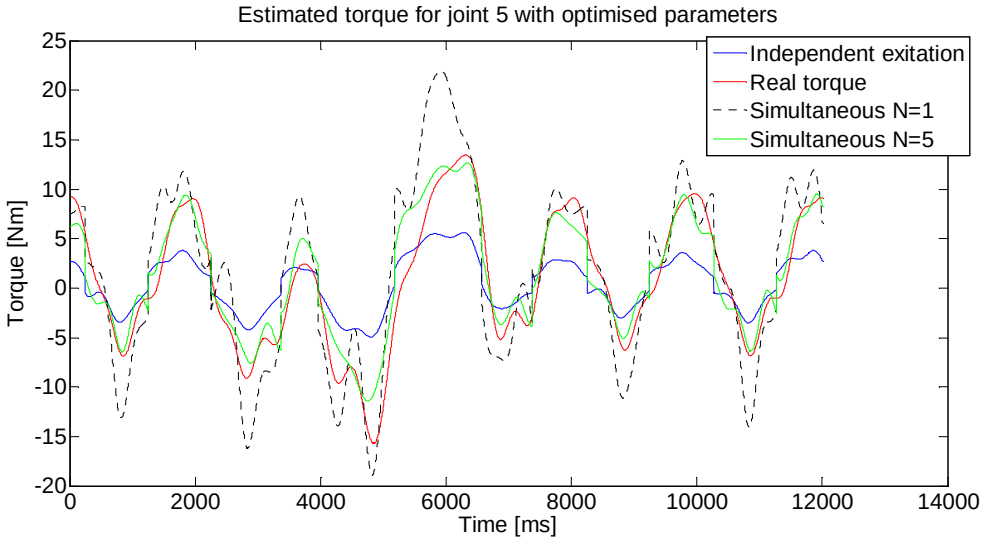

Figure 4-54. Torque estimation for joint 5 during trajectory B.

The predicted torque for the set N5 is substantially better than the others on every joint with an enormous difference with N1 and the independent excitation on second position. This difference is caused by the higher frequencies that come into action during this trajectory which excite the inertial components in a more intense manner. This result proves the postulate given in [115] which mentions that high frequencies lead a good estimation for inertial moments as long as they are not big enough to excite flexible modes of the manipulator. In terms of performance of each method, the

independent trajectory gives better predictions than simultaneous with N1 but is overcome clearly by N5. However once the trajectory optimisation have been carried out, the set of data taken with a simultaneous movement is lighter and easier to analyse. A compromise trajectory which included a small portion of each frequency would be desirable to obtain a more precise identification.

	Joint1	**Joint 2**	**Joint 3**	**Joint 4**	**Joint 5**	**Average**
Independent exc.	21.15	6.614	4.417	11.087	3.530	9.358
Simultaneous N=1	17.963	14.628	29.768	22.493	3.486	17.605
Simultaneous N=5	1.533	5.912	3.271	2.709	1.581	2.98

Table 4-32. RMS error [Nm] for the three different set of parameters during trajectory B.

4.5.4 Effects of implementing centre of mass constraints on the inertia matrix

In this experiment, the constraints highlighted in (4.32) are evaluated, proving the need of applying a set of conditions that locate the centre of gravity inside of a volume that inscribes the link.

An experimental trajectory has been used to evaluate the total torque and inertial torque obtained after simulation of two different set of parameters found beforehand. They are also compared with the real motor torque obtained from the measurements of the differential pressure.

The two different set of parameters tested are termed T5param18 and T5param19 and are shown in Table 4-33 to Table 4-36. In order to obtain the first set, conditions over the centre of gravity have been applied. However, these were eliminated before obtaining the second set of parameters. Both sets have been calculated with an optimisation process via SQP from a previous optimised set used as a seed for the algorithm.

The objective of these tests is thus to show that although two different set of parameters could present similar estimation of the total torque, one of them is giving incorrect inertia values derived from a non-definite positive inertia matrix.

In Figure 4-55 the total torque estimated with the two different set of parameters is shown to check the accuracy of the obtained estimation. As mentioned before, when adding additional constraints to the optimisation process, the prediction tends to worsen slightly.

In order to highlight the problem derived of different parameterisations, the trajectories used to obtain the graphs of Figure 4-55 have been used to compare different torque components. From Figure 4-56 to Figure 4-60, the total estimated torque and inertial torques are shown for the two sets of parameters and the five joints. The inertia torque is scaled by a factor of 10 for a better visualisation. It is important to mention that although the trajectory used for this comparison is the same than in Figure 4-55, the joint's accelerations have been forced to be positive during the estimations from Figure 4-56 to Figure 4-60. This has been done for sake of simplicity to highlight the issue introduced in this section.

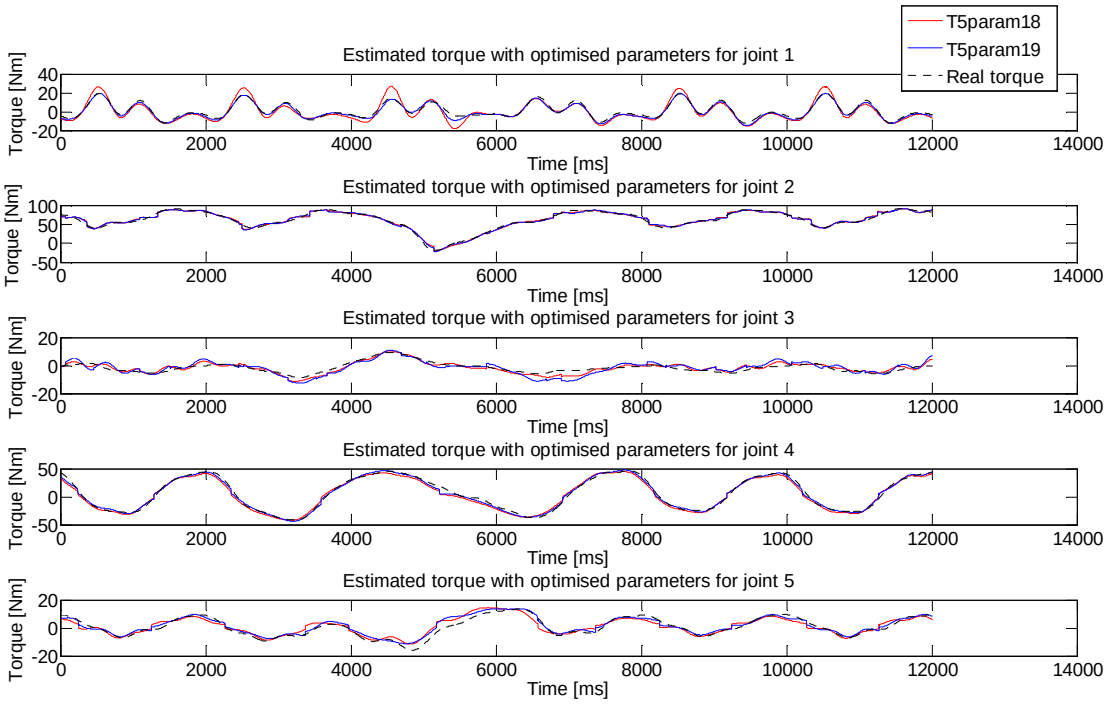

Figure 4-55. Measured torque and estimated torque with two different set of parameters. The set termed T5param18 implements constraints over the centre of gravity during the optimisation process while the set T5param19 does not. Although both estimations seem similar, the main difference lies in the distribution of the torque between the different components, i.e. gravity, inertia and Coriolis.

The total estimated torque is similar for the two different set of parameters for every joint. However it is important to see how this torque is split in its different components, i.e. Inertia, gravity and Coriolis. By applying centre of gravity constraints one achieves

a full physical sense in the set of parameters, which produces a definite positive inertia matrix for every robot configuration and hence positive inertia torque for a given positive acceleration.

The inertia torque for joints 1, 2, and 5 becomes negative at some point of the trajectory for a given positive acceleration during the estimation achieved with T5param19. However this never happens for the set of parameters with full physical sense given by T5param18.

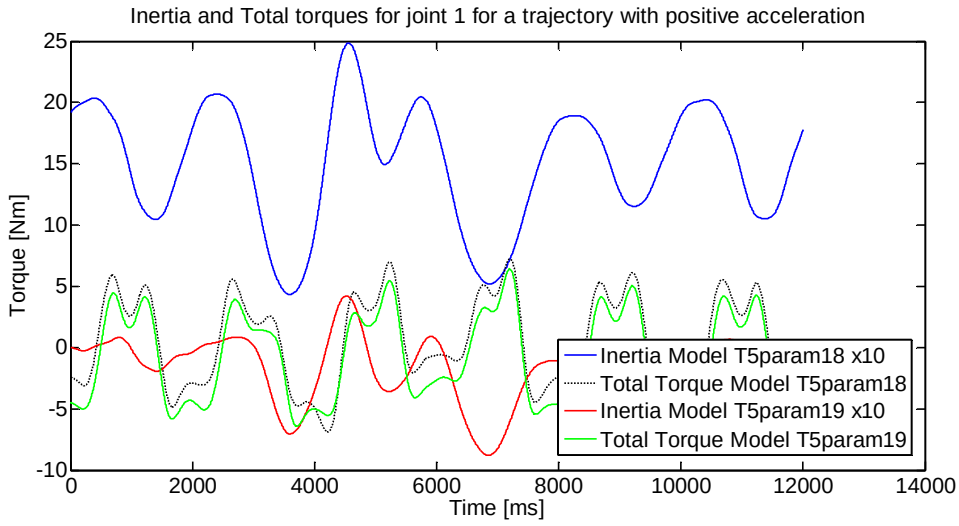

Figure 4-56. First joint's inertia and total torque for two different set of optimised parameters.

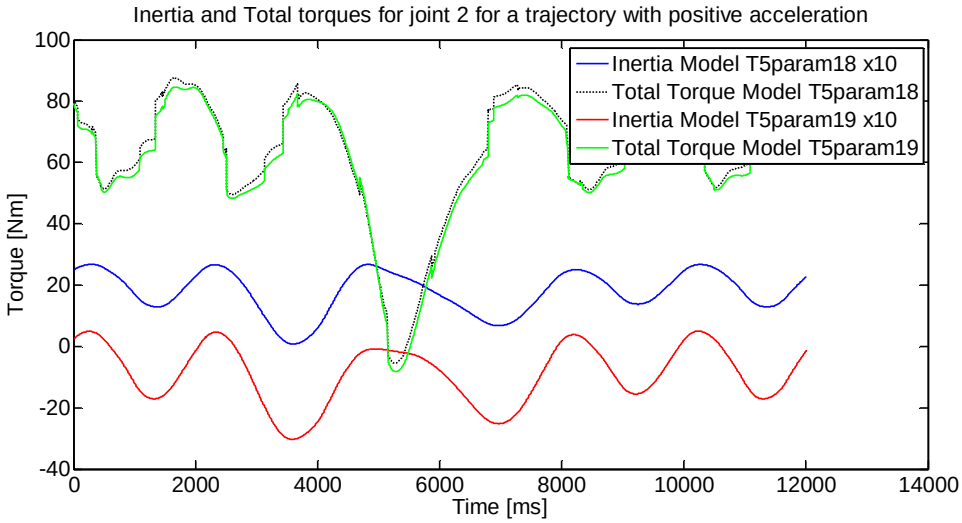

Figure 4-57. Second joint's inertia and total torque for two different set of optimised parameters.

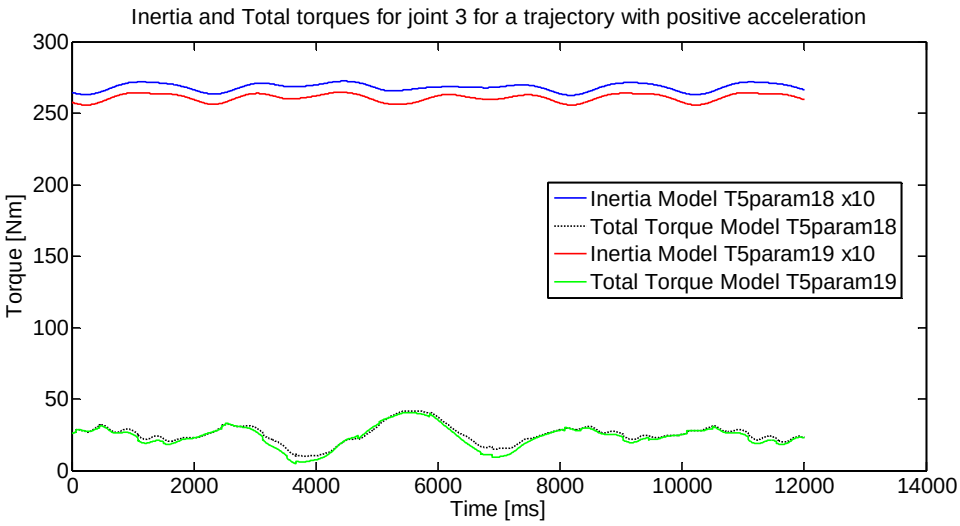

Figure 4-58. Third joint's inertia and total torque for two different set of optimised parameters.

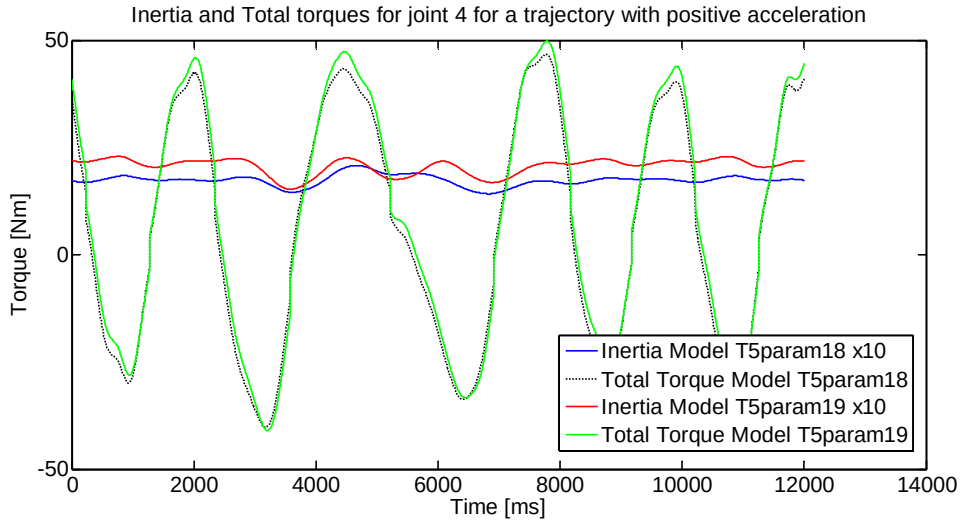

Figure 4-59. Fourth joint's inertia and total torque for two different set of optimised parameters.

In summary, new restrictions have been defined to improve the classical methods found in the literature. They are necessary to ensure a precise model with fully physical sense. The main idea is to limit the position of the optimised centre of mas in a way that this stays inside of the link's volume.

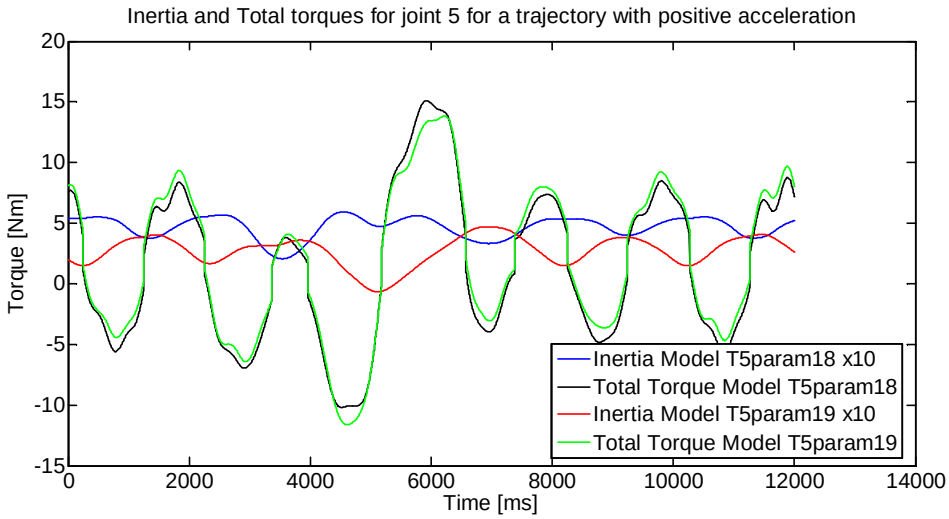

Figure 4-60. Fifth joint's inertia and total torque for two different set of optimised parameters

Parameters	Link 1	Link 2	Link 3	Link 4
$m\ [Kg]$	41.614	13.059	0.500	2.173
$m \cdot c_x\ [Kg \cdot m]$	-0.109	0.367	-0.045	0.535
$m \cdot c_y\ [Kg \cdot m]$	0.002	3.687	-0.068	0.177
$m \cdot c_z\ [Kg \cdot m]$	7.532	-0.066	0.005	0.044
$I_{xx}\ [Kg \cdot m^2]$	11.136	0.101	0.101	0.108
$I_{xy}[Kg \cdot m^2]$	-3.413	-0.001	0.000	0.004
$I_{xz}[Kg \cdot m^2]$	0.000	0.017	-0.093	-0.002
$I_{yy}[Kg \cdot m^2]$	1.907	0.103	0.100	0.102
$I_{yz}[Kg \cdot m^2]$	0.000	-0.033	-0.024	-0.001
$I_{zz}[Kg \cdot m^2]$	0.100	0.498	11.358	0.101
$f_c[Nm]$	0.000	-6.310	0.181	-3.137
$f_v[Nm \cdot s/m]$	-2.829	-2.870	8.223	-23.597

Table 4-33. Set of optimised parameters T5param18. Links 1 to 4.

Parameters	Link 5	Link 6	Link 7	Link 8
$m\ [Kg]$	2.021	0.100	7.000	6.241
$m \cdot c_x\ [Kg \cdot m]$	0.376	0.008	-0.423	-0.469
$m \cdot c_y\ [Kg \cdot m]$	-0.066	-0.005	-2.374	-0.450
$m \cdot c_z\ [Kg \cdot m]$	0.091	-0.001	0.083	0.000
$I_{xx}\ [Kg \cdot m^2]$	0.100	0.100	0.122	0.104
$I_{xy}[Kg \cdot m^2]$	0.000	0.000	-0.006	0.006
$I_{xz}[Kg \cdot m^2]$	0.000	0.000	0.140	-0.042
$I_{yy}[Kg \cdot m^2]$	0.100	0.100	0.102	0.109

$I_{yz}[Kg \cdot m^2]$	0.000	0.000	-0.037	-0.063
$I_{zz}[Kg \cdot m^2]$	0.100	0.100	0.983	0.547
$f_c[Nm]$	-1.387	-0.758	-1.900	1.196
$f_v[Nm \cdot s/m]$	-7.878	0.852	-8.337	9.999

Table 4-34. Set of optimised parameters T5param18. Links 5 to 8.

Parameters	**Link 1**	**Link 2**	**Link 3**	**Link 4**
$m\ [Kg]$	41.614	3.287	0.500	0.300
$m \cdot c_x\ [Kg \cdot m]$	-0.109	-3.847	-1.303	0.891
$m \cdot c_y\ [Kg \cdot m]$	0.002	28.900	5.183	2.866
$m \cdot c_z\ [Kg \cdot m]$	7.532	-0.037	-27.797	7.628
$I_{xx}\ [Kg \cdot m^2]$	1.802	12.300	0.101	0.100
$I_{xy}[Kg \cdot m^2]$	5.237	1.097	-0.001	0.000
$I_{xz}[Kg \cdot m^2]$	0.000	-0.455	-0.102	0.000
$I_{yy}[Kg \cdot m^2]$	16.267	0.199	0.101	0.100
$I_{yz}[Kg \cdot m^2]$	-0.001	-0.045	0.083	0.000
$I_{zz}[Kg \cdot m^2]$	0.100	13.800	12.224	0.100
$f_c[Nm]$	0.000	-5.490	0.676	-3.877
$f_v[Nm \cdot s/m]$	-2.854	-6.742	6.530	-23.028

Table 4-35. Set of optimised parameters T5param19. Links 1 to 4.

Parameters	**Link 5**	**Link 6**	**Link 7**	**Link 8**
$m\ [Kg]$	1.000	0.100	0.100	6.604
$m \cdot c_x\ [Kg \cdot m]$	30.000	0.036	4.022	4.500
$m \cdot c_y\ [Kg \cdot m]$	-0.123	0.026	-22.587	0.462
$m \cdot c_z\ [Kg \cdot m]$	-2.502	-29.403	20.747	0.000
$I_{xx}\ [Kg \cdot m^2]$	0.101	5.397	12.555	0.100
$I_{xy}[Kg \cdot m^2]$	0.091	0.000	1.117	0.000
$I_{xz}[Kg \cdot m^2]$	-0.045	0.048	0.737	0.000
$I_{yy}[Kg \cdot m^2]$	7.347	5.386	0.201	0.100
$I_{yz}[Kg \cdot m^2]$	-0.025	-0.007	0.003	0.000
$I_{zz}[Kg \cdot m^2]$	7.111	0.100	10.888	0.100
$f_c[Nm]$	-1.426	-0.379	-1.966	0.931
$f_v[Nm \cdot s/m]$	-7.718	0.432	-4.391	9.895

Table 4-36. Set of optimised parameters T5param19. Links 5 to 8.

4.6 Discussion

In this chapter it has been extensively reviewed the methods for modelling an industrial robot even in the presence of closed loops in its structure. A systematic approach has been defined, explained and demonstrated with a hydraulic manipulator from KRAFT telerobotics. A very well-defined method have been proposed to identify the parameters that define completely a robot in presence of closed loops. These parameters are the link's masses, inertias, centres of gravity and link's friction.

It has been shown how from a very poor a-priori information of the robot, obtained from a CAD model, it has been possible to develop a sensibly accurate model, with physical sense, that can be used later for different applications, such as: developing model based controllers, observers, force estimation or simulations.

It is important to highlight, that for most applications, the model needs to present physical sense. For example, if using the model for dynamic simulation when the robot accelerations are calculated from motor torques, the inverse of the manipulator's inertia matrix is needed. This computation cannot be done if any link's inertia matrix is not positive definite. Also when implementing dynamic control, the inversion of the manipulator's inertia matrix is typically needed as well. Although an available option could be to use a lambda value big enough to obtain a LMS solution which is not far from the a priori parameters, thus obtaining parameters with physical sense, the estimation error would be big. Also, with larger lambdas the physical sense is not always guaranteed.

Normalised RMS error with standard deviation						
Trajectory	**Parameterisation**	**Joint**				
		1	**2**	**3**	**4**	**5**
A	**Independent**	1.12	0.11	1.28	0.53	0.71
	N=1	0.79	0.10	0.49	0.16	0.11
	N=5	0.60	0.17	1.13	0.36	0.47
B	**Independent**	2.72	0.28	1.29	0.40	0.54
	N=1	2.31	0.62	8.71	0.81	0.53
	N=5	0.20	0.25	0.96	0.10	0.24

Table 4-37. RMS error normalised with the standard deviation of the motor torque for each joint and trajectory for the optimised parameters.

Different methods for driving the inertia matrix to be definite positive have been tested during the development of this research, especially during the work carried out for

next chapter. However, the best solution has been the introduction of the innovative set of constraints added during the optimisation process and given by (4.32). These complements the traditional constraints found in the literature which are only focused on the link's masses and inertias. It has been proved here how the constraints based only on imposing a positive value for the link's mass and a definite positive inertia matrix are not enough. By applying only those constraints, the optimisation could diverge up to a point where each link's centre of gravity is unrealistic. These findings could be considered an important step towards a better identification of the robot's parameters.

Normalised RMS error with standard deviation						
Trajectory	**Parameterisation**	**Joint**				
		1	**2**	**3**	**4**	**5**
A	**Independent**	0.89	0.13	0.86	0.64	0.81
	N=1	0.24	0.05	0.20	0.15	0.11
	N=5	0.56	0.12	0.50	0.30	0.53
B	**Independent**	2.10	0.29	3.31	0.46	0.99
	N=1	2.47	0.38	8.82	0.77	0.55
	N=5	0.13	0.13	0.50	0.08	0.22

Table 4-38. RMS error normalised with the standard deviation of the motor torque for each joint and trajectory for the LMS parameters.

Different trajectories have been tested for parameters identification. By adjusting conveniently the weights in an optimisation function and establishing proper bounds, it has been possible to get an estimator that provides an acceptable value of the motor torques via independent joint excitation. However the residual error decreases when using more elaborate trajectories when all the joints are commanded simultaneously. It has been proved in this chapter the convenience of designing adequate identification trajectories which are capable of excite the inertias without reaching the robot resonant frequency or excitation of flexible modes. A good optimised trajectory that excites the robot parameters conveniently has provided up to six times better performance than a more relaxed trajectory.

Also, it has been validated that the use of a convenient trajectory calculated by adjusting the coefficients of a formula given by (4.23) improves the estimated torque with respect a trajectory made by independent joint excitation. This result is important for future work where a robot model has to be obtained from a real device.

In Table 4-37 a summary of the normalised RMS errors for each joint and trajectory is presented. It is a good table to compare the estimation quality achieved for each

joint depending on the trajectory used for parameters identification. For most cases, the best result is achieved for joint 2 followed by joints 4 or 5 depending on the parameterisation used. The worst results are however achieved for joints 1 and 3, except for the trajectory B and parameterisation N5 where joint 1 presents good behaviour. However in Table 4-38 the same table is given for the LMS parameters were is clearly shown that joints 2 and 4 are always providing the less amount of error. Then, the inconsistencies between both tables proves that the optimisation process sometimes worsen the behaviour of these links in favour of others.

Percentage of joint's range coverage during excitation trajectory					
	Joint				
	1	**2**	**3**	**4**	**5**
Trajectory A	87.91	83.98	40.00	81.03	86.07
Trajectory B	43.16	66.01	17.03	80.93	80.85

Table 4-39. Percentage of joint's range coverage during excitation trajectory.

The greater error for joint 1 has been found to be affected by the effect of irregular friction caused by the hose movement which is less for N=5 due to the less coverage of the first joint, as given by the trajectories graphs. However, increasing the excitation frequency improves the estimation for this joint. The case of joint 3 is explained due to the small joint range covered during the excitation trajectories to maintain all the joints inside their range. This small coverage affects the reliability of estimation. Indeed, by comparing joint 3 in Table 4-38 one can compare estimations N1 and N5 in its own trajectories which are A and B respectively, how the error on joint 3 is inferior for the trajectory with more coverage (A). In Table 4-39 the percentage of each joint's coverage is given during excitation trajectories. This serves to explain why joint 3 tends to provide with less accurate estimation than others.

Also, for the estimation of joint torque in joint 1 and 3 is where the a-priori model is given the worst results and this is affecting the next steps of the identification procedure. It is important to achieve a homogeneous quality on the excitation with the same harmonic strength on every joint in order to obtain balanced joints' torque estimation errors. Also the fact that each parameter set presents much better performance on its own trajectory, although expected, suggests that more effort has to be put on defining a more complete trajectory.

On summary, care must be put on defining the excitation trajectories for identification purposes. These must excite a wide range of frequencies without affecting the robot nonlinearities and cover the maximum joint range as possible. This chapter introduces

an innovative cost function as described in (4.36). With this new approach, that includes the joint's range into the cost function, an improvement on the estimation is achieved with respect previous modelling techniques. Also, with the introduction of the new type of constraints given by equation (4.32) the physical meaning of the model is now guaranteed.

Chapter 5 Estimation of external forces for robots

In previous chapters, it has been discussed means to cope with the kinematic dissimilarity in teleoperation and the need of creating a dynamic model of the slave. However nothing has been said in relation to force estimation apart from employing the robotics dynamics equation. In this chapter, different options for force estimation found in the literature are analysed and tested. The sliding observer, a well-known method for controlling nonlinear systems has been adapted here to be used in force estimation for teleoperation, considering its particular constraints. The advantages of this new approach are extensively explained in this chapter and an analysis of the convergence is provided.

5.1 Introduction

In the literature, all teleoperation designs which involve industrial robots and most of bilateral operations where a backdrivable manipulator is used, employ force/torque sensors for measuring external forces/torques. These devices are typically attached to the robot's end-effector which implies that only external forces on that end can be measured. It has been shown in chapter 2 the advantages and disadvantages of using this type of devices. The need of additional wiring, its fragility under radiation and their high cost are the main drawbacks of these sensors. However, their proven accuracy has shown that they can be applied for teleoperation.

When performing remote handling in a radioactive environment, the use of electronic devices is forbidden due to its susceptibility to radiation and the criticality of the equipment failure. Therefore, a different research approach has been taken to estimate the forces and torques acting on a manipulator by employing a variety of methods, most of them using a type of dynamic model of the manipulator.

In this chapter, a review of the main methods for force estimation is carried out, starting from evaluating the robotics dynamics equation. A set of experiments accomplished by means of a hydraulic manipulator is shown, highlighting the benefits and drawbacks of such approach.

Later, a Luenberger observer of a robot, based on the observer presented by S. Nicosia and P. Tomei in [79] which was adapted by P. J. Hacksel and S. E. Salcudean [80] for force estimation, has been designed and tested for estimating forces and compared with the basic approach mentioned before. This method is considered one of the main approaches for force estimation so far and presents clear advantages over the evaluation of the robot dynamics equation.

However, these results have been overtaken with what it is one the most important contributions of this thesis, the adaptation of sliding observers for force estimation in teleoperation. This scenario lead the research to the search of force estimators with zero offset in absence of external forces in a way that the human operator does not receive unnecessary stimuli that could lead in tiredness and lack of concentration. Also, during a remote handling operation with high payloads it is not crucial to perceive the forces with a high accuracy, since the operation usually can be carried out with an approximate force value. Another requirement that guides this research is the need of minimum delay which is an essential for most of teleoperation tasks to avoid instability issues. With these criteria in mind, a Luenberger-Sliding observer is designed to create a robust estimator of the external forces which is able to estimate forces with minimum

offset. Its properties and convergence are explained. A complete set of experiments are presented here to prove the suitability of this observer to be used as an estimator. Also, comparative results are shown, proving the improvement achieved.

5.2 Evaluation of the forward dynamics equation

As the forces and torques applied on the master device are proportional to those applied to the slave in bilateral control using force channel, the estimation of the robot end effector torques in a sensorless system is crucial. In this section, to obtain the force information from the disturbance signal, the external torques are estimated by using the robot dynamic equation (4.1) modified to take into account the external effect.

$$\tau_m = H(q)\ddot{q} + C(q,\dot{q})\dot{q} + \tau_g(q) + \tau_f(\dot{q}) + \tau_{ext} \tag{5.1}$$

Where,

τ_m: vector of motor torques exerted in each joint.
$H(q)$ is the robot inertia matrix, which is a function of the joints' values.
$C(q,\dot{q})$: are the Coriolis and centripetal forces vector, which also depends on the joints' values and velocities.
τ_g: is the gravity forces vector depending on the robot position.
τ_f: is the friction torques vector. In general terms, it also dependent on the joints velocities.
τ_{ext}: is the vector of external torques on each joint.

The external forces can be estimated by applying the kinematic information contained in the robot jacobian and obtaining (5.2).

$$T_{ext} = J^{T^{\dagger}}(\tau_m - H(q)\cdot\ddot{q} + C(q,\dot{q})\dot{q} + \tau_g(q) + \tau_f(\dot{q})) \tag{5.2}$$

where,

T_{ext}: is the vector of forces and torques ejected in the robot end effector and expressed in the base coordinates system.
J: is the robot jacobian with $\dagger$ denoting the matrix inverse or pseudo-inverse when corresponds.

In chapter 4, the inertial parameters have been identified, the model has been built and experimental validation tests were designed. The validation process has been done

offline by gathering real data and comparing the actuator torques with the predicted ones.

When a force estimation is needed in online mode, i.e. for teleoperation purposes, a real time estimation of the speed and acceleration should be accomplished. When a tachometer is available on the robot there is no need of differentiation of the position measurements, however this is not the case of most of manipulators, and velocity and acceleration have to be obtained from position measurements. Also, generator type tachometers and encoder based velocity measurement electronics often provide unsatisfactory outputs at very slow velocities due to noise and low resolution [132] and are not compatible with radioactive environments.

It has been explained before that a recommended sampling time of 1 kHz should be used for teleoperation when requiring force feedback. Therefore any method implemented for obtaining the velocity data should not introduce a delay superior than 1 ms.

The simplest velocity estimation method is the Euler approximation that takes the difference of two sampling positions divided by the sampling period. Typically the position measurements are taken with encoders or resolvers which contain stochastic errors which result in enormous noise during the velocity estimation by the Euler approximation when the sampling period is small and the velocity low [132]. Different alternatives have been tried which utilise more backwards steps to reduce the noise but introducing a small delay. In [133] a first order adaptive method is shown which is able to vary the backward steps depending on the speed. Also, in [134] it has been found that 3 steps is the best for a sampling rate of 2500 Hz in their experiments with an encoder of 655360 pulses per revolution. They also implemented a Kalman observer and nonlinear observers, obtaining the same results than an averaging of the Euler formula. In [135] a Kalman filter is tested assuming a normal distribution of the position error. In [132] a dynamic method which varies the samples used for averaging depending on the speed is developed with very good results.

For example, given a desired relative accuracy (r_j) of the velocity calculation, with encoder measurements by the formula (5.3) taken from [132], it is possible to derive the required amount of time for obtaining a velocity measurement. This is assuming that the velocity is not calculated with two consecutive samples, but with two samples separated by a certain number of backwards steps j in order to increase the velocity resolution. For an incremental encoder with a resolution R, if the position $q(t)$ is sampled with a sampling period T, and for $k = 1, 2, ...$, the discrete sampled position at time kT is given by $\theta(k)$. The relative accuracy is given by (5.3).

$$r_j = \left|\frac{\hat{v}_j - v_j}{\hat{v}_j}\right| < \left|\frac{2R}{\theta(k)-\theta(k-j)}\right| = \left|\frac{1}{\theta(k)-\theta(k-j)}\right| 2R = 2/s_j \tag{5.3}$$

Where v_j is the real velocity and $\hat{v}_j$ is the estimated with the measurements. For example, in order to obtain a relative accuracy of $r_j = 2\%$, $s_j = 100$, i.e. 100 past pulses have to be traced back on the velocity calculation. If this is wanted to be achieved with an encoder of 10.000 lines/rev, the elapsed angular space for 100 pulses would result to be: 3.6 °. With a motor running at 1 rev/s, the required amount of time for completing that angular slot is 10 ms. This amount of delay is detrimental for a good bilateral performance.

The scheme used in this research for obtaining the smoothed position, velocity and acceleration makes use of a Savitzky-Golay filter due to its good properties for smooth differentiation. A conventional low-pass filter can be utilised for smoothing the torque data since no differentiation is needed.

5.3 Force estimation results of a hydraulic manipulator by direct evaluation of the dynamics equation

To verify the proposed method, the identification procedure described in chapter 4 was implemented in the described robot on the first 5 dof and an action against the external environment was accomplished to reproduce the real efforts performed by the robot during a remote handling operation [15]. An offline force estimation of this experiment has been performed imitating the methods that would be used during teleoperation.

The experimental setup was composed by the following elements:

- 1 x KRAFT GRIPS hydraulic telemanipulator.
- 1 x NI-PXIe-8108 Real Time controller.
- 1 x PC running Labview 2011, © National Instruments, interfacing with the PXI.
- 1 x Force/Torque sensor, ATI, Gamma SI-130-10.
- 1 x Resilient interface with an elastic constant of 5000[N/m].
- 1 x Friction foam with a thickness of 100 mm.

The elastic interface was attached on the robot end-effector with an ATI force sensor between them in order to verify the effectiveness of the proposed approach (See Figure 5-2). Initially the robot was commanded to a pose with the end effector approximately perpendicular to the horizontal plane. An up-down movement was accomplished compressing the elastic interface by commanding joint 2, while the PID controllers of each joint maintained the other joints' positions.

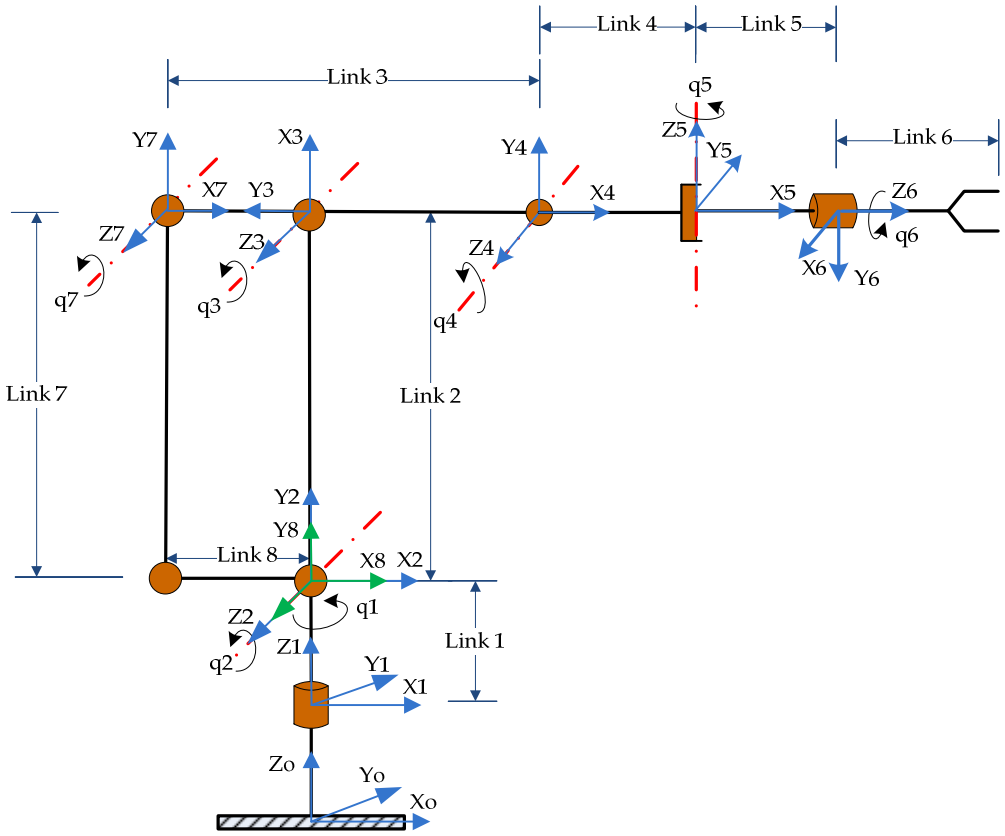

Figure 5-1. Reference system used for the identification of the manipulator's dynamics.

Figure 5-3 to Figure 5-8 present the result of the proposed method comparing the estimated torque for the given dynamics with the real torque exerted on the actuators. The external torque has been calculated by subtracting the estimated torque from the measured one.

During the compression effort, the model only estimates the dynamics given by the movement accomplished by the robot, this is, the inner torque, ignoring the existence of external elements. However the measured torque takes into account the real effort exerted by the joints which considers the addition of external forces and torques plus the torques required for moving the robot. During this test, the main effort was realized by joints 2, 3 and 4 while the non-zero torque in 1 is explained due to the non-totally perpendicular pose of the end effector during the compression effort, which is producing a tangential force on the contact point supported mainly by this joint.

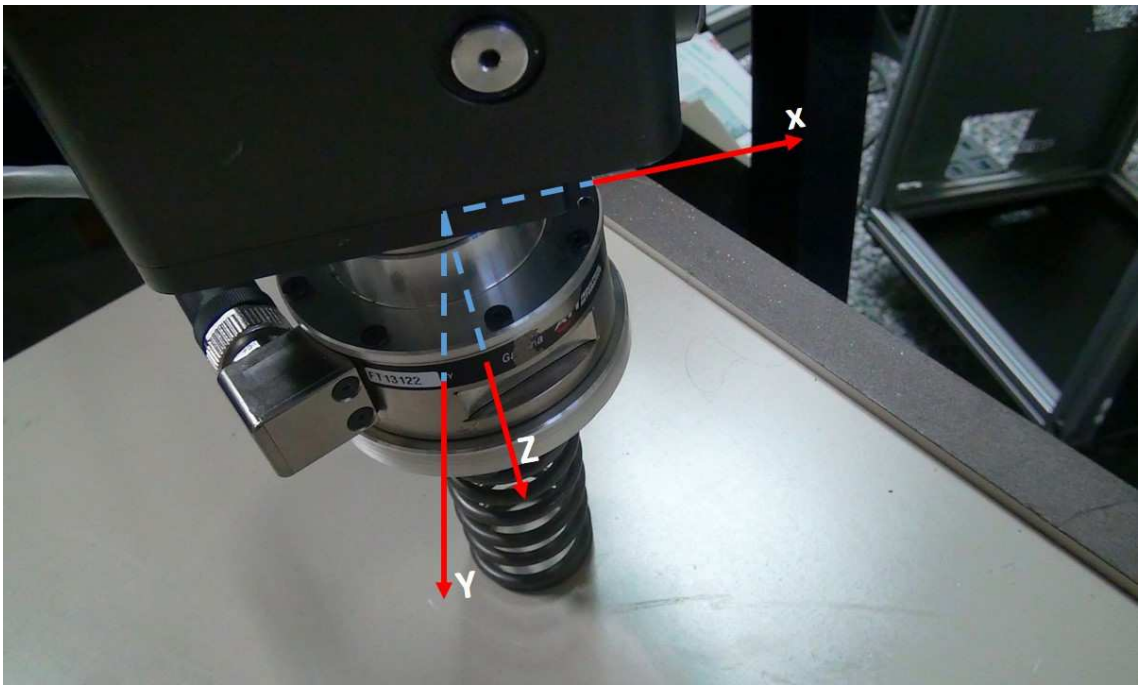

Figure 5-2. Robot's end-effector reference system equipped with the ATI torque sensor and the elastic interface.

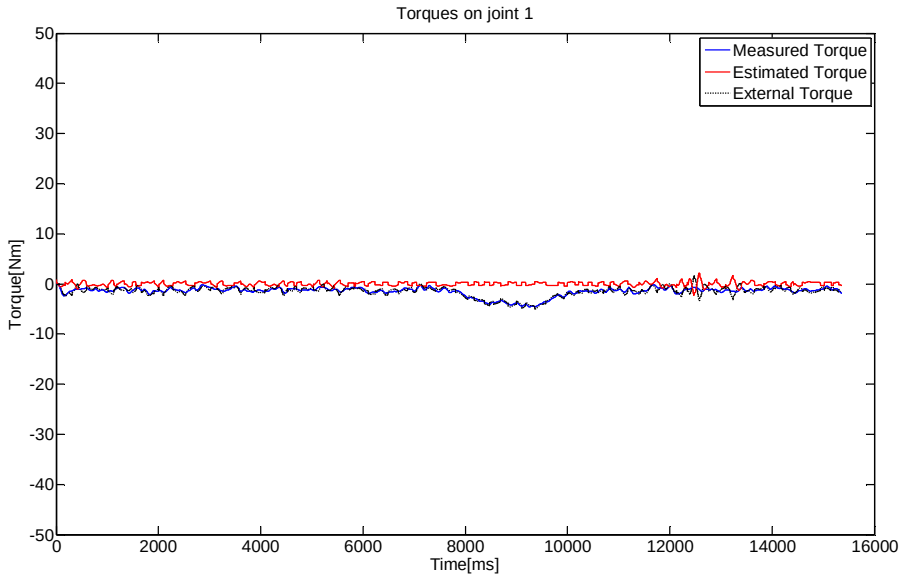

Figure 5-3. Measured, estimated and external torque on joint 1 during the compression of an elastic interface.

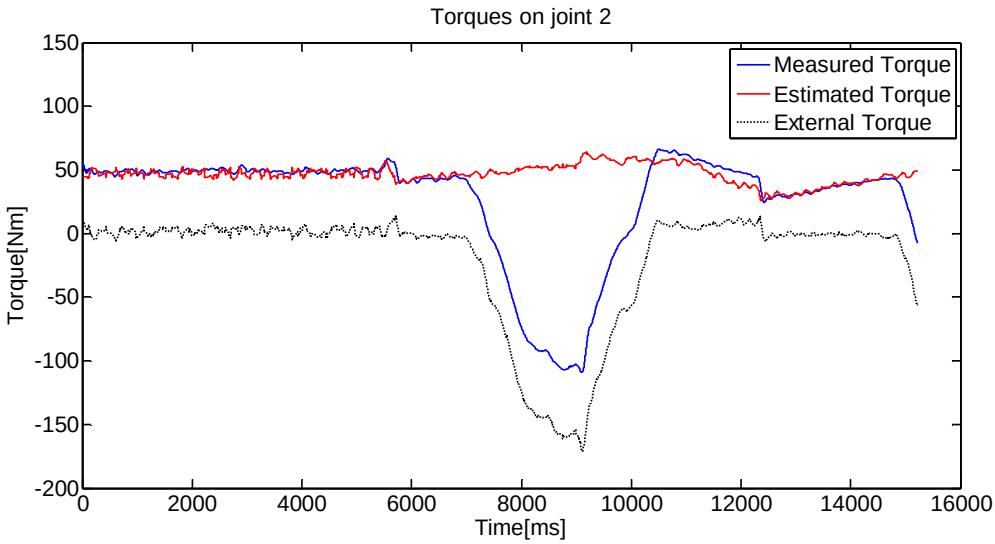

Figure 5-4. Measured, estimated and external torque on joint 2 during the compression of an elastic interface.

The good results achieved for predicted torques of the manipulator's joints conducted the research towards a further validation against the measurements provided via force sensor Figure 5-8 shows the vector sum of end-effector forces along x, y and z as indicated in Figure 5-2. So far the comparison of estimated and measured torques has been influenced by the values of the torque constant which have been characterised at the beginning of Chapter 4. If those values were inaccurate this would lead into force offsets. However, as explained before, for teleoperation purposes it is more crucial to have a fast response time without delays and minimum offset in absence of forces rather than a precise estimation of the force magnitude.

The study of the results presented in previous graphs reveals that torque estimation for some of the joints and the forces on the end effector tend to present an offset that could lead to a feedback of inexistent forces to the operator. Although an initial calibration of torques in a known pose with no external forces will ease this issue, it would not disappear completely. The main causes of this divergences are the error on the estimation of parameters and modelling inaccuracies.

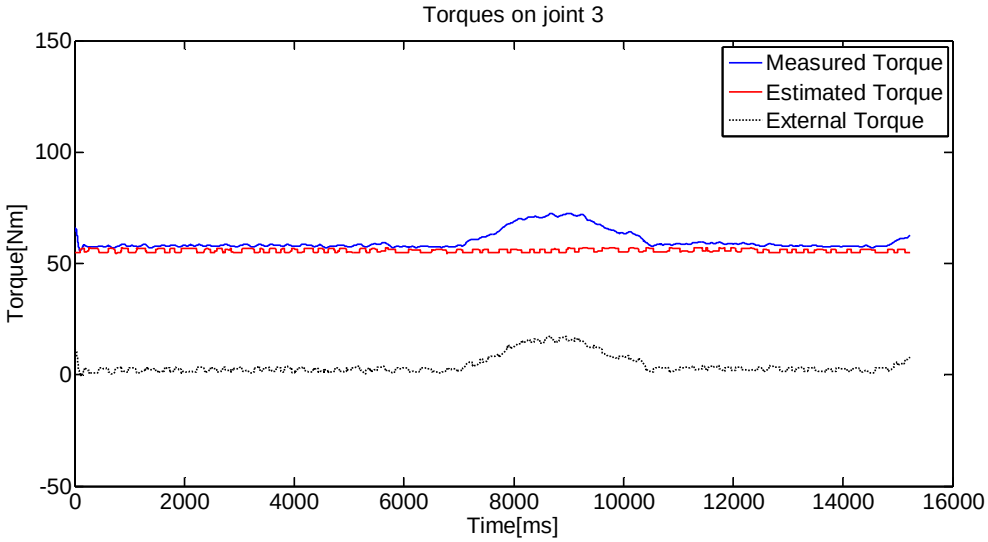

Figure 5-5. Measured, estimated and external torque on joint 3 during the compression of an elastic interface.

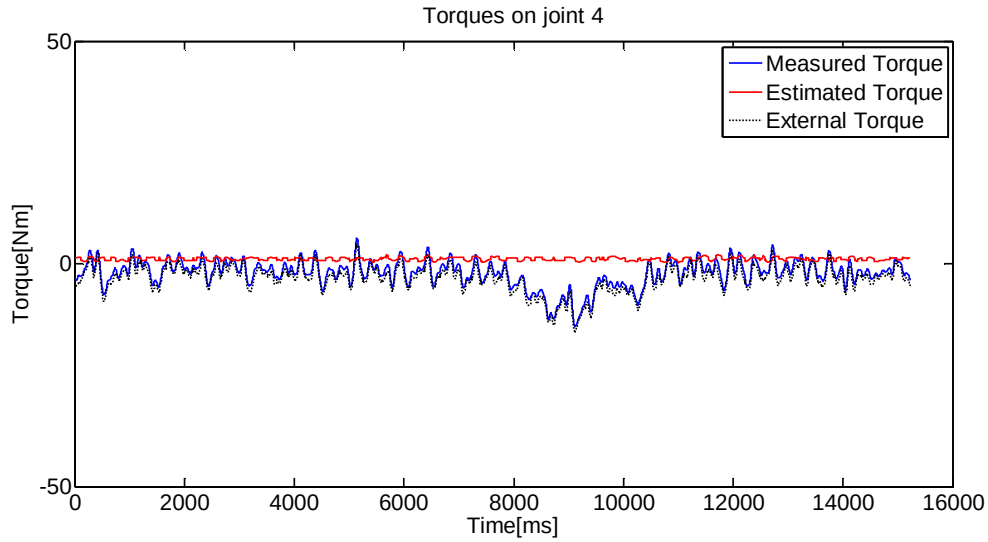

Figure 5-6. Measured, estimated and external torque on joint 4 during the compression of an elastic interface.

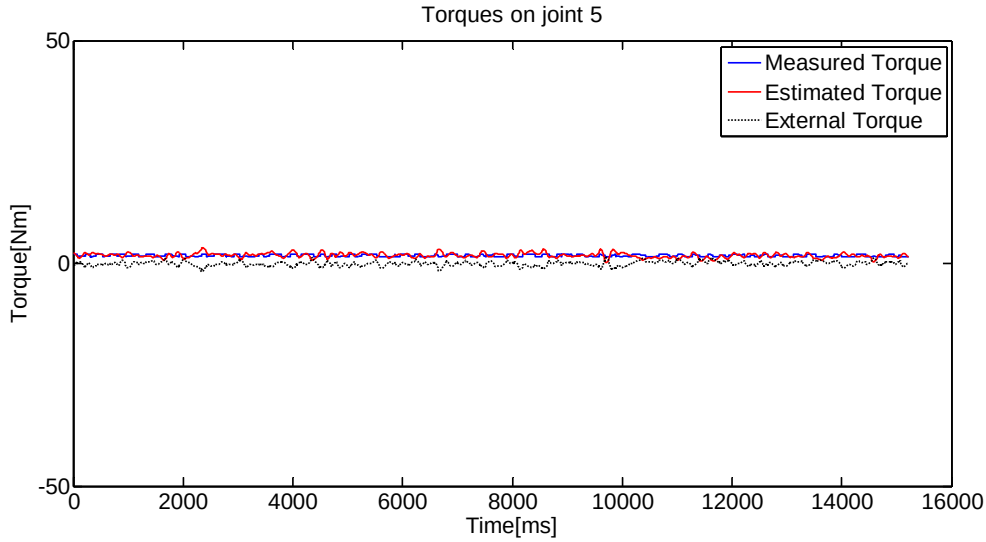

Figure 5-7. Measured, estimated and external torque on joint 5 during the compression of an elastic interface.

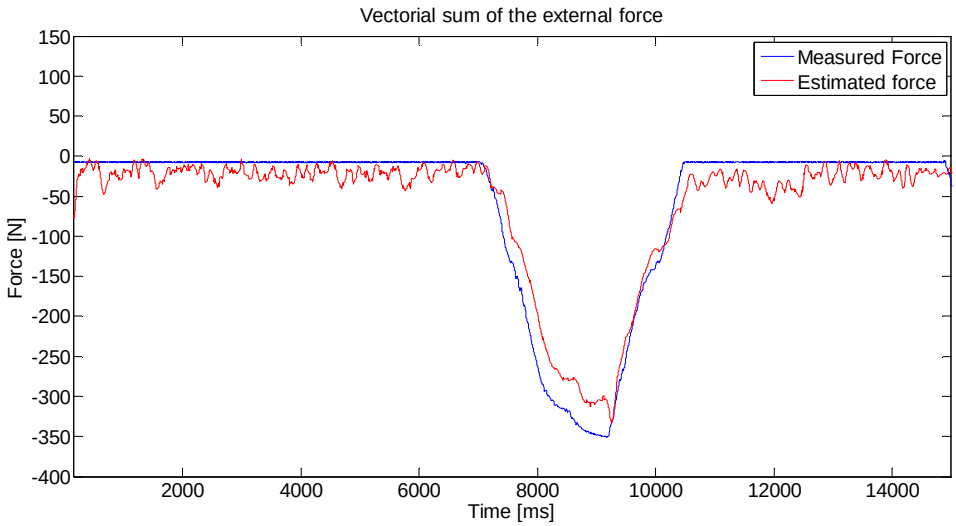

Figure 5-8. Vector sum of the forces on X, Y and Z directions.

The major issue to overcome when applying this method is the differentiation of position and velocity to obtain the joints' velocity and acceleration respectively. In this experiment the sampling rate has been 1 kHz and an offline Savitzky-Golay filtering has been applied to smooth the position and differentiate it trying to approach to a hypothetic solution given for a real time implementation. Performing this operation in real time with conventional low pass filters would lead to either unaffordable delays that would cause an unstable teleoperation or prohibitive errors due to the noisy positional feedback of the Kraft manipulator based on potentiometers and the noise am-

plification effect of the differentiation process. However, an increased sampling frequency up to a minimum of 4 kHz would help to cope with the delay caused by filtering allowing the filter to have any delay lower than 1 ms. Also the application of more advanced filtering techniques would be desirable. This important issue motivated the development of the critical part of this thesis which is explained next. A state observer was found to be useful in order to avoid differentiation of the position and the undesirable effects produced by it.

5.4 Torque estimation via observation error

This section considers defined the dynamic model of a manipulator as in (5.1). The nonlinear velocity observer of [79] will be used where $x_1{=}q$ and $x_2{=}\dot{q}$ are the joints' position and velocity respectively. The state space representation of the robot dynamics is then the following:

$$\dot{x}_1 = x_2 \tag{5.4}$$

$$\dot{x}_2 = H^{-1}(x_1)[-C(x_1,\dot{x}_1)\dot{x}_1 - \tau_g(x_1) - \tau_f(\dot{x}_1) + \tau_m - \tau_{ext}] \tag{5.5}$$

Assuming that only joint's positions are measured and without accounting explicitly for the external forces, it is possible to construct a nonlinear observer by copying the manipulator dynamics. The output variable will then be x_1.

$$\dot{\hat{x}}_1 = \hat{x}_2 + k_1\tilde{x}_1 \tag{5.6}$$

$$\dot{\hat{x}}_2 = H^{-1}(x_1)[-C\big(x_1,\dot{\hat{x}}_1\big)\dot{\hat{x}}_1 - \tau_g(x_1) - \tau_f\big(\dot{\hat{x}}_1\big) + \tau_m + k_2\tilde{x}_1] \tag{5.7}$$

$$\tilde{x}_1 = x_1 - \hat{x}_1 \tag{5.8}$$

Where $k_1$and k_2 are the Luenberger (Observer) gains and they will be symmetric and definite positive gains properly selected to place the poles of the linearized system into the desired positions.

Applying the same procedure as in [43] based on a Taylor expansion of $C(x_1,\dot{x}_1)\dot{x}_1$ it is possible to demonstrate the following expression:

$$C(x_1,\dot{x}_1)\dot{\hat{x}}_1 = C\big(x_1,\dot{\hat{x}}_1\big)\dot{\hat{x}}_1 + \pi\big(x_1,\dot{\hat{x}}_1\big)\dot{\tilde{x}}_1 \tag{5.6}$$

With $\pi\big(x_1,\dot{\hat{x}}_1\big)\dot{\tilde{x}}_1 = \frac{\partial}{\partial\dot{\hat{x}}_1}\big(C(x_1,\dot{x}_1)\dot{\hat{x}}_1\big)\big|_{\dot{x}_1=\dot{\hat{x}}_1}$. This expression will be useful to calculate the error of the Coriolis torques as:

$$\Big(C(x_1,\dot{x}_1)\dot{x}_1 - C\big(x_1,\dot{\hat{x}}_1\big)\Big)\dot{\hat{x}}_1 = C(x_1,\dot{x}_1)\cdot\big(\dot{\tilde{x}}_1+\dot{\hat{x}}_1\big) - C\big(x_1,\dot{\hat{x}}_1\big)\dot{\hat{x}}_1 \quad = \Big(C(x_1,\dot{x}_1) - C\big(x_1,\dot{\hat{x}}_1\big)\Big)\dot{\hat{x}}_1 + C(x_1,\dot{x}_1)\dot{\tilde{x}}_1 = -\pi\big(x_1,\dot{\hat{x}}_1\big)\dot{\tilde{x}}_1 + C(x_1,\dot{x}_1)\dot{\tilde{x}}_1$$

The friction torque can be divided in two different components which are the Coulomb and viscous friction and then the friction becomes:

$$\tau_f(\dot{x}_1) = D\dot{x}_1 + \gamma(\dot{x}_1) \tag{5.7}$$

Where $D = diag\{d_i\}$ and $\gamma(\dot{x}_1) = diag\{\gamma_i sgn(\dot{x}_1)\}$ for $i = 1, 2, \dots, n$, being n the dof of the system. This is, the friction is represented by means of two diagonal matrices.

Subtracting (5.7) from (5.5) we obtain the observer error:

$$\dot{\tilde{x}}_1 = \tilde{x}_2 - k_1\tilde{x}_1 \tag{5.8}$$

$$\dot{\tilde{x}}_2 = H^{-1}(x_1)[-C(x_1, \dot{x}_1)\dot{x}_1 + C(x_1, \dot{\hat{x}}_1)\dot{\hat{x}}_1 - \tau_f(\dot{\tilde{x}}_1) - \tau_{ext} - k_2\tilde{x}_1] \tag{5.9}$$

And applying the result from (5.6) it yields:

$$\dot{\tilde{x}}_1 = \tilde{x}_2 - k_1\tilde{x}_1 \tag{5.10}$$

$$\dot{\tilde{x}}_2 = H^{-1}(x_1)[-C(x_1, \dot{x}_1)\dot{\tilde{x}}_1 + \pi(x_1, \dot{\hat{x}}_1)\dot{\tilde{x}}_1 - \tau_f(\dot{\tilde{x}}_1) - \tau_{ext} - k_2\tilde{x}_1] \tag{5.11}$$

In order to obtain the dynamics of the error for $\tilde{x}_1$, (5.10) is differentiated and (5.11) it is used.

$$\ddot{\tilde{x}}_1 = \dot{\tilde{x}}_2 - k_1\dot{\tilde{x}}_1 = H^{-1}(x_1)\left[-C(x_1, \tilde{x}_1)\dot{\tilde{x}}_1 + \pi(x_1, \dot{\hat{x}}_1)\dot{\tilde{x}}_1 - \tau_f(\dot{\tilde{x}}_1) - \tau_{ext} - k_2\tilde{x}_1\right] - k_1\dot{\tilde{x}}_1 \tag{5.12}$$

Collecting the terms of (5.12) leads to:

$$\phi_2\ddot{\tilde{x}}_1 + \phi_1\dot{\tilde{x}}_1 + \phi_0\tilde{x}_1 = \tau_{ext} \tag{5.13}$$

Where,

$\phi_2 = H(x_1)$
$\phi_1 = C(x_1, \dot{x}_1) - \pi(x_1, \dot{\hat{x}}_1) + \tau_f(\dot{\tilde{x}}_1) + H(x_1)k_1$
$\phi_0 = k_2$

And thus, in the equilibrium, the expression in (5.13) could be simplified to (5.14), which provides an expression to estimate the external torques.

$$\tau_{ext} = k_2\tilde{x}_1 \tag{5.14}$$

5.4.1 Luenberger-Sliding observer

In this section the theory behind the Luenberger-Sliding observers are summarized in a way so it is possible to follow the force estimation strategy used and the results of the experiments.

5.4.1.1 Introduction to Sliding observers

Sliding observers are a special application of the first developed sliding control. This type of control is a nonlinear control method that alters the dynamics of a nonlinear system by application of a discontinuous signal that forces the system to "slide" along a cross-section of the system's normal behaviour. The state-feedback control law is not a continuous function of the time and it can switch between two different continuous functions depending on the state of the system's variables. The motion of the system is designed so that in each of the zones the system moves towards the adjacent region with a different control structure and so the ultimate trajectory will not exist entirely within one control structure. It is said that the system will slide along the boundaries of the control structures. This movement is called sliding mode and the geometrical locus consisting of the boundaries is called the sliding hyper-surface [136]. Broad detail on sliding control and sliding observers is given in the Annex II. In order for the reader to familiarize himself with the sliding effect a concise explanation of the shearing effect and sliding patches must be given here.

A sliding behaviour in a second order system needs to be created through input switching according to the value of a single component of the state. The system is then:

$$\begin{cases} \dot{x}_1 = x_2 \\ \dot{x}_2 = -k_4 \ sgn(x_1) \end{cases} \tag{5.15}$$

Where k_4 is a positive constant and sgn is the sign function. If representing the phase-plane trajectories of this system the Figure 5-9 is obtained. This clearly does not present any sliding behaviour.

Let us consider now a different system with the nonlinear control action in both variables:

$$\begin{cases} \dot{x}_1 = x_2 - k_3 sgn(x_1) \\ \dot{x}_2 = -k_4 sgn(x_1) \end{cases} \tag{5.16}$$

Where k_3 and k_4 are positive constants. The resulting phase-plane trajectories are shown in Figure 5-10. This shearing effect generates a sliding behaviour in the region given by (5.17), which is known as the sliding patch in the literature.

$$|x_2| \leq k_3, x_1 = 0 \tag{5.17}$$

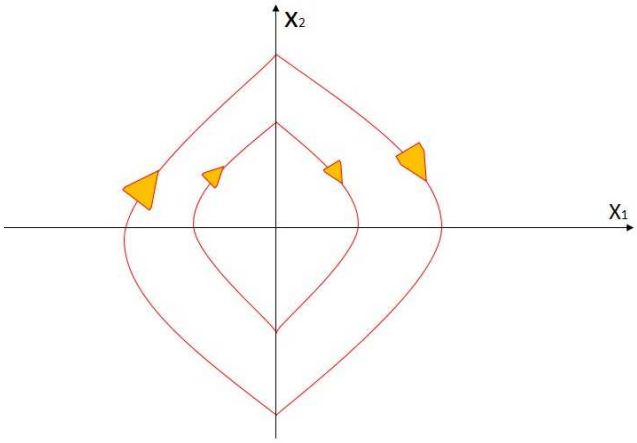

Figure 5-9. Phase-plane trajectories of the system described by equations (5.15).

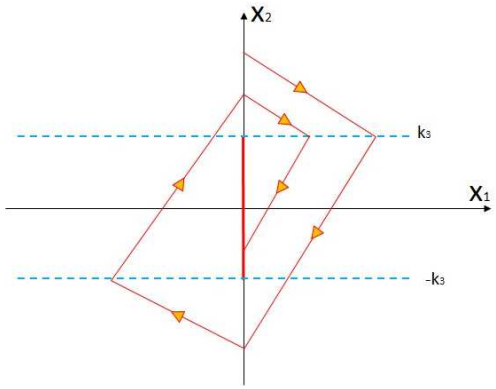

Figure 5-10. Phase-plane trajectories of the system described by equations (5.16).

The dynamics in the patch can only be a convex combination (e.g. and average) of the dynamics on each side of the discontinuity surface. Inside the patch, the dynamics are determined by the invariance of the patch itself:

$$\dot{x}_1 = 0 \;\Rightarrow\; \dot{x}_2 = -\left(\frac{k_4}{k_3}\right)x_2 \tag{5.18}$$

Thus, x_2 exponentially decreases to 0 after reaching the sliding patch with a time constant $(\frac{k_3}{k_4})$. Once the patch is reached, it is not abandoned. The sliding observer is thus defined with the error function in a way such as when the sliding patch is reached, the systems stays in a zone with minimum error. If a system with a nonlinear function f is considered, unknown function depending on the state $\bar{x} = [x_1, x_2]$:

$$\ddot{x}_1 = f \tag{5.19}$$

A sliding observer of the system would then be:

$$\begin{cases} \dot{\hat{x}}_1 = \hat{x}_2 + k_3 sgn(\tilde{x}_1) \\ \dot{\hat{x}}_2 = \hat{f} + k_4 sgn(\tilde{x}_1) \end{cases} \tag{5.20}$$

5.4.1.2 Adding a damping to the sliding observer, Luenberger-sliding observers

This section continues the previous analysis by considering now a system with damping in addition to the sliding gains. The system described in (5.16) is now converted into (5.21):

$$\begin{cases} \dot{x}_1 = -k_1 x_1 + x_2 - k_3 sgn(x_1) \\ \dot{x}_2 = -k_2 x_1 - k_4 \ sgn(x_1) \end{cases} \tag{5.21}$$

The resulting phase-plane trajectory is represented by Figure 5-11. What is happening now is that the region of attraction is expanded and all the points in the plane which verify:

$x_2 \leq k_3 + k_1 x_1 \qquad if \ x_1 > 0$

$x_2 \geq -k_3 + k_1 x_1 \quad if \ x_1 < 0$

Are affected by the sliding condition as illustrated in Figure 5-11. Also, the addition of the value k_2 only affects to the capture phase but not the dynamics of the patch itself, which remain unchanged [137].

By exploiting this result, and considering the methodology for obtaining (5.21) we now create an observer where $\boldsymbol{f}$ is a nonlinear function of the state.

$$\begin{cases} \dot{\hat{x}}_1 = \hat{x}_2 + k_3 sgn(\tilde{x}_1) + k_1 \tilde{x}_1 \\ \dot{\hat{x}}_2 = \hat{f} - k_4 sgn(\tilde{x}_1) + k_2 \tilde{x}_1 \end{cases} \tag{5.22}$$

5.4.2 External torque estimation on steady state

Let us now apply the same reasoning as in 5.4 with a completed Luenberger-Sliding observer to see how the forces and torques can be estimated when in steady state. Following the same approach but including now the sliding gains one can yield to the Luenberger-Sliding observer for robots of equation (5.23), where k_1 and k_2 are the Luenberger gains and they will be symmetric and definite positive gains properly selected to place the poles of the linearized system into the desired positions. k_3 and k_4 are the sliding gains. k_3 can be seen as a boundary of the steady state error and k_4 is chosen to be higher than the modelling error.

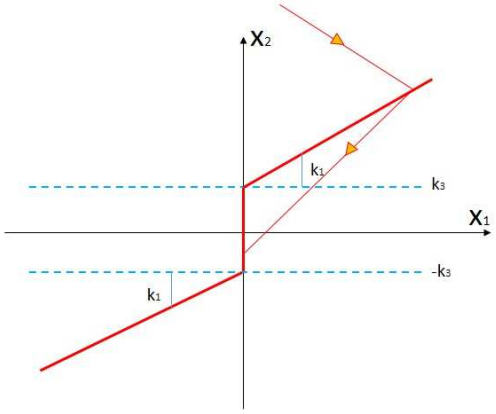

Figure 5-11. Phase-plane trajectories of the system described by equations (5.21).

$$\begin{cases} \dot{\hat{x}}_1 = \hat{x}_2 + k_3 sgn(\tilde{x}_1) + k_1 \tilde{x}_1 \\ \dot{\hat{x}}_2 = H^{-1}(x_1)\left[-C(x_1, \dot{\hat{x}}_1)\dot{\hat{x}}_1 - \tau_g(x_1) - \tau_f(\dot{x}_1) + \tau_m + k_4 sgn(\tilde{x}_1) + k_2 \tilde{x}_1\right] \end{cases} \tag{5.23}$$

with $\tilde{x}_1 = x_1 - \hat{x}_1$.

Applying the same reasoning than in previous section for manipulating Coriolis torques and friction torques, it is possible to get to the expression for the observer error:

$$\begin{cases} \dot{\tilde{x}}_1 = \tilde{x}_2 - k_1 \tilde{x}_1 - k_3 sgn(\tilde{x}_1) \\ \dot{\tilde{x}}_2 = H^{-1}(x_1)\left[-C(x_1, \dot{x}_1)\dot{x}_1 + C(x_1, \dot{\hat{x}}_1)\dot{\hat{x}}_1 - \tau_f(\dot{\tilde{x}}_1) - \tau_{ext} - k_2 \tilde{x}_1 - k_4 sgn(\tilde{x}_1)\right] \end{cases} \tag{5.24}$$

By differentiating and combining the two terms the expression for the dynamics of the position error is obtained.

$$\ddot{\tilde{x}}_1 = \dot{\tilde{x}}_2 - k_1 \dot{\tilde{x}}_1 - k_3 sgn(\dot{\tilde{x}}_1) = H^{-1}(x_1)\left[-C(x_1, \tilde{x}_1)\dot{\tilde{x}}_1 + \pi(x_1, \dot{\hat{x}}_1)\dot{\tilde{x}}_1 - \tau_f(\dot{\tilde{x}}_1) - \tau_{ext} - k_2 \tilde{x}_1 - k_4 sgn(\tilde{x}_1)\right] - k_1 \dot{\tilde{x}}_1 - k_3 sgn(\dot{\tilde{x}}_1) \tag{5.25}$$

Collecting the terms of (5.25) leads to:

$$\phi_4 \ddot{\tilde{x}}_1 + \phi_3 \dot{\tilde{x}}_1 + \phi_2 sgn(\dot{\tilde{x}}_1) + \phi_1 \tilde{x}_1 + \phi_0 sgn(\tilde{x}_1) = \tau_{ext} \tag{5.26}$$

Where,

$\phi_4 = H(x_1)$
$\phi_3 = C(x_1, \dot{x}_1) - \pi(x_1, \dot{\hat{x}}_1) + \dot{\tilde{x}}_1(\dot{\tilde{x}}_1) + H(x_1)k_1$
$\phi_2 = H(x_1)k_3$
$\phi_1 = k_2$
$\phi_0 = k_4$

And thus, the equilibrium point will be reached at (5.27) which provides an expression to estimate the external torques.

$$\tau_{ext} = k_2\tilde{x}_1 + k_4 sgn(\tilde{x}_1) \tag{5.27}$$

Although this theoretical result seems feasible during steady state force estimation, it is not adequate for practical implementation due to the likely strong chattering effect on the estimated torques. In order to avoid that effect, a smoother transition has to be created on the border around $\tilde{x}_1 = 0$. This has been done by varying the value of the k_4 gain depending on the torque predicted via Luenberger observer only, so (5.27) is converted to (5.28).

$$\tau_{ext} = k_2\tilde{x}_1 + \xi k_4 sgn(\tilde{x}_1) \tag{5.28}$$

$$\begin{cases} \xi = 0 & if\ |k_2\tilde{x}_1| < \tau_{threshold} \\ \xi = \frac{|k_2\tilde{x}_1 - \tau_{threshold}|}{\tau_{threshold}} & if\ |k_2\tilde{x}_1| \geq \tau_{threshold} \end{cases} \tag{5.29}$$

In addition to that transformation, ξ is saturated to a maximum value which is 1. This allows a progressive increase of the effect of the nonlinear observer action so the chattering is avoided.

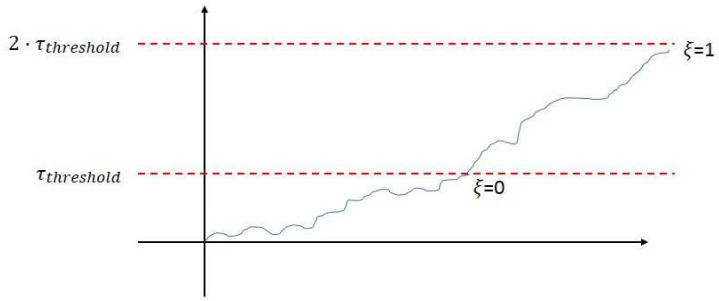

Figure 5-12. Effect of the smoothing coefficient.

5.4.3 Observer's convergence analysis.

In order to show the convergence of this observer the following assumption has to be made: the external forces acting on the slave have to be bounded for all time with some known upper bounds. Also, several properties characteristics from the robot dynamics have to be considered:

(i) $H(x_1) > 0$
(ii) $\|H(x_1)\| \leq \sigma_o$
(iii) $\|C(x_1, \dot{x}_1)\dot{x}_1\| \leq \sigma_1\|\dot{x}_1\|^2$
(iv) $H(x_1)/2 - C(x_1, \dot{x}_1)\ is\ skew - symmetric$

Let us begin by showing the stability of the first order observer state. Choosing as a Lyapunov function candidate:

$$V_1 = \tfrac{1}{2}\tilde{x}_1{}^2 \tag{5.30}$$

Let us take the derivative of the Lyapunov function along the trajectories of the system one obtains the following expression,

$$\dot{V}_1 = \tilde{x}_1\dot{\tilde{x}}_1 \;=\; \tilde{x}_1\big(\tilde{x}_2 - k_1\tilde{x}_1 - k_3 sgn(\tilde{x}_1)\big) = \tilde{x}_1\tilde{x}_2 - k_1\tilde{x}_1^2 - k_3|\tilde{x}_1| \leq |\tilde{x}_1|(|\tilde{x}_2| - k_1|\tilde{x}_1| - k_3) \tag{5.31}$$

Choosing $k_3 > |\tilde{x}_2| - k_1|\tilde{x}_1| + \varepsilon_1$, where $\varepsilon_1 > 0$, ensures that $\dot{V}_1 < 0$ for all $\tilde{x}_2 \neq k_1|\tilde{x}_1|$. As in [93], it is shown in [138] that the surface $\tilde{x}_1 = 0$ is reached in finite time with upper bound T_s. After that time, the state $\tilde{x}_1$ will have converged to the sliding surface $\tilde{x}_1 = 0$ and thus $\dot{x}_1 = 0$.

We may then choose the Lyapunov function candidate as $V_2 = (1/2)\,\tilde{x}_1{}^2 + (1/2)\,\tilde{x}_2{}^2 = (1/2)\,\tilde{x}_2{}^2$, since $\tilde{x}_1 = 0$. Deriving V_2 along the trajectories of the system, the following is obtained:

$$\dot{V}_2 = \tilde{x}_2{}^T \;\; H(x_1)\;\dot{\tilde{x}}_2 \;+ (1/2)\,\tilde{x}_2 \;\; \dot{H}(x_1)\tilde{x}_2 \tag{5.32}$$

From (5.24), (5.18) and (5.32) it is straight forward to infer:

$$H(x_1)\dot{\tilde{x}}_2 = -C(x_1,\tilde{x}_1)\dot{x}_1 + \pi\big(x_1,\dot{\hat{x}}_1\big)\dot{\tilde{x}}_1 - \tfrac{k_4}{k_3} - D]\tilde{x}_2 - \gamma(\tilde{x}_2) - \tau_{ext} \tag{5.33}$$

Leading to the expression of $\dot{V}_2$:

$$\dot{V}_2 = \; -\tilde{x}_2^T\Big[-\pi\big(x_1,\dot{\hat{x}}_1\big) + \tfrac{k_4}{k_3} + D\Big]\tilde{x}_2 + \gamma(\tilde{x}_2)\tilde{x}_2 + \tau_{ext}\tilde{x}_2 + \tilde{x}_2[\tfrac{\dot{H}(x_1)}{2} - C(x_1,\tilde{x}_1)\widetilde{]x}_2 \tag{5.34}$$

The last term of (5.35) cancels out due to the property (iv) and the gains $\frac{k_4}{k_3}$ have to be computed such that the first term of the equation is positive definite. Proceeding similarly as in [92] but letting $\alpha = \gamma(\tilde{x}_2) + \tau_{ext}$ the expression of $\dot{V}_2$ can be factorized on the following way:

$$\dot{V}_2 = -\big[\tilde{x}_2{}^T\,, \alpha^T\big]\begin{bmatrix} Q & -\frac{I}{2} \\ -\frac{I}{2} & I \end{bmatrix}\begin{bmatrix}\tilde{x}_2 \\ \alpha\end{bmatrix} + \alpha^T\;\alpha = -z^T M z + \alpha^T\;\alpha \tag{5.35}$$

Where $Q = -\pi\big(x_1, \dot{\hat{x}}_1\big) + \frac{k_4}{k_3} + D$ is the first term of equation (5.35). Now, some operations must be done in order to find an upper bound for $\dot{V}_2$ and establish the conditions where the error converges.

$$\dot{V}_2 \leq \lambda_{inf}(M)\|z\|^2 + \|\alpha\|^2 = \lambda_{inf}(M)\|\tilde{x}_2\|^2 + (1 - \lambda_{inf}(M))\|\alpha\|^2 \tag{5.36}$$

Since the external forces and friction parameters are bounded, $\|\alpha\|$ is bounded. It can be demonstrated [43] than when $\tilde{x}_1(0) = 0$, condition that can be easily accomplished since the position can be read from the positional feedback, and the rest of convergence criteria is also fulfilled, $\|\tilde{x}_2\|^2$ converges exponentially with a radius δ.

$$\delta = \left(\frac{1}{\lambda_{inf}(M)} - 1\right)\ \alpha_o \tag{5.37}$$

Where, $\alpha_o = \sup\{\|\alpha\|\}$.

5.5 Force estimation results of a hydraulic manipulator via state observers. Comparison between Luenberger and Luenberger-Sliding observers.

In this section, the theoretical approach explained before is tested with real data gathered during tests carried out with the Kraft manipulator mounted with a force/torque sensor. Although the tests are developed on simulation, all the algorithms are applicable in real time operation.

5.5.1 Development of a robot simulator

A robot simulator has been developed using Simulink and Matlab 2011 © Mathworks. This simulator is useful to interact with the robot model with a lean and agile approach. It has been proved to be extremely convenient to execute the manipulator's state observer and tune its gains properly. The measured data has been stored in a variable which is accessed during simulation to be compared with the estimation. The process followed to encapsulate the dynamic model into Simulink blocks has been the following:

a) The identification procedure carried out in Chapter 4 led to an optimised set of parameters with physical sense.
b) The iterative Newton-Euler method has been programmed and used to generate a symbolic expression of each joints torque as a function in the robot's

state space. The torque has been split into its conventional components, i.e. gravity torque, inertial torque, Coriolis torque and friction torque.

c) The symbolic expression of each torque component has been transformed into a Matlab function which is called inside a Simulink block.

The complete result is presented in Figure 5-13 with its two main components: the real robot and the state observer. The block titled “Real Kraft” reads the tests data from stored variables. Only the position measurements and joint torques are passed to the observer block, which outputs the estimated position at the next simulation step, estimated speed and the error between the last joint measurement and the joint estimation. It also outputs the gains to be used in the force estimation algorithm. There is an additional block which computes the inverse of the jacobian transpose of the manipulator in order to infer the external forces at tip from the external torques on each joint. The simulator presented in Figure 5-13. is valid for computing the Luenberger-Sliding observer, and by cancelling the Sliding gains, it gets transformed into a simpler Luenberger observer. Figure 5-14 details the observer block from previous figure. Two main sub-blocks appear in this Figure: the robot model and the S-Function of the State Observer. In the S-Function, only the integration of the dynamic model is accomplished with the time-varying parameters supplied by the Optimised model, such as: the robot inertia matrix, and the different torque.

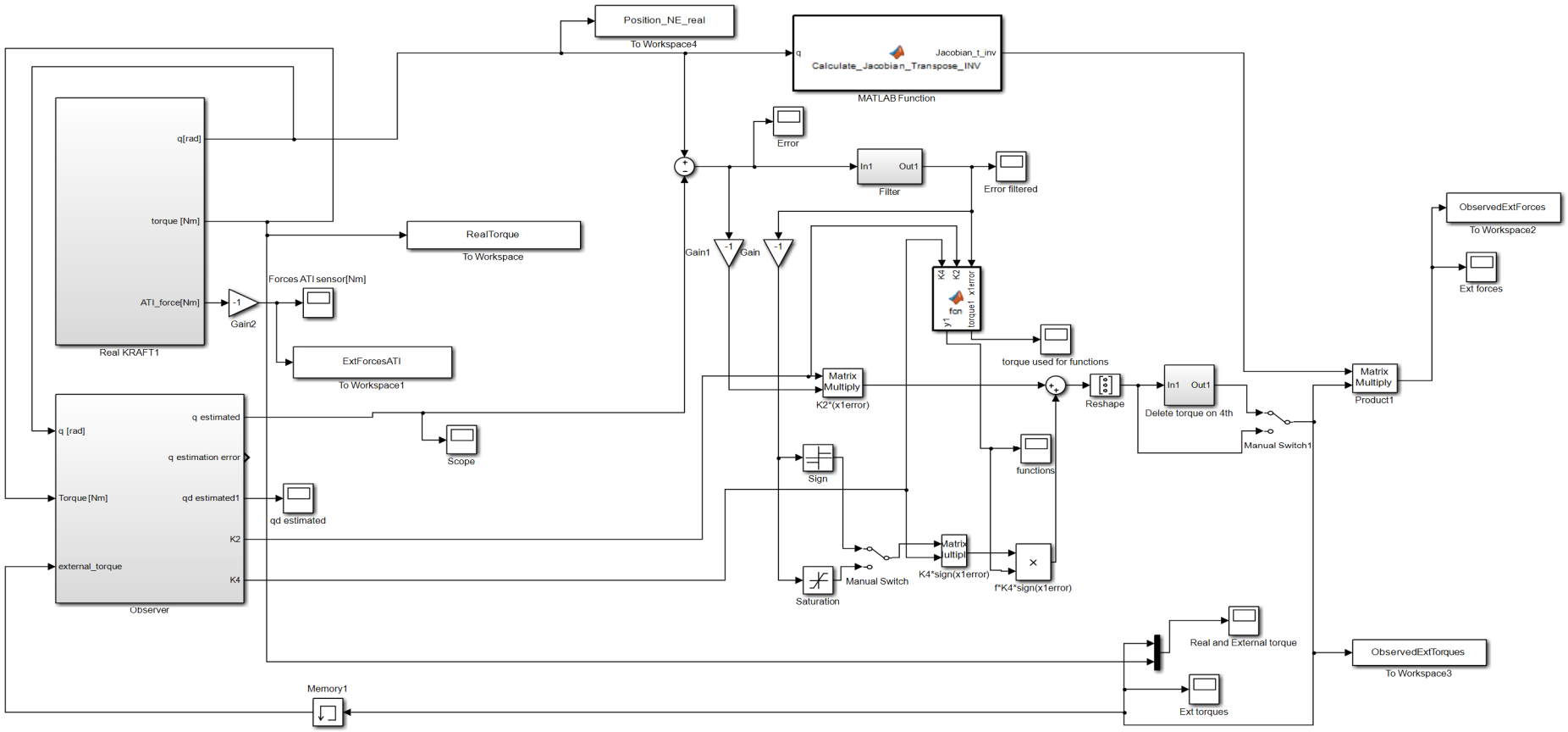

Figure 5-13. Force estimation simulator developed on Simulink ®.

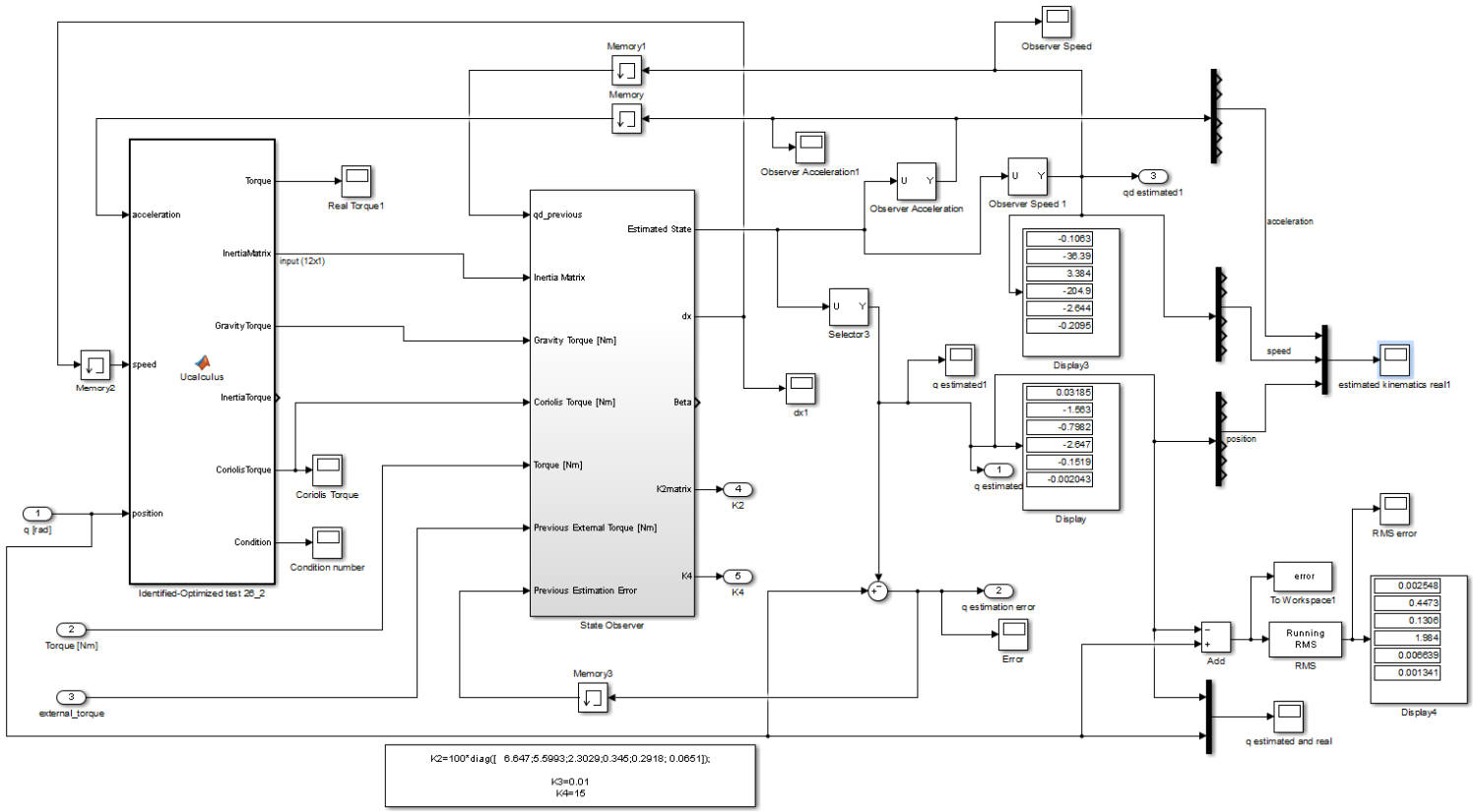

Figure 5-14. Detailed structure of the observer block.

5.5.2 Experimental results on force estimation implementing Luenberger observers

The experimental setup employed in 5.3 is used here together with the algorithm developed in 5.4.

5.5.2.1 Spring compression

During a similar scenario to the one the employed in 5.3, the KRAFT manipulator was commanded to different poses carrying an elastic interface and the ATI force/torque sensor between the interface and the last link. The objective of this test is to validate the approach presented in 5.4. and to extract conclusions. During this test the robot was moved in free space by a human operator. At intermediate points of its trajectory the robot was forced to compress the spring against the horizontal surface. The joints' trajectories of this movement are shown in Figure 5-16 and Figure 5-17

Figure 5-15. Kraft GRIPS exerting compression forces on the spring.

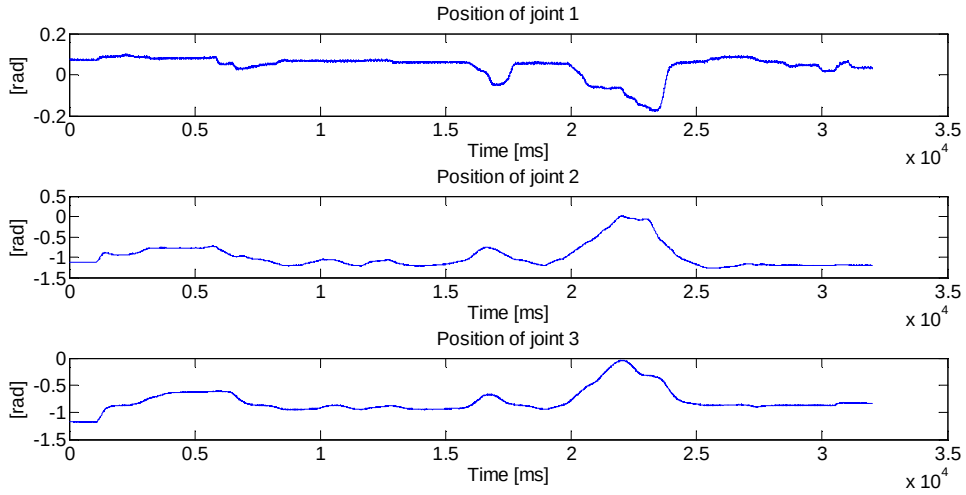

Figure 5-16. Trajectory of joints 1 to 3 accomplished during the spring compression test.

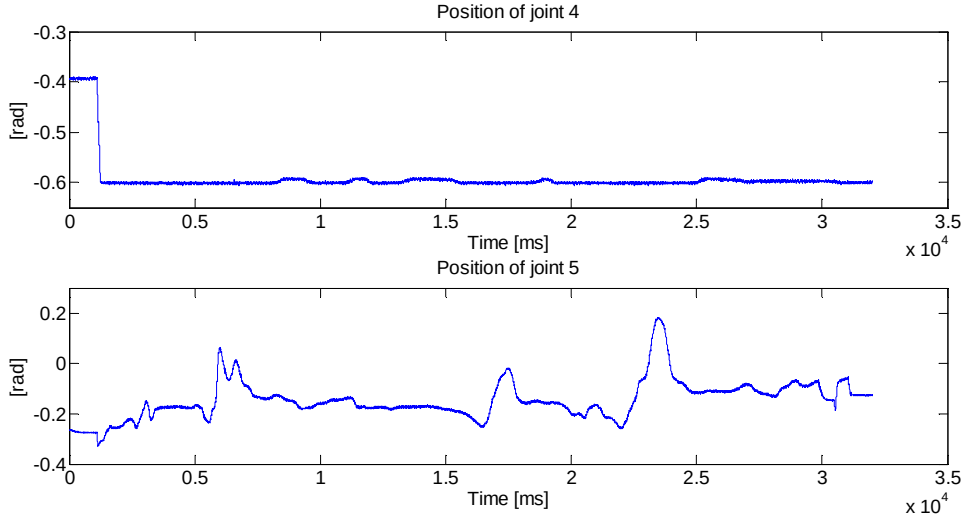

Figure 5-17. Trajectory of joints 4 and 5 accomplished during the spring compression test.

Luenberger observer gains	
K_1	50
K_2	$100 \cdot \text{diag}([1.5, 7, 2.3029, 0.345, 0.2918, 0.0651])$ (*)

Table 5-1. Observer gains used during the experiment.(*) The function diag() indicates a diagonal matrix composed by the elements between brackets.

A Luenberger observer has been tuned as described in 5.4.2 with the gains shown in Table 5-1. The motor torques which take into account all the torques involved on the manipulator movement are represented in Figure 5-18 and the external torques that

the algorithm is able to predict are shown in Figure 5-19. The observer behaves well and after a period of convergence of approximately 8 seconds, it is able to estimate the external torques. It is clear that the algorithm eliminates the torque offset due to different actions other than the external, acting as a filter in that sense. For validation purposes it is interesting to see the transformation carried out from torques to forces on the end-effector and the comparison with the sensor mounted on the last joint. This graph is shown on

Figure 5-20. Although the estimation is not perfect, the method explained here exhibits good performance and clearly improves the results of the method based on evaluating the robot's dynamics equation.

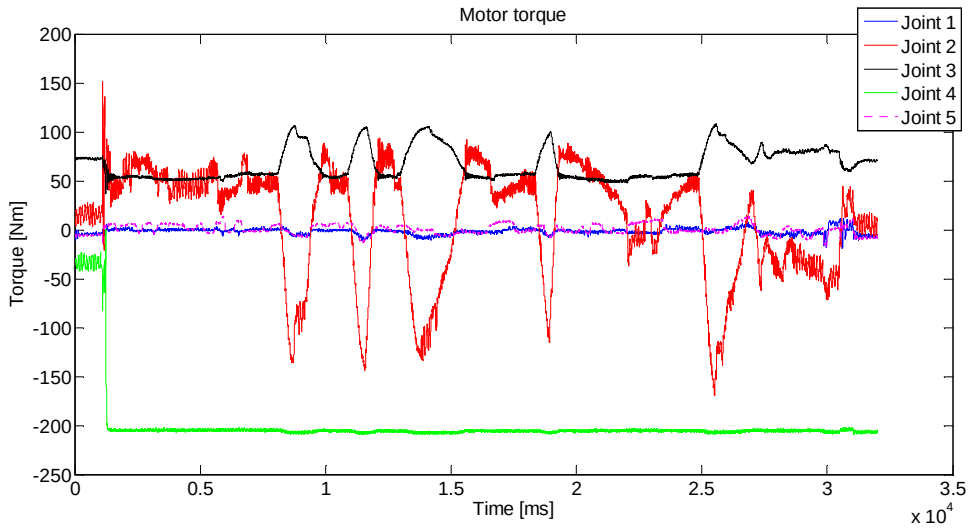

Figure 5-18. Motor torques during the spring compression test. The values represented here include the gravity, inertial and Coriolis torque and also the action of external torques and forces.

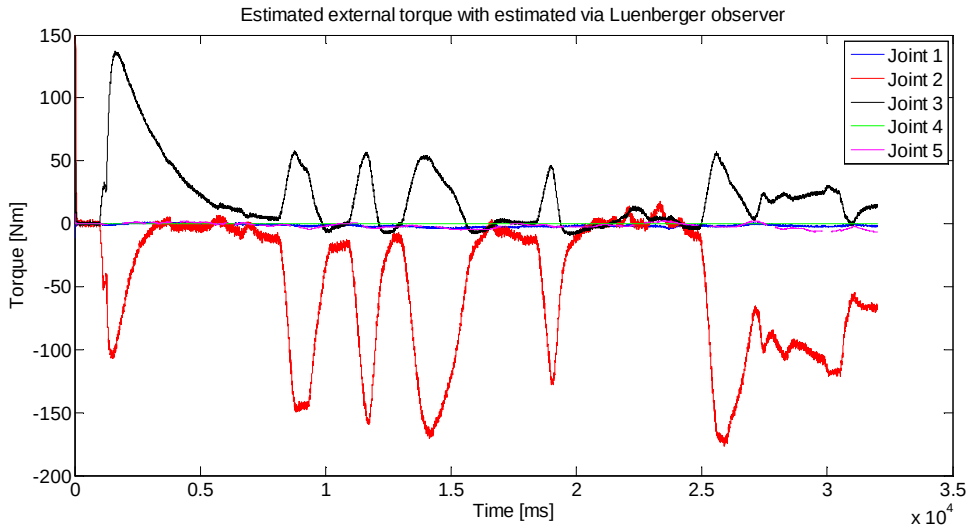

Figure 5-19. External torques predicted using the Luenberger observer during the spring compression test. Three different parts can be distinguished here, e.g. the pre-convergence stage, where external torques are estimated appear even in absence of external forces. This only happens during the first seconds of estimation until the observer converges to zero error. Afterwards, four impacts are performed on a plane surface where the spring is compressed, these conform the second stage. Finally, after 25 s, a period of instability is shown when the robot was placed on hold position and disconnected.

Additionally, this method does not need position differentiation. The force estimation offset along directions Y and Z are caused by parameterization error or incorrect torque constant calculation. Also it is dependent on the values chosen for the observer gains. Increasing the gains improves the average of the estimated torques but increases the noise of the estimation. A compromise must be reached when tuning the observer gains.

The incorrect offset presented in the force estimation on the force through Y direction (See Figure 5-20) that is seen as small waves after each impact is created by the offset during the estimation of joint torque 2. The fact that the torques on joints 2 and 3 do not match on the zero torque line is transformed by the jacobian into a force offset through the Y component.

The inaccuracies found when implementing this algorithm led this research through the search of a more robust estimator which was not affected in such a way by the modelling errors. The sliding observers were found to be an extremely effective solution with easiness of implementation.

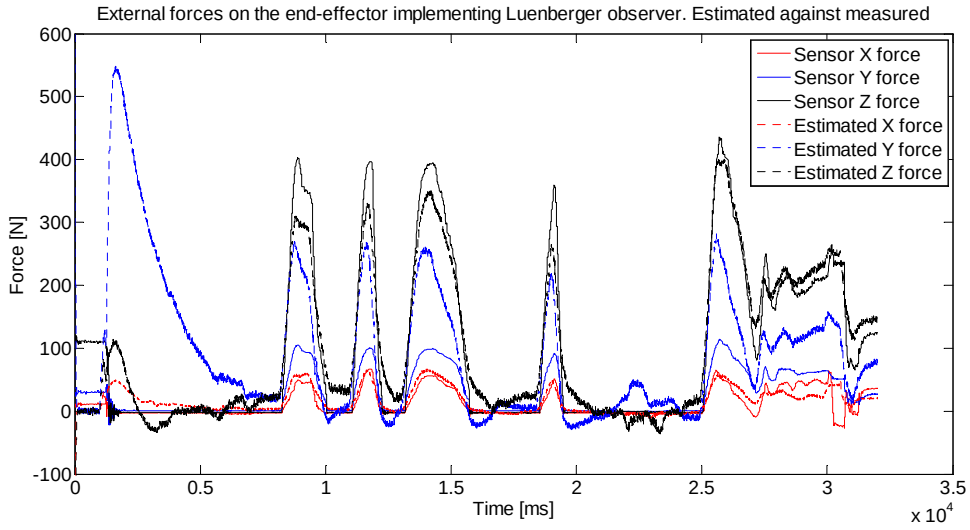

Figure 5-20. Forces obtained via Luenberger observer validated against forces measured with the ATI force sensor. Test name: TLR5. Three different parts can be distinguished here, e.g. the pre-convergence stage, where external torques are estimated appear even in absence of external forces. This only happens during the first seconds of estimation until the observer converges to zero error. Afterwards, four impacts are performed on a plane surface where the spring is compressed, these conform the second stage. Finally, after 25 s, a period of instability is shown when the robot was placed on hold position and disconnected. The estimation error shown in the graph is small for X and Z coordinates and presents a big error in Y. This is e the discrepancy found in the estimation of the torque of joint 3 and the offset of estimation on joint 2.

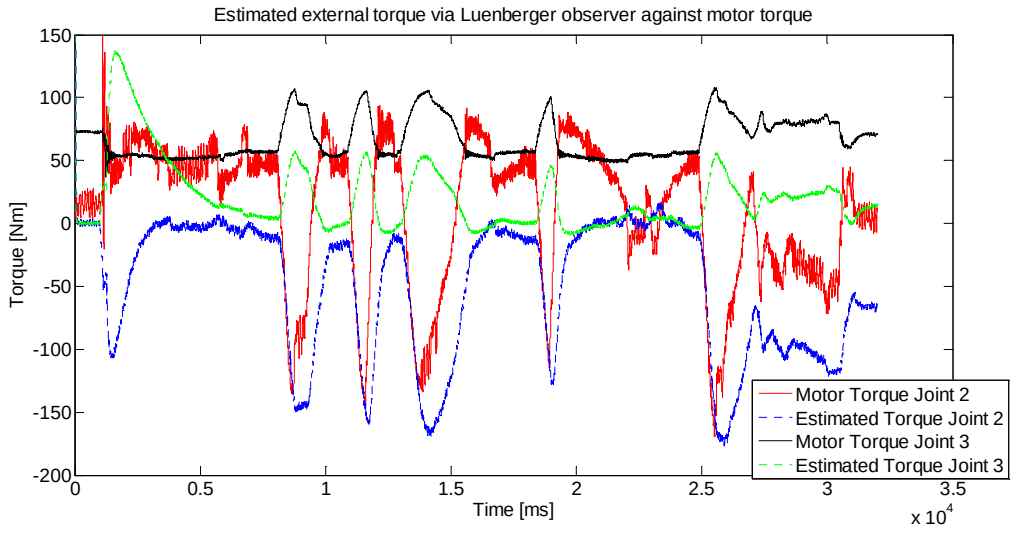

Figure 5-21. Estimated external torque via the Luenberger observer compared against the motor torque. The estimation of external forces after the convergence period eliminates the effect of the non-external torque components such as gravity and inertia.

Also, it is worth mentioning the exaggerated estimated torque of joint 3 that creates additional forces as seen in previous figure. Different causes have been studied to produce this: modelling errors, absence of a robust estimator and the lack of calibration after modelling.

Luenberger-Sliding observer gains	
K_1	$50 \cdot \text{diag}([1,1,1,1,1,1])$
K_2	$60 \cdot \text{diag}([\ 1.5;8;1;0.345;0.2918;\ 0.0651])$ (*)
K_3	0.01
K_4	$25 \cdot \text{diag}([1,2,0.9,1,1,1])$

Table 5-2. Gains used on the Luenberger-Sliding observer on the test TLSIR5.

Here the results of the robust observer which implements the gains of Table 5-2 are analysed. Predicted external torques are shown on Figure 5-22. One can appreciate big differences with respect the basic version of the observer illustrated on Figure 5-19. Offsets and unmodelled torques have almost disappeared, resulting on a clearer shape. The external forces are shown on Figure 5-22. The results are impressive, improving the performance obtained previously with Luenberger observer. The estimation of the force along Z axis is almost perfect, and the torque misalignment of joint 2 with respect to joint 3 that was causing the errors along the Y component has been eliminated. Estimated forces along X are also very accurate.

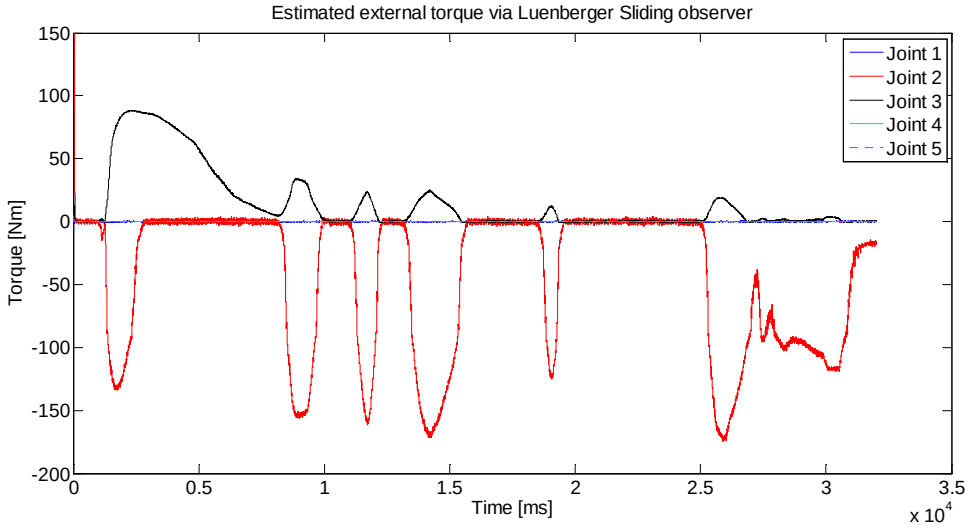

Figure 5-22. External torques predicted using Luenberger-Sliding observer. Test number TLSIR5. Data from the same test based on a spring compression have been used here with a robust estimator. One can see how only joints 2 and 3 are involved on the estimation. The little effort made on joint 5 has been neglected with this observer.

However the results are outstanding since no torque offset is present anymore after the convergence period. One can see how the convergence has not finalised before the first impact and that will lead into a force estimation errors. However, as the time passes, better estimations are obtained.

On Figure 5-23 to Figure 5-26, the estimated external forces are shown and explained. Figure 5-23 represents the estimated forces versus the measured ones for the three different directions. Estimation errors decrease greatly with respect to the estimation from previous observer. Three different parts are clearly distinguished here: the convergence period, which starts on the beginning of the estimation and is characterised by an estimation with a hill-like shape of an external force which does not exist, the impact period and the high dynamic stage where the robot was placed on stop position previous to the disconnection. The convergence period is the necessary time required for the observation error to decrease up to zero. It is only needed at the beginning of the estimation process and it will not be created again. It has been shown for illustrative purposes. After that stage, four impacts are registered on this tests and their estimated force are given for x, y and z coordinates.

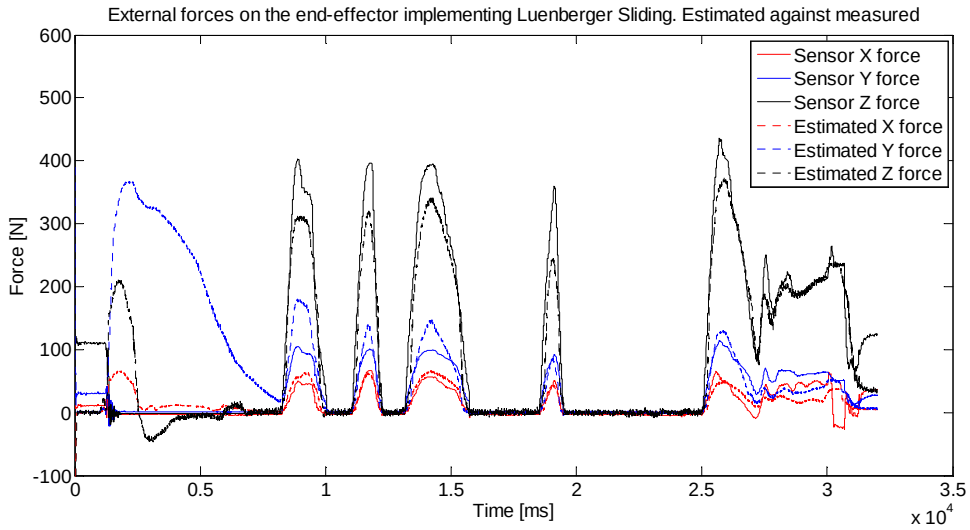

Figure 5-23. External forces predicted using Luenberger-Sliding observer. Test number TLSIR 5. This figure is comparable with

Figure 5-20 and shows the estimated forces in X, Y, and Z compared to the measured magnitude. The estimation error on X and Y decreases greatly from previous observer and the offset forces disappear totally. Although there is still a dynamic error on the estimation due to the approximations taken in the equation of the estimated torque that neglected the dynamic terms, the behaviour on static is impressive. The potential

errors introduced in the calculation of the torque constant are also affecting the accuracy of the estimation.

In Figure 5-24 comparative results for the force estimation between Luenberger and Luenberger-Sliding observers are shown for the x direction. One can check that estimations carried out without the sliding action present offset errors due to modelling errors. These offsets disappear when implementing the sliding-observer as a result of a more robust action and a perfect zero force is achieved after the convergence period.

In Figure 5-25 the resultant estimated forces for the y-axis are represented. It is worth to point out the slight depression which appears at the end of every impact when using the conventional observer. This effect is created by estimation errors on torque of joints 2 and 3 as shown in Figure 5-22. When the torque of these joints does not intersect the zero at the same time, an offset force is resultant after the application of the jacobian. This effect is eliminated in the tests carried out with the Sliding observer.

The forces in the z direction are given in Figure 5-26, presenting remarkable good behaviour. Both estimators reach similar amplitude but only the sliding action eliminates the pernicious force offset during static forces.

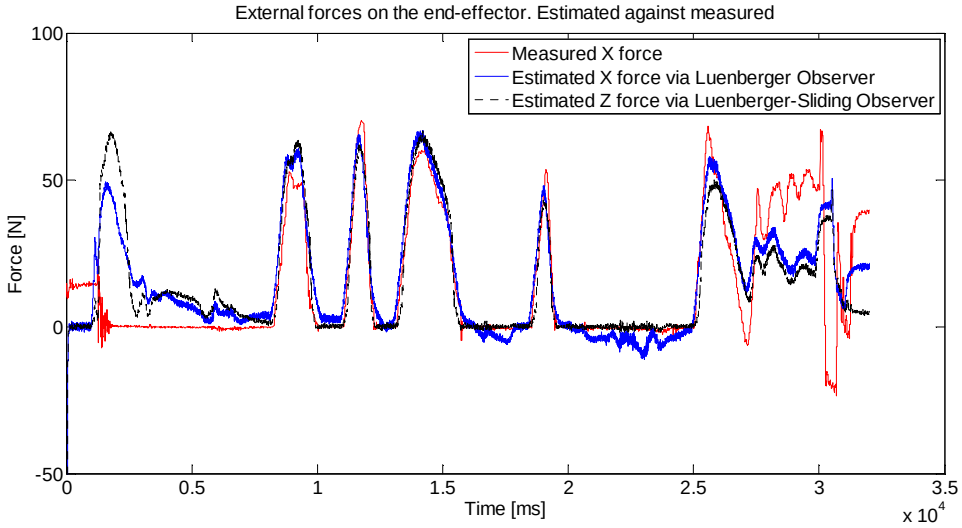

Figure 5-24. Detailed view of the estimation force through X direction during test TLSIR 5. The main difference between the two observers presented here lies in the correct estimation during absence of external forces. No offset forces are estimated for Luenberger-Sliding which however tend to appear without the sliding action.

The discrepancies found when comparing estimations against measurement arise due to different reasons. Although this method is able to distinguish a divergence of the real robot movement from the expected one, that divergence has to be translated to a

torque action applied to each joint. The observer is using the joint error fed-back into the system in order to correct the next estimations, however the comparison with the measurements taken by the force/torque sensor are in open loop, meaning that no calibration is performed on real time. A post-modelling calibration could be added to this estimator, to correct the effects of an incorrect torque constant estimation.

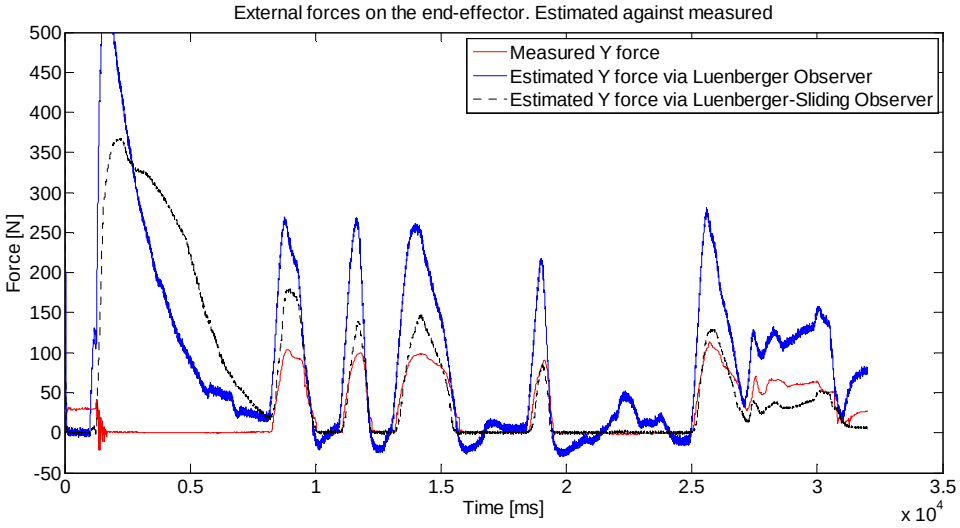

Figure 5-25.Detailed view of the estimation force through the Y direction during test TLSIR 5. The main difference between the two observers presented here lies in the correct estimation during absence of external forces. No offset forces are estimated for Luenberger-Sliding which however tend to appear without the sliding action. The estimation of the external force through Y direction for the conventional observer presents more error than through the rest of directions. This is because of estimation errors on the torque of joint 3 and the offset on the estimation of joint 2, as explained before.

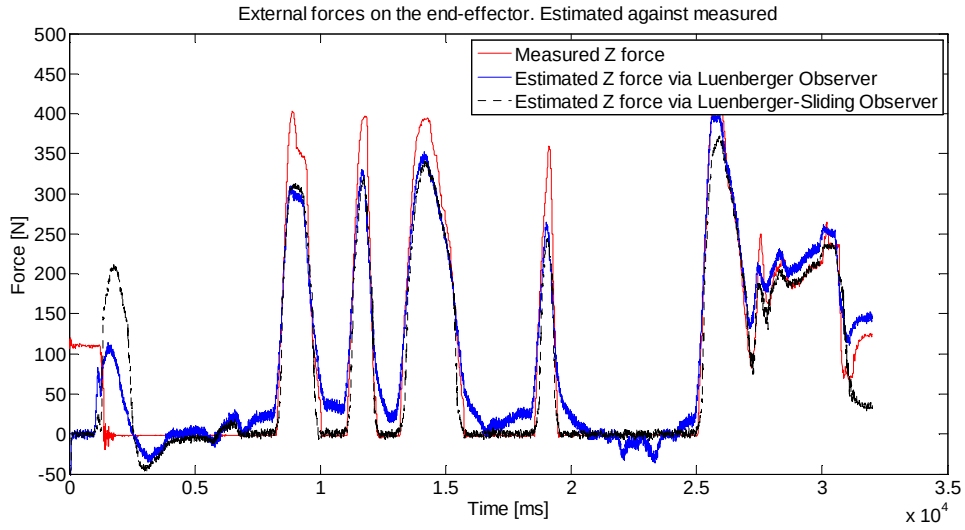

Figure 5-26. Detailed view of the estimation force through Z direction during test TLSIR 5. The main difference between the two observers presented here lays on the correct estimation during absence of external forces. No offset forces are estimated for Luenberger-Sliding which however tend to appear without the sliding action.

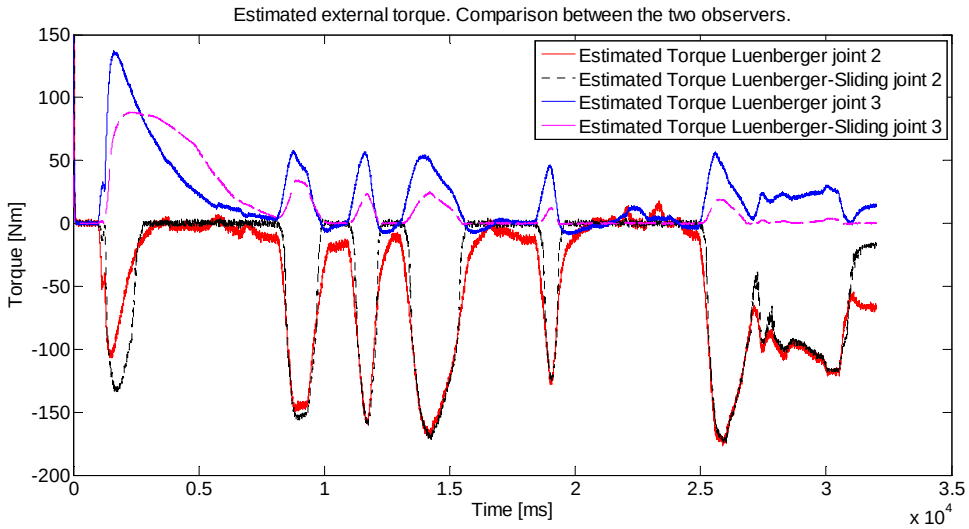

Figure 5-27. Comparison of estimated torques. Luenberger observer versus Sliding observer for joints 2 and 3 during test TLSIR 5. The main difference lays in the accuracy of the estimation of joint 3. With sliding action, the torque estimation for joint 3 improves dramatically. The torques offset also disappear when using the sliding gains, improving the forces. On joint 2, one can see how the red line does not reach the zero torque after the first and second impacts, however this effect disappears completely in sliding mode (black line).

In Figure 5-27 one can see the actual differences of the force estimation methods and the improved behaviour obtained with the Luenberger-Sliding observer.

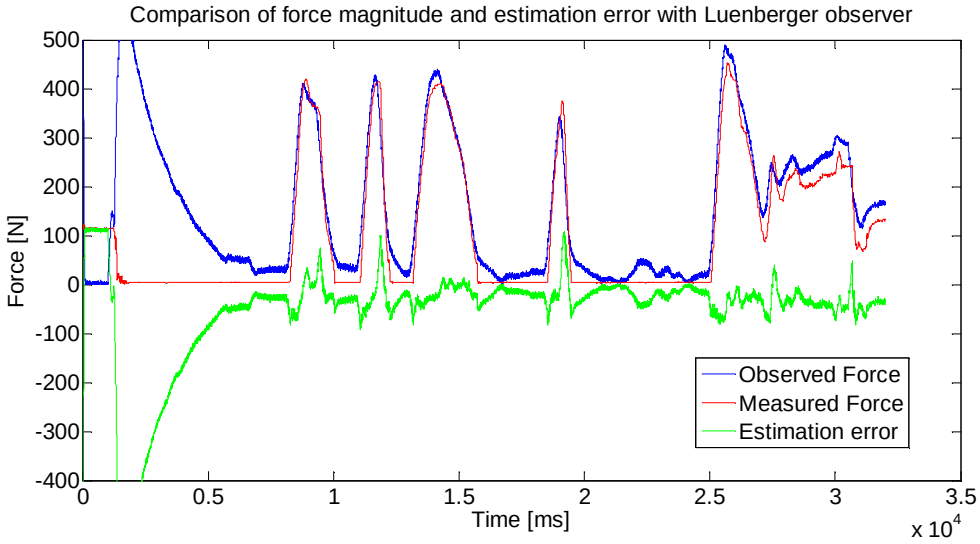

Figure 5-28. Comparison of the total force magnitude between estimation performed via the Luenberger observer during test name TLSIR 5. An average error of 7 % has been achieved during dynamic impact. In absence of external forces the error is important.

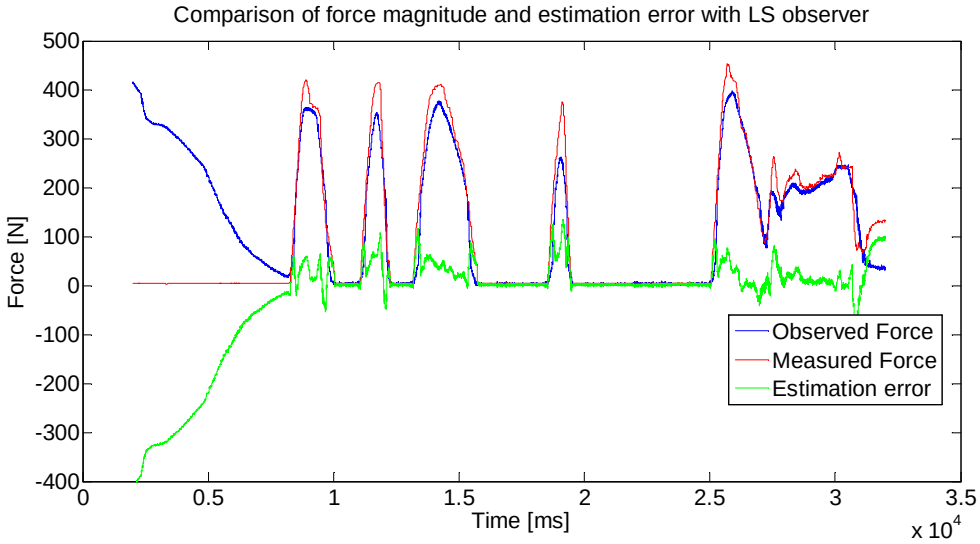

Figure 5-29. Comparison of total force magnitude between estimation performed via Luenberger-Sliding observer during test name TLSIR 5. An average error of 10% has been achieved during dynamic impact. In absence of external forces the error is negligible.

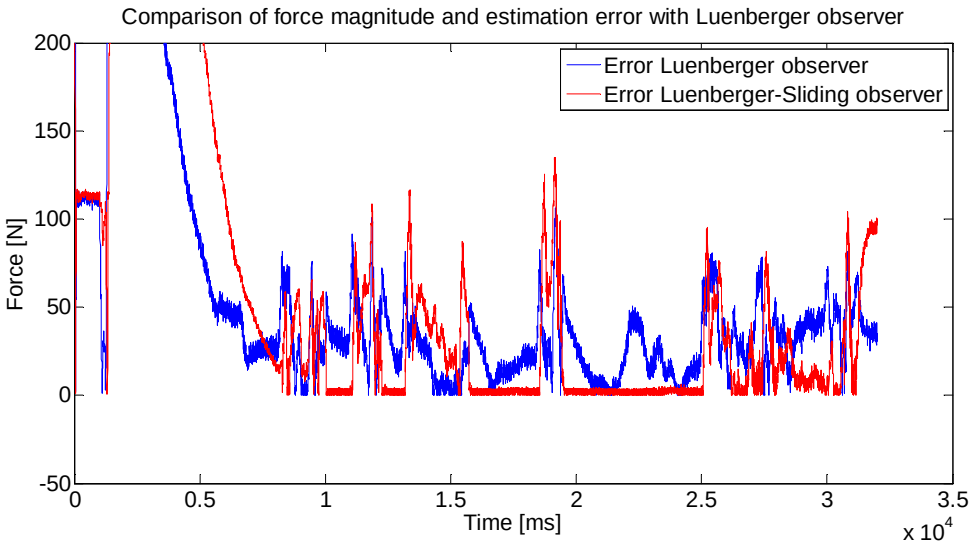

Figure 5-30. Comparison of the total error between estimation performed via the Luenberger-Sliding and the Luenberger observer during the test name TLSIR 5.

5.5.2.2 Influence of the inertia into the torque estimation

It has been highlighted multiple times the importance of obtaining a sensible model based on parameters with physical sense. Otherwise the model will tend to instabilities and thus, incorrect force estimation. It is also important for the modeller to obtain an acceptable estimation of the inertia matrix that can be used when integrating the equation of the robot dynamics to estimate joint's accelerations.

An example of this issue is illustrated in Figure 5-31. In this example the inertia has been lowered deliberately, resulting into an acceleration which is faster than real and thus an estimated position which goes ahead of the real position. This results into a model with a faster response which might correspond to a lighter mechanism. Its links tend to accelerate faster than the real links would do with the same motor torque and an advanced estimation is then obtained.

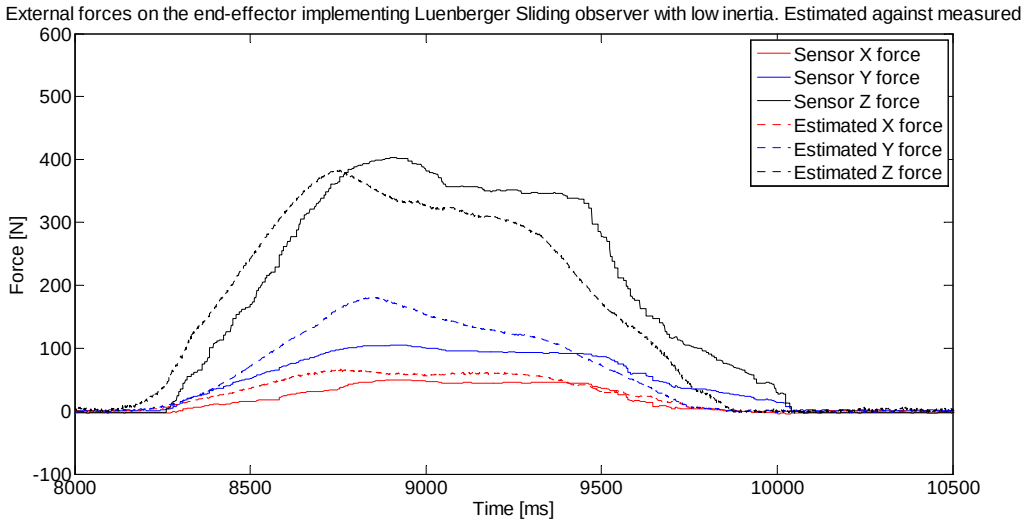

Figure 5-31. Estimation of external forces implementing a deliberate lower inertia.

5.6 Observer based teleoperation

5.6.1 Modelling a bilateral system

The results presented on previous sections are promising for a final implementation of a sensorless force estimator. The good results achieved with the sliding observer led the research to a test under a bilateral scenario. Is thus important to study the influence of the robust estimator when closing the loop, in order to discover further possible issues which could be introducing instabilities in the system. Also, a simulation of such a system could help to compare the proposed approach against traditional teleoperation architectures such as position-position.

The objective of this section is then, to explain the development of a bilateral teleoperation simulator made with previous results which can be used to test and compare different bilateral teleoperation schemes.

In Figure 5-32 and Figure 5-33 the simulators for position-position and force-position bilateral control developed in Simulink from Mathworks © are shown. The objective of the model developed on Figure 5-32 was to reproduce the classical approach made with the model of the Kraft robot, embedded in the block named “slave device” and shown on Figure 5-34. Additional detail on the robot model is given in Figure 5-35. An embedded Matlab function has been used to simulate the real device. The identified and optimised parameters have been used here to build a physically realistic model of the Kraft robot. By integrating the robot’s dynamic equation it is straight forward to

infer the robot movement. The starting position and the motor torques are required to generate the movement and obtain the acceleration of the links. This value will be integrated two times to obtain the joints' velocity and position and decompose the motor torque in all the elements.

The slave controller shown in Figure 5-35 comprises of an independent joint controller and a gravity compensation implemented by using the identified model. Once the model has been obtained it is easy to use it for more advanced controlling purposes.

In Figure 5-36, two additional blocks used during the force-position teleoperation with observers are shown. The observer block includes the algorithm explained before on Figure 5-14. This block employs the Luenberger-Sliding observer to estimate the theoretical new positions that the robot would have if no external forces were present on the environment. Later on, the so called "External force estimation" block computes the external forces based on the error of the predicted position with respect to the real position.

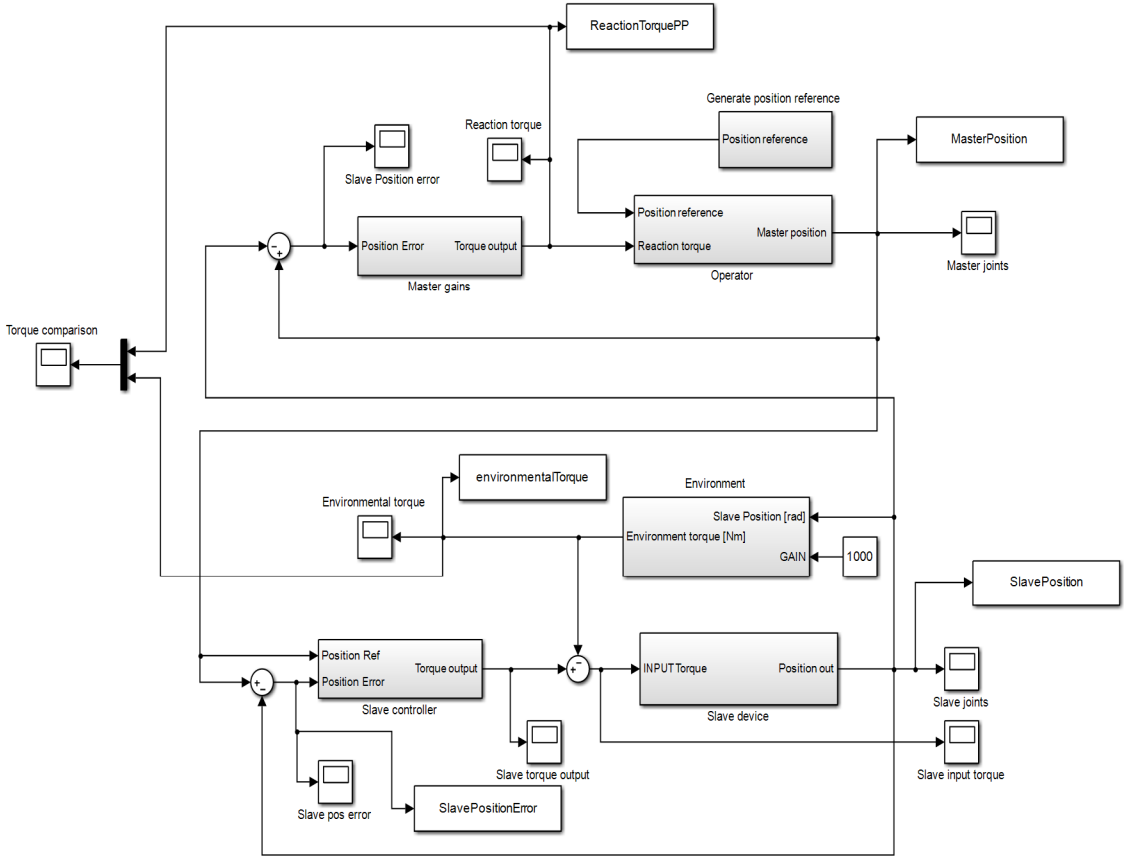

Figure 5-32. Position-Position simulator. Five main blocks are shown here, these are: The slave and slave control action, the operator action, master gains and the effect of the environment.

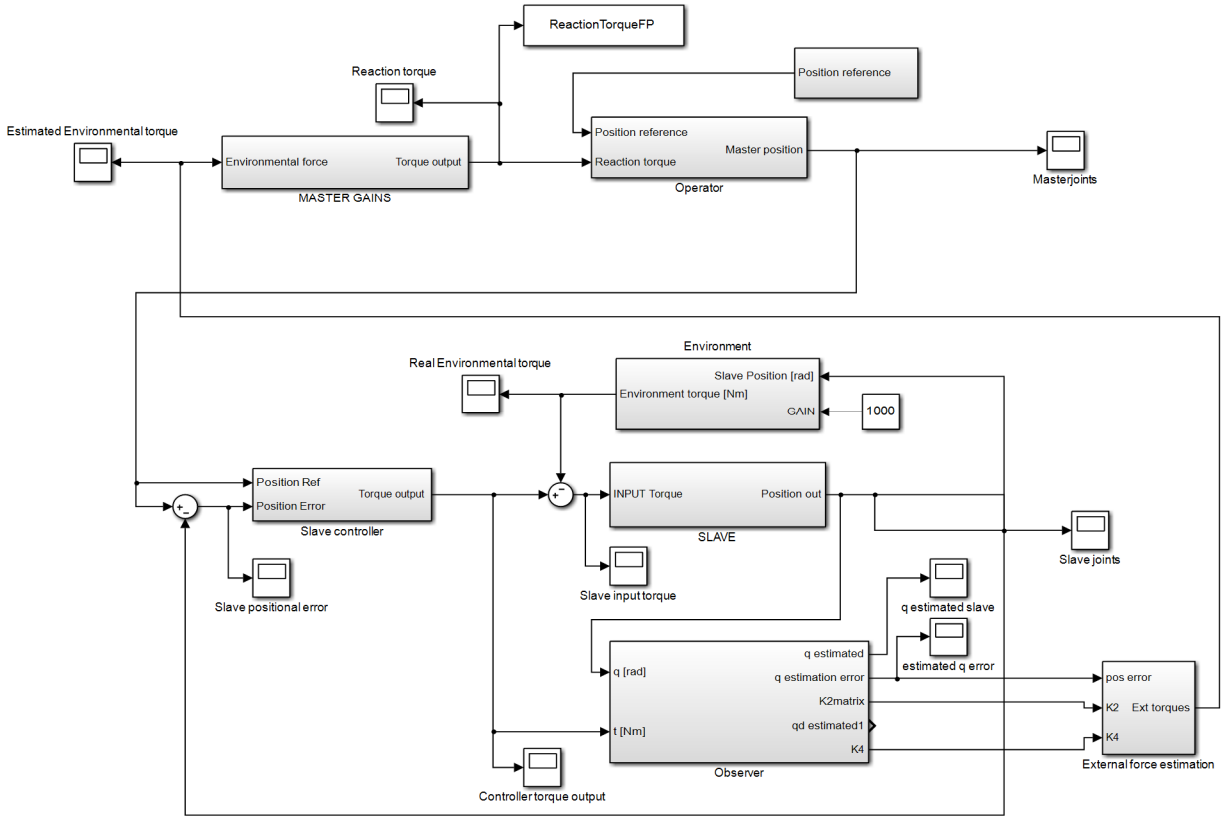

Figure 5-33. Simulator for Force-position control scheme via Luenberger-Sliding observer. In addition to the common blocks shown in position-position, this system includes the observer block and the force estimation calculations.

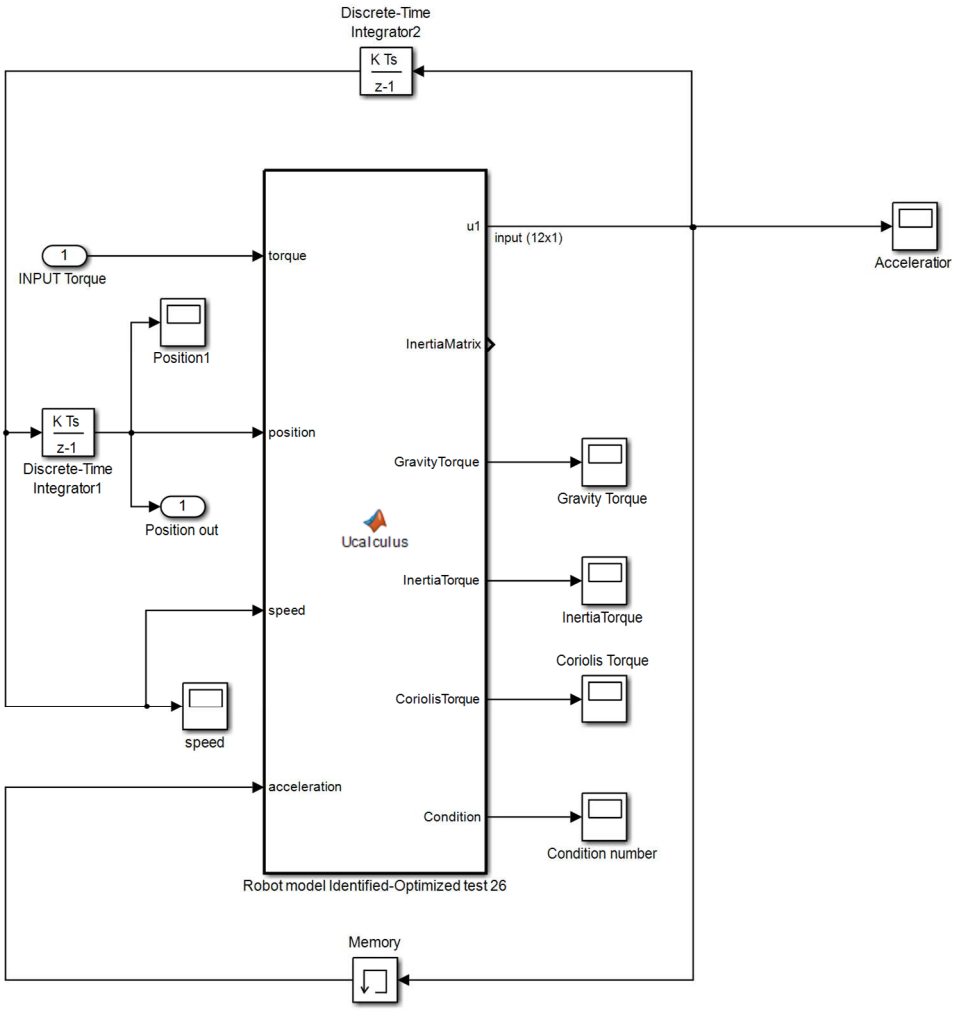

Figure 5-34. Simulink model of the Kraft hydraulic robot. An embedded Matlab function represented as a Simulink block performs the integration of the dynamic equation of a robot. The input element is the motor torque and the main output is the acceleration. After integrating, position and velocity are obtained which are used in the next steps to calculate the torque components.

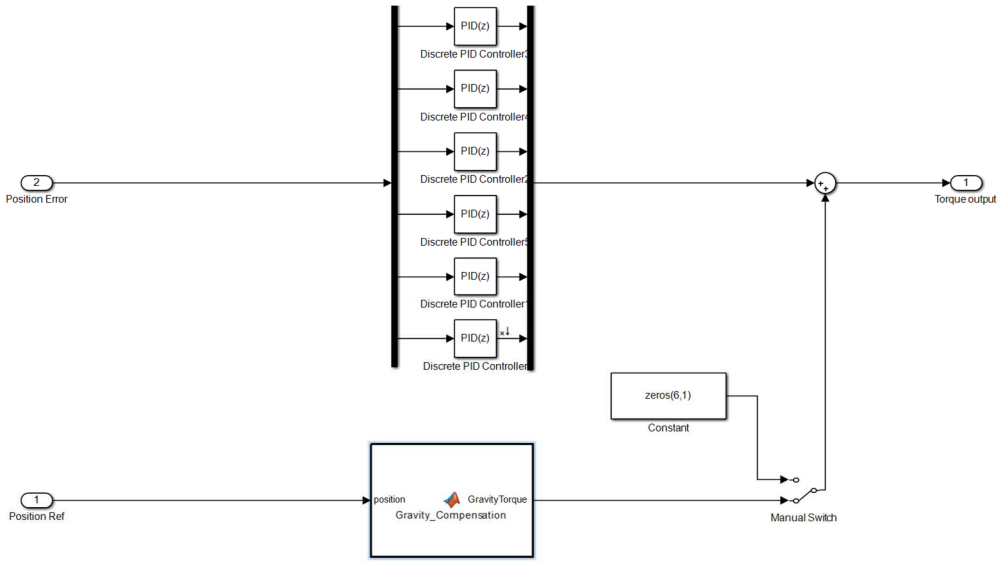

Figure 5-35. Slave controller used during the simulations of a bilateral control. An independent joint control with gravity compensation has been used for these tests.

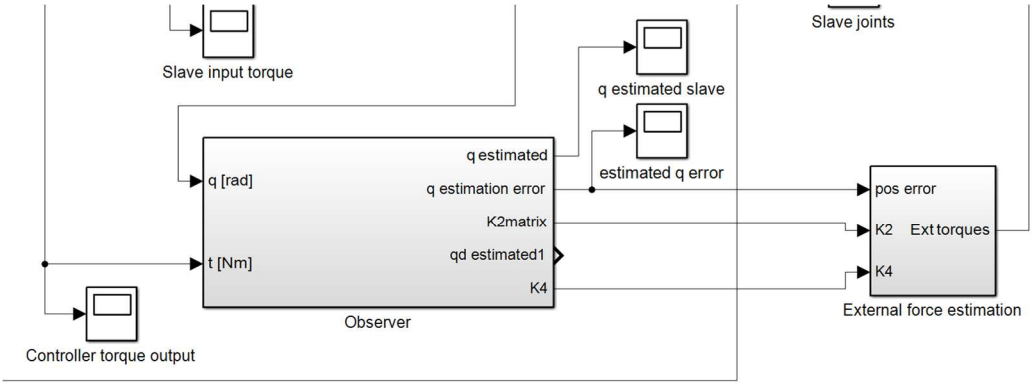

Figure 5-36. Additional blocks on the force-position teleoperation with observers.

5.6.2 Tests on bilateral control. Comparison of conventional position-position control against force-position with the Luenberger-Sliding observer.

An extensive set of tests implementing the presented approach has been performed to study the possible issues that could arise when teleoperating a manipulator with a man in the loop. The main expected issues could be derived from the calculation delays or lack of sensibility which could introduce instabilities or poor performance.

A closed loop simulation has been performed on a system including a simulated slave with its own control with gravity compensation, a human operator and the characteristics elements of the two different teleoperation architectures that are considered here, i.e. position-position and force-position. The simulated operator is closing the loop by receiving an external force and transforming it into a movement that introduces an error with respect to the ideal trajectory. In Figure 5-37 the trapezoidal reference position is shown involving 0.9 rad of angular movement of joint 2. The rest of the joints are not commanded in this test, although they are free to move in the slave robot.

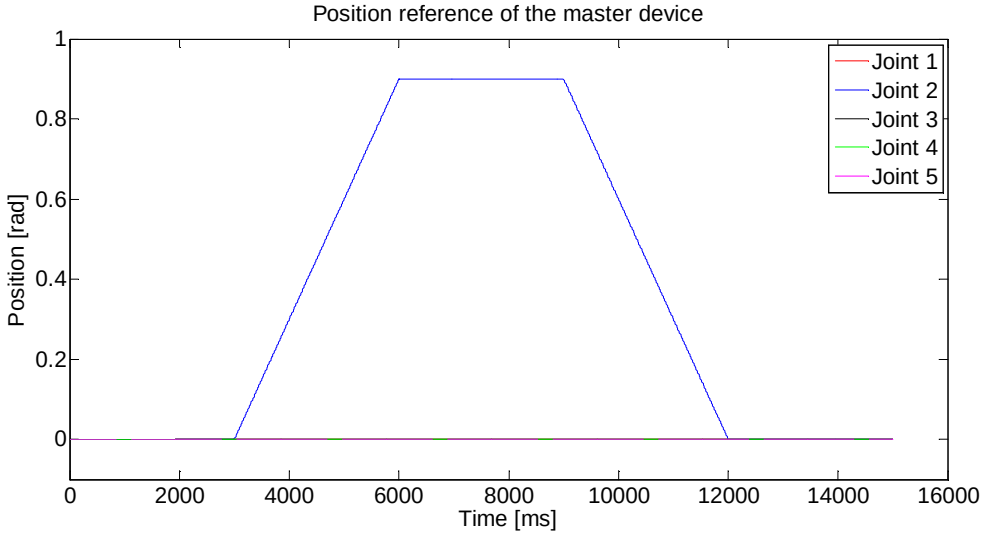

Figure 5-37. Position reference of the master device during the simulation. The reference or desired position is the objective that the human operator is trying to achieve. However, different effects act against the accomplishment of the reference. Here, a more realistic operator is considered and the action of the external forces. Those factors will deviate the operator from the desired trajectory.

A virtual force is created, simulating a real environment, whose action depends on the position of joint 2 as if that joint was acting against an external element. This is shown on Figure 5-38 and the equation that describes the behaviour of this force is given by (5.39). Basically, there is no torque until the slave's second joint reaches the position of 0.4 rad, then it receives an elastic force whose torque constant is 1000 Nm/rad until a certain value is reached in joint 2. Later, a fixed torque value of 100 Nm is added, simulating a stiff collision.

$$\tau_{ext}(q_2) = \begin{cases} 0, \ q_2 < 0.4 \ \ rad \\ 1000 \cdot (q_2 - 0.4), \ q_2 \ \epsilon \ [0.4, 0.9] \ rad \\ 1000 \cdot (q_2 - 0.4) + 100, \ q_2 > \ 0.9 \ rad \end{cases} \tag{5.38}$$

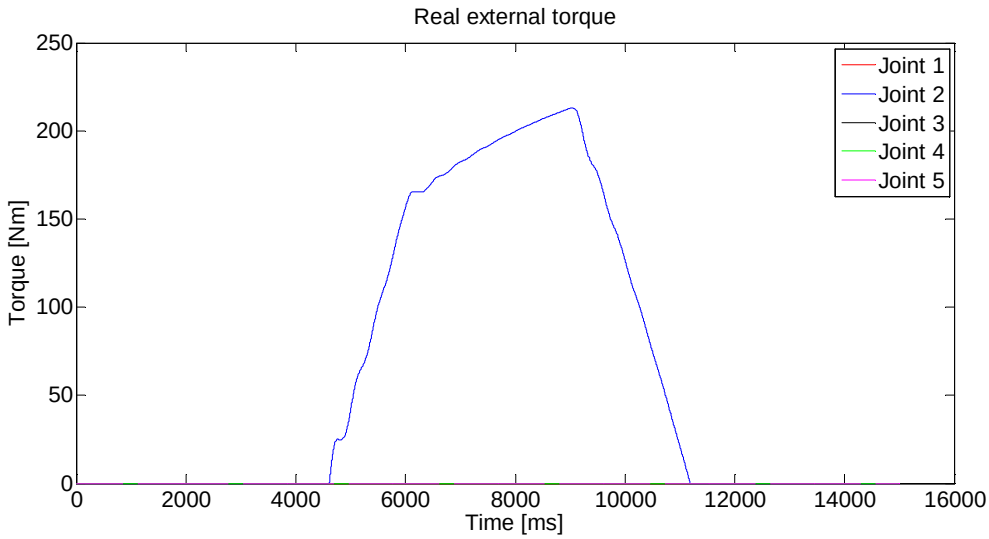

Figure 5-38. Real torque exerted by the environment on the slave device. Several stages are distinguished here. Firstly, no torque is created on the slave and it is free to move during a small distance. When the second joint value is greater than 0.4 rad, a force proportional to the distance to that value is created with a torque constant of 1000 Nm/rad. This resembles an elastic force on the slave device. Finally, if the manipulator overcomes 0.9 rad, a fixed torque of 100 Nm acts suddenly into the second joint. This can be considered as a strong collision against a very stiff surface.

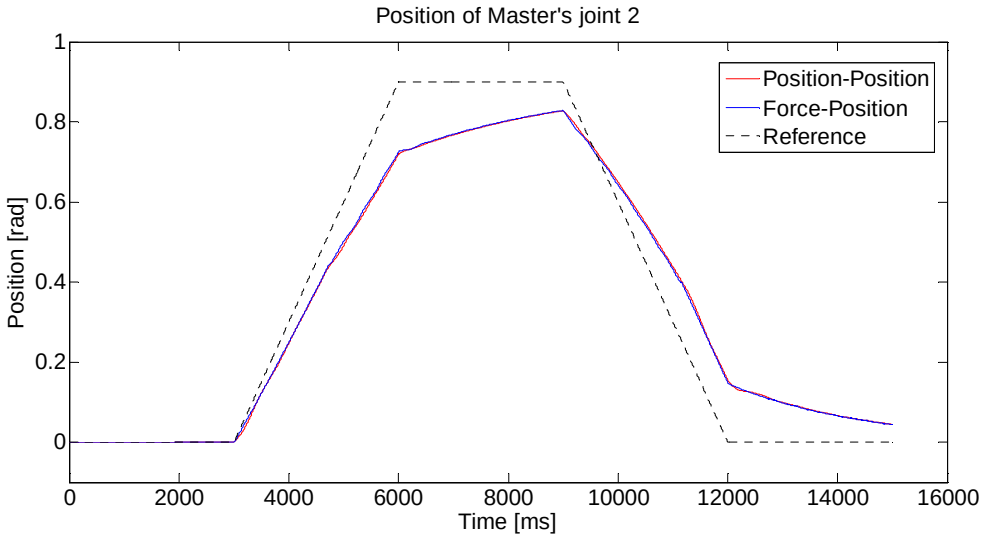

Figure 5-39. Real position of master's device second joint during the teleoperation experiment. Two control architectures are compared here against the reference, position-position and force-position with observed forces. No important differences between both methods are observed in terms on the master´s position. The ideal reference cannot be followed perfectly due to the action of the external force. The human operator has to accommodate his movement to that external action.

The action of external torques is affecting the movement of the haptic master, and the operator is trying to correct his movement against the external action. This effect can be seen in Figure 5-39. While not important deviations are obtained depending on the control methods, they both present similar divergence from the reference. This means that no difference is perceived by the operator in terms of position error, and the potential torque differences are being absorbed by the man in the loop.

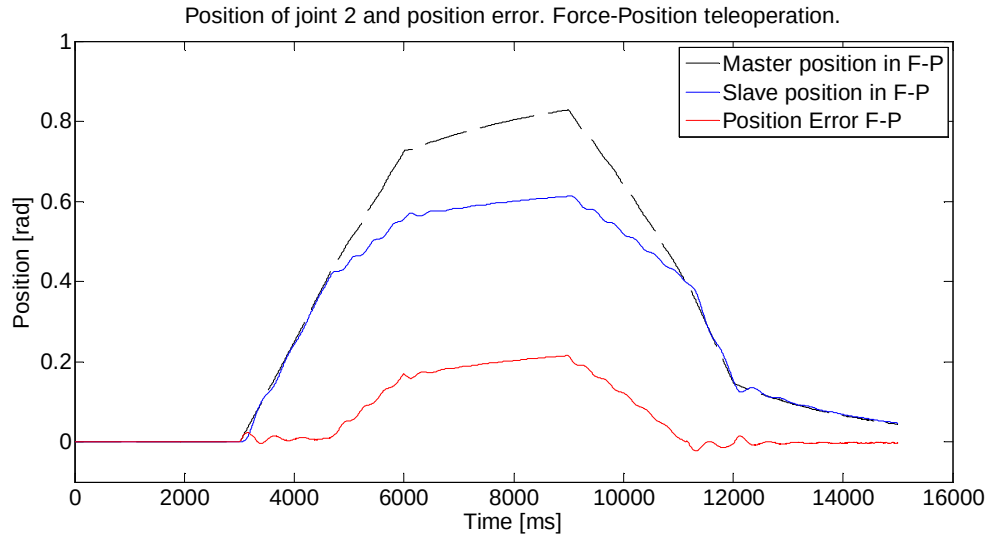

Figure 5-40. Master and Slave position for joint 2 during F-P teleoperation. The appearance of positional error is caused by the action of the external force. With gravity compensation no important position errors are obtained.

Figure 5-41. Comparison of positional errors on the slave device depending on the control architecture used. Both methods are proved to provide similar behaviour under slave's performance point of view.

In Figure 5-40 the slave's position error is represented together with the reference given by the master device and the real slave's position when performing the movement against an external force. Position errors are due to the action of this force. On Figure 5-41 both control systems are compared in terms of positional error on the slave. No differences are found. For sake of completeness, it has been included in Figure 5-42, the slave's error in absence of external forces. It is clear that the control is performing well and only slight errors are observed for both control architectures.

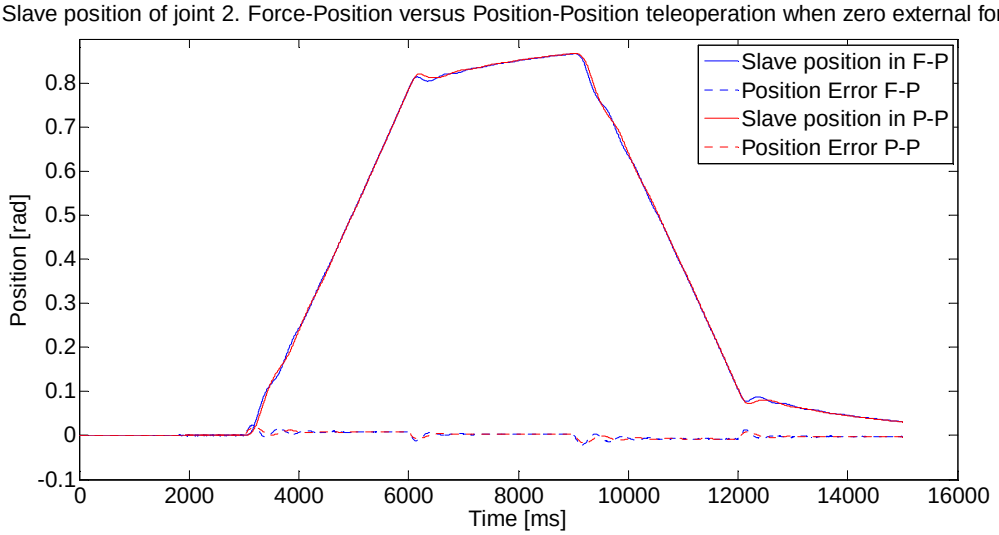

Figure 5-42. Slave position and position error in absence of external forces.

Figure 5-43 is probably the most important result of this section. In this figure the differences in force estimation for the two studied control methods are shown. The performance of Position-Position from the point of view of the force feedback depends on the slave's control performance. It is clear than the oscillations represented in the graph prove that the feedback to the operator is influenced by the control performance and in this case it is creating an undesirable effect on which is perceived by the operator. More advanced control architectures could be used, based on additional channels, to improve the performance of the force estimation by including, for example, the velocity error. However, the performance of Force-Position control via observers, depends on the observer error and it is independent on the control technique employed on the slave. Figure 5-44 complements the previous figure by giving an analysis of the force estimation error of each control strategy with respect to its own environmental force. Although the maximum amplitude of both errors is comparable, P-P maintains a constant force estimation error during most of the contact phase which is slightly superior to the error found in F-P. Also, during motion in absence of external forces, the drag effect in the classical control method is creating an inexistent torque which is eliminated by the Sliding action on the F-P technique.

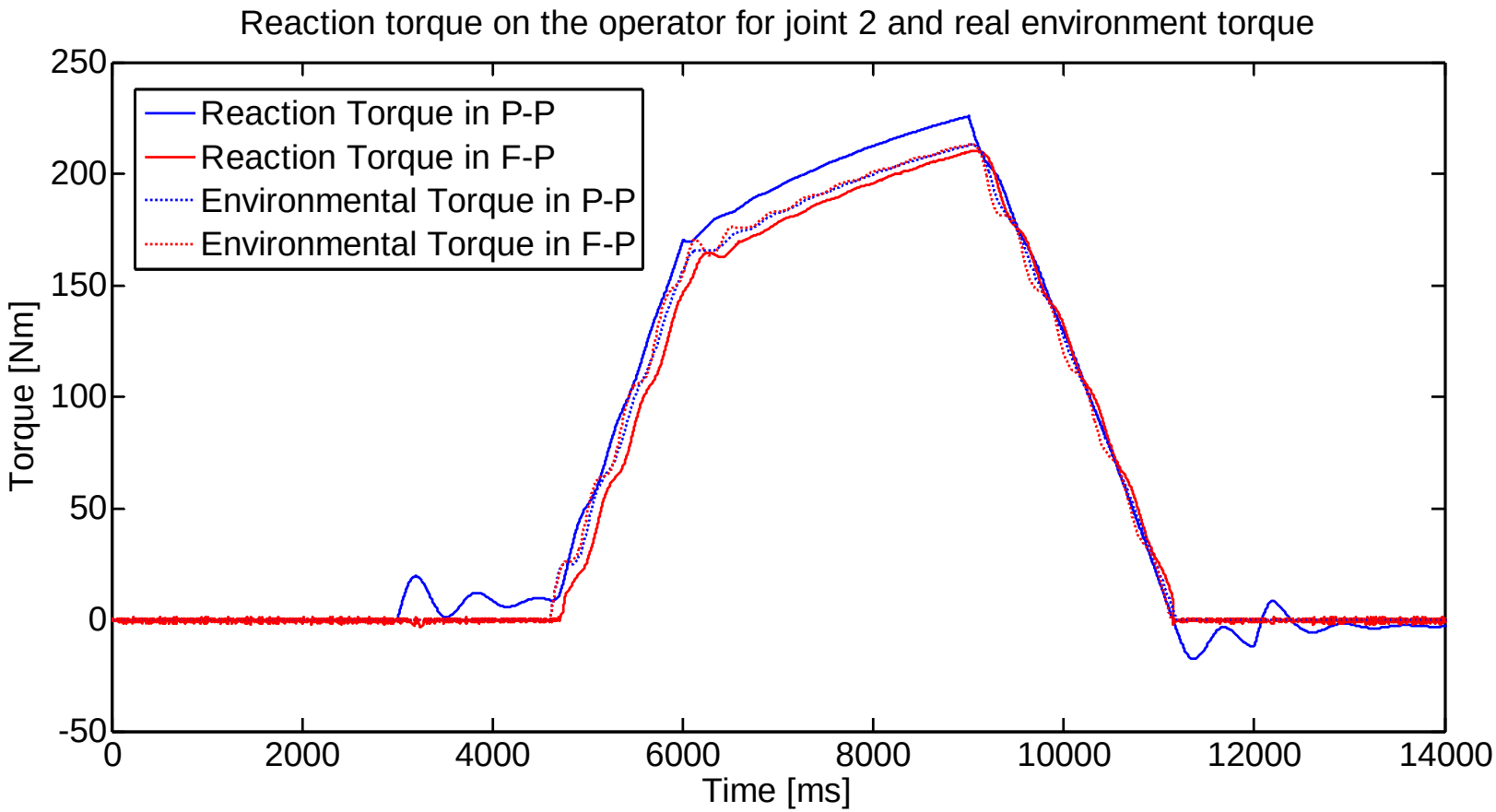

Figure 5-43. Reaction torque on the operator due to external forces depending on the control strategy. The real environmental torque for each control strategy is also shown. The last two are important to be considered since due to different control strategy and estimation method used

for the prediction of external forces, the force feedback on the operator might vary, varying as well his commanded position as a consequence of the feedback. In conventional P-P control, the force error depends on the control performance, this is, having a poor slave's control leads to a bad accuracy on force feedback. However, on F-P via observer error, the estimated torque depends on the observer error and it is independent on the control used for the slave. This effect can be seen in the oscillations of the P-P force estimation due to control errors when the robot is in movement which do not appear in the F-P algorithm.

The drawback of F-P in terms of force estimation error is the amount of noise obtained due to the chattering provoked by the sliding action. This noise effect could probably be filtered without a great dismiss of the force estimation because it only appears when the external torque is closed to zero.

During periods of non-zero external torque, the estimation error of the observer comes from modelling errors and non-optimised tuning. These modelling errors are more important on the gravity torque when the manipulator moves at low speed or is exerting a static force. However, during periods of more intense acceleration, deviations on the inertial terms of the torque become important as well. Also, it should not be forgotten that the estimation used in this approach comes from equation (5.26) which has been simplified on the terms depending on speed and acceleration to avoid the differentiation of the position and the numerical problems related with that operation. This simplification is also introducing a component of error during non-static force estimation. Nevertheless the implementation of the Luenberger-Sliding observer improves previous methods and drastically reduces the error when the external forces are zero.

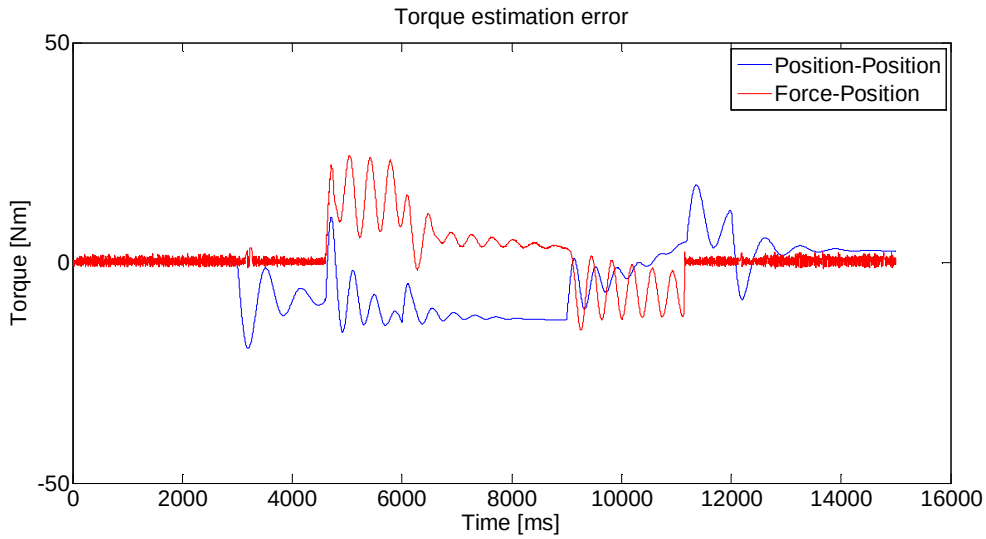

Figure 5-44. Force estimation error depending on the control strategy used.

5.7 Discussion

It has been widely explained the use of Luenberger-Sliding observers for force estimation during this chapter. Particularly when the application of force sensors is not possible due to radiation issues which impose a high dose rate that makes impossible the application of electronics in certain environments. Also, when it is not practical in terms of cost or additional wiring, this approach could be substituted by the use of

observers which do not require additional hardware and software processing other than the performed on a usual robot controller which always exists.

The pros and cons of this approach have been explained through the development of this chapter during simulations and real implementation with a hydraulic manipulator.

During the development of the chapter, the theoretical basis of the proposed observer have been explained, resulting that the external torque can be approximated by the estimation error of the observer with respect the real robot. This estimation process does not need position differentiation and then, avoids a noisy velocity and acceleration which would introduce a huge amount of noise as it has been demonstrated at the beginning of the chapter when evaluating the robotics dynamics equation. It was proved that the simple evaluation of this equation was not possible due noise problems unless the position was sampled at a much higher frequencies than those used for the bilateral loop. This approach should only be used when estimating forces during an off-line process, when for example, the determination of the end-effector mass is wanted.

Afterwards, this chapter introduced the use of Luenberger observer for estimating the internal state of a robot manipulator, a common mathematical tool. However, this observer has been proved to be also useful for force estimation by demonstrating that the observation error is proportional to the external force.

During the development of this research, it was found and proved that the only use of a Luenberger observer does not provide accurate results when the robot model is not perfectly known, which most of the cases are. Real tests were implemented on the Kraft manipulator, showing that incorrect torque offsets were introduced when the model was not perfectly known. This lead the research to the search of a more robust observer which was more reluctant to model inaccuracies. A simple but powerful non-linear observer was found, called Sliding observer which was previously used to control highly nonlinear processes. The main disadvantage of this observer was the chattering action which provoked a switching around the zero torque which created a high level of noise. This chattering action was corrected with a coefficient depending on the value of the Luenberger observer in a way that the Sliding strength was made softer when less external forces were observed and stronger when they become bigger. This proposed solution gave good results allowing the Sliding action to reduce the offset error almost totally with minimum chattering. The results were shown by estimating external forces in a manipulator and evaluating them against the measurements taken by a force sensor. During the tests performed based on spring compression, the average error on force estimation during the impact was 7% for Luenberger and 10% for Luenberger-

Sliding. The direct comparison is not totally fair since the offset errors on the Luenberger observer tend to decrease the error observed during the impact, i.e. the estimation is moved upwards. Thus, good results have been achieved and a promising solution has been identified to be used as a force estimator.

In the last part of the chapter, a simulator to study teleoperation algorithms has been presented. The simulator was developed in Simulink © to compare the classical Position-Position control scheme against the proposed solution based on observers. It was demonstrated that a similar capabilities for force estimation can be achieved with the observer method than the ones obtained by means of the conventional position error. Even less error was achieved during theoretical simulation assuming certain error on the robot model. While the accuracy of force estimation based on Position-Position depends on the slave's controller, the accuracy on the observer-based estimation depends on the observer. Luenberger-Sliding observer eliminates steady state torque estimation errors in absence of external torques, which constitutes the major improvement of this technique. With this technique, the two requirements set at the beginning of the chapter for a force estimator for teleoperation, are satisfied. An estimator with very low force offset in absence of external forces has been obtained with enough accuracy to carry out a remote handling task.

However, one cannot ignore the difficulties related to this approach. Firstly a complete robotic model is needed, and the accuracy of the force estimation will depend strongly on the quality of the obtained model. Although an important robustness has been added with the Sliding action, this is mainly concentrated during the zero external torque situations. For obtaining a decent model, useful techniques go through parameter identification and optimisation in order to give the model physical sense. Once the model is obtained, the translation to mathematical functions that could be evaluated with enough speed should not be a problem but the major difficulty resides in the correct tuning of the observer gains. It has been experienced after numerous tests that tuning on the first place the Luenberger gains and, later on, the Sliding gains was the best approach. When these last ones have been tuned, an iteration can be done to decrease the value of the previous ones in order to achieve a reduced noise observation.

No instabilities have been created with this method during the teleoperation scenarios analysed which is an excellent result.

Chapter 6 On the effect of cable length on control performance for teleoperation in radioactive environments. Implementation of solutions.

Due to the increase of the energy levels on the scientific facilities and fusion reactors such as CERN, ITER and other particle accelerators, it has been foreseen that the maintenance operations will be carried out remotely. In case of ITER the total amount of maintenance operations will be performed by remote means, either by pre-programmed routines or with the man in the loop. At CERN, the remaining operations performed manually have to be progressively substituted by remote handling means. The robot controller is conveniently sheltered far from the radioactive area, in dedicated rooms, which can be hundreds of meters away from the operations zone. In this chapter, the drawbacks of increasing the cable length on motor safety and performance are presented and a list of possible solutions is analysed. Several solutions are tested on a motor test bench and on simulation. The preferred one has been selected for further study. An extensive set of tests has been designed to analyse the influence of the proposed solution on the control performance of a brushless motor, which is the most common option for electrical manipulators. The result of the extensive set of trials prove that the preferred solution does not alter significantly the control performance of the motor and can be implemented on teleoperation when using most common control methods.

6.1 Introduction

Since radiation levels in most modern nuclear facilities or nuclear experiments are increasing dramatically, new protection measures are needed and the use of remote handling techniques becomes crucial. For example, the radiation conditions inside the ITER vessel (See Figure 6-1) impose that the remote handling equipment entering into the tokomak shall not contain any conventional electronic devices (See Chapter 1). For that reason, power and control drivers for electrical motors (called "servo-drives") must be mounted in cubicles placed at distant locations with respect to the remote handling equipment under control. In these circumstances the cable length for this equipment is expected to be significantly longer than the typical values recommended by the manufacturers. On [139] Allen-Bradley recommends maximum distances based on the insulation rating of the motor, and establishes limitations on 15 m for a 1000 Volts peak-to-peak insulator rated, 40 m for 1200 Vpp and 170 m for 1600 Vpp. On this document it is mentioned that longer distances can be achieved with special devices connected to the drive output. For Delta Tau drives [140] used for controlling Dexter manipulator, maximum distances of 15 m are recommended for 480 V drives and 60 m for 230 V. ABB [141] recommends a maximum length of 50 m for its ACS 150 when driving a motor without any external protection.

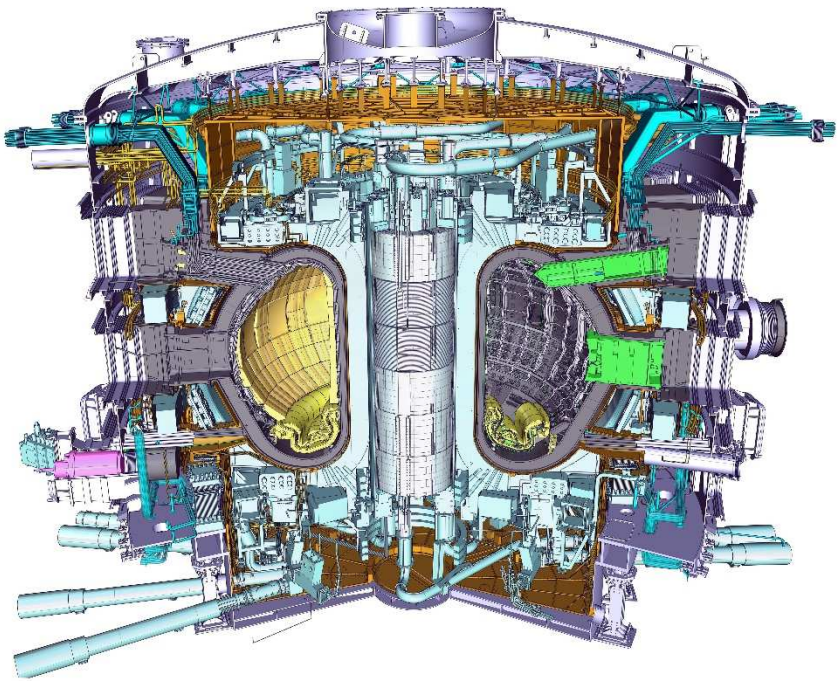

Figure 6-1. ITER: The world largest Tokomak. Retrieved from www.iter.org on 28/04/2015.

When commanding servo motors with a PWM output via long cables, a well-known effect in transmission line theory arises, called reflections or standing waves. Two main issues may appear from this when teleoperating these devices. Firstly, the safety of the system drive and motor can be compromised, and secondly, a reduction on the motor control performance with the effect of noise, vibrations and oscillations. When the remote handling equipment is accomplishing critical activities such as dexterous manipulation, the effect of the noise, vibrations and oscillations could lead to unacceptable performance.

In this chapter, a theoretical introduction on the effects of PWM signals over long cables will be given. Then, a summary of the main solutions to deal with this issue is explained. Afterwards, the results of an extensive set of measurements to characterise the effect of the standing wave in form of overvoltage is shown. On the third part, simulations have been performed to identify adequate solutions for this problems. Finally a commercial solution is selected and the core of this chapter is focused on evaluating the performance of this solution according to different aspects such as the overvoltage reduction and the effects on the control quality of that device. In order to analyse the efficiency of this device, an extensive set of trials has been designed. Different control methods are tested, such as torque control and velocity control.

6.1.1 Standing waves in PWM drives

The inverter of the PWM (Pulse Width Modulation) drives does not produce sinusoidal output voltage waveforms; instead, it generates a continuous train of pulses which are transmitted to the motor terminals via the motor cable. Peak pulse voltage at the drive output is equal to the drive DC bus magnitude (V_{bus}) and it is characterised by the step rise and fall times (t_{rise}, t_{fall}) controlled by the GTO, BJT or IGBT semiconductor switching device used. The peak pulse seen at the motor end is not necessarily the V_{bus} sent by the drive as it depends on a combination of factors which define the whole system behaviour. These factors are, the t_{rise} and t_{fall} characteristics of the PWM, the cable transmission line characteristics, cable length and motor impedance [142]. Theoretically [142] peak voltages up to twice of the V_{bus} can appear at the motor end of the cable, although in other references [143], more than double of that voltage is observed in practical experiments. Unfortunately is not straight forward to derive theoretically the effects of a combination of factors on the standing wave magnitude and a practical study is recommended.

The PWM pulse rise times are so short that time needed for the signal to travel to the motor can easily exceed the rise time. The velocity of the pulse is close to half of the

speed of light, typically $1.7 \cdot 10^8\ ms^{-1}$, so in 100 ns it has travelled only 17 m. When this happens, one needs to rely on the transmission line theory. This mechanism follows basically these steps:

- At each pulse, the drive has to charge the characteristic inductance and capacitance of the cable. This pulse of energy travels at a speed characteristic to the cable, which typically is around $1.7 \cdot 10^8\ m/s$, approximately half of the speed of light.
- When the pulse reaches the motor end of the cable a reflection occurs because of the step change in impedance (that of the motor is almost invariably much higher than that of the cable). This effect is more pronounced with small motors due to their higher impedance, consequently they constitute the critical conditions for the cable length issue. The voltage tends towards the double of the initial step magnitude.
- The impedance of an induction motor Z_{load} is not well documented, not easily measured, nor well understood, since it requires a new high frequency induction motor equivalent circuit that is dominated by stray winding parameters. Experimental results show motors $<$ 5hp have a surge impedance of 2kΩ to 5kΩ, a 125 hp motor has around 800 Ω, while a 500 hp motor has a load surge impedance in the vicinity of 400 Ω [142]. Note that typical cables are $<$ 200 Ω. A possible explanation to this effect is the skin effect. This effect results from the fact that at high frequencies the real conduction area is limited to a very thin volume which in case of small motors is even more reduced due to the small cable section.
- The reflection returns to the drive where it is reflected again but with reverse polarity, and when it returns to the motor, it cancels the over-voltage. More detail of this effect can be found in [143]. Therefore the overshoot lasts about twice the time of flight in the cable. If the rise time of the pulse is longer than twice the time of flight in the cable, the overshoot is cancelled before it reaches 100 %.

A measure of the overshoot size that can be caused in the motor end of a cable is defined has a "Reflection Coefficient", Γ, and it is a function of the cable surge impedance (Z_0) and the load surge impedance (Z_{load}) presented at the receiving end of the cable [142].

$$Vmotor_{end} = (1 + \Gamma)\ Vdrive_{end} \tag{6.1}$$

$$\Gamma = \frac{Z_{load} - Z_0}{Z_{load} + Z_0} \tag{6.2}$$

$$Z_0 = \sqrt{L/C} \quad \text{(assuming lossless cable)} \tag{6.3}$$

$$Z_0 = \sqrt{\frac{R+j\omega L}{G+j\omega C}} \quad \text{(real cable)}$$

Where L is the cable inductance per unit length of cable and C is the cable capacitance per unit length of cable. Whenever the cable surge impedance does not match the surge impedance of the motor, a reflected wave will occur at the motor terminals.

6.1.2 Effects of the Standing waves in drives, motors and control performance

It has been found in the literature that the effect of the voltage overshoot on the motor end has little effect in the main motor insulation systems between phases and from phase to earth, which are designed to withstand large overvoltage pulses. This may only become a problem with some small low-cost motors whose insulator has not properly chosen [144]. In that research, it is mentioned that the effect on the inter-turn insulation and between windings turns should not be very harmful except in small motors when the coils ends are in close proximity. However there is a set of requirements defined for cables transporting PWM signals [145] which fixes the insulation depending on the rise time of the signal and voltage. In [142] it is mentioned that the long term use of long cables with PWM over-voltages can reduce the life expectancy of the cables. Standard insulation voltages ratings are 600 Vrms (850 Vpk), 2 kVrms and 5 kVrms, with 1 kVrms available on a limited basis. But reflected wave stress of 2 to 2.4 times the Vdc on 480 V systems is 1300 to 1560 Vpk. A concern is whether a 20 year service life of a 600 V rated cable is achievable with 2 to 2.4 p.u peak repetitive reflected wave stress.

In the literature, little is mentioned about the effects of the reflections on power drives, however it has become the weakest point of the chain on this research. What is more, it has constituted the only point of failure during the trials.

There is a common agreement in the literature about the adverse effects in motor control when using long cables due to overshoot voltages. In [146] a different set of cables are simulated with a PMSM (Permanent magnet synchronous motors) motor in Matlab ©. They implement a PI regulator and study the influences on the control performance during velocity control. The results show speed controller rejects load disturbance faster at shorter cable length. In a different test, loading the motor at a certain instant with a constant torque, they prove that steady state error is increased when the speed is lowered. However, on the author's knowledge, there is no information

in the literature about experiments evaluating the control performance under real standing waves.

6.1.3 Established solutions to the reflected wave issue

In order to protect drive, cables and motors from the overvoltage caused by reflections the obvious solution would be to reduce the bus voltage [142] with respect the cable insulation rating. Even with 100% overshoot in voltage, an IGBT drive with 300 Vdc bus can use a standard 1000 Vpk cable since the overshoot of 600 V will be far from the cable insulation limits. When this is not possible most solutions are based on inserting special electronic devices to reduce the standing wave via impedance matching, filtering or active modification of the PWM pulses [150], [149].

Simpler solutions consist in an output reactor at inverter end. In [142] it is proved how this approach modifies the reflected waveform by changing it into a less destructive wave with slower rise-time and possibly a reduced amplitude. The reactor equivalent core resistor provides damping to the circuit. The disadvantage of this solution is the potential introduction of a voltage drop at the fundamental output frequency. This effect would reduce the ability of the motor to provide the rated torque. The overvoltage suppression is almost proportional to the reactor impedance, and a high value of impedance will cause an increase in cost and weight, and it will also deteriorate the drive systems' power factor.

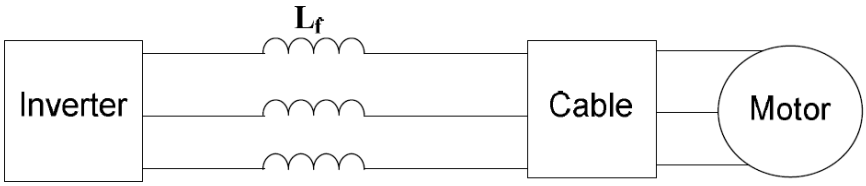

Figure 6-2. Output reactor at inverter end.

The effects of adding a reactor at motor end are similar to those of adding a reactor at the drive end. A very interesting solution mentioned in [142], [147] is the potential installation of $\frac{dv}{dt}$ filters which transform the PWM driver output into a smooth sine wave. These filters combine appropriate R-L-C components to form a damped low pass filter. The critical distance for a sine wave is around hundreds of kilometres so the voltage at the motor end will match the voltage at the drive end. The major drawback of this system, apart from the cost, is that although the line to line voltage waveform is sinusoidal, it has been found that the motor stator neutral to ground voltage widely

overshoots Vdc because the new inductance of the filter resonates with the line to ground capacitance.

A low-loss LC filter clamped by diode bridges, as shown in Figure 6-3, has been put forward in [147]. For this filter, the LC resonating voltage is clamped to the dc-bus voltage by virtue of the fast recovery diodes, and the rising time of inverter output voltage can be controlled by the values of L and C of the filter. Compared with the traditional LC filters, the physical dimensions of diode clamping filters are smaller. Moreover, the power losses in the clamping circuit are decreased in comparison to the losses in the damping resistors of RLC filters [147].

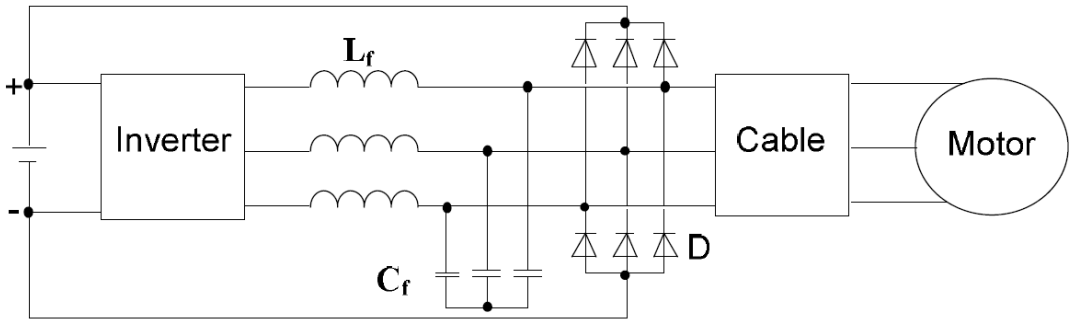

Figure 6-3. LC clamp filter with diode bridge at the inverter terminal.

A cost effective method for controlling the voltage reflection is a termination network or a terminator device that removes impedance discontinuities to maintain the reflected waveform below potentially destructive levels. A terminator device is installed in parallel with the motor and based on the transmission lines theory, it loads the receiving end of the cable with a Z_{load} ohmic resistor value equal to the cable Z_o, which makes $\Gamma = 0$ in (6.2) and eliminates the reflected wave.

6.2 Experimental analysis of reflections on the system safety and performance

In order to study the magnitude of the reflections on a real setup and its hazardous effects, an experimental test bench has been designed and commissioned. This system reproduces the conditions that could be found on a manipulator based on electrical motors, performing telerobotics operations on a scientific facility or fusion reactor.

6.2.1 Experimental setup and equipment

The proposed test bench cabling setup is composed of the elements described in the electrical diagram shown on Figure 6-4. In order to study the effects of long cables in motor safety and control performance, two different types of motors were selected, termed “tested motor” and “load motor” respectively. The load motor is used to convey resistance torques which are varied very accurately depending on different parameters.

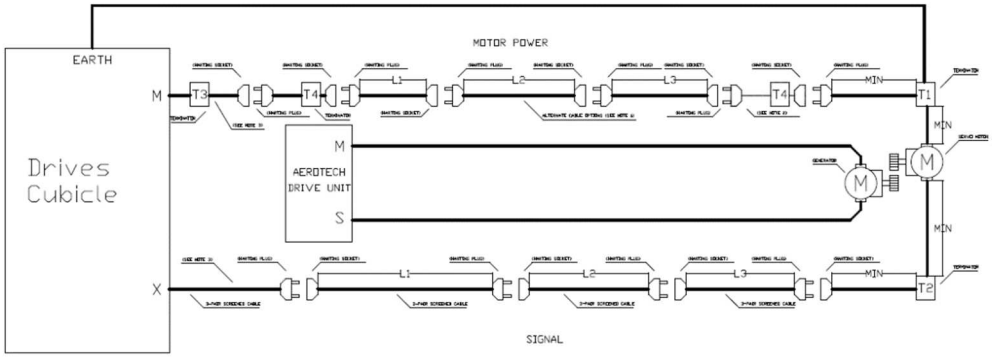

Figure 6-4. Electrical diagram of the test.

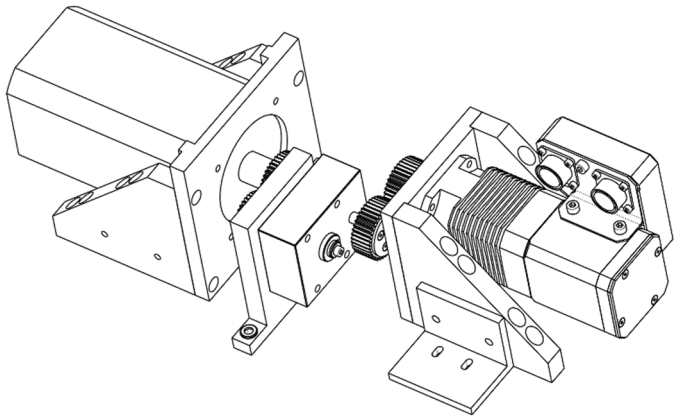

Figure 6-5. CAD design of the test. Load and motor are coupled via gearbox.

Both motors are coupled together by means of gears for three primary reasons: firstly to reduce the effects of the rotors’ misalignment from the solution based on coupling both motors to the same shaft. Also, avoiding the possible effects of shaft bending and the convenience of reproducing the real conditions led the test design to a gear based implementation.

Section	Cable length [m]
Short	5
Long	100(95+5)
Very long	200
Extremely long	300 (200+95+5)

Table 6-1. Length of selected cable sections.

The power cable for the tested motor will be composed of 4 different lengths described in Table 6-1. On Figure 6-4 the cabling setup is explained. The main motor can be powered via different cable lengths which are varied to study the influence of the distance on the reflected waves. The positional feedback cable was varied accordingly.

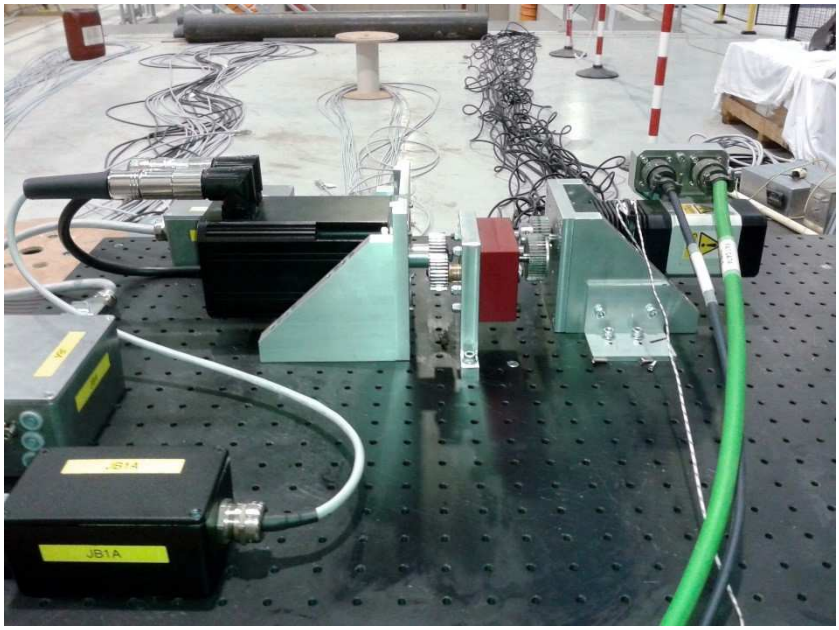

Figure 6-6. Experimental equipment with the long cables.

The experimental equipment of Figure 6-6 consisted on the following elements:

- Oscilloscope, Iso-Tech IDS8104 Calibrated
- LCR meter, Agilent U1733C Calibrated
- Tektronix P5200A Differential probe Calibrated
- TH10A hall effect current sensors mounted in a measuring box.

- PC with Signal Express, © National Instruments and Soloist © Aerotech drivers.
- Resolver cables, Niltox LF-316, 3-pair screened cable 0.5mm².
- Power cable Niltox LF-329 LSHF
- Tested motor drive, Delta Tau drive GPH 102.
- Load motor drive, Aerotech Soloist Hpe
- Infranor motor XtraforsPrime FP0609, 400V.
- Set of gearbox and gears with a total transformation ratio of 3:28.
- Supporting structure for motors.

Parameter	**Units**	**Value**
Nominal voltage	Vo/V	300/500
Max voltage AC and 3 phase	V	-
Peak value	V	-
Test voltage	V	2000
Insulation resistance	MΩ/km	-
Coupling resistance	M/km	-
Radiation resistance	Mrad	-
Insulation material	-	-
Cores x cross-sec	n x mm2	7 x 1.5
Screening	-	Double
Capacitance core/core (specified)	nF/m	-
Capacitance core/core (measured in 5m length)	nF/m	0.113
Capacitance core/screen (specified)	nF/m	-
Capacitance core/screen (100 Hz, measured in 5m length)	nF/m	0.153
Resistance core (100 Hz, measured in 5m length)	Ω/m	0.0167
Resistance core (120 Hz, measured in 5m length)	Ω/m	0.0167
Resistance core (1 KHz, measured in 5m length)	Ω/m	0.0169
Resistance core (10 KHz, measured in 5m length)	Ω/m	0.0194
Inductance core (100 Hz, measured in 5m length)	mH/m	0.0015

Characteristic impedance assuming lossy line (13.554 KHz)	Ω	100.1710
Attenuation constant (13.554 KHz)	Np/m	1.012E-04

Table 6-2. Characteristics of the Niltox LF-329 LSHF power cable use don the experiment. Some of those values were given by the manufacturer but most of them were experimentally acquired with a calibrated LCR meter.

Details on the internal characteristics and impedance of the power cable can be found on Table 6-1. Each one of the motors was commanded with a different motor controller and drive. The oscilloscope was utilised with a differential probe to measure the voltage waveforms on the motor end and the drive end. The Infranor motor was equipped with resolver because this is the main feedback method in radioactive environments. In these scenarios, the use of electronic devices such as encoders is forbidden.

6.2.2 Drive, motor and cable safety conditions. Voltage at drive and motor ends.

In this section, oscilloscope captures of the PWM waveform in both drive and motor ends are shown and explained. The measurements represented on each image have to be scaled by a factor of X 500 in order to convert them to volts due to the reduction factor applied on the oscilloscope probe.

A.) 5 m of cable

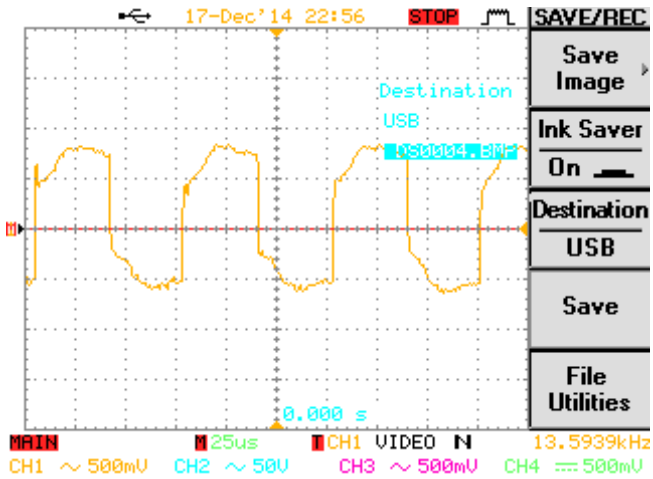

Figure 6-7. PWM waveform on the power cable with 5 m length at drive end. Time length of 25 us for each square on the horizontal axis.

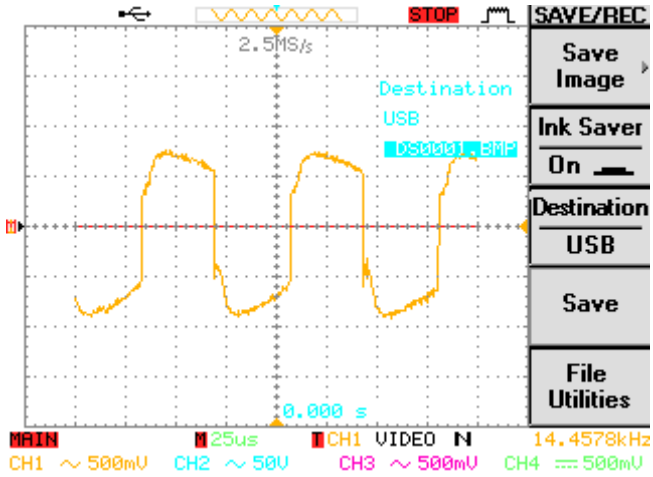

Figure 6-8. PWM waveform on the power cable with 5 m length at motor end. Time length of 25 us for each square on the horizontal axis.

B.) 100 m of cable

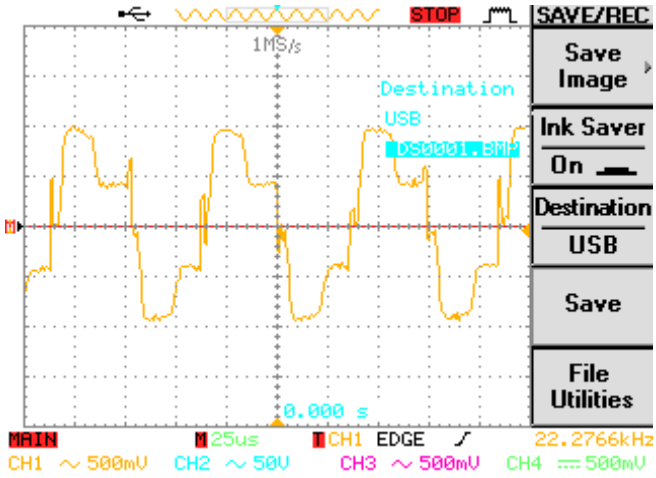

Figure 6-9. PWM waveform on the power cable with 100 m length at drive end. Time length of 25 us for each square on the horizontal axis.

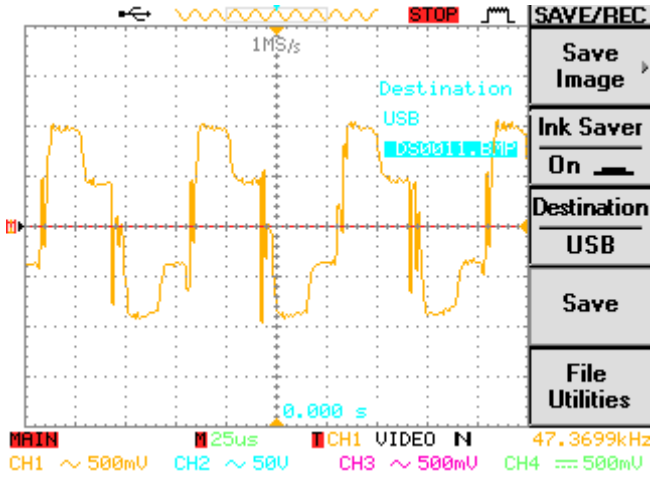

Figure 6-10. PWM waveform on the power cable with 100 m length at motor end. Time length of 25 us for each square on the horizontal axis.

C.) 200 m of cable

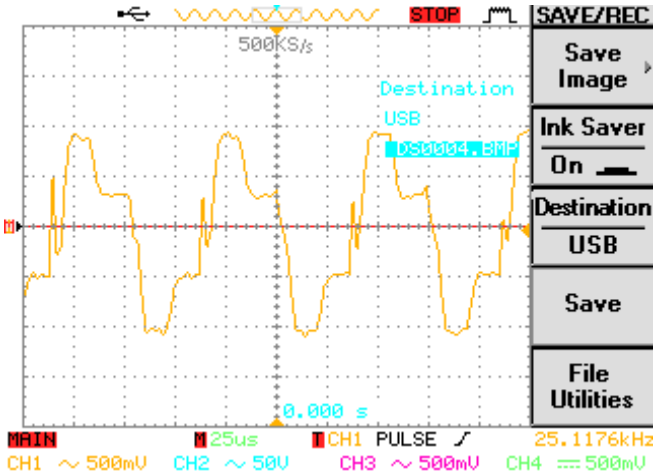

Figure 6-11. PWM waveform on the power cable with 200 m length at drive end. Time length of 25 us for each square on the horizontal axis.

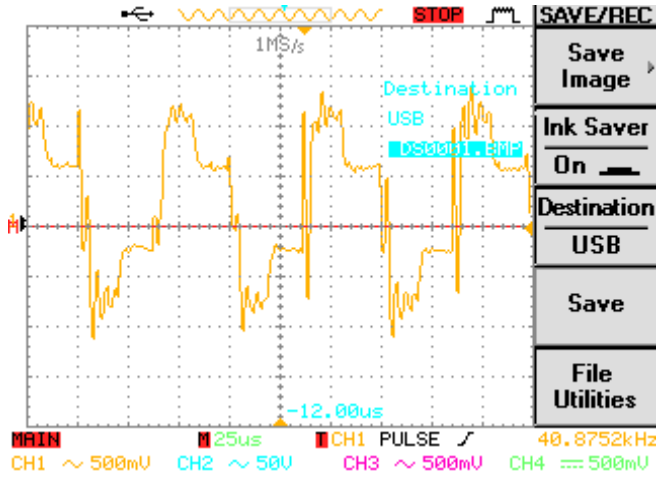

Figure 6-12. PWM waveform on the power cable with 200 m length at motor end. Time length of 25 us for each square on the horizontal axis.

6.2.2.1 Issues found during motor testing related to cable length

During the testing of 5 m cables no problems were found and the experiment could be accomplished successfully. When the cable length was progressively increased, some difficulties were found.

Residual current device protection tripping

The residual current protection started tripping when the cable was changed from 5m to 100. The control cubicle was designed with a Siemens 3+N Pole Type AC Residual Current Circuit Breaker, 25A, 30mA. This device had to be substituted for a new one with sensitivity of 300 mA. After this change, no further problems were observed.

Motor drive failure

When the cable length was increased to 200 m, and after 2 minutes of testing, the drive failed giving a “C” code fault. This error code means:” DC bus fault, or no voltage input, voltage has dropped below the permissible threshold”. This error is believed to be produced by the accumulative effect of the reflected wave on the drive components. It was not necessarily caused by the 200 m cable explicitly because the standing wave amplitude of 200 m does not differ much from the 100 m as explained above. The experiment had to be stopped and the drive sent to be repaired.

6.2.2.2 Discussion on the standing wave voltage depending on the cable length

Considering the 5m length cable as the unitary value, with amplitudes of PWM values of approximately 650 V, the differences on voltage levels when this distance is increased will be analysed further.

From the oscilloscope measurements, it can be seen how the reflected wave amplitude increases greatly when the distance is increased to 100m. In relative terms, the change observed on the amplitude is approximately of 150%, reaching to 1000 V in both cables. When varying the length from 100 m to 200 m it was found that no additional increase on amplitude is observed on the drive end. However, slightly greater readings are registered on the motor end, reaching in worst cases 1250 V, which constitutes a 190 % of the original amplitude with short cable. This result proves one of the main assertions of the reflected wave theory, which establishes that the motor end is the critical point on the transmission line. The reflected waves are attenuated on their way back to the motor controller.

For medium or short distances there appears to be no great differences on the voltage depending on the cable length and only a slightly major harmonic content can be seen on the waveform of motor end. This effect increases substantially when the length is increased to 200 m, at this point the harmonics content on the motor end is a significant component. In Figure 6-12 it can be seen how harmonics of higher frequencies increase its amplitude with respect the input end and shorter lengths. The original wave is distorted more when the length is increased but specially on the motor end. One possible explanation of this difference is the attenuation of the smaller harmonics when the wave returns to the drive end due to the cable impedance.

Due to the strong overvoltage observed and the breakage of the motor drive, no further testing was accomplished on terms of control performance without protection means. For this reason it is not necessary to evaluate the worsening on control performance of electric motors when commanded with long cables without any means of copping with this effect. The overvoltage is so harmful for the drive and motor that it is not practical to drive a manipulator in these conditions without implementing any corrective action.

6.3 Implementing a corrective action against the standing wave. Simulation on PSPICE.

In order to limit the number of possible solutions to the reflected wave issue and to find adequate values for the electronic components involved, a complete set of simulations were performed using Orcad and PSPICE. Several alternatives were evaluated based on the most critical components, this is: controlling a low-power motor with 300 m of cable. All the simulated circuits are based on an idealized PWM waveform with trapezoidal profile and a frequency similar to the real conditions measured as appear on the Delta Tau drive. The PWM frequency of the drive that was selected was 13.554 KHz, which is a compromise between the maximum frequency recommended by the manufacturer for the particular drive model used and the minimum frequency required to drive the motor.

The minimum PWM frequency of a system is based on the time constant of the motor. In general, the lower the time constant, the higher the PWM frequency should be. The motor time constant is calculated by dividing the motor inductance by the resistance (phase-phase). The minimum PWM Frequency is then determined using the following relationship [148]

$$\tau_{sec} > \frac{20}{2 \cdot \pi \cdot f_{PWM}} \tag{6.4}$$

Where $\tau_{sec} = \frac{L_h}{R_{ohm}}$, L_h is the line-line inductance of the motor in Henries whereas R_{ohm} is the line-line resistance of the motor in Ohm. By isolating the PWM frequency it yields to (6.5).

$$f_{PWM}(Hz) = \frac{20 \cdot R_{ohm}}{2 \cdot \pi \cdot L_h} \tag{6.5}$$

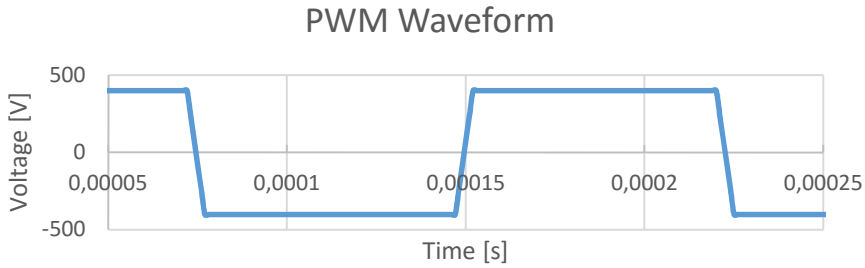

Figure 6-13. Simulated PWM waveform.

And evaluating (6.5) with the motor parameters given by Table 6-3 a minimum PWM frequency of 12.4 kHz is obtained. Infranor motor parameters for calculating the minimum PWM frequency. Equations (6.4) and (6.5) establish the minimum PWM frequency so that the current ripple is negligible. Maintaining the PWM period several times lower than the electrical time constant of the motor windings guarantees that the inductance of the windings is not charged and discharged on every PWM period. Furthermore, several PWM periods would be needed to charge and discharge it, reducing the current ripple for a PWM waveform. This minimum PWM frequency should not be confused with the minimum frequency when the motor is being driven by a sinusoidal current, value which depends on the required dynamic performance of the motor.

Inductance Line-Line (Measured)[mH]	1.25
Resistance Line-Line (Measured) [Ohms]	4.9
Time constant [s]	2.56E-04
Minimum PWM frequency [Hz]	12437.94

Table 6-3. Characteristics of the Infranor motor.

The equivalent circuit per phase of 300 m of Niltox power cable, drive and stall motor is shown on Figure 6-14. The inductance, resistance and capacitance per unit length are also displayed at 16 KHz. This equivalent circuit has been used for all the simulations performed.

It is also important to estimate the maximum electrical frequency of the motor, this can be done with equation (6.6).

$$f_{electrical\ MAX} = \frac{P \cdot \omega_m}{2\pi} \tag{6.6}$$

Where P is the pair of poles of the motor and ω_m is the maximum foreseen mechanical speed in rad/s.

For example, for the Infranor motor, and assuming a maximum speed of 1000 deg/s, substituting into (6.6) leads to:

$$f_{electrical\ MAX} = \frac{8 \cdot (\frac{1000 \cdot 2\pi}{360})}{2\pi} = 22.2\ Hz$$

Ideally, the equivalent sinusoidal current of the PWM should be able to provide at least that electrical frequency, so that the motor can run at desired speed. In case of using a PWM filter, the cut-off frequency shall be greater to that value.

In Figure 6-14 the equivalent circuit for one electrical phase of 300 m of cable, drive and stall motor is shown. The values used for the cabling resistance, capacitance and inductance were taken from the measurements carried out on the Niltox 329 cable at 16 KHz which is a realistic frequency for a common inverter. By building the equivalent circuit with a series of π-shape circuits it is possible to study the behaviour at intermediate points and to perform a more realistic simulation. With this model as a starting point, several solutions for the standing wave were implemented and tested.

In Figure 6-15, the output of the simulated circuit of Figure 6-14 is presented. The PWM waveform with the correct output voltage is highlighted in red, and on green line the output voltage at motor end. It is very noticeable how the reflections produce a multiplication effect of the voltage up to 1.3 kV and at higher frequencies than the PWM.

6.3.1 LC filter

On Figure 6-16 an implementation of an LC filter has been simulated. Resistors have been included on the model with the objective of reproducing the behaviour of real and non-ideal components. The cut-off frequency of this filter was placed on 1300 Hz based on equation (6.7).

$$f_c = \frac{1}{2\pi\sqrt{L_f C_f}} \tag{6.7}$$

Where L_f and C_f are the inductance and capacitance selected for the filter. For a 5μF capacitor and 3 mH inductor, the resulting cut-off frequency is: 1299 Hz. The simulated effect on the motor voltage is shown on Figure 6-17 The good results for reducing the standing wave effect are noticeable. The main action of the filter is transforming the high frequency of the inverter into a smoother sinusoidal wave whose main harmonic is equal to the electrical frequency of the motor. With this approach, the cut-off frequency shall be chosen between the PWM frequency and the maximum angular frequency of the motor.

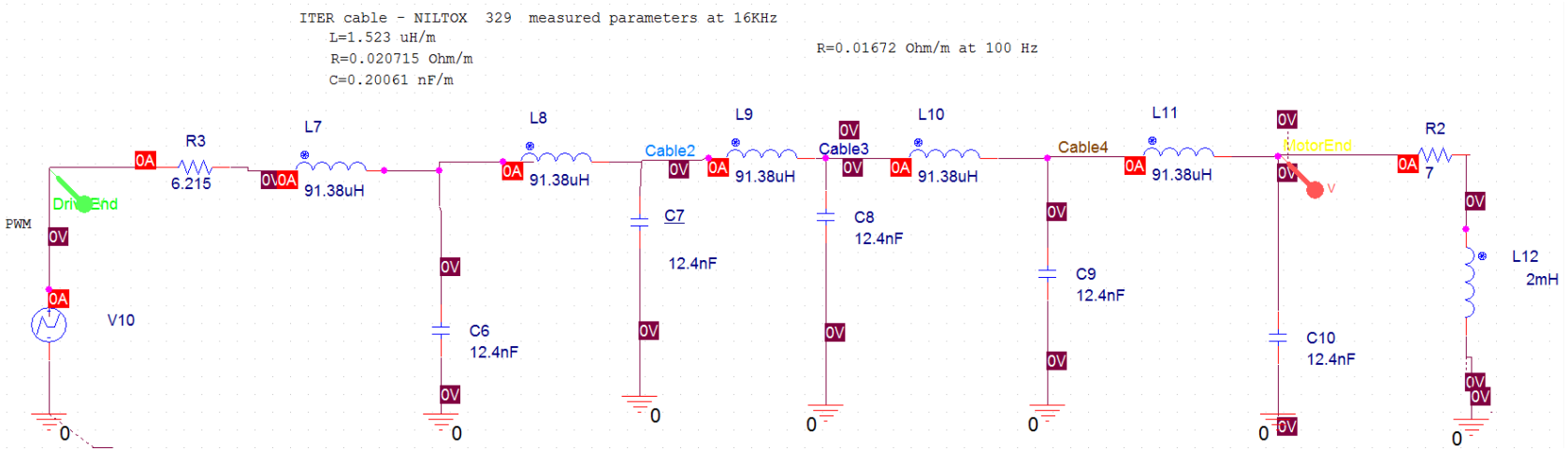

Figure 6-14. Equivalent circuit for one phase of the system composed by PWM drive, 300 m of cable and Aerotech stall motor.

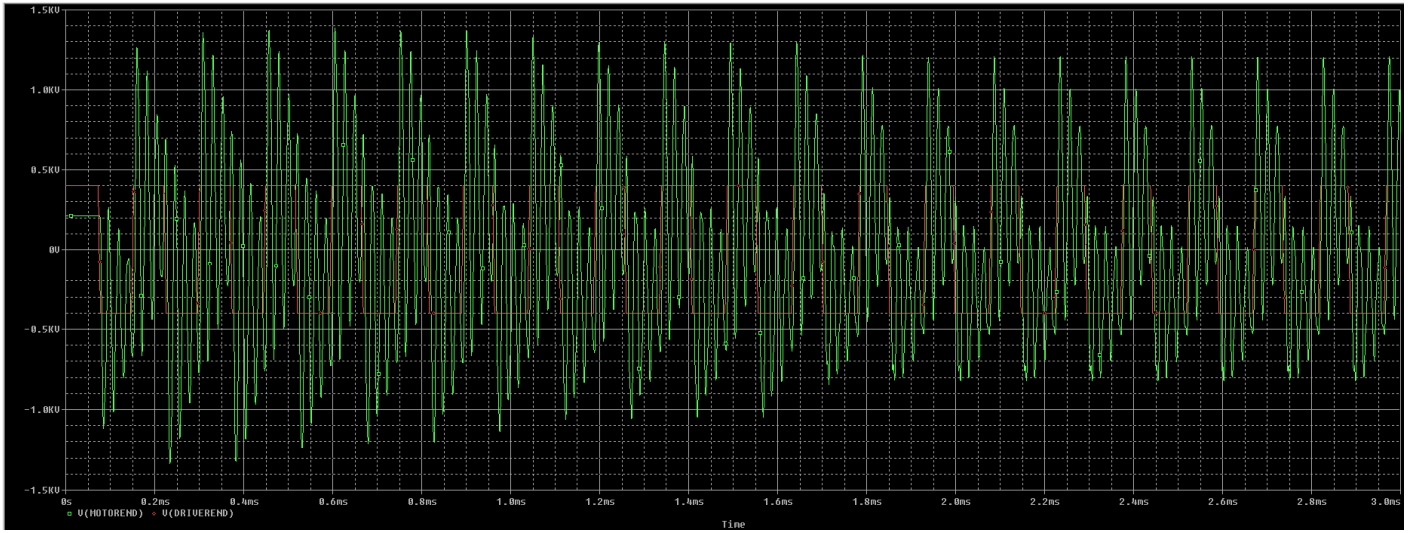

Figure 6-15. Simulated voltages at drive end and motor end on 300 m of cable without implementing any correction.

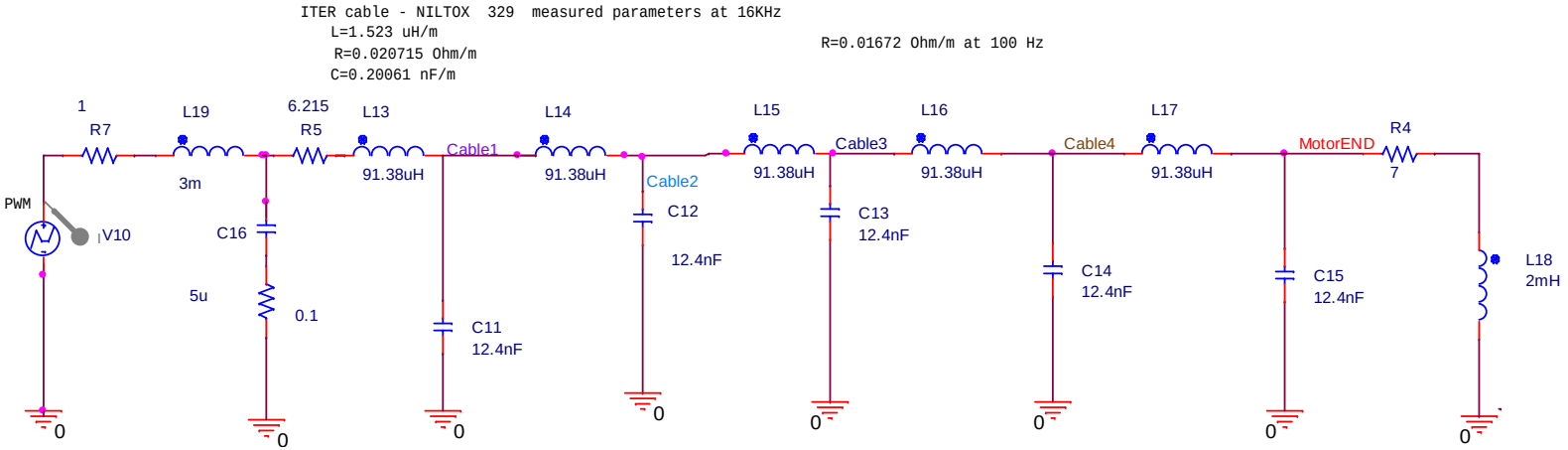

Figure 6-16. LC filter at drive end with 300 m of cable.

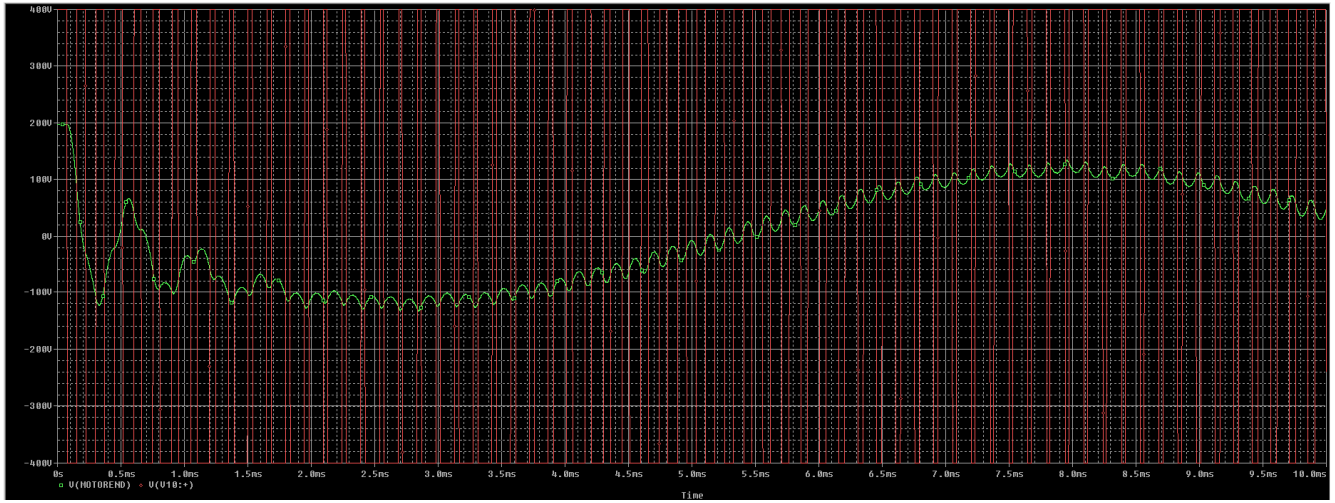

Figure 6-17. Voltage at inverter and at the motor end when implementing an LC filter.

6.3.2 Termination network

A cost effective method for controlling the voltage reflection is a termination network or a snubber that maintains the reflected waveform below potentially destructive levels. A terminator device is installed in parallel with the motor and based on the transmission line theory, it loads the receiving end of the cable with a Z_{load} ohmic resistor value equal to the cable Z_o, which eliminates the reflected wave. This solution provides a superior motor voltage reduction vs cable length.

The characteristic impedances of the Balanced and Niltox cables are 115 Ω and 100 Ω respectively. The termination network is composed by a parallel branch to the motor which presents the same impedance than the cable. In order to reach a compromise between these characteristic impedances and the market availability, the chosen values for the components are: R=94 Ω and C=2 µF. In Figure 6-18 a simulated circuit implementing the termination network is shown. The results of the simulation are presented in Figure 6-19, and show how this device is able to reduce the reflections caused by the long cable. Although the resulting wave is not as smooth as when using an LC filter, it manages to reduce the mentioned effect and reduce the voltage at motor from 1.5 kV to 500 V. The drawback of this solution with respect the LC filter is the dissipated energy from the resistors that have to be included for impedance matching. This would produce an energy loss depending on the current that goes through them.

6.3.3 Other tested techniques

Other techniques were tested on simulation such as different LCR filters, reactors, etc. It is worth mentioning the good effect of LCR filters on the reflected wave, although these implementations were not chosen due to the energy loss in the resistive elements. The circuit and the simulated results are shown on Figure 6-20 and Figure 6-21.

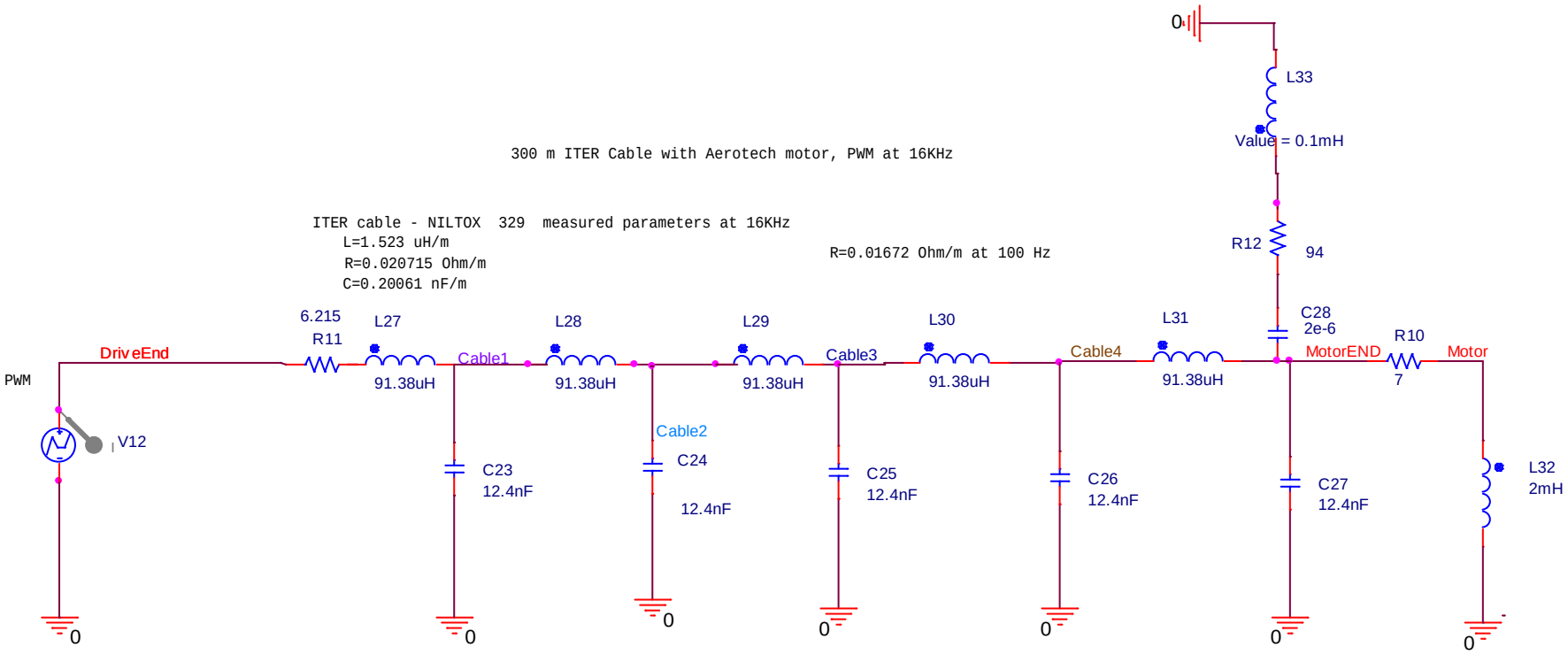

Figure 6-18. Simulated circuit implementing a Line Terminator or Snubber at motor end with 300 m of cable.

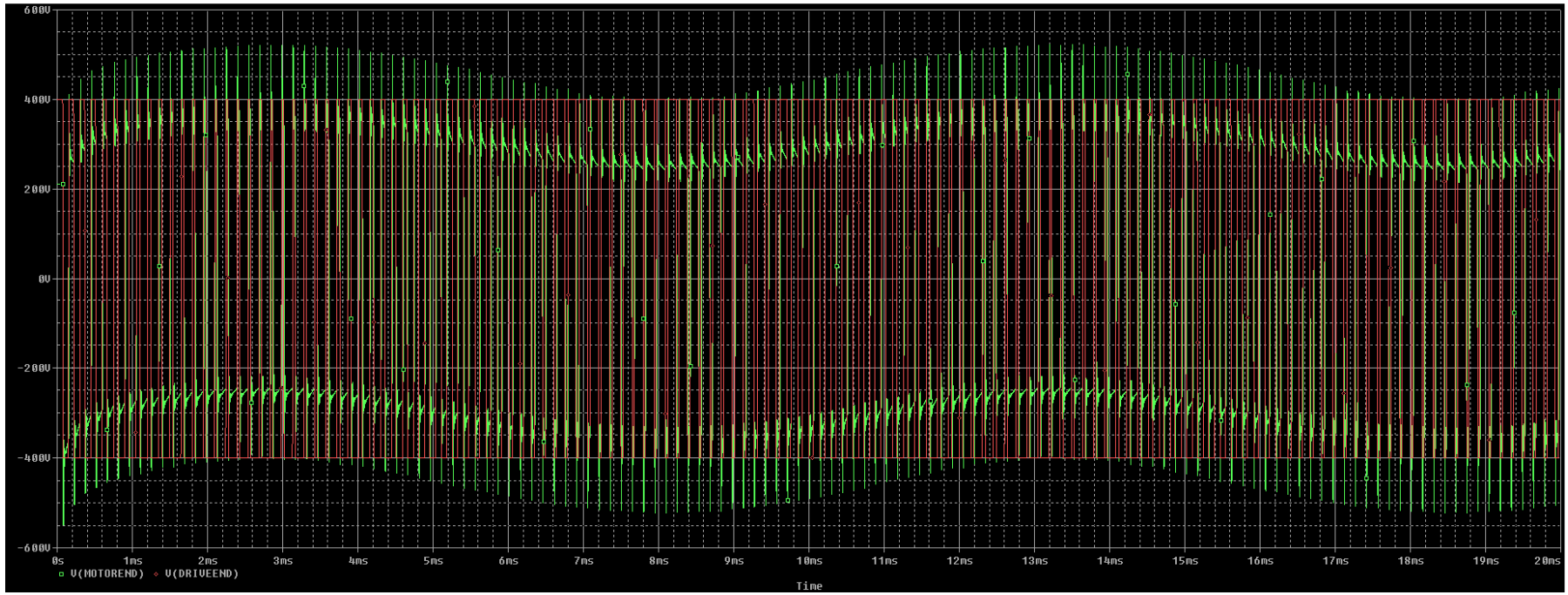

Figure 6-19. Voltage at inverter and at the motor end when implementing a Line Terminator or snubber.

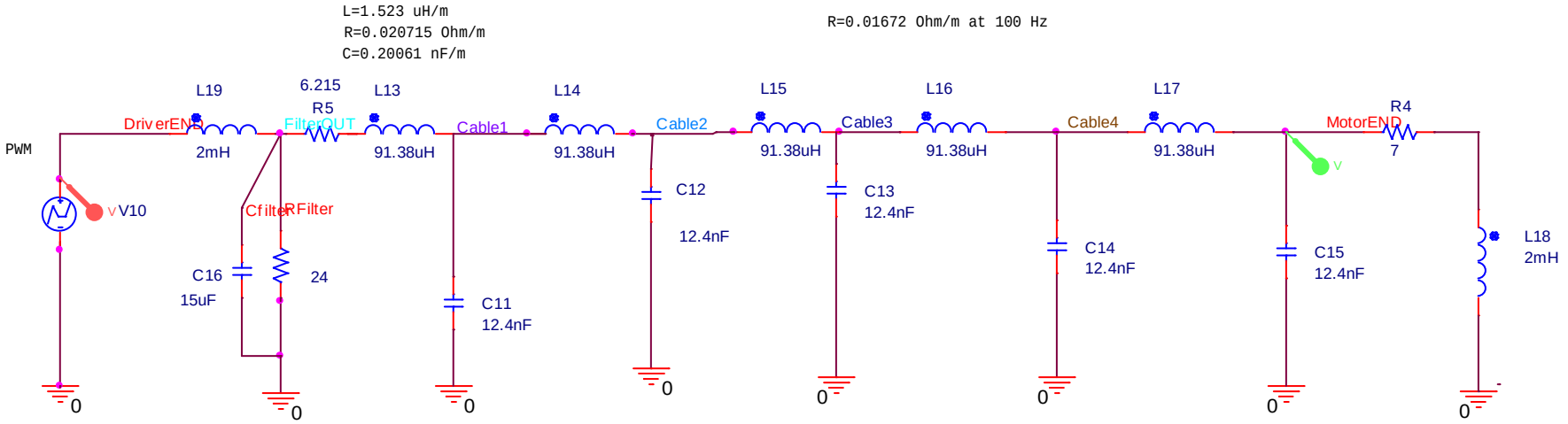

Figure 6-20. Simulated circuit implementing an LCR filter.

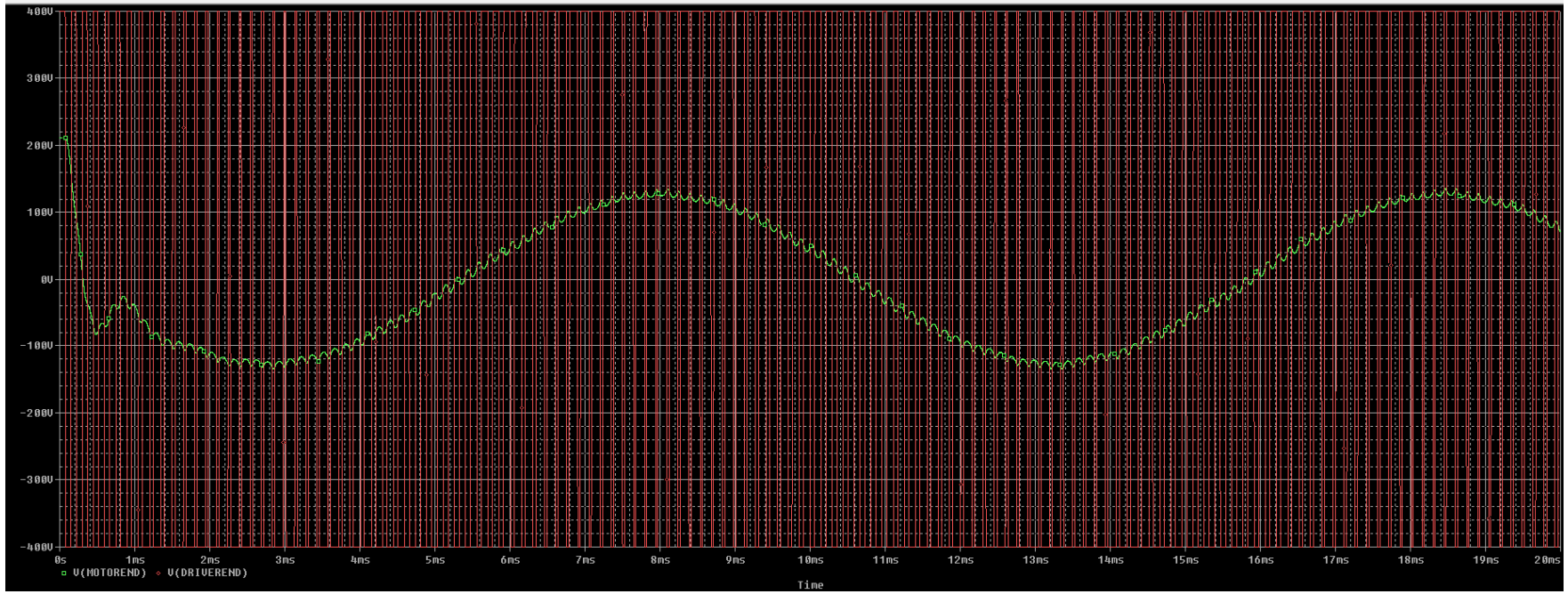

Figure 6-21. Voltage at inverter and at the motor end with an LCR filter.

6.4 Solving the overvoltage issue. Real implementation of a commercial LC filter.

Once the simulation results were carried out to identify the most reliable alternative, a commercial LC filter (Schaffner FN 530-4-99) was selected for a real implementation. An oscilloscope with a calibrated differential probe was used to capture the inverter waveform in both drive and motor ends. The measurements represented on each image have to be scaled by a factor of X 500 in order to convert them to volts due to the reduction factor applied on the oscilloscope probe.

6.4.1 Overvoltage reduction with a Schaffner FN 530-4-99 LC filter

The outstanding results obtained with this commercial filter (See Figure 6-22) are presented from Figure 6-23 to Figure 6-25. The filter accomplishes its specification and manages to reduce the high frequency harmonics from the inverter and transforms them to a sinusoidal-like waveform of around 150 Hz. With this frequency, the cable length required to reproduce a standing wave would be much longer than 300 m, which is the maximum cable length studied on this experiment. For that reason, in all the cases the result is equivalent and no difference has been found for any length, cable end, motor control, etc. in terms of voltage amplitude.

Figure 6-22. Schaffner FN-530-4-99 LC filter installed in the control cubicle.

In [142] and [151], an equation to find the critical cable length depending on the voltage frequency is given by (7) for sinusoidal voltages.

$$l_c = \lambda/4 \tag{6.8}$$

Which applied to a sinusoidal frequency of 150 Hz, and wavelength ($\lambda = c/f$) of 2e6 m, gives a critical length of 500 km. For that reason, the cable length expected at facilities such ITER will not be subjected to standing waves for voltage frequencies of 150 Hz.

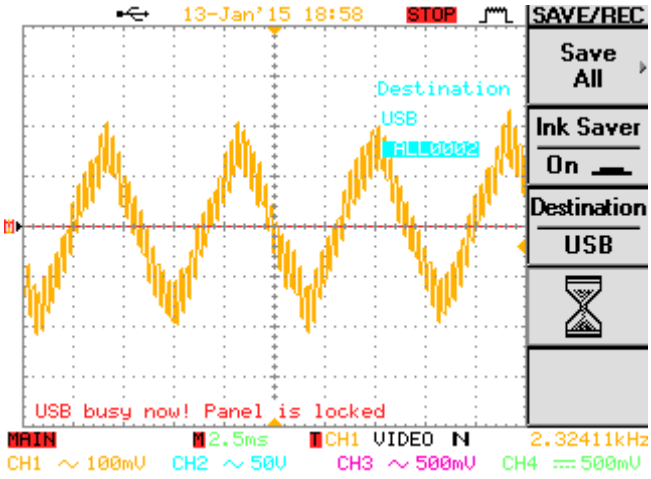

Figure 6-23. PWM waveform on the Niltox cable with 5 m length at motor end. Time length of 2.5 ms for each square on the horizontal axis. Scale factor x500.

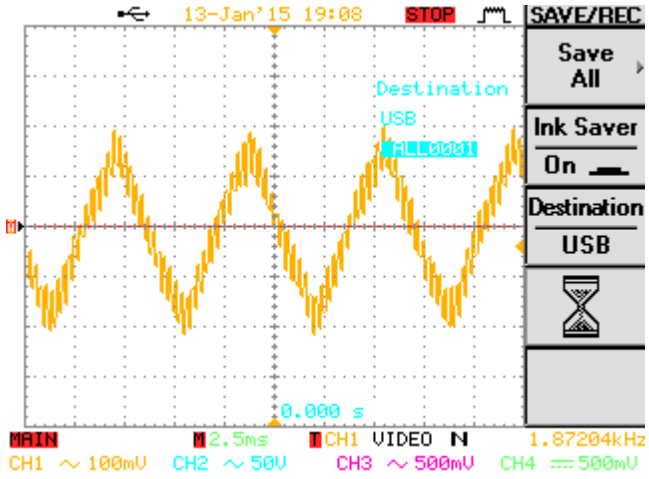

Figure 6-24. PWM waveform on the Niltox cable with 100 m length at motor end. Time length of 2.5 ms for each square on the horizontal axis. Scale factor x500.

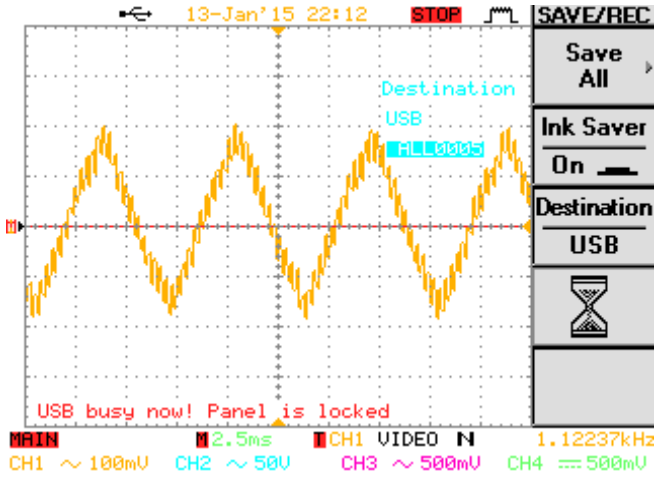

Figure 6-25. PWM waveform on the Niltox cable with 300 m length at motor end. Time length of 2.5 ms for each square on the horizontal axis. Scale factor x500.

Of every mitigation strategy analysed, most include energy dissipating elements that waste energy and are inefficient from that point of view. The LC filter is one of the few solutions which dissipate a very reduced amount of energy. It also presents best results in terms of harmonic suppression. It has been found in the literature, that the LC filter could resonate under some circumstances that have to be carefully determined. In order to avoid that, advanced versions of these filters implement a protective system based on diodes or include resistors that damp the possible oscillations. Some Schaffner filters include these protective strategies to ensure that the system does not resonate. Unfortunately the exact circuit diagram could not be obtained because of confidentiality for the manufacturer but it could be confirmed with Schaffner that they actually are a type of LC filter.

In addition to the system safety and the reduction of the over-voltage, it is important to quantify the influence on the control performance, when using this kind of filtering caused by the reduction of the voltage frequency. Although the Schaffner FN 530-4-99 is rated up to 200 Hz of motor frequency, this reduced effect, over the conventional KHz of the inverter, could lead in decreased dynamic performance. This introduces the next section, where the control performance of the best solution is analysed and compared with the direct connection between inverter and motor.

6.5 Influence of using a Schaffner FN 530-4-99 LC filter on the control performance. Comparison with direct connection for 5 m cable.

In this section the control performance when implementing a commercial solution for the standing wave is carefully analysed. Two different control methods are analysed here for the Infranor motor and Niltox cable, these are: torque control and servo control.

6.5.1 Torque control

The objective of these tests is to evaluate the dynamic characteristics of the system composed by drive, filter and motor being driven by short cables. To study and isolate the filter influence, a set of torque steps were issued with only a setup mounting 5 m cables. In Figure 6-29 and Figure 6-32, a torque step in two directions has been issued with two different torque amplitudes. For each of them, a different resistant torque was created on the load motor in order to set the steady state speed to a different values. Friction torque has the form described by equation (6.9) and the current command of the load motor is given by (6.10).

$$\tau_f = K_f \omega \tag{6.9}$$

$$I_c = K_e K_f \omega \tag{6.10}$$

where,

K_f is the viscous friction constant in [Nm s /rad],

K_e is the torque constant of the load motor [Nm/A],

ω is the angular speed of the load motor in [rad/s].

The control scheme used for torque control is shown on Figure 6-26 and Figure 6-27. On the amplifier side, the current of the two phases are sampled, and sent to the PMAC motion controller. The phases currents are transformed into direct and quadrature currents to be controlled. On a brushless motor the magnetization current or direct current is zero because it employs permanent magnets.

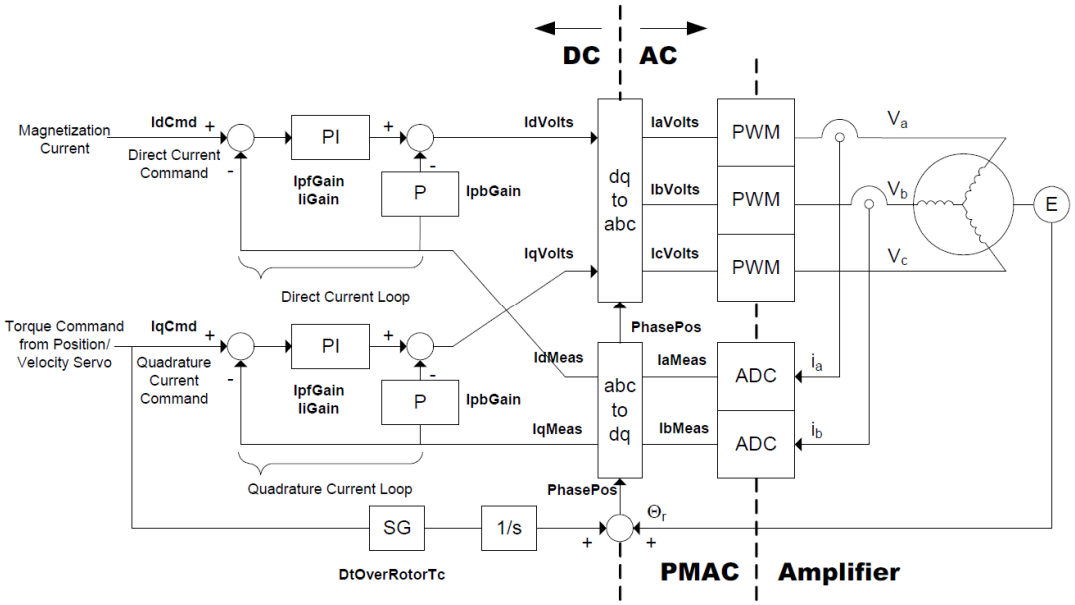

Figure 6-26. Torque control diagram for the PMAC controller.

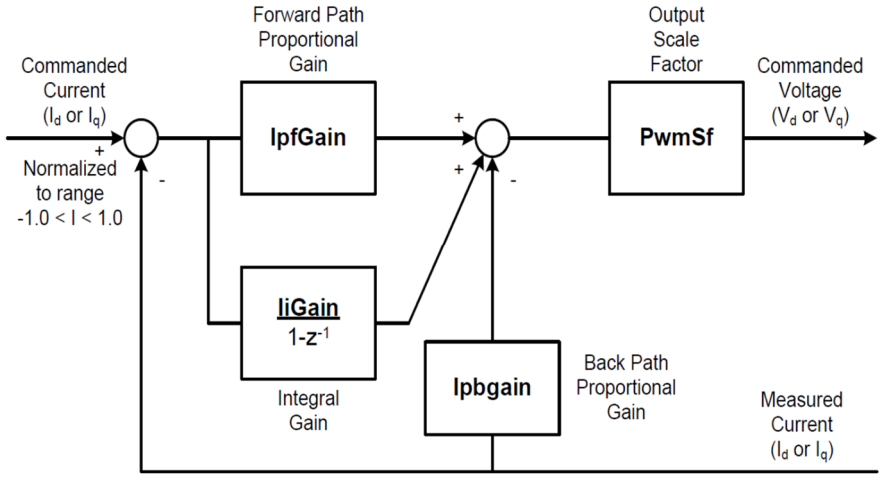

Figure 6-27. Detail of current loop with expanded IpfGain and IiGain.

IpfGain, IpbGain, and IiGain are the gains of the PI (proportional-integral) current-loop algorithm. The algorithm is the same for both current loops. Iigain is the integral gain term. There are two proportional gain terms: IpfGain is the “forward-path” proportional gain, and IpbGain is the “back-path” proportional gain. IpfGain is multiplied by the current error (commanded minus actual) and the result is added to the output command. IpbGain is multiplied by the actual current value and the result is subtracted from the output command.

A.) Load 1 ($Kf = 0\ Nm \cdot s/rad$), equal current controller

The control gains shown on Table 6-4 were implemented on this test.

	Direct connection	Schaffner filter
IIGAIN	**0.2278**	**0.2278**
IPFGAIN	**0**	**0**
IPBGAIN	**1.9461**	**1.9461**

Table 6-4. Gains implemented on the current loop when maintaining the same tuning configuration.

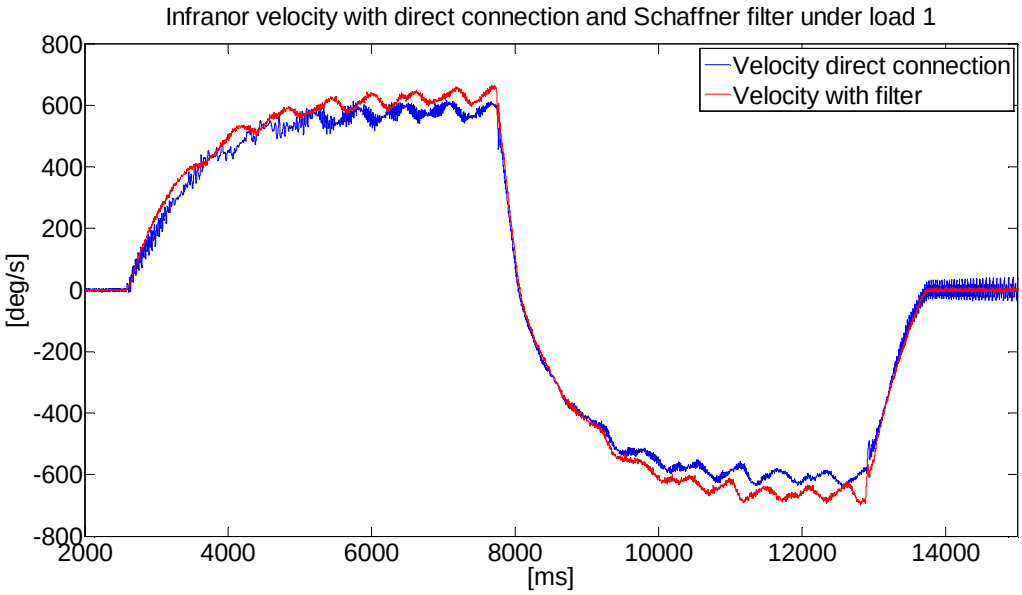

Figure 6-28. Comparison of velocity profiles of Infranor motor running with direct connection and Schaffner filter. Test case correspond with a friction load type 1.No tuning variations on the current control. Data test TR3.

The same test was repeated without performing any variation on the current control. Thus, the control via direct connection was similar to the one used during the tests accomplished by using the filter. The current control was tuned with the filter installed. The results observed indicate that the velocity achieved when implementing the filter is slightly greater than when not using the filter. However the difference decreases with respect the previous test. The average measured current during the stage of positive command is 0.1956 A and 0.1975 A for the non-filtered and filtered cases respectively. Thus, there is a very small difference on the average current that influences the velocity. The frequency of the small waves on the speed corresponds with the rotational frequency and it is due to the irregular friction on the shaft and possibly the coupling

imperfections. This differential velocity is translated into a positional difference of 272 deg as seen on Figure 6-30. Due to the fact that the motor presents the same amount of differential speed in both directions, the final position matches with that achieved by implementing a direct connection. This effect is explained in terms of a more efficient energy conversion in the motor when applying a reduced voltage frequency than when a high frequency PWM signal is applied.

As in the previous case, no particularly striking vibrations were observed during this test.

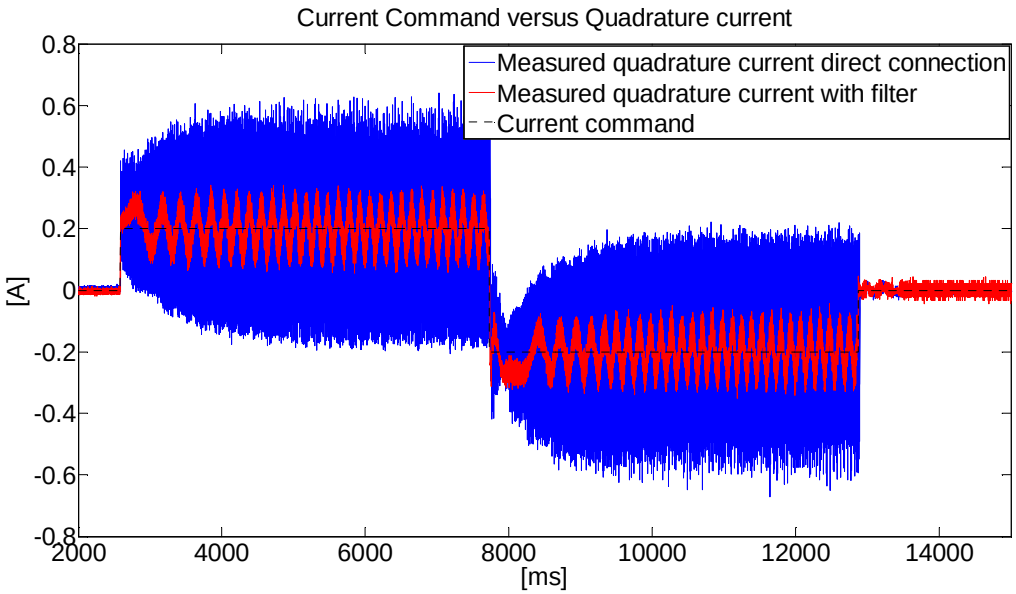

Figure 6-29. Comparison of quadrature current of Infranor motor running with direct connection and Schaffner filter. Friction load type 1. No tuning variations on the current control. Data test TR3.

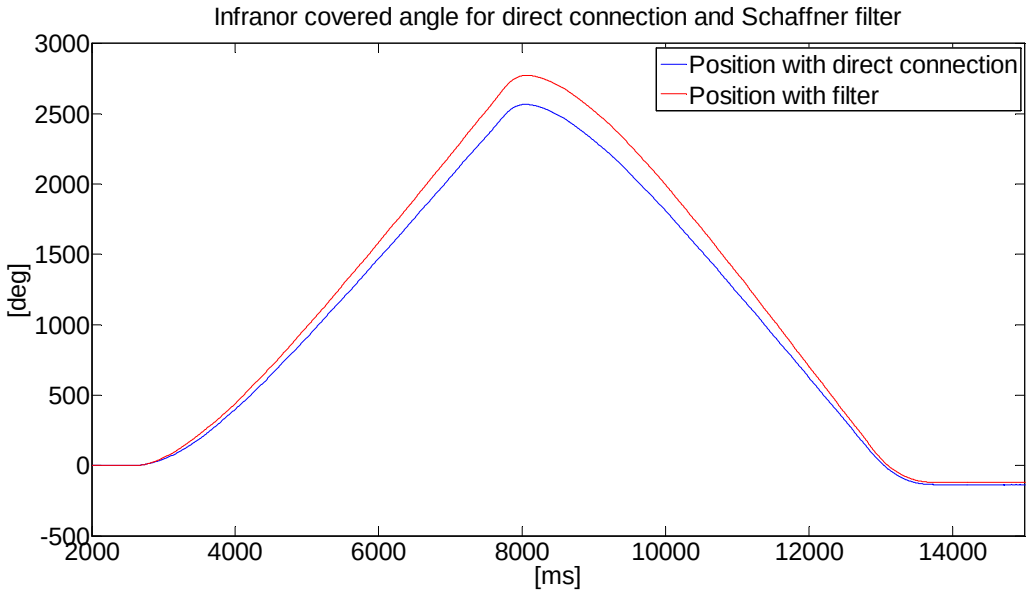

Figure 6-30. Angle covered by the motor during its movement performing torque control. Data test TR3.

B.) Load 2 ($Kf = 2e-4\ Nm \cdot s/rad$), equal current controller

For the realisation of this test, control gains of Table 6-4 were implemented.

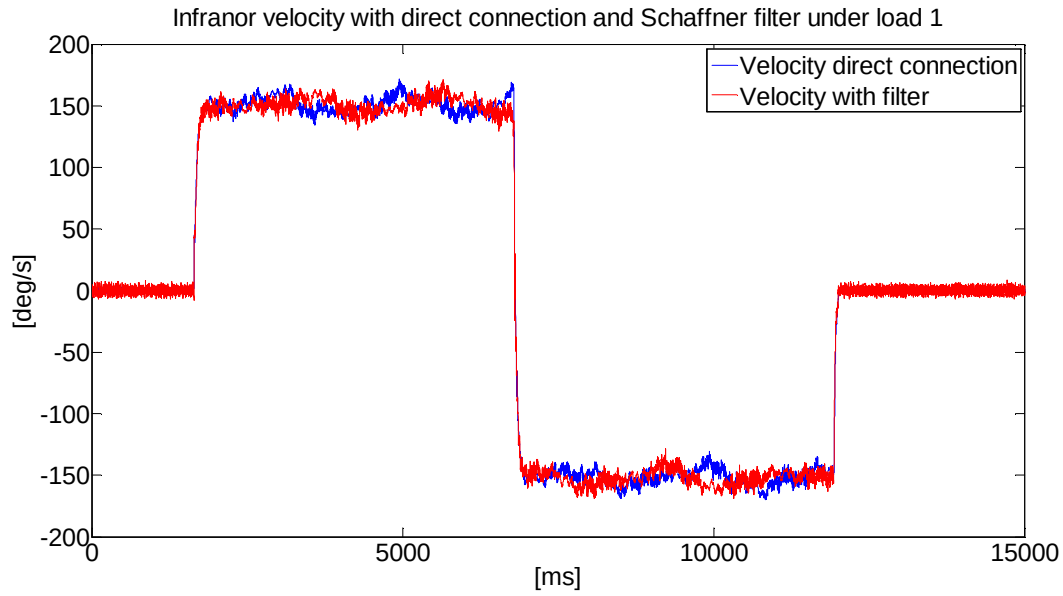

Figure 6-31. Comparison of velocity profiles of Infranor motor running with direct connection and Schaffner filter. No tuning variations on the current control. Data test TR3.

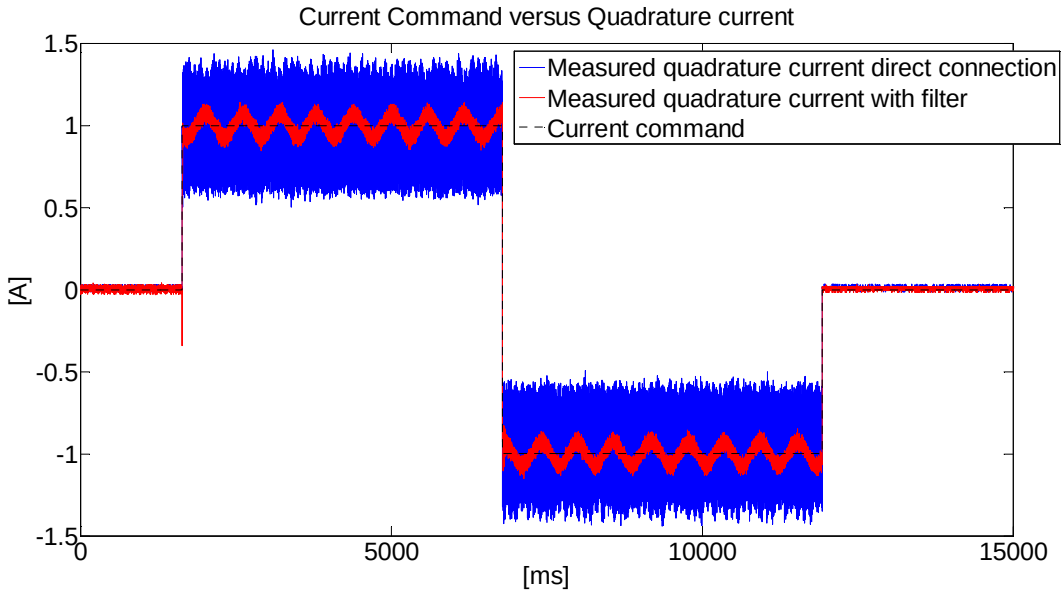

Figure 6-32. Comparison of quadrature current of Infranor motor running with direct connection and Schaffner filter. Test corresponding with a friction load type 2. No tuning variations on the current control. Data test TR3.

The velocity discrepancies under load can be considered negligible. This is because as the friction load increases, the effect of small changes on the current average value decreases. No important vibration effects were observed during the realisation of this test.

6.5.2 Servo Control

A basic PID servo control algorithm was implemented on the PMAC (See Figure 6-33). The desired position is compared with the actual position. In this control scheme, K_p is the proportional gain. Delta Tau implements the derivative gain in a non-conventional way, because this is affecting the real velocity, instead of the velocity error. K_{vfb} is the derivative gain on this case. And K_{vifb} is a different derivative gain which affects the system before the integration is done. K_i is the integral gain and a set of feed-forward gains are also employed. On the point of view of the current loop, the control configuration from Table 6-4 was used. A servo control strategy was implemented instead of velocity control due to the expected better performance for the control scheme used on PMAC.

K_p: proportional gain

K_{vfb}: derivative gain proportional to the velocity after integral term.

K_{vifb}: derivative gain proportional to the velocity before the integral term.

K_i: integral gain.

K_{vff}: velocity feed-forward gain.

K_{aff}: acceleration feed-forward gain.

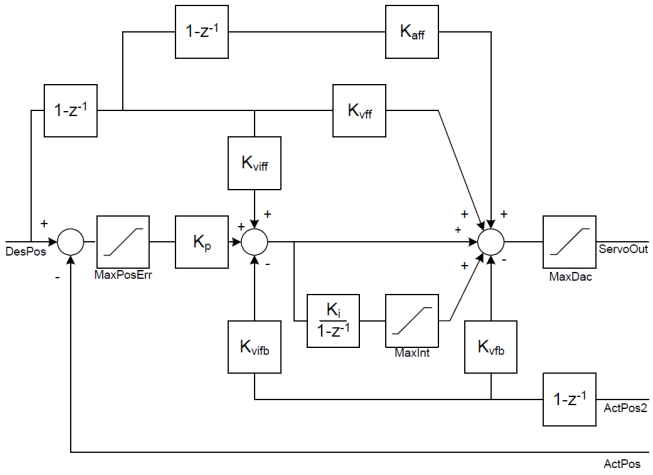

Figure 6-33. Power PMAC basic servo control algorithm.

A step response has been tested in order to compare the effect of the Schaffner filter under the point of view of servo control performance. The angle covered can be seen in Figure 6-34 together with the angle reference. The detail view is shown in Figure 6-35 to Figure 6-36 and it includes the range of ±1% of the steady state value, represented by the dashed red lines. It can be seen how the filter introduces a very small delay on the step response which, for a margin of ±1% of the steady state, presents a value of 3 ms. No delay is observed on the rise time. As in every test carried out with short cables, no particularly striking vibrations were observed during this test. A dashed circle on Figure 6-35 shows the point where the settling time has been measured for both graphs. The control gains employed for this test are:

$\boldsymbol{K_p}$	1.2
$\boldsymbol{K_{vfb}}$	105
$\boldsymbol{K_{vifb}}$	0
$\boldsymbol{K_i}$	6e-4
$\boldsymbol{K_{vff}}$	165
$\boldsymbol{K_{viff}}$	0
$\boldsymbol{K_{aff}}$	100
$\boldsymbol{K_{fff}}$	0

Table 6-5. Control gains employed for servo control loop.

It is worth mentioning, that in the position graph (Figure 6-36), it can be seen a lag on the filtered option. This is due to maintaining the same control gains for the two scenarios. This deterioration of the control performance could be corrected by tuning the control gains accordingly.

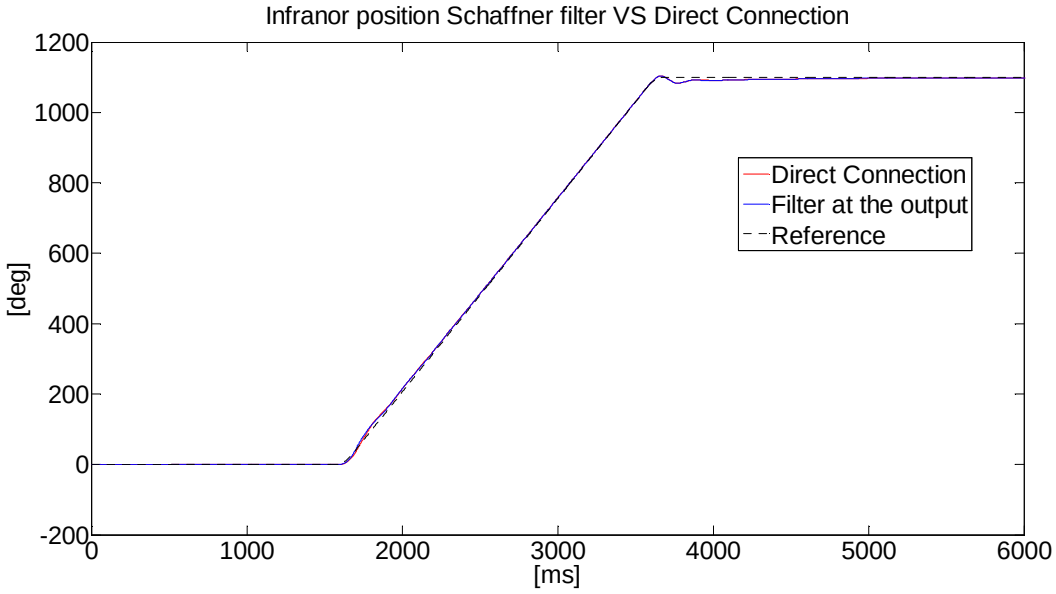

Figure 6-34. Covered angle for a step response during servo control. Comparison between filtering and non-filtering for 5 m cable. Data test VC4.

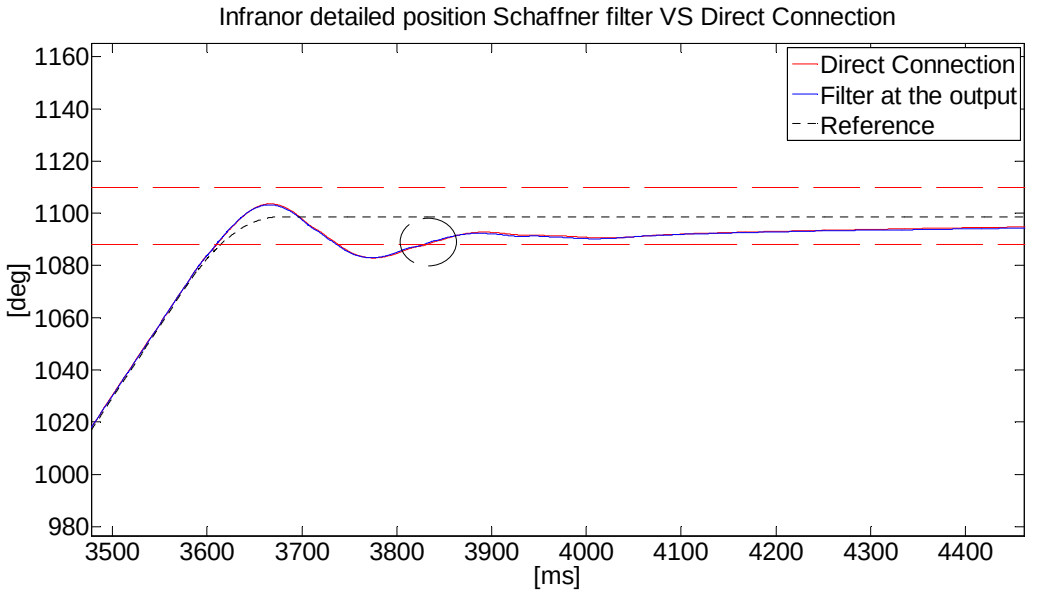

Figure 6-35. Detailed view of the covered angle for a step response during servo control showing where the settling time has been measured. Comparison between filtering and

non-filtering for 5 m cable. Dashed lines correspond with ±1% of the steady state value. Data test VC4.

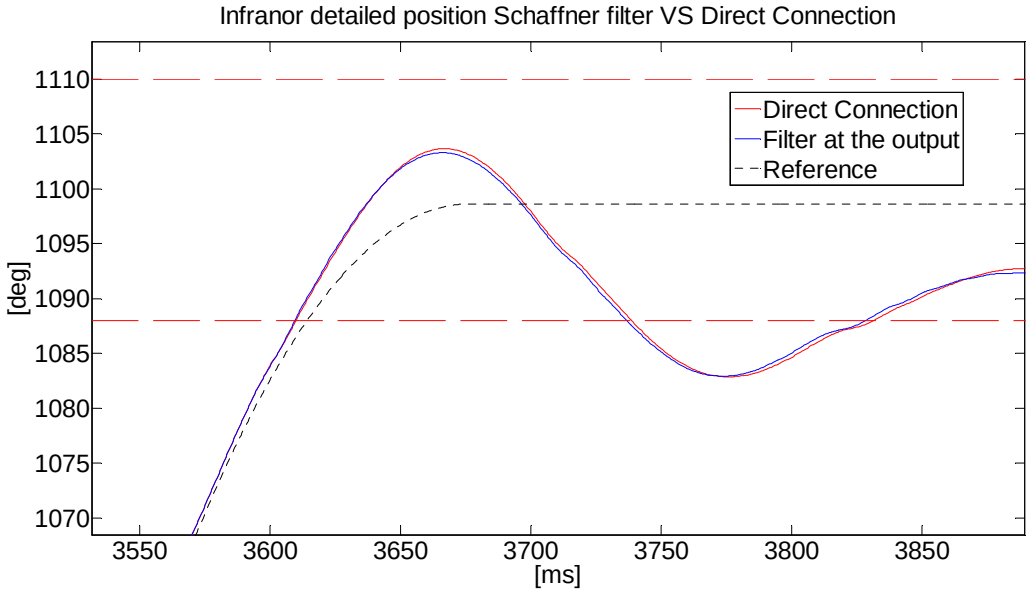

Figure 6-36. Detailed view of the covered angle for a step response during servo control. Comparison between filtering and non-filtering for 5 m cable. Dashed lines correspond with ±1% of the steady state value. Data test VC4.

6.5.3 Effect of the Schaffner FN 530-4-99 LC filter real manipulator trajectories during a remote handling task.

Given the frequency limit that the use of the filter imposes on the motor movement, 200 Hz with the selected model, it is worth studying potential harmful effects when in a real application. For this purpose, a real remote handling operation was designed and remotely performed with Dexter manipulator (See Figure 6-37).

A bolting operation was carried out at a speed slightly higher than a conventional remote handling operation would be carried out. This was done in order to obtain the worst possible conditions. The position profile of Dexter's actuators is shown in Figure 6-38. The vertical axis are displayed in motor units. One can easily infer that the actuator termed Motor[4] is executing one the most demanding trajectories in terms of velocity and covered angle. The trajectory of this actuator was selected to be imitated on this test.

The objective of this test is thus to compare the performance of 5 m cable implementing a filter against the same length without any filtering. This allows to check if the cut-

off frequency of the filter would affect the control performance when using it in a manipulator similar than Dexter.

A servo control was tuned properly to be able to follow the mentioned trajectory. The remote handling operation was sampled at 500 Hz and the set of points was supplied to the PMAC controller of Delta Tau during approximately 60 s. This is shown in Figure 6-39. Three detail views are shown in Figure 6-40 to Figure 6-42 for different sets of time. They all shown that no important discrepancies are observed between the two solutions. It is then proved that introducing the Schaffner filter does not affect to the performance on this type of manipulator.

Figure 6-37. Dexter manipulator in one arm version. Designed and manufactured by Oxford Technologies Ltd.

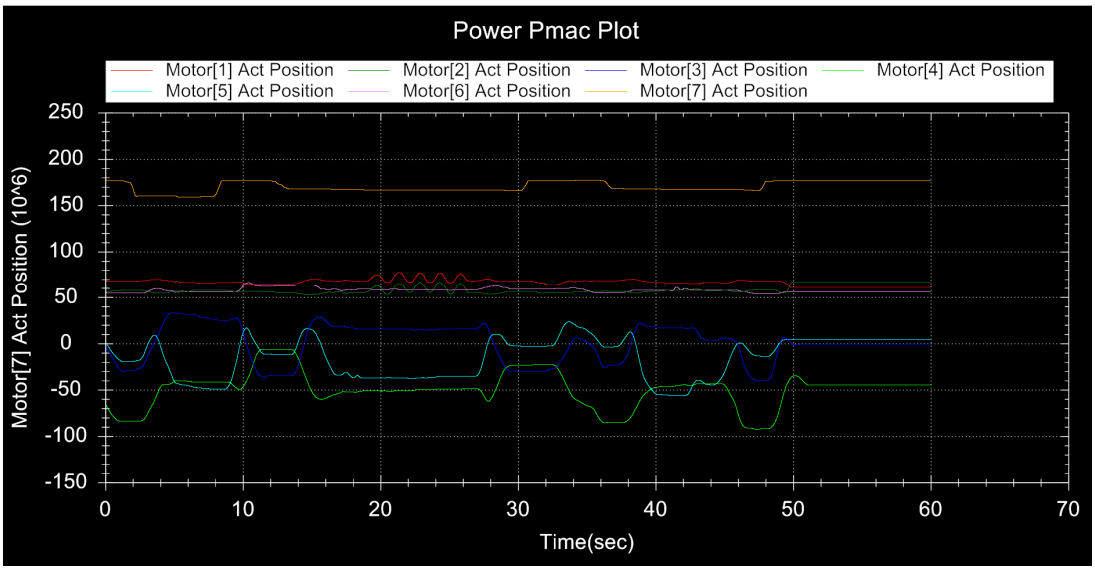

Figure 6-38. Dexter's actuators movements when performing a remote handling task. Vertical axis is in motor units, horizontal axis is in seconds.

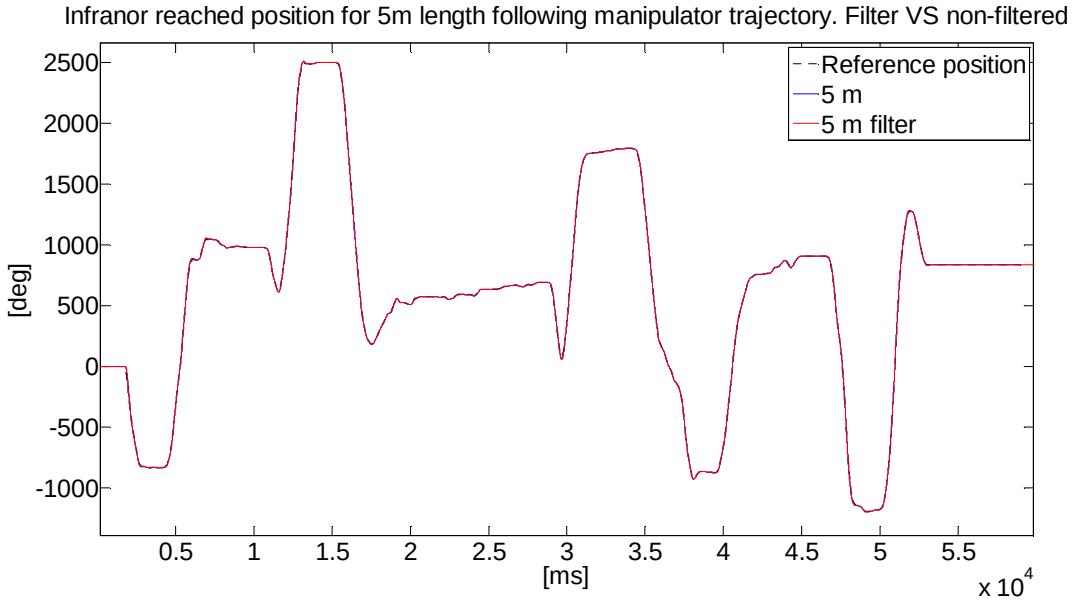

Figure 6-39. Position of Infranor motor when following Dexter's trajectory for 5m cable.

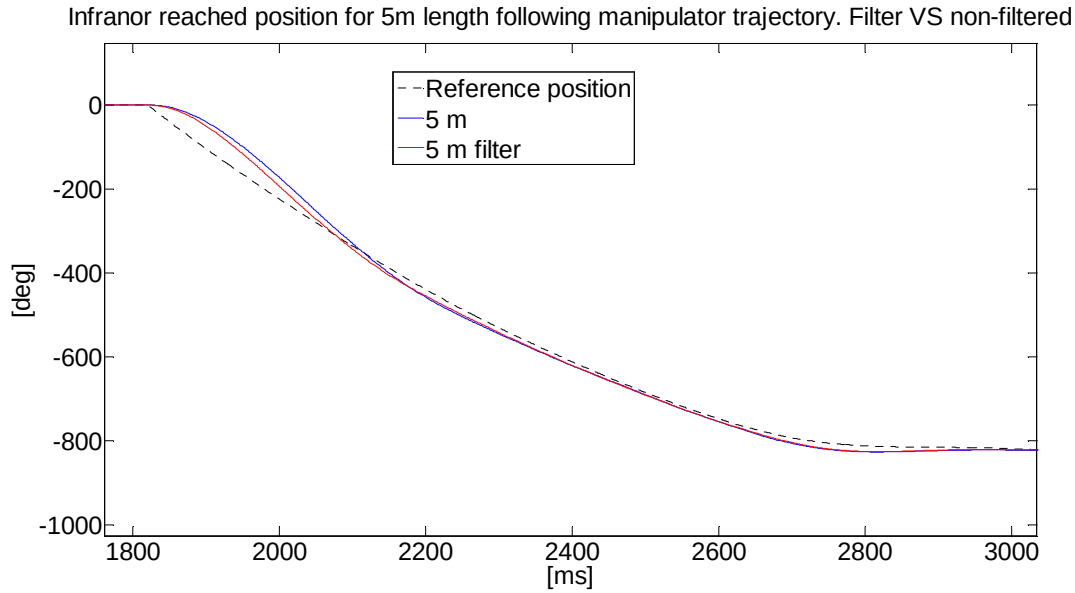

Figure 6-40. Detailed view of Figure 6-39.

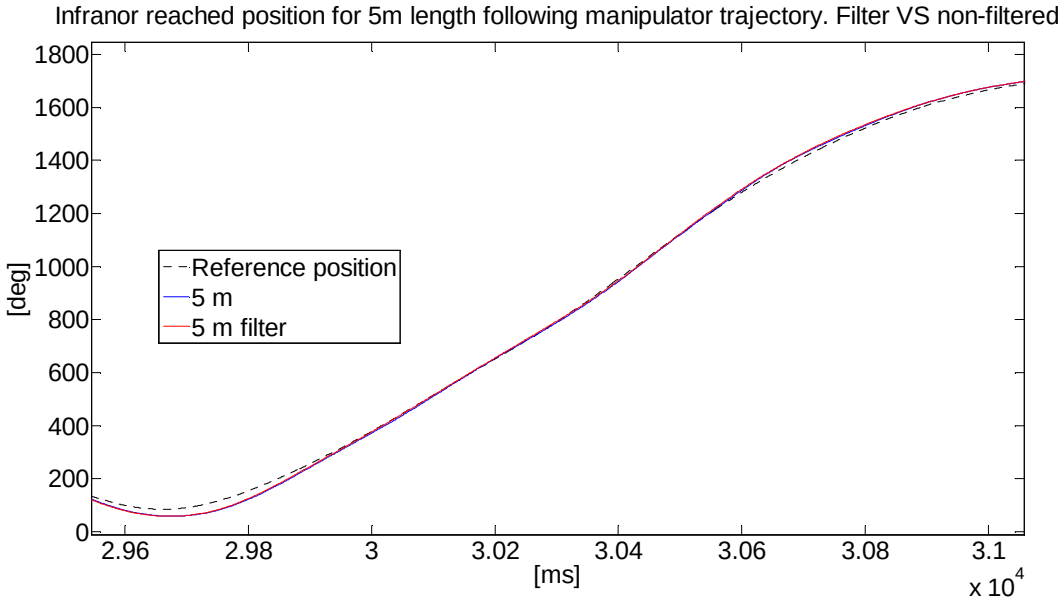

Figure 6-41. Detailed view of Figure 6-39.

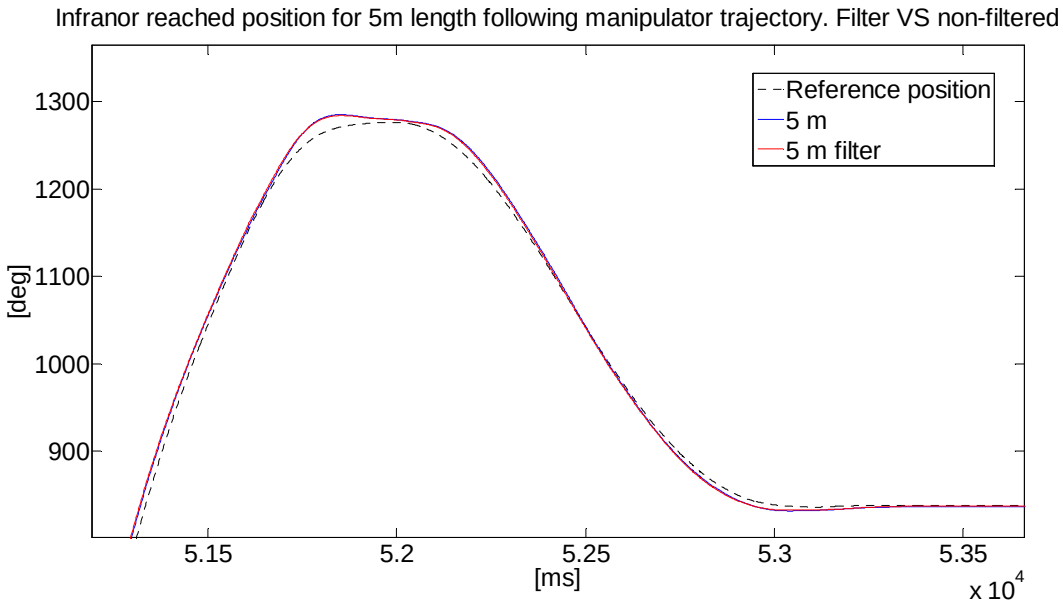

Figure 6-42. Detailed view of Figure 6-39.

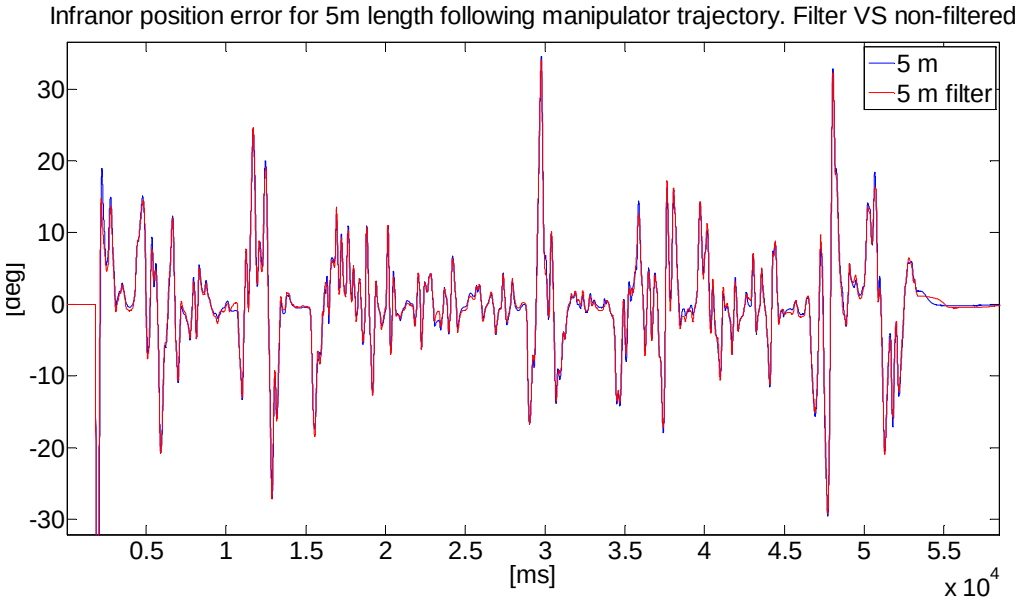

Figure 6-43. Position error for 5 m cable length. Direct connection versus connection through filter.

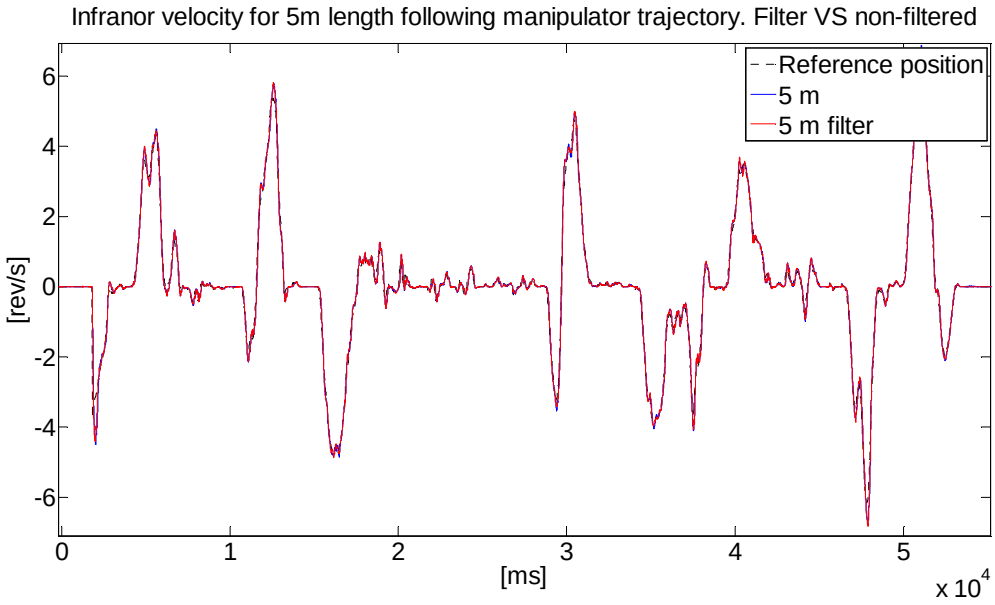

Figure 6-44. Velocity profile for 5 m cable length during the following of a real manipulator trajectory.

Figure 6-44 shows the velocity profile for the required trajectory. In revolutions per second. This is important to characterise Dexter's trajectory and identify the order of magnitude of the motor frequency. It is possible to see how a maximum frequency of 6 Hz is expected on a real teleoperation task. Multiplying this value by the pole pairs of the Infranor motor it yields to 48 Hz. This value is still far from the maximum recommended frequency by Schaffner for the FN 530-4-99 which is 200 Hz. Nevertheless it is possible than if a different manipulator design requires much higher motor frequencies, the capabilities of the motor in following the trajectory could deteriorate.

6.6 Influence of using a Schaffner FN 530-4-99 LC filter on the control performance for long cables.

In this section, an analysis of the effect of increasing the length of the cable is performed when the LC filter is used. The same control methods than in previous section are analysed here for commanding the Infranor motor: torque control and servo control.

6.6.1 Torque control

A set of tests involving 4 different lengths was performed in order to compare the performance of torque control when increasing the cable length. A first order low pass

filter was implemented in the first stage of the data processing that the drive carries out when reading the resolver signal (Called Encoder Conversion Table on Delta Tau software).

A.) Load 1 ($Kf = 0\ Nm \cdot s/rad$)

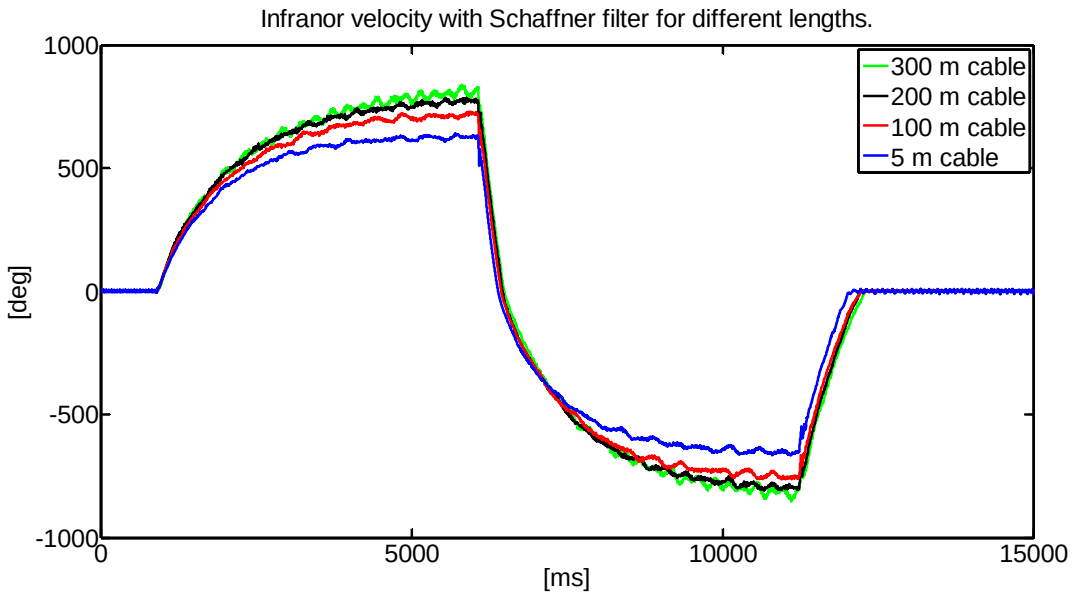

Figure 6-45. Velocity profiles for different cable lengths measured on the Infranor motor when implementing a filter. Test code TR1.

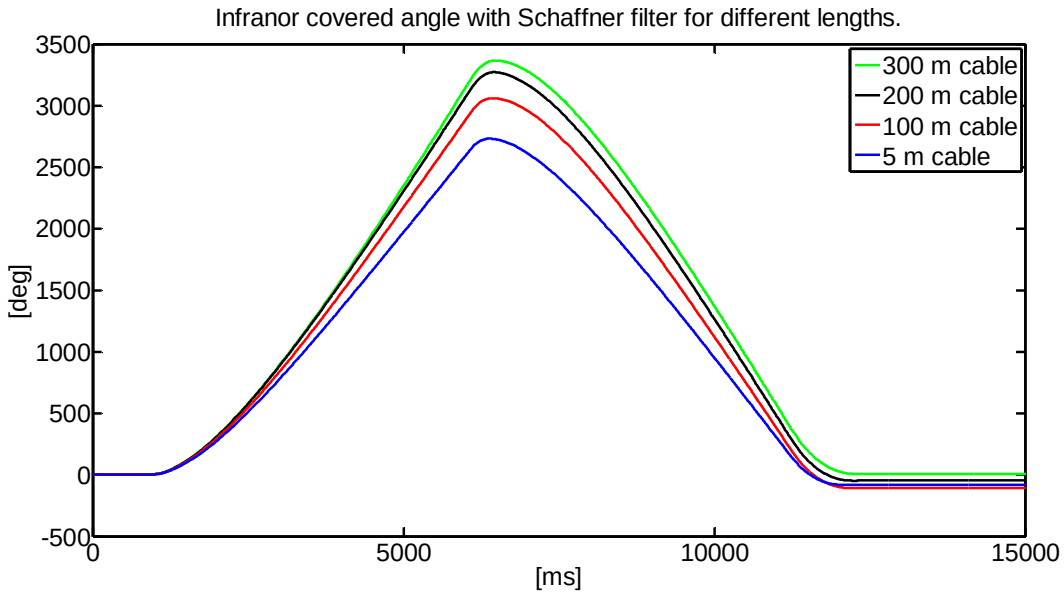

Figure 6-46. Angle covered for different cable lengths measured on the Infranor motor when implementing a filter. Test code TR1.

B.) Load 2 ($Kf = 2e-4\ Nm \cdot s/rad$)

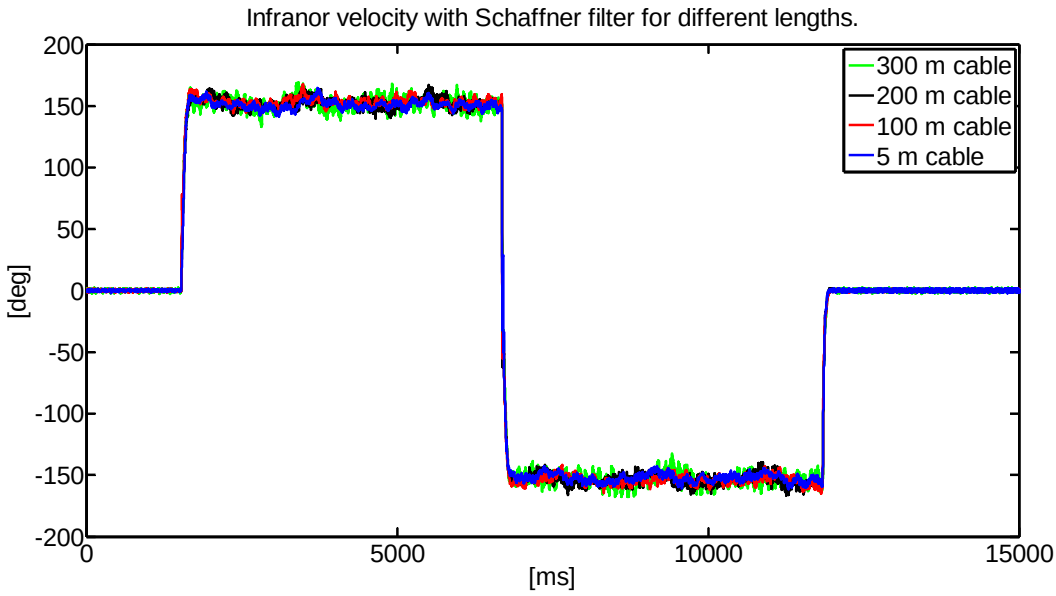

Figure 6-47. Velocity profiles for different cable lengths measured on the Infranor motor when implementing a filter. Test code TR1.

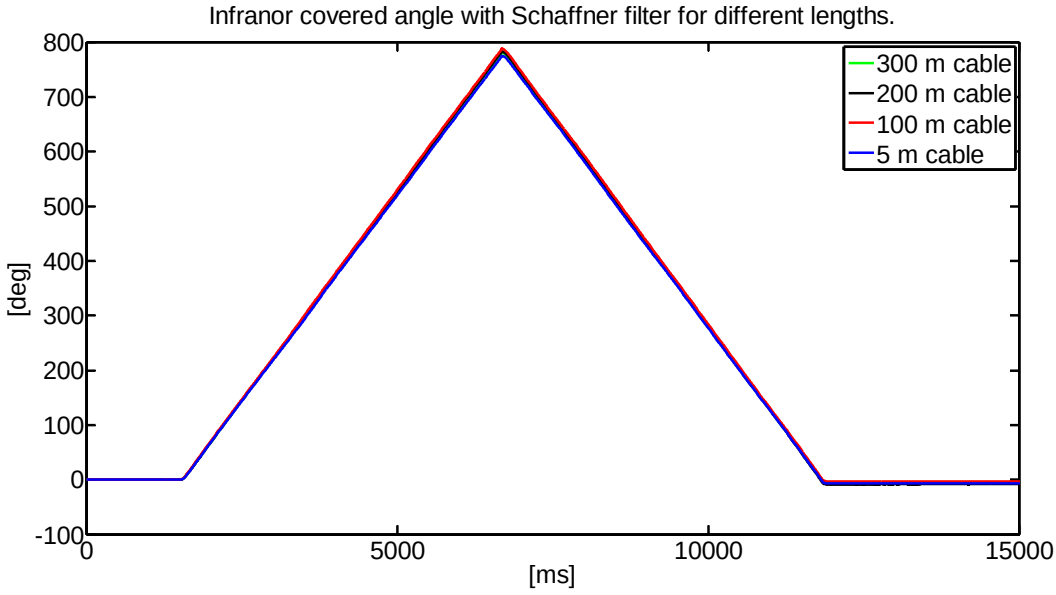

Figure 6-48. Angle covered for different cable lengths measured on the Infranor motor when implementing a filter. Test code TR1.

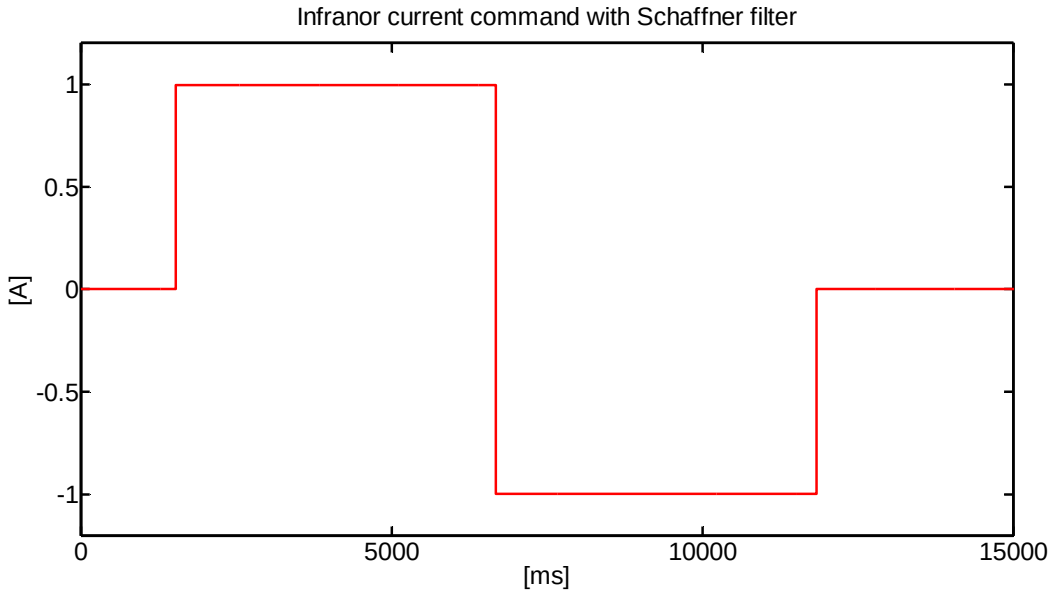

Figure 6-49. Current reference issued on the motor. Test code TR1.

An interesting effect is obtained when the load is kept to the minimum. Although intuitively one can predict the opposite effect, the maximum speed is achieved with longer cables. However, when increasing the friction load, the speed differences become negligible and no special differences between cables are observed.

6.6.2 Servo control

A servo control strategy was implemented due to the better performance for the control scheme used on PMAC. A complete set of tests was designed in order to check the control performance of this control strategy when mounting long cables.

K_p	0.2
K_{vfb}	40
K_{vifb}	0
K_i	5e-5
K_{vff}	40
K_{viff}	0
K_{aff}	100
K_{fff}	2

Table 6-6. Control gains employed for servo control loop.

Two different position profiles were defined and a step torque disturbance was issued by means of the load motor during the ascending slope of the position profile.

The control gains implemented for every servo control experiment which follow are shown in Table 6-6.

Cable length [m]	Res. Excitation Gain	Res. Excitation Frequency	Phase Shift (*)	Sum of Squares (**)
5	Full magnitude	Phase frequency	70	28000-29000
100	Full magnitude	Phase frequency	22	29000-30000
200	3/4 full magnitude	Phase frequency	115	28000-29000
300	3/4 full magnitude	Phase frequency	63	28000-29000

Table 6-7. Feedback configuration for different cable lengths. (*)Range= [0, 254], in units of 1/512 of an excitation cycle. (**) Only a range can be given due to the noise. Maximum value admitted on the variable is 37.767

K_{fff} affects on the derivate of the desired position. By adding a saturation effect of the velocity between [-1 and 1] and multiplying by the gain, the effects of static friction are taken into account.

These tests study the influence of long cables in the torque control performance when the configuration of the resolver is optimised for each different case. The optimised parameters for the feedback configuration were taken from Table 6-7. Two different reference profiles are tested for measuring the velocity tracking during the application of a disturbance torque.

Position reference profile B

Again, the similarities between waveforms of position and speed lead to the conclusion that no important differences are observed when the cable length is increased if the feedback has been configured adequately. During the realisation of this test, no particular increase on vibration was observed when increasing the cable length.

No noticeable differences under the control point of view are observed when choosing the proper values for the feedback configuration. A small deviation when driving the motor through the 300 m cable can be seen. However its effect is not always disadvantageous. Since the resolver configuration could vary slightly between different lengths and the Sum of Squares cannot be maintained exactly constant, the difference is always going to exist, affecting the commutation and hence, the velocity. During the realisation of this test, no particular increase on vibration was observed when increasing the cable length.

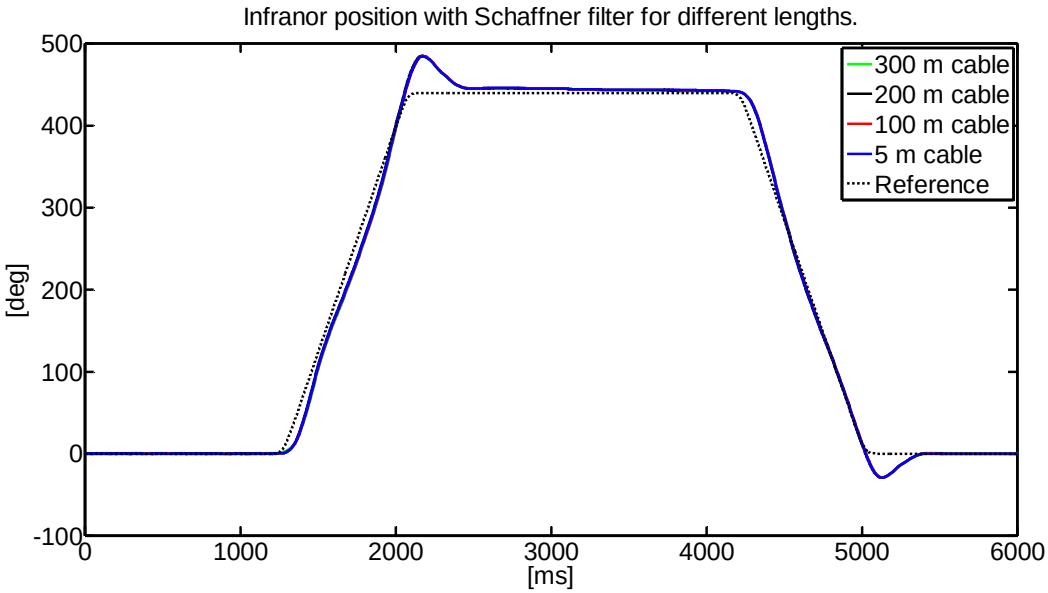

Figure 6-50. Position profile B accomplished with the Infranor motor at different cable lengths. Power cable and signal cable present same length.

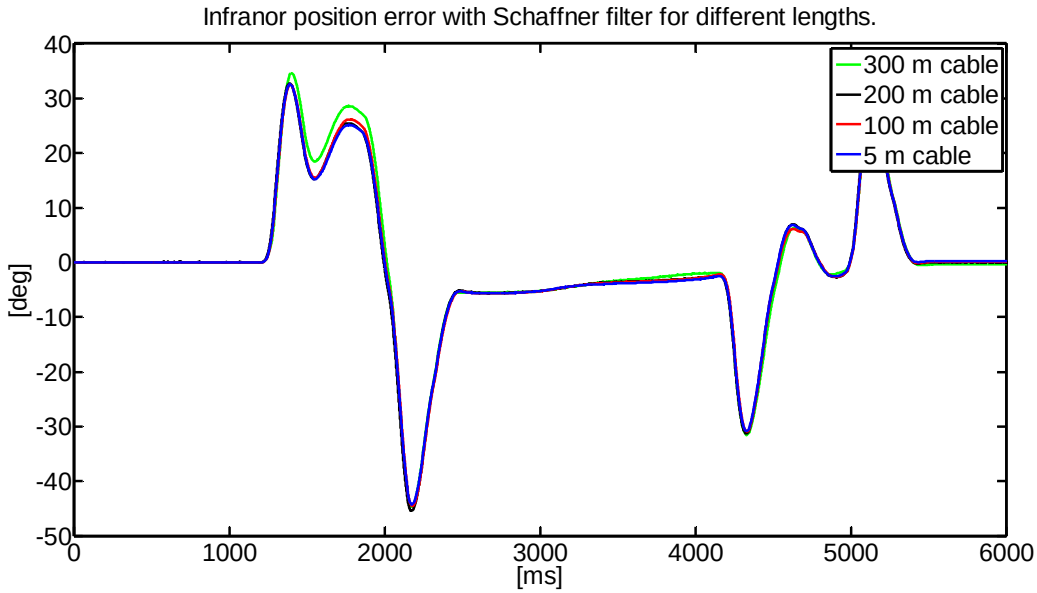

Figure 6-51. Position error obtained with the Infranor motor at different cable lengths. Power cable and signal cable present same length.

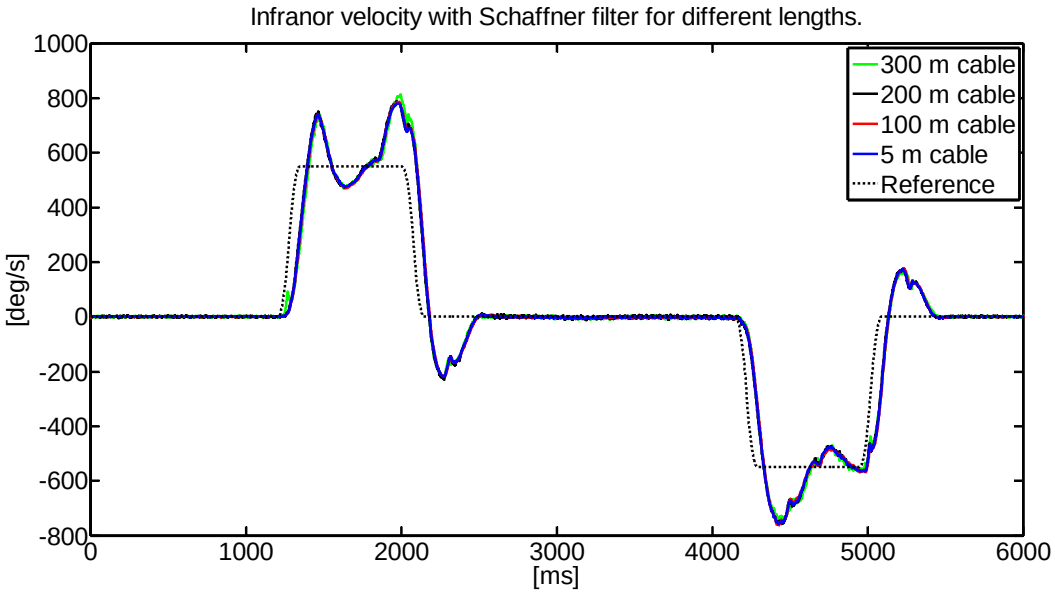

Figure 6-52. Velocity accomplished with the Infranor motor at different cable lengths. Power cable and signal cable present same length.

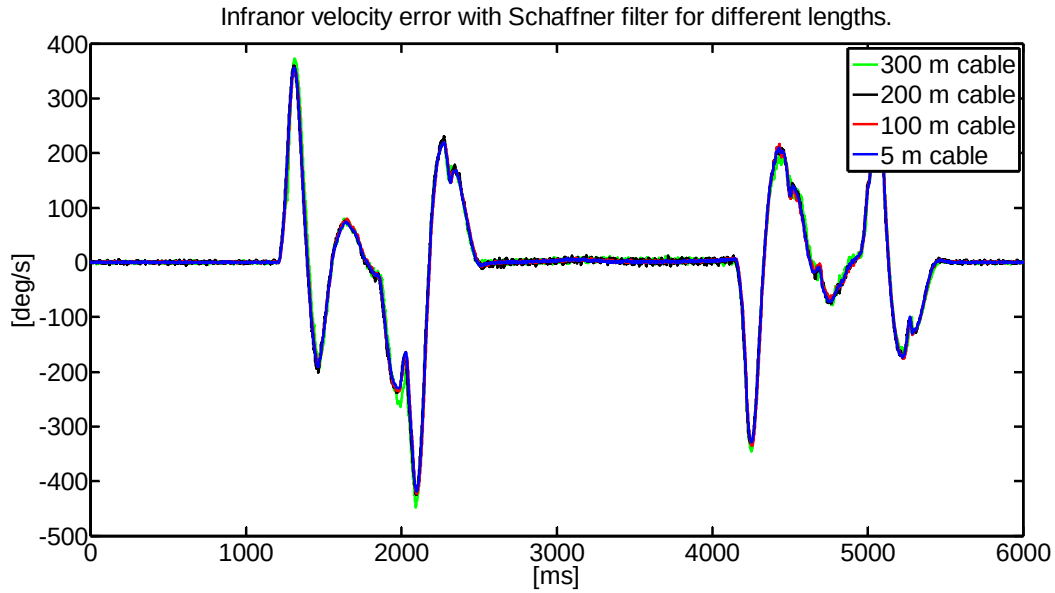

Figure 6-53. Velocity error obtained with the Infranor motor at different cable lengths. Power cable and signal cable present same length.

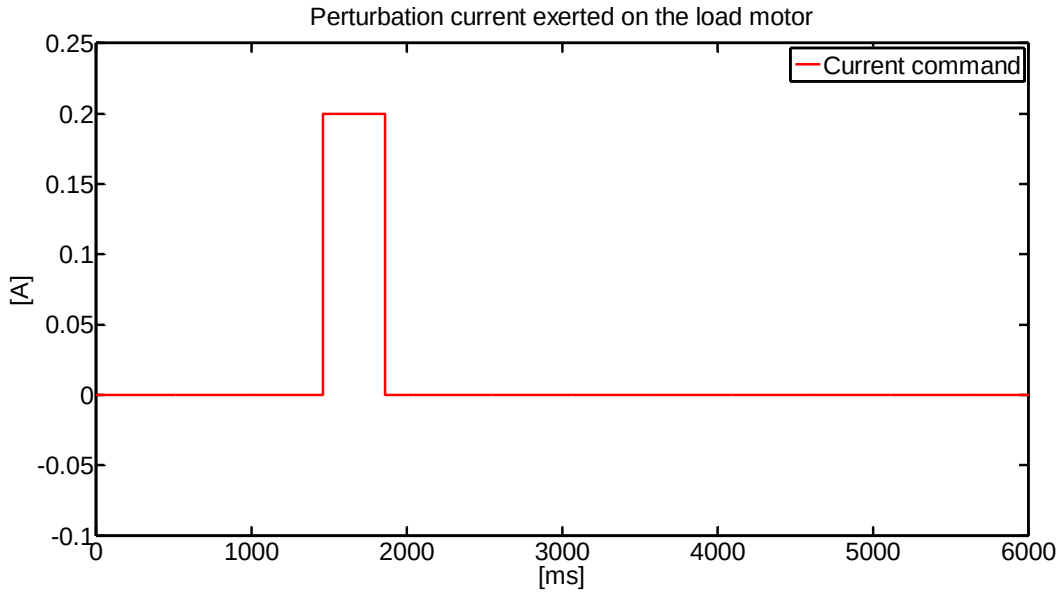

Figure 6-54. Disturbance torque reference issued with the load motor.

6.7 Discussion

When controlling electric motors via very long cables and PWM technique, reflections may occur due impedance mismatch. This is translated into a hazardous effect whose minimum consequence is poor control performance. A review of this effect and the mitigation methods is given in this chapter and a solution is proposed. Also, an extensive analysis of the performance obtained when implementing the proposed solution is carried out.

The dangerous effects of the reflected wave on the system composed by the drive, cable and motor can be successfully corrected with different techniques as demonstrated during simulation. These are LC filters, LCR filters, Snubbers, etc. The proposed commercial LC filter (Schaffner FN 530-4-99) presents good performance for motor frequencies under 200 Hz and it manages to filter the inverter signal up to frequencies where no visible standing wave is generated.

Under the control performance point of view, the implementation of the FN 530-4-99 has introduced a delay of about 3 ms in the settling time for the step response that has been analysed, however no delay on the rise time has been seen. This behaviour corresponds with the foreseen results since the filter acts as a damping for high frequencies, thus increasing the response time. However, this effect could be corrected by optimising the servo loop gains accordingly when a PWM filter is introduced.

This issue arises an important point for teleoperation stability and performance. Although servo control is not the most common type of control for dexterous manipulators operating in radioactive environments, it could be used in some configurations. It should not be confused the harmful effects produced by a delay in the communications between master and slave with delays due to a non-optimised slave control. The former is a very well-known source of instabilities and could lead in an unusable system. It is well-known from the literature that at least 1 kHz real-time update rate is advised in order to achieve haptic fidelity in teleoperation with force feedback [152]. On the other hand, when implementing a bilateral system with no delay or minimum delay in the communications but a non-optimised slave control, a settling time delay can be observed. This settling time delay is different than the communications delay in the sense that the operator would perceive it and thus, he would be able to react. Besides, depending on the bilateral algorithm implemented, a force on the master would be applied so that the operator movements will be restricted with the slave's dynamics. In this way, if the slave is not able to react as fast as the operator wants, he would not be able to move. This is equivalent of perceiving a system with increased inertia. It becomes slower but not necessarily unstable.

During this research it has been extensively proved that increasing the power cable length when implementing the FN 530-4-99 does not introduce major discrepancies with respect to the 5 m connection. Also, increasing the cable length up to distances of 300 m does not affect the control performance significantly and it is expected the same behaviour for even longer distances since no reflections are generated on sinusoidal waves for this order of magnitude.

These results are extremely important to guarantee the teleoperability in these scenarios where the control cubicles must to be placed hundreds of meters far from the manipulator area. It is crucial to know how to deal with the harmful over-voltage effects that are produced due to the PWM voltages when operating with long cable distances. And also, it is important to know that no major drawbacks are introduced when implementing this filtering techniques. It has been also proved how the filter does not affect the capabilities of the drive to deliver the required current demanded on a real teleoperation task with a dexterous manipulator. These results complement the first part of this thesis, and allow a force feedback teleoperation over long distances for radioactive environments.

Chapter 7 Conclusions

This thesis presents a step forward on the force estimation for industrial robots on a radioactive environments. It analyses the requirements of the final application which is, the teleoperation or remote handling on facilities subjected to ionizing radiation. These are facilities such as particle reactors, heavy ion reactors, fusion reactors, fission reactors or other nuclear environments. In this scenarios, the increasing radiation levels make prohibitive the use of electronics such as force and torque sensors. Although conventional teleoperation techniques could be applied without needing a force sensor, this would require the manipulator to be backdrivable in order to be implemented appropriately. However, the more demanding payload capabilities in the most modern nuclear facilities such as ITER, tend to increase gear ratios and backdrivability. Additionally, as explained on the first chapter, the potential adaptability of an industrial robot to operate in a radioactive environment would not involve huge modifications and facilities such as the Isolde at CERN would be able to count with an alternative method of operation if the automated routines fail.

There was little done on the literature for teleoperating industrials robots on nuclear environments. Most of it was performed by the CEA (Commissariat à l'énergie atomique et aux énergies alternatives) and it was based on implementing force/torque sensors with certain rad-hard capabilities. However those sensors would not operate for long on harsher environments such as ITER. For these reasons it was important to investigate additional paths that could lead in a stable teleoperation under these demanding requirements.

The development of this thesis was divided in three topics, which study three important aspects of the teleoperation in these facilities. Firstly, it is important to consider the kinematic disparities between master and slave. While the control room of a nuclear facility which requires remote handling could employ optimised haptic masters prepared for the man in the loop activity, the remote devices or slaves could vary depending on the remote task. This variation requires the definition of new framework

which simplifies the dissimilar kinematics. A novel algorithm is proposed which optimises the overlapping of master and slave's workspaces in terms of the kinematic manipulability in order to select an adequate scale and translation coordinates.

A study on a real ABB robot was performed showing the difficulties of teleoperating robots with closed system and a set of manufacturers which provide easiness of interfacing for real time control was given.

Finally an experiment with a Phantom OMNI haptic device was explained to prove the applicability of mentioned algorithms. Proposed control algorithm resulted very good for teleoperating master and slave with dissimilar kinematics and the novelty of using optimisation for adjusting the parameters of the transformation was important.

Afterwards, the research work looked towards the dynamics and the need of force estimation to create a force feedback on the master device. When only proprioceptive sensors can be involved, one possible solution to the problem goes through modelling the robot and comparing the expected output with the real one. In order to fulfil this approach, it was necessary to develop an acceptable robotic model which was able to predict external forces. A lot of effort was put on modelling and parameter identification of robots equipped with a parallelogram structure and an optimum way was broadly explained and developed. We quickly realised that no appropriate robot's dynamics integration could be done if the estimated parameters did not present physical sense. This led the research through an optimisation of the identified parameters which transforms a predictive model into a structural one. This worked satisfactorily and allowed to complete a structural model of a robot which was adequate for developing a state observer.

During the parameters identification stage, it was required to design an appropriate trajectory to excite most of robot dynamics without affecting the structural flexibilities. It was proved that increasing the harmonic content of the identification trajectory tends to improve the accuracy of the estimation if the number of samples is kept constant. Innovative techniques for the calculation of the excitation trajectories were developed during this thesis which maximise the joint's movement range. Also, novel constraints applied during the optimisation of identified parameters were proposed in order to obtain a robotic model with full physical sense.

Obtaining a complete robot model was crucial to test different force estimations algorithms. Firstly, the direct evaluation of the robot dynamics equation was performed. This method showed excellent behaviour when involving an off-line estimation. It was explained the convenience of this approach for load off-line load characterization when for example a new end-effector tool is introduced. We investigated the use of observers for force estimation. They were initially developed for velocity estimations but it was

proved that they were quickly adaptable for external force estimation. A classical Luenberger observer was developed and tested for predicting forces during the teleoperation of a hydraulic manipulator and the results were validated against an ATI force/torque sensor. The results were acceptable but any deviation of the model could be transformed in a torque offset for each joint that would be fed back to the operator creating inexistent forces. This led the research to the investigation of more robust alternatives to cope with model inaccuracies. The Sliding observer was found useful when controlling highly nonlinear systems. However the issue laid on a strong chattering effect of the control action, difficult to achieve in real systems. Nevertheless, this did not become a problem since the sliding effect was used in an observer instead of in a control system. The combination of Luenberger and Sliding action resulted excellent for eliminating the torque offset experienced before, in absence of external forces.

A complete bilateral teleoperation system was simulated using Simulink © employing the previous results. This was used to test the applicability of this approach before real implementation and to study potential issues. The simulator was proved useful for comparing the classical Position-Position algorithm with the newer approach based on observers. It has been demonstrated how the Force-Position algorithm based on force observer is comparable to previous scheme and superior in some circumstances since avoids the drag effect and its performance does not depend on the control performance.

The remote handling maintenance and operation of nuclear facilities is characterised for the occurrence of unexpected events that could require unexpected solutions operated by a man in the loop. It has been seen in numerous occasions that the use of off-the-shelf robots or so called industrial robots could open new ways for remote operations by decreasing cost, avoiding development of new dexterous manipulators and ensuring an excellent behaviour. The new approach presented on this thesis must be considered when a teleoperation of an industrial robot is desired on a nuclear environment. However some issues must not be underestimated. Although the technique has been widely detailed here, the application to a new device could result complicated and efforts to automate the deployment on different equipment would be appreciated. Design, develop, identify and optimise a new dynamic model for a robot although possible, it is not an easy task that could be done as quickly as setting-up a new force sensor in a manipulator. Also, building the robot observer and tuning its gains properly is time consuming. It is then understandable that other research lines are investigating the development of new hard-rad FPGA based sensors which could replace traditional sensors. However, currently there is no such a solution available in the market and this justifies the application of observer techniques.

During the last part of this thesis the attention has been focused on solving the additional problems that arise during the teleoperation in nuclear facilities. Teleoperation

is not only about perceiving the environment satisfactorily, but also about exerting motor actions that mimic operator's movements. Slave's actuators are powered via long power cables in electrical manipulators which are typically placed at long distances from the control cubicle on radioactive facilities. This is done to protect the control system against radiation. In these circumstances, cable length could reach hundreds of meters in facilities such as ITER. It is well-known that transmitting high frequency signals, like those ones employed on the drive's PWM, through long distances, leads in undesirable reflections. Reflections could damage any element in the system composed by drive, cable and motor and are then unacceptable in remote handling. In order to cope with this issue, this effect was studied and characterised in a representative motor of a dexterous manipulator. Several solutions were found on the literature to solve the overvoltage but only the most important were selected and simulated using PSPICE ©. Finally an LC filter was selected in the end for final implementation, proving extremely good performance. Extensive tests and comparison scenarios were performed to study the influence of the filter on the control performance. The results indicated that, in our range of frequencies, the filter was completely acceptable for eliminating the standing wave, without deteriorating the control performance.

ANNEX I: Specifications and kinematic model of ABB IRB 2400-16 and Phantom OMNI

ABB IRB 2400-16 industrial robot

The schematic representation of each link overlaid with the robot is shown on Figure A1-1. It should be noticed that ABB IRB 2400-16 presents and offset on the elbow which makes the calculation of the inverse kinematics more consuming. This manipulator is a 6 dof robot with rotational joints whose main characteristics are shown on Table A1-1.

ABB IRB 2400 16 Specifications	
Main applications	Arc welding, cutting/deburring, gluing/sealing, grinding/polishing, machine tending, material handling
Specification	Reach Payload Protection IRB 2400-16 1.55 m 20 kg FoundryPlus Number of axes 6
Physical	Dimensions IRB 2400-10 IRB 2400-16 Total height 1564 mm 1564 mm Robot base 723x600 mm 723x600 mm Robot weight 380 kg 380 kg
Performance (according to ISO 9283)	Position repeatability (RP) 0.03 mm Path repeatability 0.11-0.15 mm
Movements	Axis IRB 2400-16 Working range: Axis 1 360° Axis 2 210° Axis 3 125° Axis 4 400° Axis 5 240° Axis 6 800°

Table A1-1. Specifications of the ABB IRB 2400-16 industrial robot.

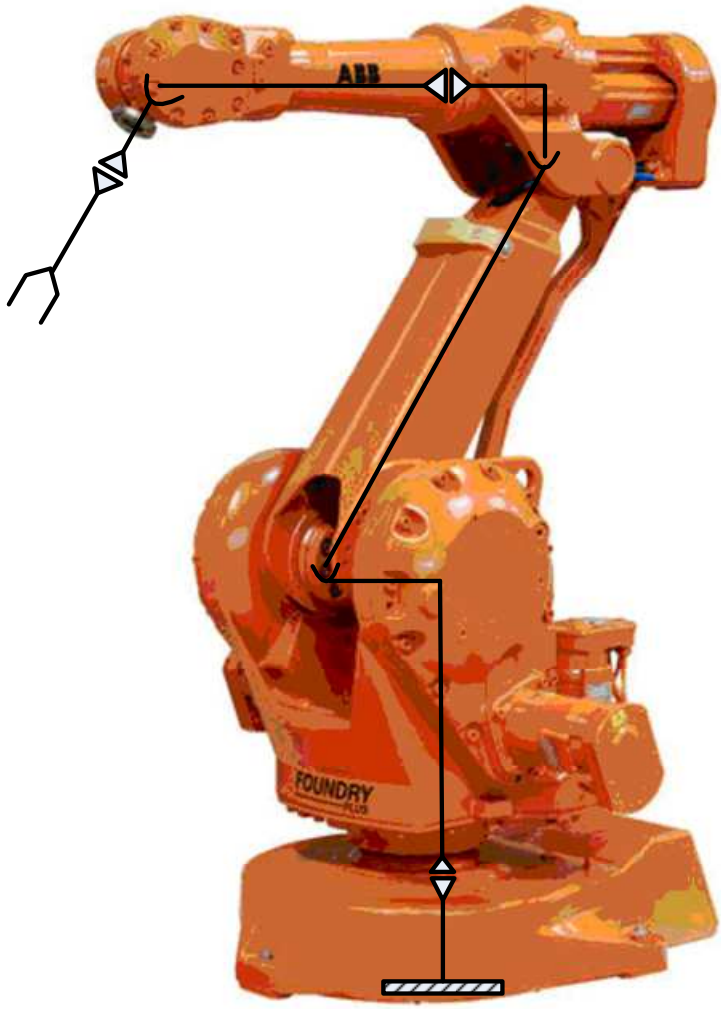

Figure A1-1. ABB IRB 2400-16 simplified link model.

On Figure A1-2, a more detailed schematic of the ABB robot is illustrated, with link dimensions and the reference system of each link used for the kinematics calculations. Also the Denavit-Hartember table for these reference system is shown on Table A1-2. Six transformation matrices which contain all the necessary information to compute the forward kinematics are also shown

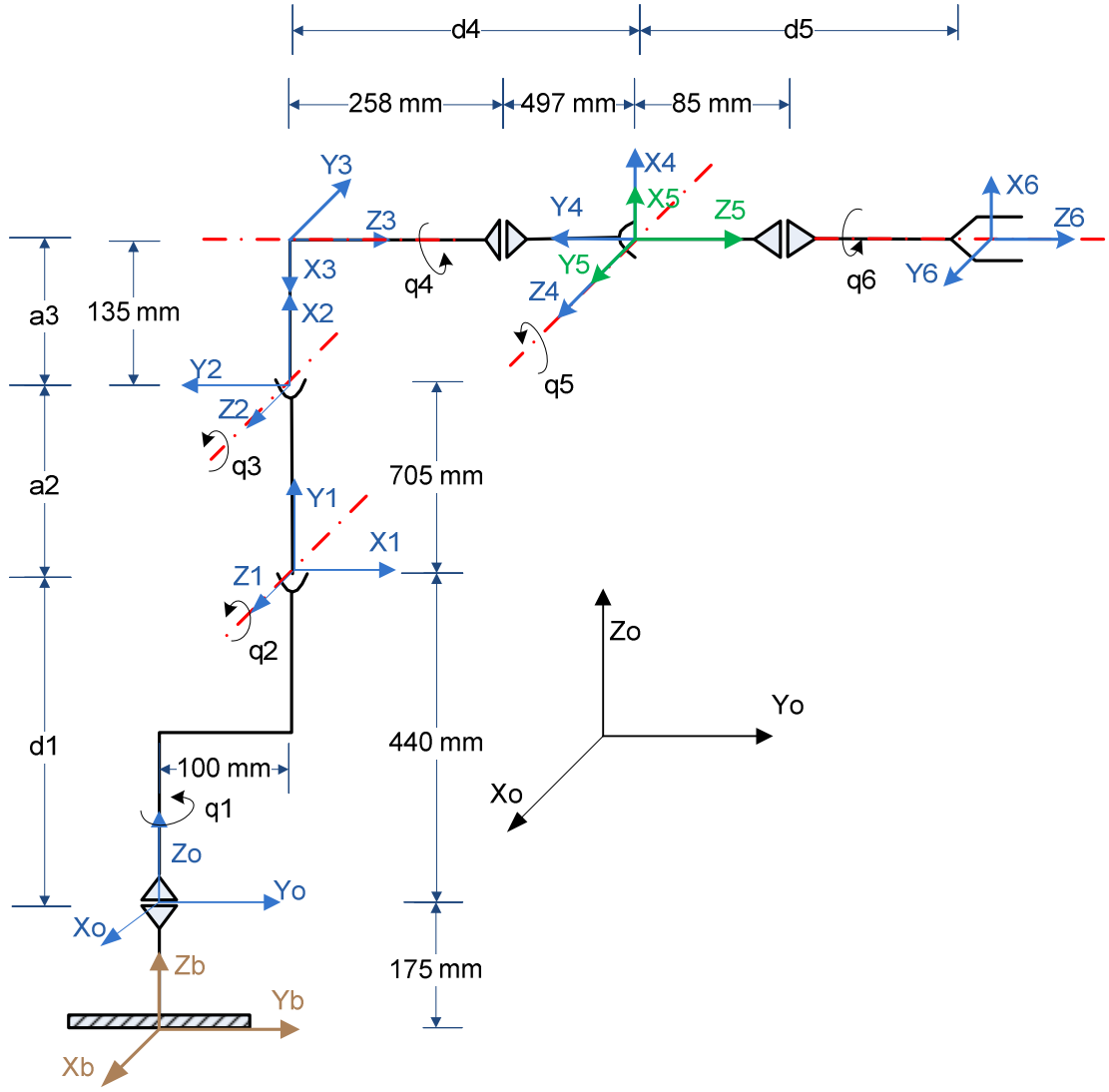

Figure A1-2. Reference systems and link dimensions for ABB IRB 2400-16.

The Denavit-Hartember parameters of this manipulator are shown on Table A1-2.

	$\boldsymbol{\theta}$	$\boldsymbol{d}$	$\boldsymbol{a}$	$\boldsymbol{\alpha}$
1	q_1	d_1	a_1	$\pi/2$
2	$\pi/2 + q_2$	0	a_2	0
3	$\pi + q_3$	0	$-a_3$	$-\pi/2$
4	$\pi + q_4$	d_4	0	$-\pi/2$
5	q_5	0	0	$\pi/2$
6	q_6	d_5	0	0

Table A1-2. Denavit-Hartember parameters of the ABB IRB 2400-16.

Joint	Max. value [deg]	Min. value [deg]
q_1	180	-180
q_2	100	-110
q_3	65	-65
q_4	180	-180
q_5	120	-120
q_6	180	-180

Table A1-3. Joint range for the ABB IRB 2400-16

Forward Kinematics of the ABB IRB 2400-16

From the Denavit-Hartember parameters expressed on Table A1-2 it is straight forward to calculate the Denavit Hartember matrices for the ABB robot on the reference system indicated on Figure A1-2:

$$ {}^{0}A_1 = \begin{pmatrix} \cos(q_1) & 0 & \sin(q_1) & a_1\cos(q_1) \\ \sin(q_1) & 0 & -\cos(q_1) & a_1\sin(q_1) \\ 0 & 1 & 0 & d_1 \\ 0 & 0 & 0 & 1 \end{pmatrix} \tag{A1.1} $$

$$ {}^{1}A_2 = \begin{pmatrix} -\sin(q_2) & -\cos(q_2) & 0 & a_2\sin(q_2) \\ \cos(q_2) & -\sin(q_2) & 0 & a_2\cos(q_2) \\ 0 & 0 & 1 & 0 \\ 0 & 0 & 0 & 1 \end{pmatrix} \tag{A1.2} $$

$$ {}^{2}A_3 = \begin{pmatrix} -cos(q_3) & 0 & sin(q_3) & a_3\,cos(q_3) \\ -sin(q_3) & 0 & -cos(q_3) & a_3\,sin(q_3) \\ 0 & -1 & 0 & 0 \\ 0 & 0 & 0 & 1 \end{pmatrix} \tag{A1.3} $$

$$ {}^{3}A_4 = \begin{pmatrix} -cos(q_4) & 0 & sin(q_4) & 0 \\ -sin(q_4) & 0 & -cos(q_4) & 0 \\ 0 & -1 & 0 & d_4 \\ 0 & 0 & 0 & 1 \end{pmatrix} \tag{A1.4} $$

$$ {}^{4}A_5 = \begin{pmatrix} cos(q_5) & 0 & sin(q_5) & 0 \\ sin(q_5) & 0 & -cos(q_5) & 0 \\ 0 & 1 & 0 & 0 \\ 0 & 0 & 0 & 1 \end{pmatrix} \tag{A1.5} $$

$$ {}^5A_6 = \begin{pmatrix} cos(q_6) & -sin(q_6) & 0 & 0 \\ sin(q_6) & cos(q_6) & 0 & 0 \\ 0 & 0 & 1 & d_5 \\ 0 & 0 & 0 & 1 \end{pmatrix} \tag{A1.6} $$

As in (3.1), it is possible to find the matrix T, $T = {}^0A_1 \cdot {}^1A_2 \cdot {}^2A_3 \cdot {}^3A_4 \cdot {}^4A_5 \cdot {}^5A_6 = {}^0A_3 \cdot {}^3A_6$

And also grouping the two transformation matrices in two parts, the first part takes into account the first 3 dof which define the position of the wrist, and the second part groups the last 3 dof which define the orientation of the end effector. This will allow to find useful expressions for the inverse kinematics. Each one of the matrices ${}^0A_3$ and ${}^3A_6$ can be expressed as four column vectors where the first three define an orthonormal triad which expresses the rotation of the final reference system with respect the original system. The last vector defines the final reference system's position with respect the initial.

$$ {}^0A_3 = [n_{03}\ o_{03}\ a_{03}\ p_{03}] \tag{A1.7} $$

$$ n_{03\,x} = sin(q_2 + q_3) \cdot cos(q_1) \tag{A1.8} $$

$$ n_{03\,y} = sin(q_2 + q_3) \cdot sin(q_1) \tag{A1.9} $$

$$ n_{03\,z} = -cos(q_2 + q_3) \tag{A1.10} $$

$$ o_{03\,x} = -sin(q_1) \tag{A1.11} $$

$$ o_{03\,y} = cos(q_1) \tag{A1.12} $$

$$ o_{03\,z} = 0 \tag{A1.13} $$

$$ a_{03\,x} = cos(q_2 + q_3) \cdot cos(q_1) \tag{A1.14} $$

$$ a_{03\,y} = cos(q_2 + q_3) \cdot sin(q_1) \tag{A1.15} $$

$$ a_{03\,z} = sin(q_2 + q_3) \tag{A1.16} $$

$$ p_{03\,z} = -cos(q_1) \cdot (a_3 \cdot sin(q_2 + q_3) - a_1 + a_2 \cdot sin(q_2)) \tag{A1.17} $$

$$ p_{03y} = -cos(q_1) \cdot (a_3 \cdot sin(q_2 + q_3) - a_1 + a_2 \cdot sin(q_2)) \tag{A1.18} $$

$$ p_{03\,z} = d_1 + a_3 \cdot cos(q_2 + q_3) + a2 \cdot cos(q_2) \tag{A1.19} $$

$$ {}^3A_6 = [n_{36}\ o_{36}\ a_{36}\ p_{36}] \tag{A1.20} $$

$$n_{36\,x} = sin(q_4) \cdot sin(q_6) - \ cos(q_4) \cdot cos(q_5) \cdot cos(q_6) \tag{A1.21}$$

$$n_{36\,y} = \ - cos(q_4) \cdot sin(q_6) - \ cos(q_5) \cdot cos(q_6) \cdot sin(q_4) \tag{A1.22}$$

$$n_{36\,z} = \ -cos(q_6) \cdot sin(q_5) \tag{A1.23}$$

$$o_{36\,x} = \ cos(q_6) \cdot sin(q_4) + \ cos(q_4) \cdot cos(q_5) \cdot sin(q_6) \tag{A1.24}$$

$$o_{36\,y} = \ cos(q_5) \cdot sin(q_4) \cdot sin(q_6) - \ cos(q_4) \cdot cos(q_6) \tag{A1.25}$$

$$o_{36\,z} = sin(q_5) \cdot sin(q_6) \tag{A1.26}$$

$$a_{36\,x} = \ -cos(q_4) \cdot sin(q_5) \tag{A1.27}$$

$$a_{36\,y} = \ -sin(q_4) \cdot sin(q_5) \tag{A1.28}$$

$$a_{36\,z} = \ cos(q_5) \tag{A1.29}$$

$$p_{36\,x} = \ \ -d_5 \cdot cos(q_4) \cdot sin(q_5) \tag{A1.30}$$

$$p_{36\,y} = \ -d_5 \cdot sin(q_4) \cdot sin(q_5) \tag{A1.31}$$

$$p_{36\,z} = \ d_4 \ + d_5 \cdot cos(q_5) \tag{A1.32}$$

Inverse Kinematics of the ABB IRB 2400-16

Inverse kinematics deals with the problem of finding the required joint angles to produce a certain desired position and orientation of the end-effector. Finding the inverse kinematics solution for a general manipulator can be a very tricky task. Generally they are nonlinear equations. Close-form solutions may not be possible and multiple, infinity, or impossible solutions can arise. Nevertheless, special cases have a closed-form solution and can be solved.

The sufficient condition for solving a six-axis manipulator is that it must have three consecutive revolute axes that intersect at a common point: Pieper condition [153]. Three consecutive revolute parallel axes is a special case of the above condition, since parallel lines can be considered to intersect at infinity. The ABB IRB 2400 meets the Pieper condition due to the spherical wrist. Since this manipulator has analytic solution for the inverse kinematics one must take advantage of it in order to reduce computational cost with respect the numeric solution. Below, the steps followed for the calculation of the complete inverse kinematic are explained. On Figure A1-3, the main angles and length parameters used for the calculation of the inverse kinematics are shown.

Firstly it is useful to know the coordinates of the wrist (Pm point) with respect the system 0. This simple operation facilitates the calculation of all the joints.

$$P^{0}_{m} = T \cdot (0, 0, -d_5, 1)^T \tag{A1.33}$$

Where the matrix T expresses the forward kinematics of the robot. This operation transforms the wrist point expressed on the robot end-effector system to the system 0. Once the coordinates of this point are obtained, it is straight forward to get the first joint angle:

$$q_1 = atan2(P_{my}, P_{mx}) \tag{A1.34}$$

In order to obtain q_2 it is necessary to translate now the P_m point to the system 1. For doing that,

$$P^{1}_{m} = ({}^{0}A_1)^{-1} \cdot {}^{0}P_m \tag{A1.35}$$

And then translating this point to polar coordinates to simplify, taking into account that the reference of system 1 has different orientation than system 0:

$$P^{1}_{m\ vertical} = P^{1}_{m_y} \text{ and } P^{1}_{m\ radial} = \left| P^{1}_{m_x} \right| \tag{A1.36}$$

By calculating now, l_3 and the angle β, it is possible to infer the angle α and distinguish two different scenarios:

$$l_3 = sqrt(\left(P^{1}_{m\ radial}\right)^2 + \left(P^{1}_{m\ vertical}\right)^2) \tag{A1.37}$$

$$\beta = atan2(P^{1}_{m_x}, P^{1}_{m_y}) \tag{A1.38}$$

$$\begin{cases} \alpha = \text{acos}\left(\frac{a_2^2 + l_3^2 - a_3^2 - d_4^2}{2a_2 \cdot l_3}\right), & if \ \left|\frac{a_2^2 + l_3^2 - a_3^2 - d_4^2}{2a_2 \cdot l_3}\right| < 1 \\ \alpha = 0, \ if \ \left|\frac{a_2^2 + l_3^2 - a_3^2 - d_4^2}{2a_2 \cdot l_3}\right| \geq 1 \end{cases} \tag{A1.39}$$

Once α and β are obtained, the calculation of the second joint value is straight forward by looking the schematic:

$$\begin{cases} q_2 = -(\beta - \alpha), & if \ P^{1}_{m_x} > 0 \\ q_2 = -\beta + \alpha, \ if \ P^{1}_{m_x} \leq 0 \end{cases} \tag{A1.39}$$

Now for q_3, the P_m point is utilized again and its representation in different reference systems, thus:

$$P^{0}_{m} = {}^{0}A_1 \cdot {}^{1}A_2 \cdot {}^{2}A_3 \cdot {}^{3}A_4 \cdot (0, 0, 0, 1)^T \tag{A1.40}$$

$$({}^{1}A_2)^{-1} \cdot ({}^{0}A_1)^{-1} \cdot P^{0}_{m} = {}^{2}A_3 \cdot {}^{3}A_4 \cdot (0, 0, 0, 1)^T \tag{A1.40}$$

And operating both sides of the equality, taking into account than the left side is known, it yields to:

$$\begin{pmatrix} i_1 \\ i_2 \\ i_3 \end{pmatrix} = \begin{pmatrix} a_3\cos(q_3) + d_4 \cdot \sin(q_3) \\ a_3\sin(q_3) - d_4 \cdot \cos(q_3) \\ 0 \\ 1 \end{pmatrix} \tag{A1.41}$$

$$q_3 = \text{asin}(\tfrac{d_4 \cdot i_1 + a_3 \cdot i_2}{d_4^2 + a_3^2}) \tag{A1.43}$$

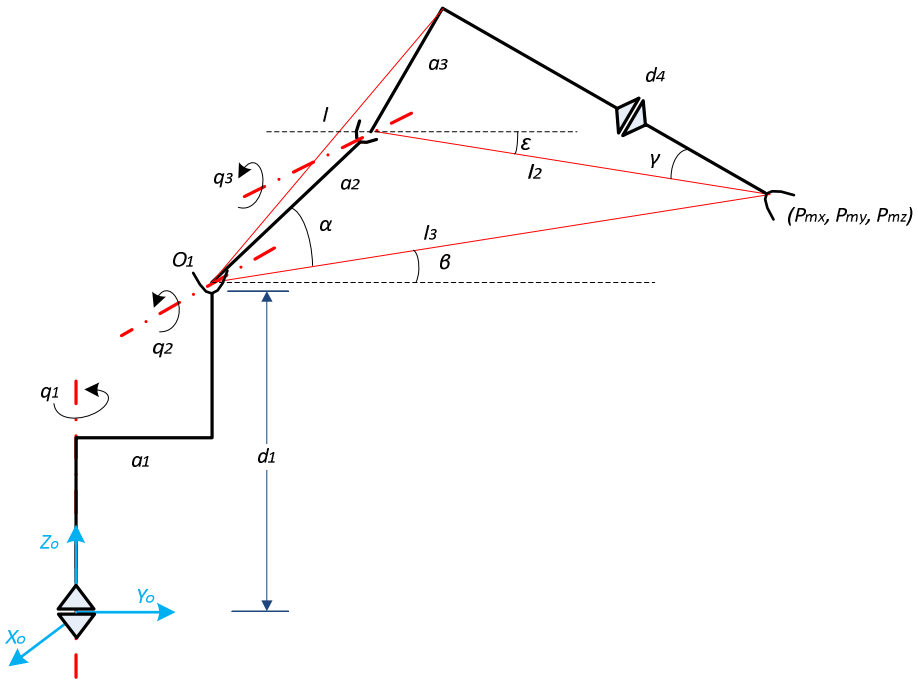

Figure A1-3. Schematic of the ABB robot showing the main angles and points used for the inverse kinematics calculation. Now, the remaining 3 dof are easily calculated by doing a simple transformation based on the joints that have already been calculated:

$$^3A_6 = (^0A_3)^{-1} \cdot T \tag{A1.44}$$

And the expression of the rotation matrix $^3R_6$ is then:

$$^3R_6 = \begin{pmatrix} \text{s}(q_4)\text{s}(q_6) - c(q_4)c(q_5)c(q_6) & \text{c}(q_4)\text{c}(q_5)\text{s}(q_6) + s(q_4)c(q_6) & -c(q_4)s(q_5) \\ -\text{c}(\text{q}_4)\text{s}(q_6) - s(q_4)c(q_5)c(q_6) & s(q_4)\text{c}(q_5)s(q_6) - c(q_4)c(q_6) & -s(q_4)s(q_5) \\ -s(q_5)c(q_6) & s(q_5)s(q_6) & c(q_5) \end{pmatrix} \tag{A1.45}$$

So q_5 is directly inferred from $^3R_6$ taking into account the two possible solutions which can give the same $\cos(q_5)$,

$$q_{51} = \text{acos}(^3R_6(3,3)) \tag{A1.46}$$

$$q_{52} = -q_{51} \tag{A1.47}$$

$$q_4 = atan2({}^3R_6(2,3), {}^3R_6(1,3)) \tag{A1.48}$$

And finally the last joint is calculated with the following expression:

$$q_6 = atan2(-{}^3R_6(3,2), -\ {}^3R_6(3,1)) \tag{A1.48}$$

Also, in case of a singularity occurs, that, for this manipulator, happens when:

$q_{51} = 0$ or $q_{52} = 0$, q_4 will take the previous value, which is a good choice $q_4 = q_{4previous}$, and then it only left to calculate q_6:

$$q_{46} = atan2({}^3R_6(1,2), -{}^3R_6(1,1)) \tag{A1.49}$$

$$q_6 = q_{46} - q_4 \tag{A1.50}$$

RAPID code for teleoperating the ABB IRB 2400-16

```
%%%
  VERSION:1
  LANGUAGE:ENGLISH
%%%

MODULE TELEOPERAT1302
  VAR jointtarget jointTARGET1:=[[-0.15,-
1.11,0.08,0.01,0.44,2.48],[9E+09,9E+09,9E+09,9E+09,9E+09,9E+09
]];
  VAR string jointsVALstring:="";
  VAR jointtarget jointsVAL:=[[-0.15,-
1.11,0.07,0.01,0.44,2.49],[9E+09,9E+09,9E+09,9E+09,9E+09,9E+09
]];
  VAR robjoint AXISrobjoint:=[0,0,0,0,0,0];
  <DDN>
  CONST string delim:="\09 ";
  VAR string string3:="";
  CONST string string2:="";
  CONST string string1:="";
  CONST string q1s:="";
  VAR num q1:=0;
  VAR num q6:=0;
  VAR num q5:=0;
  VAR num q4:=0;
  VAR num q3:=0;
  VAR num q2:=0;
  VAR num count1:=0;
  VAR iodev PC;
```

```
  PROC main()
    WHILE count1<10 DO
      Open "COM3:",PC\Read;
      q1:=ReadNum(PC\Delim:=delim);
      q2:=ReadNum(PC\Delim:=delim);
      q3:=ReadNum(PC\Delim:=delim);
      q4:=ReadNum(PC\Delim:=delim);
      q5:=ReadNum(PC\Delim:=delim);
      q6:=ReadNum(PC\Delim:=delim);
      Close PC;
      AXISrobjoint:=[q1,q2,q3,q4,q5,q6];
      jointsVAL:=CJointT();
      jointTARGET1.robax:=AXISrobjoint;
      jointTARGET1.extax:=[0,9E+09,9E+09,9E+09,9E+09,9E+09];
      StopMove;
      ClearPath;
      MoveAbsJ\Conc,jointTARGET1\NoEOffs,v1000,z50,tool0;
      Open "COM3:",PC\Write;
      jointsVALstring:=ValToStr(jointsVAL.robax);
      Write PC,jointsVALstring;
      Close PC;
    ENDWHILE
  ENDPROC
ENDMODULE
```

Phantom OMNI haptic master

On Table A1-4 the main characteristics of the Phantom OMNI haptic master are shown. The same procedure is applied to the haptic master in order to get the forward kinematic which will be needed. The schematic representation of each link overlaid with the master is shown on Figure A1-4. It should be mentioned that this haptic master is a 6 dof device with rotational joints. The schematic of the links and their dimensions is represented on Figure A1-5. It also contains the chosen reference system for obtaining the Denavit-Hartemberg parameters of Table A1.5.

Phantom OMNI Specifications	
Force feedback workspace	~160 W x 120 H x 70 D mm
Footprint (Physical area device base occupies on desk)	~168 W x 203 D mm
Weight (device only)	1.79 kg
Range of motion	Hand movement pivoting at wrist
Nominal position resolution	~ 0.055 mm
Backdrive friction	< 0.26 N

Maximum force at nominal (orthogonal arms) position	3.3 N
Continuous force (24 hrs)	0.88 N
Stiffness	X axis > 1.26 N / mm Y axis > 2.31 N / mm Z axis > 1.02 N / mm
Inertia (apparent mass at tip)	~ 45 g
Force feedback	x, y, z
Position sensing [Stylus gimbal]	x, y, z (digital encoders) [Pitch, roll, yaw (± 5% linearity potentiometers)]
Interface	IEEE-1394 FireWire® port: 6-pin to 6-pin
Supported platforms	Intel or AMD-based PCs

Table A1-4. Phantom OMNI specifications.

Figure A1-4. Phantom OMNI simplified link model

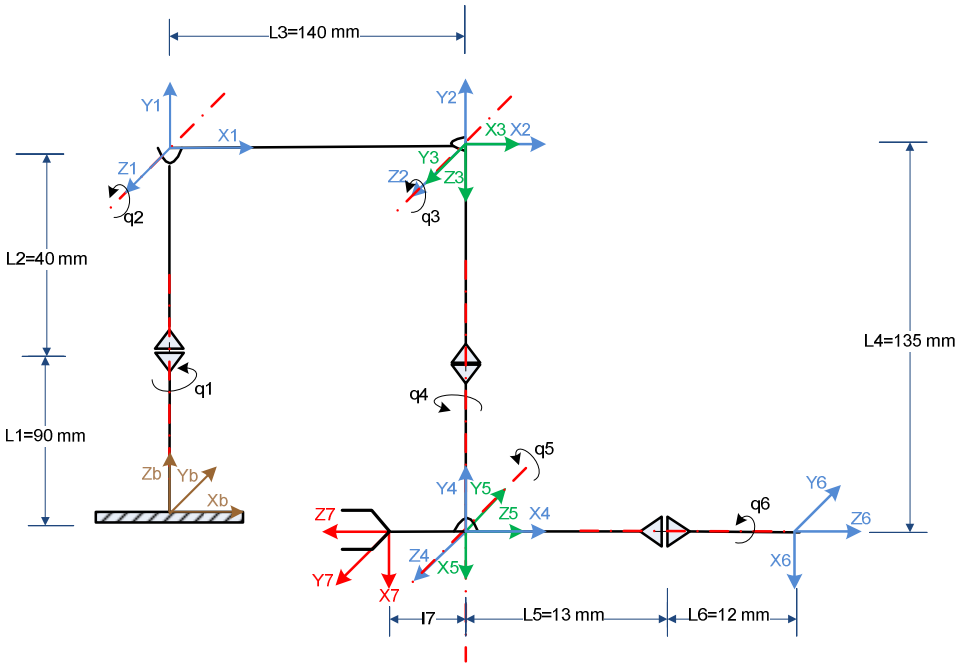

Figure A1-5. Reference systems and link dimensions for Phantom OMNI haptic master.

The Denavit-Hartember parameters of this haptic master are shown on Table A1.5

	$\boldsymbol{\theta}$	$\boldsymbol{d}$	$\boldsymbol{a}$	$\boldsymbol{\alpha}$
1	q_1	$l_1 + l_2$	0	$\pi/2$
2	q_2	0	l_3	0
3	q_3	0	0	$\pi/2$
4	q_4	l_4	0	$-\pi/2$
5	$q_5 - \pi/2$	0	0	$-\pi/2$
6	q_6	$l_5 + l_6$	0	0
7	0	$-(l_5 + l_6 + l_7)$	0	π

Table A1.5. Denavit-Hartember parameters of the Phantom OMNI.

Joint	**Max. value [deg]**	**Min. value [deg]**
$\boldsymbol{q_1}$	55	-55
$\boldsymbol{q_2}$	100	0
$\boldsymbol{q_3}$	80	-10
$\boldsymbol{q_4}$	147	-147
$\boldsymbol{q_5}$	55	-75
$\boldsymbol{q_6}$	180	-180

Table A1.6. Joint range of the Phantom OMNI haptic master.

ANNEX II: Sliding control

Most of literature on sliding surfaces refers to the concept investigated in [154] by Filippov where it was used to stabilize a class of nonlinear system [137].

Although it has been used to stabilize a huge variety of systems due to its properties in the presence of parametric uncertainty, classical sliding control presents several drawbacks which limit its practical application on real control systems.

For instance, it requires a large control authority and control chattering [137]. Some methods have been developed in [138] to cope with that chattering by smoothing the transition. Similar solution has been employed on this research to reduce the strong control action of the sliding mode when alternating from one zone to the next.

Sliding observers present similar benefits than sliding control, in particular inherent robustness of parametric uncertainty and easy application to important class of non-linear systems. In contrary to the sliding control, the observer implementation is not affected by mechanical implementations and only by numerical problems.

Let us summarize the basic idea of a sliding mode and the advantages and disadvantages of using discontinuous control actions. Considering the dynamic system given by (A2.1).

$$x^{(n)}(t) = f(\bar{x}, t) + b(\bar{x}, t)u(t) + d(t) \tag{A2.1}$$

Where $u(t)$ is a scalar control input, x is the scalar output of interest and $\bar{x} = [x, \dot{x}, \dots, x^{(n-1)}]^T$is the state of the system. The function $f(\bar{x}, t)$ is in general nonlinear and non-exactly known, but the absolute value of the error is upper bounded by a function of $\bar{x}$ and t. $b(\bar{x}, t)$ is the control gain which is also not exactly known but it is also bounded and its sign is known. The disturbance $d(t)$ is unknown but bounded in absolute value by a function of time.

The control problem is to get the state $\bar{x}$ to track a specific state $\bar{x}_d = [x_d, \dot{x_d}, \dots, x^{d(n-1)}]$ in the presence of model imprecision in $f(\bar{x}, t)$ and $b(\bar{x}, t)$, and of disturbances $d(t)$.

Let $\tilde{\bar{x}} = \bar{x} - \bar{x}_d$ be the tracking error in the vector $\bar{x}$. Defining a time-varying sliding surface $s(t)$ in the state space R^n as $s\left(\tilde{\bar{x}}, t\right) = 0$ with (A2.2) and the constant λ being

positive. The problem of tracking $\bar{x} = \bar{x}_d$ is equivalent to remaining on the surface $s(t)$ for all $t > 0$.

$$s(\tilde{\bar{x}}, t) = (\tfrac{d}{dt} + \lambda)^{n-1}\tilde{\bar{x}}, \lambda{>}0 \tag{A2.2}$$

For instance, if n=2,

$s = \dot{\tilde{x}} + \lambda\tilde{x}$ i.e., s is simply a weighted sum of the position error and the velocity error, if n=3, $s = \ddot{\tilde{x}} + 2\lambda\dot{\tilde{x}} + \lambda^2\tilde{x}$.

If the initial conditions are established as: $\tilde{x}|_{t=0} = 0$, $s = 0$ represents a linear differential equations whose unique solution is $\tilde{x} = 0$. The problem of tracking the n-dimensional vector $\bar{x}_d$ can in effect be replaced by a 1st order stabilization problem in s Indeed, from A2.2 the expression of s contains $x^{(n-1)}$, we only need to differentiate s once for the input u to appear.

The simplified, 1st-order problem of keeping the scalar s at zero can no be achieved if having a control law which satisfies the sliding condition (A2.3) with the constant η being positive, this control law has to be discontinuous across the sliding surface, thus leading to control chattering.

$$(\tfrac{1}{2})\tfrac{d}{dt}s^2(x;t) \leq -\eta|s| \tag{A2.3}$$

Condition (A2.3) guarantees that the error decreases in every trajectory. Thus, it constraints trajectories to point towards surface s as illustrated in Figure A2-1.

$$s \cdot \dot{s} \leq -\eta|s|, \tag{A2.4}$$

$$\begin{cases} if\ s > 0, \dot{s} \leq -\eta \\ if\ s > 0, \dot{s} \geq \eta \end{cases} \tag{A2.5}$$

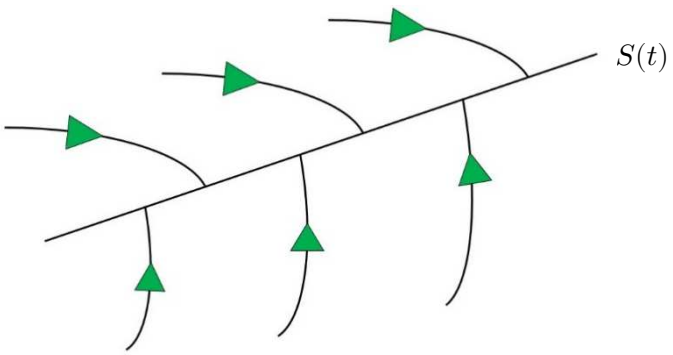

Figure A2-1. The sliding condition

Once on the surface, the system trajectories remain on the surface. In other words, satisfying (A2.3), or sliding condition, makes the surface an invariant set. Furthermore,

A2.3 also implies that in presence of some disturbances or dynamic uncertainties the surface is still invariant. Graphically, this corresponds to the fact that in Figure A2-1, the trajectories can "move" while stil pointing towards the surface.

The other interesting aspect of the invariant set S(t) is that once on it, the system trajectories are defined by $(\frac{d}{dt}+\lambda)^{n-1}\tilde{\tilde{x}}=0$.

The idea behind the conditions (A2.2) and (A2.3), is to select a well defined function of the tracking error, s, according to (A2.2) and then select the feedback control law $u(t)$ that satisfies (A2.3) even in presence of model uncertainties and disturbances [137]. If the initial conditions are not meet it can be demonstrated that the time in reaching the sliding surface would be $t_{reach} \leq s(t=0)/\eta$, and once on the surface, the tracking error tends exponentially to zero, with a time constant $(n-1)/\lambda$.

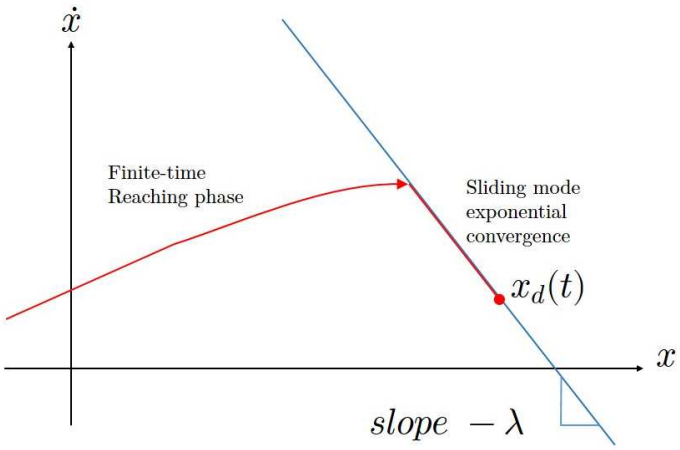

Figure A2-2. Graphical interpretation of equations (A2.2) and (A2.3) (n=2).

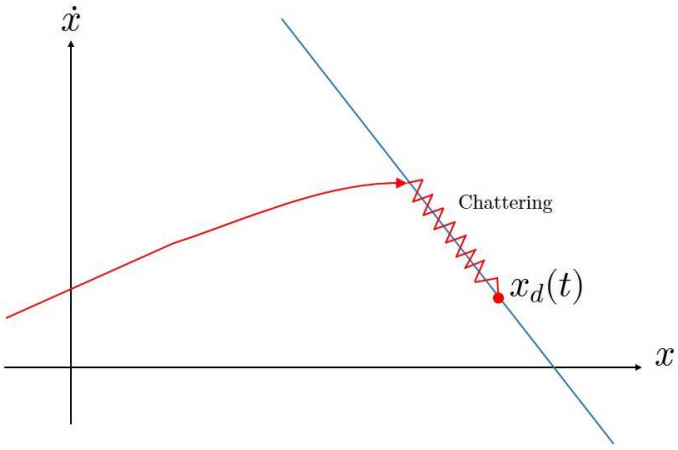

Figure A2-3. Chattering as a result of imperfect control switching.

Control laws that satisfy (A2.3) have to be discontinuous across the sliding surface leading to control chattering. Obviously this approach has to be slightly modified to cope with the lack of knowledge of the complete state space.

Equivalent dynamics

The Filippov's construction of the sliding surface gives a geometric interpretation as an average of the system on both sides of the surface. If the dynamics when in sliding mode can be written as $\dot{s} = 0$. After solving this for the control input it is possible to obtain an expression for u, called equivalent control, u_{eq}, which can be interpreted as the control law that would maintain $\dot{s} = 0$ if the dynamics were exactly known. For example, a system of the form:

$$\ddot{x} = f + u \tag{A2.6}$$

The sliding surface would take the form: $s = \dot{\tilde{x}} + \lambda\tilde{x}$, then $\dot{s} = \ddot{\tilde{x}} + \lambda\dot{\tilde{x}} = 0$, and it yields to: $\ddot{x} = \ddot{x}_d - \lambda\dot{\tilde{x}}$. And (A2.6) will take the new form of:

$$u_{eq} = -f + \ddot{x}_d - \lambda\dot{\tilde{x}} \tag{A2.7}$$

And the system dynamics while in sliding mode is of course,

$$\ddot{x} = f + u_{eq} = \ddot{x}_d - \lambda\dot{\tilde{x}} \tag{A2.8}$$

Geometrically, the equivalent control can be constructed as (A2.9).

$$u_{eq} = \alpha \cdot u_{+} + (1 - \alpha)u_{-} \tag{A2.9}$$

Which correspond to the convex combination of the control action at both sides of the surface $s(t)$.

A basic example

Consider the second order system:

$$\ddot{x} = f + u \tag{A2.10}$$

Where u is the control input, x is the output of interest, and the dynamics f (possibly nonlinear or time-varying) is not exactly known, but estimated as $\hat{f}$. The estimation error on f is assumed to be bounded by some known function F.

$$|\hat{f} - f| \leq F \tag{A2.11}$$

In order to have the system track $x(t) \equiv x_d(t)$, we define a sliding surface $s = 0$, according to (A2.2) as:

$s = (\frac{d}{dt} + \lambda)\tilde{x} = \dot{\tilde{x}} + \lambda\tilde{x}$, and it is possible to yield:

$\dot{s} = \ddot{x} - \ddot{x}_d + \lambda\dot{\tilde{x}} = f + u - \ddot{x}_d + \lambda\dot{\tilde{x}}$, gives the best approximation of a control law $\hat{u}$ that would achieve $\dot{s} = 0$:

$$\hat{u} = -\hat{f} + \ddot{x}_d - \lambda\dot{\tilde{x}} \tag{A2.12}$$

In order to satisfy the sliding condition (A2.3) despite uncertainty on the dynamics f, it is possible to add to $\hat{u}$ a term discontinuous across the surface $s = 0$:

$$u = \hat{u} - k \cdot sgn(s) \tag{A2.13}$$

where $sgn(s)$ is the sign function. And by choosing $k = k(x, \dot{x})$ in (A2.13)to be large enough, it is being guaranteed that (A2.3) is verified. Indeed we have from previous equations:

$$\frac{1}{2}\frac{d}{dt}s^2 = \dot{s} \cdot s = \left[f - \hat{f} - k \cdot sgn(s)\right]s = \left(f - \hat{f}\right)s - k \cdot |s|$$

So that, letting

$$k = F + \eta \tag{A2.14}$$

It yields from (A2.11):

$$\frac{1}{2}\frac{d}{dt}s^2 \leq -\eta|s|$$

As it was desired. It is worth mentioning that the control discontinuity k across the surface $s = 0$ increases with the extent of parametric uncertainty.

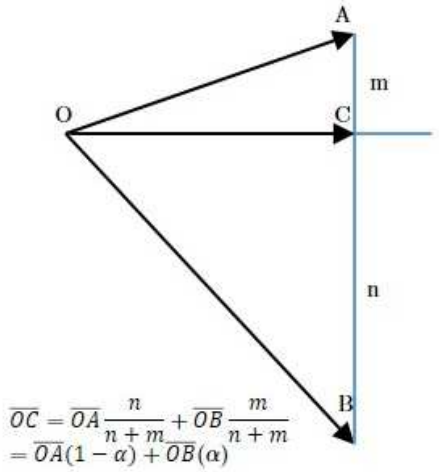

Figure A2-4. Complex combination of two vectors.

ANNEX III: Publications

List of publications and dissemination activities that were published during the realisation of this thesis.

- **Book chapters**

E. del Sol “Designing for Remote Handling”, openSE (an open, lean and participative approach to systems engineering), (in press).

- **Journal publications**

E. del Sol, R. King, R. Scott and M. Ferre. “External Force Estimation for Teleoperation Based on Proprioceptive Sensors”. In: International Journal of Advanced Robotic Systems, 2014, 11:52. doi: 10.5772/58468

E. del Sol, R. Meek, E. Ruiz Morales, R. Vitelli and S. Esqué. “On the control performance of motors driven by long cables for remote handling at ITER”. In: Fusion Engineering and Design (In review).

- **Conferences**

E. del Sol, 2015 “Force estimation based on proprioceptive sensors for teleoperation in radioactive environments”. PURESAFE final conference, CERN, Geneva, Switzerland, January 2015.

E. del Sol, P. Pagala, R. King, and M. Ferre. "External force estimation for telerobotics without force sensor". In Proceedings of the Robot 2013 First Iberian Robotics Conference. 2013, Oct 28-29; Madrid, Spain. Berlin: Springer. vol 2, pp.631-644.

E. del Sol, R. Scott, R. King. "A sensorless virtual slave control scheme for Kinematically dissimilar master-slave teleoperation". In Proceedings of HOTLAB 2012. ISBN: 978-3-668-06270-2

References

[1] CERN, Conseil Européen pour la Recherche Nucléaire, 2014. [Online]. URL http://home.web.cern.ch/about (Accessed 20-06-2014)

[2] European Fusion Development Agreement, 2014. [Online] URL http://www.efda.org/jet/ (Accessed 21/06/2014)

[3] J.M. Shuler. Understanding Radiation Science: Basic Nuclear and Health Physics. First edition, Boca Raton, Florida, USA. Universal-Publishers, 2006. ISBN: 1-58112-907-6.

[4] ICRP, 2007. *The 2007 Recommendations of the International Commission on Radiological Protection*. ICRP Publication 103. Ann. ICRP 37 (2-4)

[5] *Radiation Safety Code, F Rev*. Radiation Protection Documents, CERN, 2006.

[6] M Brugger, The radiological situation in the beam-cleaning sections of the CERN Large Hadron Collider (LHC), Ph.D. dissertation, Inst. Theo. Phys., Graz Tech. University, Graz., 2003.

[7] United Kingdom, The Ionising Radiations Regulations 1999, Health and Safety, 1999 No. 3232, p. 29-32.

[8] T. Honda, Y. Hattori, C. Holloway, E. Martin, Y. Matsumoto, T. Matsunobu, T. Suzuki , A. Tesini, V. Baulo, R. Haange. "Remote handling systems for ITER". In *Fusion Engineering and Design*, vol. 63, pp. 507–518, 2002.

[9] H. Lida. Dose Rate Estimate around the Divertor Cassette after Shutdow. ITER Joint Work Site, Max-Planck-Inst. f. Plasmaphysik, Munich, Germany, Analysis Report ITER_D_24VFBN, Oct, 2006.

[10] K. Shibanuma and T. Honda. " ITER R&D Remote handling systems: Blanket remote handling systems". In *Fusion Engineering and Design*, vol. 55, pp. 249–257, 2001.

[11] EFDA ITER. *Iter design description document - remote handling equipment - wbs23*. Technical report, EFDA, ITER, 2001.

[12] A. Fernandez, F. Berghmans, B. Brichard, and M. Decréton. "Towards the development of radiation-tolerant instrumentation data links for thermonuclear fusion experiments". In *IEEE Transations Nuclear Science*, vol. 49, no. 6, pp. 2879–2887, Dec. 2002.

[13] R.Villari, P. Batistoni, S.Conroy, A. Manning, F. Moro, L. Petrizzi, S. Popovichev and D.B. Syme. "Shutdown Dose Rate Benchmark Experiment at JET to Validate the Three-Dimensional Advanced-D1S Method". In *Fusion Engineering and Design*, vol. 87, no. 3, 2012.

[14] K. Kershaw, B. Feral, J.-L. Grenard, T. Feniet, S. D. Man, C. Hazelaar-Bal, C. Bertone and R. Ingo. "Remote Inspection, Measurement and Handling for Maintenance and Operation at CERN". In *International Journal of Advanced Robotic Systems*, 2013, 10:382. doi: 10.5772/56849

[15] A. C., Rolfe, P. Brown, P. Carter, R. Cusack, A. Gaberscik, L. Galbiati, B. Haist, R. Horn, M. Irving, D. Locke, A. Loving, P. Martin, S. Mills, R. Minchin, J. Palmer, S. Sanders, S.G Sanders, R. Stokes. "A report on the first remote handling operations at JET". In Fusion Engineering and Design, vol. 46, no. 2, pp. 299–306, 1999.

[16] A. Tesini, J. Palmer. "The ITER remote maintenance system". In *Fusion Engineering and Design*, vol. 83, no. 7, pp. 810–816, 2008.

[17] G. Dubus, O. David, Y. Measson, F.-X. Russotto, J.-P. Friconneau . "Development of a water hydraulics remote handling system for ITER maintenance". In *Proceedings of the IARP/EURON Workshop on Robotics for Risky Interventions and Environmental Surveillance*. 2008 Jan. 7-8; Benicassim, Spain. pp. 145-148, 2008.

[18] Muhammad A., S. Esque, J. Mattila, M. Tolonen, P. Nieminen, O. Linna, M. Vilenius, M. Siuko, J. Palmer, M. Irving. "Development and design of Water Hydraulic Remote Handling System for ITER". In *Symposium on Fusion Technology (SOFT)*. 2009 Jun. vol. , pp. 1-4.

[19] J. K. Lee, K. Kim ; B. S. Park ; J. S. Yoon. "Force-reflecting servo-manipulators for remote handling task in radioactive environments". In: *Proceedings of International Conference on Control, Automation and Systems*, 2007, 17-20 Oct.; Seoul, Korea. New York: IEEE Press. pp. 1025-1028.

[20] R. J. Stone "Haptic feedback: a brief history from telepresence to virtual reality". In: *Proceedings on the first international workshop on haptic human-computer interaction*, Glasgow, UK, 31-Aug., 1-Sept. Springer: Berlin. pp. 1-16. 2001.

[21] R. Sharp and M. Decréton. "Radiation tolerance of components and materials, in nuclear robot applications," *Reliability Engineering & System Safety*, vol. 53, pp. 291–299, 1996.

[22] Soichiro, Shigematsu. *Blanket Remote Handling System R&D reports*, IDM UID 3V8UDF.

[23] EFDA, *ITA Task Final Report, Rad-hard Programme: Evaluation of rad-hard COTS components for RH equipment, CMM in particular.*

[24] V. Ganti, "Analysis of 4-dof force/torque sensor for intelligent gripper", B.Tech. thesis, Mech. Eng. Dept., Nat. Inst. of Tech., Rourkela, Orissa, 2011.

[25] M. Fassler. *Force Sensing technologies, Studies on Mechatronics.* ETH, Autonomous System Laboratory, 2010. (Available in: http://www.sensorzine.com/force-sensing-technologies-on-mechatronics-1208.html)

[26] C.L. Hanks and D. J. Hamman. *Radiation Effects Design Handbook*, NASA Report. Washington D.C., 1971.

[27] Frank M. Heckerdorn. *Radiation Hardness design manual for the ITER. Appendix A-1.* European Home Team Radiation Hardness Development Report, Dec 1997.

[28] G. Piolain, F. Geffard, A. Coudray, P. Garrec, J.F. Thro, Y. Perrot. "Dedicated and standard industrial robots used as force-feedback telemaintenance remote devices at the Areva recycling plant". In *Proceedings of 1st International Conference of Applied Robotics for the Power Industry (CARPI). Montreal, Canada.* Oct., 2010. doi: 10.1109/CARPI.2010.5624418

[29] ATI Industrial Automation (2011). Customized F/T Transducers [Online]. URL http://www.ati-ia.com/products/ft/ft_CustomApps.aspx. [Accessed 16-07-2014]

[30] P. Nieminen, S. Esque, A. Muhammada, J. Mattilaa, J. Väyrynena, M. Siukob, M. Vileniusa., "Water Hydraulic Manipulator for Fail Safe and Fault Tolerant Remote Handling Operations at ITER", Fusion Eng. Design, vol. 84, 1420–1424, 2009.

[31] J. Verbeeck, Y. Cao, M. V. Uffelen, L. Mont Casellas, C. Damiani, R. Meek, B. Haist, M. Steyaert, and P. Leroux. "A MGy Radiation-Hardened Sensor Instrumentation SoC in a Commercial CMOS Technology". In *IEEE Nuclear and Space Radiation Effects Conference.* Paris, France, July 14-18, 2014.

[32] ITER, Japan Home Team. *Iter Task Agreement S 72 TT 14 95-04-11 FJ: Irradiation Testing of Standard Components (T252)*, Japan, 1998.

[33] P. Fischer, R. Daniel, K.V. Siva. "Specification and design of input devices for teleoperation". In *IEEE International Conference on Robotics and Automation, Proceedings.*1990, vol. 1 pp. 540–545.

[34] G. Cody, B. Russell, A. White, M. Miller, and A. Stoytchev. "An effective and intuitive control interface for remote robot teleoperation with complete haptic feedback." In *proceedings of the Emerging Technologies Conference-ETC.* 2009.

[35] Siciliano, Bruno, and Oussama Khatib, eds. Springer handbook of robotics. Springer Science & Business Media, 2008. pp. 741-771.

[36] P. F. Hokayem , M.W. Spong. "Bilateral teleoperation: An historical survey". *Automatica*, vol. 42, no. 12, pp. 2035–2057.

[37] A.K. Bejczy. *Towards advanced teleoperation in space.* In Teleoperation and robotics in space, Prog. Astronaut. Aeronaut. 1994 , vol. 161, ed. by Skaar S.B., Ruoff C.F. (American Institute of Aeronautics and Astronautics, Preston 1994), pp 107-138.

[38] T. B. Sherindan. "Teleoperation, telerobotics and telepresence: A progress report". In *Control Engineering Practice*, 1995 vol.3 pp. 205-214.

[39] G. Dogangil, B.L. Davies and F. Rodriguez y Baena. "A review of medical robotics for minimally invasive soft tissue surgery". In *Proceedings of the Institution of Mechanical Engineers, Part H: Journal of Engineering in Medicine.* 2010 224(5):653-79.

[40] B.M. Yamauchi. "PackBot: A versatile platform for military robotics", In *Defense and Security, International Society for Optics and Photonics.* 2004, 228-237.

[41] H. G. Nguyen, J.P. Bott. *Robotics for Law Enforcement: Beyond Explosive Ordnance Disposa.*Technical Report, SPAWAR Systems Center, San Diego, CA, 2000.

[42] S. C. Jacobsen, F. M. Smith, D. K. Backman, and E. K. Iversen. "High performance, high dexterity, force reflective teleoperator". In *Proceedings of 38th Conference Remote Systems Technology.* Washington, DC, 1990, pp. 180–185.

[43] L.F. Peñin, R. Aracil, M.Ferre, E. Pinto, M. Hernando, A. Barrientos. "Telerobotic system for live-power line maintenance: ROBTET". In *Control Engineering Practice*, 1998, vol. 10, pp. 1271-1281.

[44] Oxford Technologies Ltd. internal report. *JAC-436-REP-001 A TR12 ITER Standard WorkCell- Final Report*, 2011.

[45] Simone Marchesi, Antonio Frisoli, Carlo Alberto Avizzano and Massimo Bergamasco. "A method for modeling and control complex tendon transmissions in haptic interfaces". In *Proceedings of the 2005 IEEE International conference on Robotics and Automatio.* Barcelona, Spain, April 2005.

[46] D. Hamilton. *RH Control System Standard Parts Catalogu.* ITER, Report A6CMLW, Jun. 2012.

[47] D.A. Lawrence. "Stability and transparency in bilateral teleoperation". In *IEEE Transations on Robotics and Automation.* vol. 9, no. 5, pp. 624-637.

[48] D.G. Alciatore, R. Miranda. *A winding number and Point-in-Polygon Algorithm.* Technical report, Department of Mechanical Engineering Colorado State University, Fort Collins, CO, 1995.

[49] A.C. Rolfe, P. Brown, P. Carter, R. Cusack, A. Gaberscik, L. Galbiati and R. Stokes. "A report on the first remote handling operations at JET". In *Fusion Engineering and Design.* 1999, vol. 46, no. 2, pp. 299–306.

[50] O. David, A.B. Loving, J.D. Palmer, S. Ciattaglia and J.P. Friconneau. "Operational experience feedback in JET Remote Handling". In *Fusion Engineering and design.* 2005, vol. 75, pp. 519–523.

[51] K. Kershaw. "Remote Inspection , Measurement and Handling Applied to Maintenance and Operation at CERN". In *International Journal of Advanced Robotic Systems.* 10.382 (2013): 1-11., Available: http://www.intechopen.com/books/international_journal_of_advanced_robotic_systems/remote-inspection-measurement-and-handling-for-maintenance-and-operation-at-cern.

[52] R. Lundqvist, T. Söreling. "New Interface for Rapid Feedback Control on ABB-robots". A Master Thesis in Sensor-Integrated Industrial Robot Control at Linköping Institute of Technology, Department of Mechanical engineering, Division of Production Systems, Linköping, 2005.

[53] T. Maruyama, A. Aburadani, N. Takeda, S. Kakudate, M. Nakahira, A. Tesini. "Robot vision system R&D for ITER blanket remote-handling system". In *Fusion Engineering and Design*, 89.9 (2014): 2404-2408.

[54] P. Nieminen, S. Esque, A.Muhammad, J. Mattila, J. Väyrynen, M. Siuko, M. Vilenius." Water hydraulic manipulator for fail safe and fault tolerant remote handling

operations at ITER". In: Fusion Engineering and Design. 2009, vol. 84, no. 7, pp. 1420-1424.

[55] N. Skyes, C. Belcher, C.H. Choi, O. Crofts, R. Crowe, C. Damiani, S. Delavalle, L. Meredith, T. mindham, J. Raimbach, A. Tesini, M. V. Uffelen. "Status of ITER Neutral Beam Cell Remote Handling System". In *Fusion Engineering and Design. 2013,* 88.9, 2043-2047.

[56] R. Bogue. "Robots in the nuclear industry: a review of technologies and applications". *Industrial Robot: An International Journal*. 2011, vol. 38 Iss 2 pp. 113 - 118.

[57] L. A. Cooney. "Development of a Low-Cost underwater manipulator". PhD dissertation, Massachusetts Institute of Technology, 2006.

[58] Farum, Energy Technologies. TA40 manipulator. URL http://www.f-e-t.com/images/uploads/A001-350-044_iss_8_TA40_Manipulator.pdf [Accessed 10-08-2014].

[59] P.T. Spampinato, E.C. Bradley, T.W. Burgess, J.B. Chesser, V.B. Graves, M.J. Rennich. "Remote Handling Systems Development for the Spallation Neutron Source Target System". No. P04-119468. ORNL, 2004.

[60] Buss, Martin, Rafael Aracil, Claudio Melchiorri, and Carlos Balaguer, eds. *Advances in telerobotics.* Vol. 31. Heidelberg: Springer, 2007, 166p.

[61] International Atomic Energy Agency. *Remote technology applications in spent fuel management.* IAEA-TECDOC-1433, 2005.

[62] P. Desbats, P. Garrec, Y. Perrot, Y. Measson, F. Geffard, O. David, L. Gargiulo, J.-M. Idasiak, and G. Piolain "Overview of robotic technologies for nuclear hazardous environments". In *Proceedings of ANS Joint topical meeting. Emergency Management & Robotics for Hazardous Environments.* 2008, pp. 9-12.

[63] S.H. Ahn, J.H. Jin and J.S. Yoon. "Development of a Teleoperated Manipulator System for Remote Handling of Spent Fuel bundles". In *Nuclear Engineering and Technology.* 2003, 35, no. 3, 214-225.

[64] P. Desbats, F. Geffard, G. Piolain and A. Coudray. "Force-feedback teleoperation of an industrial robot in a nuclear spent fuel reprocessing plant". In *Industrial Robot: An International Journal. 2006, 33, no. 3, 178-186.*

[65] F. Gosselin, A. Riwan. "Design of Virtuose 3D: a new haptic interface for teleoperation and virtual reality". *In Proceedings of ICAR.* 2001 pp. 205-212.

[66] E. Del Sol, P. Pagala, R. King, and M. Ferre. "External force estimation for telerobotics without force sensor". In *Proceedings of the Robot 2013 First Iberian Robotics Conference.* 2013, Oct 28-29; Madrid, Spain. Berlin: Springer. vol 2, pp.631-644.

[67] T. Raimondi and L. Galbiati. "Manipulators Mascot IV Used in Jet and Prospects of Enhancement". *Teleoperation: Numerical Simulation and Experimental Validation*. Springer Netherlands, 1992. 139-161.

[68] B. Schott, K. Hendrich, K. Doering, H. Bressem. "First operation experience with the electrical master slave manipulator EMSM3." In *Proceedings 7th international topical meeting on robotics and remote systems*. 1997 April, Augusta Georgia (USA).

[69] E. del Sol, R. King, R. Scott and M. Ferre. "External Force Estimation for Teleoperation Based on Proprioceptive Sensors". In *International Journal of Advanced Robotic Systems*, 2014, 11:52. doi: 10.5772/58468

[70] B. Hannaford, L. Wood, D.A. McAffee and H. Zak. "Performance evaluation of a six-axis generalized force-reflecting teleoperator," *In IEEE Transactions on Systems, Man and Cybernetics*, vol.21, no.3, pp.620,633, May/Jun 1991 doi: 10.1109/21.97455

[71] J. Barrio, M. Ferre, F. Suárez-Ruiz, R. Aracil. "A remote handling rate-position controller for telemanipulating in a large workspace". In Fusion Engineering and Design. 2014, 89(1), 25-28.

[72] E. Del Sol, R. Scott, R. King. "A sensorless virtual slave control scheme for Kinematically dissimilar master-slave teleoperation". In *Proceedings of HOTLAB 2012.*

[73] M.T. White, M, Tomizuka, and C, Smith. "Improved track following in magnetic disk drives using a disturbance observer." In *IEEE/ASME Transactions on Mechatronics. 2000,* no. 5 , pp. 3-11.

[74] A. Sabanovic and I. Khalil. *Sensorless Torque/Force Control*. Advances in Motor Torque Control, Dr. Mukhtar Ahmad, editors. 2011, InTech, DOI: 10.5772/20741. Available:http://www.intechopen.com/books/advances-in-motor-torque-control/sensorless-torque-control

[75] K. Fujiyama, R. Katayama, T. Hamaguchi, and K.Kawakami. "Digital controller design for recordable optical disk player using disturbance observer." In *IEEE Proceedings of 6th International Workshop on Advanced Motion Control.* 2000 , pp. 141-146.

[76] M. Nakao, K. Ohnishi, and K. Miyach. "A robust decentralized joint control based on interference estimation". In *Proceedings on IEEE International Conference on Robotics and Automation*. 1997, vol. 4, pp. 326-331.

[77] Murakami T et al. (1993) Torque sensorless control in multidegree of freedom manipulator. In: IEEE Trans. on ind. elec., vol. 40, no 2, pp. 259-265.

[78] K. Ohnishi, S. Masaaki and M. Toshiyuki. "Motion Control for advanced mechatronics". *IEEE/ASME Transactions on Mechatronics*. 1996, vol. 1, no 1, pp. 56-67.

[79] S. Nicosia and P. Tomei. "Robot Control by using only joint position measurements". In *IEEE Transactions on Automatic Control*, 1990, vol. 35 no. 9, pp.1058-1061.

[80] P. J. Hacksel and S. E. Salcudean, Estimation of environmental forces and rigid body velocities using observers, Department of electrical engineering, University of British Columbia.

[81] A. Alcocer, A. Robertsson, A. Valera, and R. Johansson. "Force Estimation and control in robot manipulators". In *Proceedings of the 7th Symposium on Robot Control (SYROCO 2003)*. 2003 Sept. 1-3. Wroclaw, Poland. pp. 31-36.

[82] A. Colome, D. Pardo, G. Alenya, and C. Torras. "External force estimation during compliant robot manipulation". In *IEEE International Conference on Robotics and Automation (ICRA)*. 2013, May 6-10; Karlsruhe, Germany, pp. 3535, 3540.

[83] C.J. Kempf and S. Kobayashi. "Disturbance observer and feedforward design for high-speed direct-drive position table". In: IEEE Transactions on Control System Technology. 1999, vol. 7, pp. 513-526.

[84] K.S. Eom, H.S. Il , and K.C. Wan. "Disturbance observer based path tracking of robot manipulator considering torque saturation". In *Mechatronics*. 2000, vol. 11, pp. 325-343.

[85] X. Chen, F. Toshio and K.D. Young. "A new nonlinear robust disturbance observer." In *Systems & Control Letters 41*. 2000, no. 3 189-199.

[86] J.R. Ryoo, D. Tae-Yong, and J.C. Myung. "Robust disturbance observer for the track-following control system of an optical disk drive". In *Control Engineering Practice*. 2004, vol. 12, pp. 577-585.

[87] S. Komada, N. Machii, T. Hori. "Control of redundant manipulators considering order of disturbance observer". In *IEEE Transations on Industrial Electronics*. 2000, vol. 47, pp. 413-420.

[88] Liu, Chia-Shang, and Huei Peng. "Inverse Dynamics Based State and Disturbance Observers for Linear Time-Invariant Systems". In *Journal of Dynamics systems Measurement and Control. 2002,* vol. 124, pp 375-381.

[89] K.S. Eom, I.H. Suh, W.K. Chung, and S.R. Oh. "Disturbance observer based force control of robot manipulator without force sensor". In P*roceedings of IEEE international conference on Robotics and Automation.* New York: IEEE Press. 1998, pp. 3012-3017.

[90] K. Ohishi, M. Miyazaki, M. Fujita and Y. Ogino. "Hinf observer based force control without force sensor". In *Proceedings of Industrial Electronics, Control and Instrumentation*. 1991. IECON'91., 1991 International Conference on Industrial Electronics, Control and Instrumentation, pp. 1049-1054.

[91] L. Sang-Chul, Ahn. Hyo-Sung. "Sensorless Torque Estimation using adaptive Kalman filter and Disturbance estimator". In *IEEE/ASME International Conference on Mechatronics and Embedded Systems and Applications (MESA).* 2010, pp. 87-92.

[92] C. Canudas de Wit and J. J. E. Slotine, Sliding observers for robot manipulators, Automatica, Vol 27, No 5, pp 859-864

[93] J.M. Daly and D. W. Wang. "Bilateral teleoperation ising unkown input observers for force estimation". In *IEEE American Control Conference*, ACC'09. 2009, pp. 89-95.

[94] W. Wang and Z. Gao. "A comparison study of advanced state observer design techniques". In *Proceedings of the 2003 American Control Conference*. IEEE, 2003, vol. 6, pp. 4754-4759).

[95] H.K. Khalil. "High-gain observers in nonlinear feedback control. New directions in nonlinear observer design". In *Lecture Notes in Control and Information Sciences. 1999,* vol. 24, no. 4, pp. 249-68.

[96] J. Han. "A class of extended state observers for uncertain systems". In Automatica. 1998, vol. 34, no. 6, pp. 757-764.

[97] J.G. García, A. Robertsson, J. G. Ortega y R. Johansson. "Estimacion de la fuerza de contacto para el control de robots manipuladores con movimientos restringidos". RIAII, 2007, vol. 4. no. 1, pp. 70-82.

[98] J.G. Garcia, A. Robertsson, A. Valera, R. Johansson. "Sensor fusion for compliant robot motion control". In IEEE Transactions on Robotics. 2008, vol. 24, no. 2, pp. 430-441.

[99] Ishikawa, T.; Sakane, S.; Sato, Tomomasa; Tsukune, H., "Estimation of contact position between a grasped object and the environment based on sensor fusion of vision and force". In IEEE/SICE/RSJ International Conference on Multisensor Fusion and Integration for Intelligent Systems. 1996, pp. 116-123. IEEE, 1996. doi: 10.1109/MFI.1996.572167

[100] Y. Zhou, B.J. Nelson, B. Vikramaditya. "Fusing force and vision feedback for micromanipulation". In Proceedings of the IEEE International Conference on Robotics and Automation. 1998, vol.2, pp.1220,1225, 16-20 May 1998. doi: 10.1109/ROBOT.1998.677265

[101] T. Kröger, D. Kubus, F.M. Wahl. "Force and acceleration sensor fusion for compliant manipulation control in 6 degrees of freedom". In *Advanced Robotics*. 2007, vol. 21 no.14, pp.1603-1616.

[102] R. A. Horne et al. (1978) "MANTIS: a compact mobile remote handling system for accelerator halls and tunnels". In *Transactions American Nuclear Society*, 30 (1978) pp.758-9

[103] M. Radi. *Workspace scaling and haptic feedback for industrial telepresence and teleaction systems with heavy-duty teleoperators*. Vol. 261. Herbert Utz Verlag, 2012.

[104] A. Khalifa, A. Ramadan, K. Ibrahim, M. Fanni, S. Assal and A. Abo-Ismail. "Workspace mapping and control of a teleoperated endoscopic surgical robot." In: 19th International Conference On *Methods and Models in Automation and Robotics (MMAR)*. 2014 pp. 675-680. IEEE.

[105] ABB. *RAPID reference manual, BaseWare, RobotWare-OS 4.0, 3HAC 7774-1, Revision A.*

[106] M.M. Dalvand, S. Nahavandi. "Improvements in Teleoperation of Industrial Robots without Low-Level Access". In: *2014 IEEE International Conference on Systems, Man and Cybernetics (SMC). 2014,* pp. 2170-2175. IEEE.

[107] T. Yoshikawa. "Manipulability and redundancy control of robotic mechanisms." In: Proceedings of the 1985 IEEE International Conference on*Robotics and Automation. 1985,* vol. 2, pp. 1004-1009. IEEE.

[108] D. Kubus, A. Sommerkorn, T. Kroger, J. Maaß, and F. M. Wahl. "Low-level control of robot manipulators: distributed open real-time control architectures for Staubli, RX and TX Manipulators." *In IEEE International Conference on Robotics and Automation (ICRA),* May, pp. 38-45. 2010.

[109] P. K. Artemiadis, and K. J. Kyriakopoulos. "Teleoperation of a Robot Arm in 2D Catching Movements using EMG Signals and a Bio-inspired Motion Law". In: The First IEEE/RAS-EMBS International Conference on Biomedical Robotics and Biomechatronics, 2006. BioRob 2006. , pp. 41-46. IEEE.

[110] V. Lippiello, L. Villani, and B. Siciliano, "An open architecture for sensory feedback control of a dual-arm industrial robotic cell". In: *Industrial Robot: An International Journal. 2007,* vol. 34, no. 1, pp. 46–53.

[111] A. Albu-Schaffer, C. Ott, and G. Hirzinger, "A unified passivity-based control framework for position, torque and impedance control of flexiblejoint robots," The International Journal of Robotics Research. 2007, vol. 26,no. 1, pp. 23–39.

[112] F. Pertin and J. Bonnet des Tuves. "Real time robot controller abstraction layer". In: *Proceedings of the International Symposium on Robotics 2004.*

[113] J.L. Blackburn. *Symmetrical Components for Power Systems* Engineering. CRC Press, 1993. ISBN 0-8247-8767-6.

[114] R. Featherstone. *Rigid body dynamics algorithms.* The Austrailian National University, Camberra, ACT, Australia. Springer . ISBN 978-0-387-74314-1

[115] J. Swevers, W. Verdonck, J.D. Schutter. "Dynamic model identification for industrial robots". In: *IEEE Control Systems Magazine.* 2007, vol 10, pp.58-71.

[116] N.D. Vuong, and H. Marcelo Ang Jr. "Dynamic model identification for industrial robots." *Acta Polytechnica Hungarica 6.* 2009, no. 5, pp. 51-68.

[117] V. Mata, B. Francesc, F. Nidal, A. Valera. "Dynamic parameter identification in industrial robots considering physical feasibility". In: *Advanced Robotics. 2005,* vol. 19, no 1, pp. 101-119.

[118] Atkeson, G. Christopher, C. H. An, and J. M. Hollerbach. "Estimation of inertial parameters of manipulator loads and links." In: *The International Journal of Robotics Research.* 1983, vol. 5, no. 3, pp. 101-119.

[119] J. Hollwebach, W. Khalil, M. Gautier. "Model identification". Siciliano B, Khatib O, editors. *Handbook of robotics.* Berlin: Springer, 2008. pp 321 -340.

[120] B. Amstrong. "On finding exciting trajectories for identification experiments involving systems with nonlinear dynamics". In: International journal of robotics research". 1986, vol 8, no. 6, pp.28-48.

[121] Schittkowski K (2002) NLPQL: A New Fortran Implementation of a Sequential Quadratic Programming Algorithm – User's Guide, Department of Mathematics, University of Bayreuth.

[122] M. Gautier. "Numerical calculation of the base inertial parameters of robots". In: *Proceedings of the IEEE International Conference on Robotics and Automation.* 1990 , vol. 2, pp. 1020-1025. doi: 10.1109/ROBOT.1990.12612

[123] H. B. Olsen and G. A. Bekey, Identification of robot dynamics, presented at: 1986 IEEE International Conference on Robotics and Automation, San Francisco, CA (1986).

[124] C.G. Atkeson, C.H. An and J.M. Hollerbach. "Estimation of inertial parameters of manipulator loads and links". In: *International journal of robotics research.* 1986, vol. 5, pp. 101–119.

[125] M. Gautier and C. Presse. "Sequential identification of base parameters of robots". In: *Advanced Robotics*, 1991. Fifth International Conference on Robots in Unstructured Environments, 91 ICAR,IEEE, 1991, pp. 1105-1110.

[126] S.K. Lin. "An identification method for estimating the inertia parameters of a manipulator". In: Journal of Robotics Systems. 1992, vol. 9, pp. 505–528.

[127] K. Otani and T. Kakizaki. "Motion planning and modeling for accurately identifying dynamic parameters of an industrial robotic manipulator". In: *Proceedings of the international symposium on industrial robots.* International federation of robotics, & robotic industries. 1993, vol. 24, pp. 743-743. .

[128] B. Armstrong, On finding exciting trajectories for identification experiments involving systems with nonlinear dynamics, Int. J. Robotics Res. 8, 28–48 (1989).

[129] C. Presse and M. Gautier. "New criteria of exciting trajectories for robot identification". In: Conference on Robotics and Automation, Atlanta, CA 1993.

[130] J. Swevers, C. Ganseman, D. B. Tukel, J. DeSchutter and H. VanBrussel. "Optimal robot excitation and identification". In: *IEEE Transactions on Robotics and Automation.* 1997, vol. 13, pp. 730–740.

[131] J. Swevers, C. Ganseman, J. DeSchutter and H. VanBrussel. "Generation of periodic trajectories for optimal robot excitation". In: Journal of Manufacturing Science Engineering Transations, ASME 119. 1997, 611–615.

[132] G. Liu. "On velocity estimation using position measurements". In: *Proceedings of the american control conference,* Anchorage, AK May 8-10. 2002, vol. 2, pp. 1115-1120.

[133] F. Janabi-Sharifi, V. Hayward, C-S.J. Chen. "Discrete-time adaptive windowing for velocity estimation". In: IEEE Transactions on *Control Systems Technology.*2000, vol.8, no.6, pp.1003-1009. doi: 10.1109/87.880606

[134] A. Jaritz, M.W. Spong. "An experimental comparison of robust control algorithms on a direct drive manipulator". In: IEEE Transactions on Control Systems Technology. 1996, vol.4, no.6, pp.627-640. doi: 10.1109/87.541692

[135] P.R. Belanger, P.Dobrovolny, A. Helmy, and X. Zhang. "Estimation of angular velocity and acceleration from shaft-encoder measurements." *The International Journal of Robotics Research.* 1998, vol. 17, no. 11, pp. 1225-1233.

[136] A.SI. Zinober. *Deterministic control of uncertain systems*. No. 40. IET, 1990.

[137] J.-J. E. Slotine, J.K. Hedrick, E.A. Misawa, On sliding Observers for Nonlinear Systems. Journal of Dynamics Systems, Measurement and Control, Sept. 1987, vol 109/245.

[138] J.J.E. Slotine, and S.S. Sastry. "Traking control of nonlinear systems using sliding surfaces, with application to robot manipulators". In: International Journal Control. 1983, vol. 38. p. 465.

[139] Allen-Bradley, Power Flex 40, Adjustable frequency AC Drive, User manual. Rockwell Automation, FRN 1.xx - 6.xx.

[140] Delta Tau Geo MACRO Drive 500-603701-xUxx, User manual.

[141] ABB, ACES 150 drive, User manual.

[142] L. Saunders, G.L. Skibinski, T.E. Steve, and D. L. Kempkes. "Riding the reflected wave-IGBT drive technology demands new motor and cable considerations." In: Petroleum and Chemical Industry Conference, 1996, Record of Conference Papers. The Institute of Electrical and Electronics Engineers Incorporated Industry Applications Society 43rd Annual. IEEE, 1996, pp. 75-84.

[143] R. Kerkman R., Leggate D, Skibinski G, Interaction of Drive Modulation and Cable Parameters on AC motor transients", IEEE Industry Application Conf, Oct. 1996.

[144] B. Drury. "The Control Techniques Drives and Controls Handbook". The Institution of Engineering and Technology. 2nd edition. no. 35, IET 2001.

[145] R. Gambica. *Motor insulation voltage stresses under PWM Inverter Operation*, *Technical Report no.1*, 3rd Edition.

[146] C. Y. Seng, Z. Ibrahim. "Vector controlled drives of Permanent Magnet Synchronous Motor Using PI Speed Controller for Long Cable Application" In: 2011 IEEE Student Conference on Research and Development. 2011, pp. 381-385.

[147] Jiangbiao He, Gennadi Y Sizov et al., A Review of Mitigation Methods for Overvoltage in Long-Cable-Fed PWM AC Drives. Dept. of Electr. & Comput. Eng., Marquette Univ., Milwaukee, WI, USA. Energy Conversion Congress and Exposition (ECCE), 2011 IEEE.

[148] GEO Direct PWM Amplifier Installation manual, 2013. 500-603700-xIxx, 5 November 15, 2013.

[149] V. Naumanen, J. Korhonen, P. Silventoinen, and J. Pyrhonen. "Mitigation of high du/dt-originated motor overvoltages in multilevel inverter drives". In: *IET Power Electronics*. 2010, vol. 3, no. 5, pp. 681-689.

[150] S. Lee, and K. Nam. "An overvoltage suppression scheme for AC motor drives using a half dc-link voltage level at each PWM transition". In: *IEEE Transactions on Industrial Electronics. 2002,* vol. 49, no. 3, pp. 549-557.

[151] J. Luszcz. "Motor Cable Effect on the Converter-Fed AC Motor Common Mode Current". In: 2011 7th International Conference-Workshop of *Compatibility and Power Electronics (CPE). 2011,* pp. 445-450. IEEE.

[152] B. Hannaford and A. M. Okamura. Chapter 30: Haptics. In B. Siciliano and O Khatib editor, Springer Handook of robotics, pages 719-739. Springer, 2008.

[153] D.L. Pieper. "The kinematics of manipulators under computer control". No. CS-116. Stanford Univ Ca Dept Of Computer Science, 1968.

[154] Filippov, A. F. , Transations of the American Mathematics Society. 1960, vol. 62, p. 199.